Technische Universität München
Institut für Energietechnik

Lehrstuhl für Thermodynamik

Influence of Acoustically Induced Vorticity Perturbations on High-Frequency Thermoacoustic Instabilities in Gas Turbine Combustors

Thomas Erich Hofmeister

Vollständiger Abdruck der von der Fakultät für Maschinenwesen der Technischen Universität München zur Erlangung des akademischen Grades eines

DOKTOR – INGENIEURS

genehmigten Dissertation.

Vorsitzender:
Prof. Dr. Marco Caccamo
Prüfer der Dissertation:
1. Prof. Dr.-Ing. Thomas Sattelmayer
2. Assoc. Prof. Dr.-Ing. Mirko Bothien

Die Dissertation wurde am 15.04.2021 bei der Technischen Universität München eingereicht und durch die Fakultät für Maschinenwesen am 28.06.2021 angenommen.

Vorwort

Diese Arbeit entstand in den Jahren 2018 bis 2021 im Rahmen meiner Tätigkeit als wissenschaftlicher Mitarbeiter am Lehrstuhl für Thermodynamik der Technischen Universität München. Sie wurde von der Deutschen Forschungsgemeinschaft (DFG) gefördert.

Mein besonderer Dank gilt meinem Doktorvater Herrn Prof. Dr.–Ing. Thomas Sattelmayer für die Möglichkeit unter seiner Betreuung promovieren zu dürfen. Sein Input inspirierte mich zur Entwicklung und Umsetzung neuer Ideen, die maßgeblich zum Erfolg dieser Arbeit beigetragen haben.

Herrn Assoc.-Prof. Dr.–Ing. Mirko Bothien danke ich für die freundliche Übernahme des Koreferates und Herrn Prof. Dr. Marco Caccamo für den Vorsitz bei der mündlichen Prüfung.

Außerdem möchte ich mich bei Dr.–Ing. Tobias Hummel bedanken, der mich 2017 beim Verfassen meiner Master's Thesis betreut und mich zur Fortsetzung seines Forschungsprojektes am Lehrstuhl für Thermodynamik ermutigt hat. Ohne sein Vertrauen in mich hätte ich diese Reise wahrscheinlich nicht begonnen.

Ein ganz besonderer Dank geht auch an meine Kolleginnen und Kollegen für die tolle Zeit am Lehrstuhl. Viele sind auch zu sehr guten Freunden geworden. Ich möchte an dieser Stelle auch gar nicht anfangen einzelne Personen zu nennen, da die Liste wohl zu lang für dieses kurze Vorwort wäre. Durch unzählige fachliche Diskussionen, Treffen und Partys in und außerhalb des Lehrstuhls habt Ihr meine Zeit am Lehrstuhl zu einer der schönsten in meinem Leben gemacht – und das trotz erschwerter Bedingungen durch COVID-19.

Meine drei Korrekturleser Gerrit Heilmann, Pedro Romero und Jonathan McClure möchte ich auch nicht unerwähnt lassen, da sie erheblich zur Qualität dieser Dissertation beigetragen haben. An dieser Stelle ein ganz besonderer Dank an Gerrit Heilmann.

Ebenso möchte ich mich bei meinen Studenten bedanken, die mich während meiner Promotion begleitet haben.

Liebe Claudia, du hast mich immer unterstützt und an mich geglaubt. Dafür danke ich Dir von ganzem Herzen.

Zuletzt bedanke ich mich bei meiner Familie, die mir immer zur Seite steht. Ich bin froh, Euch als sicheren Hafen zu haben, zu dem ich jederzeit zurückkehren kann.

München, im Juli 2021 Thomas Hofmeister

Abstract

The goal of this work is to provide a reliable and time-efficient computational tool for the prediction of high-frequency thermoacoustic instabilities in lean-premixed gas turbine combustors. A stability analysis strategy is proposed, which unfolds into three steps: #1 assessment of the linear thermoacoustic stability, #2 analysis of limit-cycle oscillations as well as identification of non-linear saturation effects and #3 consideration of modal interactions between multiple unstable acoustic eigenmodes. Particular focus is put on the correct incorporation of the influence of acoustically induced vorticity disturbances on the thermoacoustic stability behavior to these three analysis steps. This is achieved by the integration of new models as well as by removing numerical errors in stability computations. Fundamental numerical studies together with the application of decomposition methods provide detailed physical insight into the dynamical behavior of high-frequency thermoacoustic systems and support the development process of the stability prediction tool.

Kurzfassung

Das Ziel dieser Arbeit ist die Bereitstellung eines zuverlässigen und effizienten Berechnungsverfahrens zur Vorhersage von hochfrequenten thermoakustischen Instabilitäten in mager vorgemischten Gasturbinenbrennkammern. Dafür wird eine Strategie zur Durchführung einer Stabilitätsanalyse vorgeschlagen, welche sich aus drei Stufen zusammensetzt: #1 Beurteilung der linearen thermoakustischen Stabilität, #2 Analyse von Oszillationen im Grenzzyklus sowie die Identifikation von nicht-linearen Sättigungsmechanismen und #3 die Berücksichtigung von modalen Interaktionen zwischen mehreren instabilen akustischen Eigenmoden. Besonderer Fokus liegt dabei auf dem korrekten Einbezug des Einflusses von akustisch induzierten Wirbelstärke-Fluktuationen auf das thermoakustische Stabilitätsverhalten in diesen drei Analyseschritten. Dies wird durch die Integration von neuen Modellen sowie durch das Beseitigen von numerischen Fehlern in Stabilitätsberechnungen erreicht. Fundamentale numerische Studien zusammen mit der Anwendung von Zerlegungsansätzen geben einen detaillierten physikalischen Einblick in das dynamische Verhalten von hochfrequenten thermoakustischen Systemen und unterstützen damit den Entwicklungsprozess des Berechnungsverfahrens.

Contents

List of Figures

List of Tables

Nomenclature

Latin Letters

$\mathbf{A}$	[−]	System matrix of spatial derivatives
$\mathbf{A}$	[−]	State-space system matrix
$A_{p'}$	[W/m³]	Source term amplitude
$\mathbf{B}$	[−]	Load vector/matrix
b	[−]	Azimuthal mode order
c	[m/s]	Speed of sound
c_p	[J/kgK]	Specific heat capacity
C	[−]	Mode coupling strength
$\mathbf{C}$	[−]	State-space output matrix
d	[m²/s]	Diffusivity constant
D	[W/m³]	Dissipation per unit volume
$D_\mathrm{net,a}$	[W]	Acoustic net dissipation
$\mathbf{D}$	[−]	State-space feedthrough matrix
E	[J/m³]	Disturbance energy per unit volume
$\mathbf{E}$	[−]	System matrix of time derivatives
f	[Hz]	Frequency
$f^\mathrm{cut\text{-}on}$	[Hz]	Cut-on frequency
h	[J/kg]	Enthalpy per unit mass
H	[m]	Mesh element size
H_f	[J/kg]	Lower heating value
$\mathbf{I}$	[W/m²]	Intensity flux vector
$\underline{\mathbf{I}}$	[−]	Unity matrix
k	[m²/s²]	Turbulent kinetic energy
$\boldsymbol{\mathscr{L}}$	[m/s²]	Lamb vector
$\mathbf{m}$	[kg/sm²]	Mass flow per unit surface
$\dot{\bar{m}}_\mathrm{fuel}$	[kg/s]	Fuel mass flow

m_{p}	[W/m³]	Volumetric source term of energy
$\mathbf{m_u}$	[N/m³]	Volumetric source term of momentum
m_ρ	[kg/m³s]	Volumetric source term of mass
n	[−]	System size
n	[−]	Time step
$\mathbf{n}$	[−]	Normal vector
N	[−]	Degree of rotational symmetry
p	[Pa]	Pressure
P_{th}	[kW]	Thermal power
$\dot{q}$	[W/m³]	Heat release rate per unit volume
Q	[W/m³]	Excitation per unit volume
r	[m]	Radial coordinate
R	[J/kgK]	Specific gas constant
R	[−]	Reflection coefficient
R_{c}	[m]	Radius of the combustion chamber
$\mathscr{R}_{\hat{p}}$	[Pa/s]	Residual of linearized pressure equation
$\mathscr{R}_{\hat{\mathbf{u}}}$	[N/m³]	Residual of linearized momentum equation
s	[rad/s]	Laplace variable
s	[m/s]	Flame speed
$s_{\mathrm{T1,T2}}$	[−]	First/second root of Bessel function
S	$[\mathrm{m}^2]$	Surface
t	[s]	Time
T	[K]	Temperature
T_{p}	[s]	Oscillation period
$\mathbf{u}$	[m/s]	Velocity vector
$\mathbf{u}$	[−]	Input vector
v	$[\mathrm{m}^3/\mathrm{kg}]$	Specific volume
V	$[\mathrm{m}^3]$	Volume
w	[J/m³]	Work per unit volume
W	[W]	Work
x	[m]	Axial coordinate
$\mathbf{x}$	[m]	Spatial coordinate vector
$\mathbf{y}$	[−]	Output vector
Y_{f}	[−]	Fuel mass fraction
Z	[−]	Impedance

Greek Letters

α	[rad/s]	Damping rate
α_{wall}	[W/m²K]	Heat transfer coefficient
α_{τ}	[−]	Numerical stabilization parameter
β	[rad/s]	Driving rate
γ	[−]	Ratio of specific heats
$\delta_{p'}$	[−]	Spatial distribution function
Δ	[−]	Difference operator
Δ	[m]	Displacement vector
ϵ	[−]	Non-linear damping coefficient
ϵ	[J/kgs]	Turbulence dissipation rate
ζ	[W/sm³]	Mean flow source term in wave equation
η	[Pa]	Complex Fourier coefficient signal
$\boldsymbol{\eta}$	[−]	State vector
θ	[rad]	Angular coordinate
θ_{rot}	[rad]	Spatial phase distribution
Θ	[−]	Progress variable
κ	[m/sN²]	Non-linear saturation coefficient
λ	[m]	Wavelength/length scale
λ	[−]	Air excess ratio
λ_{th}	[−]	Thermal conductivity
μ	[kg/ms]	Dynamic viscosity
ν	[rad/s]	Growth rate
Ξ	[W/sm³]	White noise source term in wave equation
ρ	[kg/m³]	Density
σ	[1/m]	Flame surface density
τ	[−]	Numerical stabilization parameter
$\underline{\boldsymbol{\tau}}$	[N/m²]	Stress tensor
$\boldsymbol{\phi}$	[−]	Solution vector/eigenvector
Φ	[m²/s]	Scalar potential
$\boldsymbol{\chi}$	[m²/s]	Vector potential
$\psi_{\hat{p}}$	[−]	Weighting function of pressure equation
$\psi_{\hat{\mathbf{u}}}$	[−]	Weighting function of momentum equation
ψ_{Φ}	[−]	Weighting function of scalar potential
Ψ	[−]	Spatial amplitude distribution/mode shape

ω	[rad/s]	Angular frequency
$\mathbf{\Omega}$	[1/m]	Vorticity vector

Superscripts

$(\ )'$	Perturbation
$\hat{(\ )}$	(Complex valued) amplitude
$\bar{(\ )}$	Period-averaged value
$\tilde{(\ )}$	ROM matrix
$(\ )^*$	Conjugate complex
$\dot{(\ )}$	First order time derivative
$\ddot{(\ )}$	Second order time derivative

Subscripts

$(\ )_\mathrm{a}$	Acoustic quantity
$(\ )_{\mathrm{BL}_{\mu/\mathrm{th}}}$	Visco-thermal boundary-layer losses
$(\ )_\mathrm{CFD}$	In/from CFD simulation
$(\ )_\mathrm{corr}$	Corrected growth rate
$(\ )_\mathrm{D}$	Dissipation terms
$(\ )_{\mathrm{D}_{\mathbf{\Omega}},1-4}$	Dissipation terms associated with Lamb vector
$(\ )_\mathrm{e}$	Entropy quantity
$(\ )_\mathbf{e}$	Position of edge
$(\ )_\mathrm{eff}$	Effective
$(\ )_\mathrm{f}$	Flame
$(\ )_\mathrm{i}$	i-th eigenmode
$(\ )_\mathbf{I}$	Flux terms
$(\ )_\mathrm{in}$	Inlet
$(\ )_\mathrm{lim}$	Limit-cycle
$(\ )_\text{l-s}$	Large-scale
$(\ )_{\hat{\mathbf{m}}}$	Fluctuating mass flow
$(\ )_\mathrm{max}$	Maximum value
$(\ )_\mathrm{net}$	Net/overall
$(\ )_\mathrm{NL}$	Non-linear
$(\ )_\mathrm{r}$	Radial vector component
$(\ )_\mathrm{r}$	Reduced

$(\ )_{\text{ref}}$	Reference
$(\ )_{\text{rest}}$	Remaining/rest
$(\ )_{\text{s}}$	Flame speed
$(\ )_{\text{s-s}}$	Small-scale
$(\ )_{\text{stab}}$	Numerical stabilization
$(\ )_{\text{sync}}$	Synchronization
$(\ )_{\nabla \bar{s}}$	Non-homentropic mean flow
$(\ )_{\text{t}}$	Turbulent/stochastic quantity
$(\ )_{\text{T1}}$	First transversal eigenmode
$(\ )_{\text{T2}}$	Second transversal eigenmode
$(\ )_{\text{u}}$	Unburned
$(\ )_{\text{v}}$	Vortical quantity
$(\ )_{\text{x}}$	Axial vector component
$(\ )_{\Delta}$	Flame displacement
$(\ )_{\theta}$	Azimuthal vector component
$(\ )_{\rho}$	Flame deformation

Dimensionless Numbers

He	Helmholtz number
$M(\mathbf{M})$	Mach number (vector)
Pe	Peclet number

Abbreviations

APE	Acoustic Perturbation Equations
CAA	Computational Aero Acoustics
CFD	Computational Fluid Dynamics
CCW	Counter-ClockWise
CW	ClockWise
DNS	Direct Numerical Simulation
(s)FEM	(stabilized) Finite Element Method
FGM	Flamelet Generated Manifold
FTF	Flame Transfer Function
LEE	Linearized Euler Equations
LES	Large-Eddy Simulation

LNSE	Linearized Navier-Stokes Equations
NSE	Navier-Stokes Equations
OH*	Electronically excited state of a hydroxyl radical
PSPG	Pressure-Stabilizing-Petrov-Galerkin
RANS	Reynolds-Averaged Navier-Stokes
RI	Rayleigh integral
ROM	Reduced Order Model
SUPG	Streamline-Upwind-Petrov-Galerkin
T1	First transversal eigenmode
T2	Second transversal eigenmode
URANS	Unsteady Reynolds-Averaged Navier-Stokes

1 Introduction

Every human being strives for the improvement of its own living conditions. This natural phenomenon has been strongly connected to increasing energy consumption to satisfy the continuous up-scaling level of personal requirements [1]. Since the mid-19th, the wide application of electrical energy has rapidly accelerated the development of living standards and wealth [2]. Nowadays, electricity has become an indispensable part of our everyday lives. The explosive increase of electricity demand was and is mostly met by using fossil fuels [3]. However, it was already recognized decades ago that these technologies not only harm the environment locally in terms of pollutants [4], but also influence the global climate in a negative manner [5,6]. These effects may have severe implications for humanity in the future [7]. In order to prevent a break-even-point, where the positive gradient of living conditions is cancelled by the worsening of environmental conditions, alternative electricity generation technologies are required. At the moment, the continuous replacement of fossil power plants by renewable ones represents the most promising answer to this global problem [8]. However, providing a functioning infrastructure for the supply of sustainably produced electricity has proven to be a crucial aspect [9]. One major challenge is that power production with renewables is subject to fluctuations due to intermittent weather influences [10,11]. The associated uncertainties in the grid stability must thus be counterbalanced to ensure a reliable power supply. A technical solution to this issue represents the integration of state-of-the-art gas turbines into the renewable power supply infrastructure [12]. The operational flexibility of gas turbines, for instance fast start-ups and shut-downs, on-demand load changes and wide operating windows allows quick response to power fluctuations in the electric grid. Additionally, their operation is in compliance with environmental regulations. In particular, the so-called lean-premixed combustion technology ensures low pollutant emissions, most notably nitrogen oxide (NO_x), while its high efficiency levels –even in part-load operation– reduce the relative amount of greenhouse gases produced [13]. Gas turbines emerged as a key technology to achieve the climate targets defined in the Paris Agreement of 2015 [14]. Therefore, putting more effort in the development of new gas turbine combustion concepts or in the advancement of existing systems contributes to a successful green energy transition. This counteracts global climate change and local environmental pollution, which in turn helps to keep or even improve living conditions for each individual person.

The present thesis is generally allocated in the gas turbine combustion field. Specifically, it deals with high-frequency thermoacoustic instabilities, which are one of the major challenges of lean-premixed combustion technology research. These instabilities may manifest in large amplitudes of pressure and heat release rate oscillations, which can damage burner hardware and/or limit the operational window of the gas turbine. In order to avoid or mitigate them, accurate prediction tools need to be established, which represents the research topic of this thesis.

1.1 Thermoacoustic Instabilities and Control Strategies

In particular, lean-premixed combustors are susceptible to develop thermoacoustic instabilities [15–17]. As displayed in Fig. 1.1, thermoacoustic instabilities are the result of an undesirable constructive, self-sustained feedback loop between the natural acoustics of the combustion chamber, i.e. its acoustic eigenmodes [18], and the flame's unsteady heat release rate [19]. Generally, an unsteady heat release rate $\dot{q}$ represents a source of sound. It leads to a temporal change of the specific gas volume v at a certain pressure value p and thus, performs work w on the gas [17,20]:

$$\frac{\mathrm{d}v}{\mathrm{d}t} \propto \dot{q} \quad \rightarrow \quad w \propto \oint p\dot{q}\mathrm{d}t \tag{1.1}$$

In Fig. 1.1, several mechanism that cause fluctuations of the heat release in gas turbines are shown: stochastic ones caused by turbulence in the flame region constantly generate broadband combustion noise, which in turn excites the combustor's acoustic eigenmodes. Corresponding acoustic waves travel up- and downstream and impinge on the combustion chamber boundaries, i.e. walls as well as in- and outlets. There, the waves are (partially) reflected into the chamber, where they interact with the flame as well as with the bulk flow.

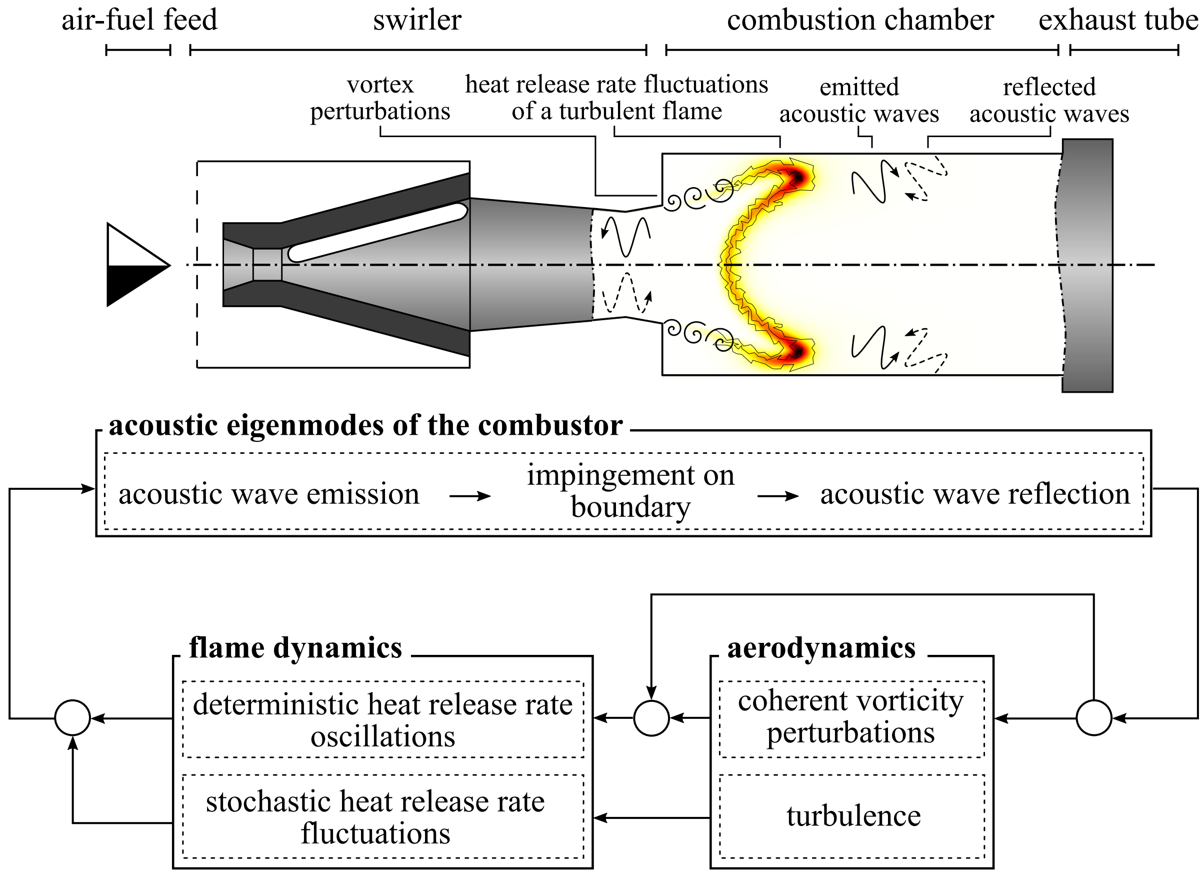

Figure 1.1: *Thermoacoustic feedback loop in a gas turbine combustion system.*

The first interaction scenario (cf. "deterministic heat release rate oscillations" in Fig. 1.1) indicates that acoustic waves directly induce heat release rate oscillations [21, 22]. Under certain conditions, which will be explained below this paragraph, heat release rate oscillations amplify the natural acoustics of the chamber. In turn, these reinforced waves are reflected at the boundaries and interact with the flame. As a result, a constructive thermoacoustic feedback loop is established. Another indirect path towards heat release fluctuations is given by the interaction of acoustics with the combustor's aerodynamics [23–26]: hydrodynamic instabilities in the bulk flow but also the interaction of acoustic velocity oscillations with shear-layers provokes the shedding of coherent vortex perturbations. While convecting downstream, these vortices change the flame surface and entrain burned reaction products, which creates pockets of lower and higher fresh gas concentration. These perturbations cause fluctuations of the reactants consumption and ultimately of the heat release rate, which indirectly closes the thermoacoustic feedback loop. A third option to close the feedback loop relevant for technically and non-premixed combustion systems is acoustic modulation of the equivalence ratio [25, 27]. As this thesis focuses on perfectly-premixed systems, equivalence ratio fluctuations are absent, which explains why this closure path is not present in the feedback loop schematic of Fig. 1.1.

The generation of heat release rate fluctuations in confined systems –such as gas turbine combustors– does not automatically lead to a thermoacoustic instability. As indicated at the beginning of this section, a *constructive* thermoacoustic feedback loop represents the necessary (but still not sufficient) condition to induce an instability. *Constructive* in this context means that the acoustic waves emitted by the unsteady heat release rate process interact coherently with the acoustics of the chamber. The opposite, i.e. a *destructive* feedback loop, would result in waves of decreased amplitude with less energy. The interference between acoustics and heat release rate fluctuations can be described with the Rayleigh integral RI in Eq. (1.2) [28]:

$$W \propto \frac{1}{T_\mathrm{p}} \int_V \int_0^{T_\mathrm{p}} p' \dot{q}' \mathrm{d}t \mathrm{d}V = RI > D_\mathrm{net,a} = \frac{1}{T_\mathrm{p}} \int_0^{T_\mathrm{p}} \left(\int_V D_\mathrm{a} \mathrm{d}V + \int_S \mathbf{I}_\mathrm{a} \cdot \mathbf{n} \mathrm{d}S \right) \mathrm{d}t. \tag{1.2}$$

Depending on the phase shift between pressure and unsteady heat release, constructive, neutral or destructive interference occurs (if the shift $< 90°$, $= 90°$ or $> 90°$ respectively). This means that either acoustic energy is supplied ($RI > 0$), remains constant ($RI = 0$) or is removed ($RI < 0$) within one acoustic period T_p. If constructive interference arises and the energy supplied by the feedback loop exceeds the sum of acoustic dissipation D_a in the chamber and acoustic intensity $\mathbf{I}_\mathrm{a}$ leaving or entering the domain normally through its boundary surfaces S ($\mathbf{n}$ is the normal vector), i.e. $RI > D_\mathrm{net,a}$, a self-excited thermoacoustic instability forms. Then, amplitudes of acoustics and heat release rate perturbations mutually start to grow exponentially in the linear regime.

A thermoacoustically unstable eigenmode can be associated with high amplitudes of pressure and heat release rate oscillations. These potentially harm the operational integrity of the combustor and decrease its life cycle or even lead to catastrophic failure of the gas turbine [29]. Thermoacoustic instabilities must either be avoided across the entire operational range of the combustion system or their pulsation amplitudes must be limited to an acceptable level.

In state-of-the-art lean-premixed gas turbines combustors, essentially two passive control strategies are applied to prevent or minimize thermoacoustic oscillations [20,30,31]:

- The first strategy seeks to artificially increase dissipation of acoustic waves, i.e. the term $D_{\mathrm{net,a}}$ in Eq. (1.2), at critical resonant frequencies. This counteracts the feed of energy W due to the constructive thermoacoustic feedback loop [32]. In practice, this strategy is realized by the implementation of damping devices [33], such as $\lambda/4$ absorbers [34] or Helmholtz resonators [35]. However, these dampers increase the system complexity, especially because they often require cooling air to avoid overheating and/or mistuning [30,36].
- The second strategy is a design optimization approach [37]. It aims to thermoacoustically "optimize" a given combustor by minimizing the undesired interaction between an acoustic eigenmode and the unsteady heat release rate [20,31,38]. As a result, the strength of the feedback loop between acoustics and heat release is weakened such that dissipative effects dominate, i.e. $D_{\mathrm{net,a}} > W$.

In industrial combustor configurations a combination of both strategies is possible to obtain the desired stability behavior. A third option, namely an active control strategy, might be followed as well [29,39]. However, this option is rarely used due to lower reliability and higher costs compared with passive control strategies [20].

The application of these approaches to the design process of new combustors, or retrofitting of existing concepts, requires in-depth knowledge about critical eigenmodes as well as understanding of the physical mechanisms promoting thermoacoustic instabilities:

- Increasing dissipation of acoustic modes by damping devices requires detailed information on which acoustic eigenmodes tend to be unstable in the frequency band of interest [30,36]. Knowing this, the damper device geometry can be optimized to maximize acoustic dissipation at these distinct, critical frequencies. Furthermore, knowing the associated spatial distributions of the acoustic fields at these eigenfrequencies, i.e. the eigenmode shapes, allows precise positioning of the damping devices at the combustion chamber walls [30]. This is essential for their effective operation.

- Unstable eigenfrequencies and the corresponding eigenmode shapes represent the starting point for the design optimization approach. Additionally, a design optimization approach demands a profound knowledge of the physical mechanisms, which modulate the heat release or contribute to acoustic damping [37, 40, 41]. Next, relevant effects need to be described in a mathematical sense, for instance analytically or by adequate numerical models, to predict the thermoacoustic behavior [22,29,42–48]. This allows systematic attenuation of the feedback loop by means of re-designing the combustor geometry, flame shape and/or redesign the operational window to avoid operating points with thermoacoustic instabilities. Additionally, similar measures can be taken to optimize, i.e. maximize, naturally occurring, acoustic damping effects.

In real gas turbines the prediction of thermoacoustic instabilities is a complex problem. A large number of different phenomena taking place simultaneously must be considered by a successful control strategy. These reach from the root-cause and onset of a thermoacoustic instability up to interactions between multiple unstable eigenmodes.

1.2 Thermoacoustic Stability Prediction

The qualitative and quantitative prediction of thermoacoustic instabilities represents the fundamental basis for the systematic application of countermeasures, i.e. the control strategies introduced in Section 1.1. Conceptually, a thermoacoustic stability analysis may be separated into three steps, shown in Fig. 1.2:

1. The **linear stability assessment** seeks to predict the acoustic eigenmodes in the frequency band of interest which tend to develop thermoacoustically unstable behavior at the specified operating conditions of the gas

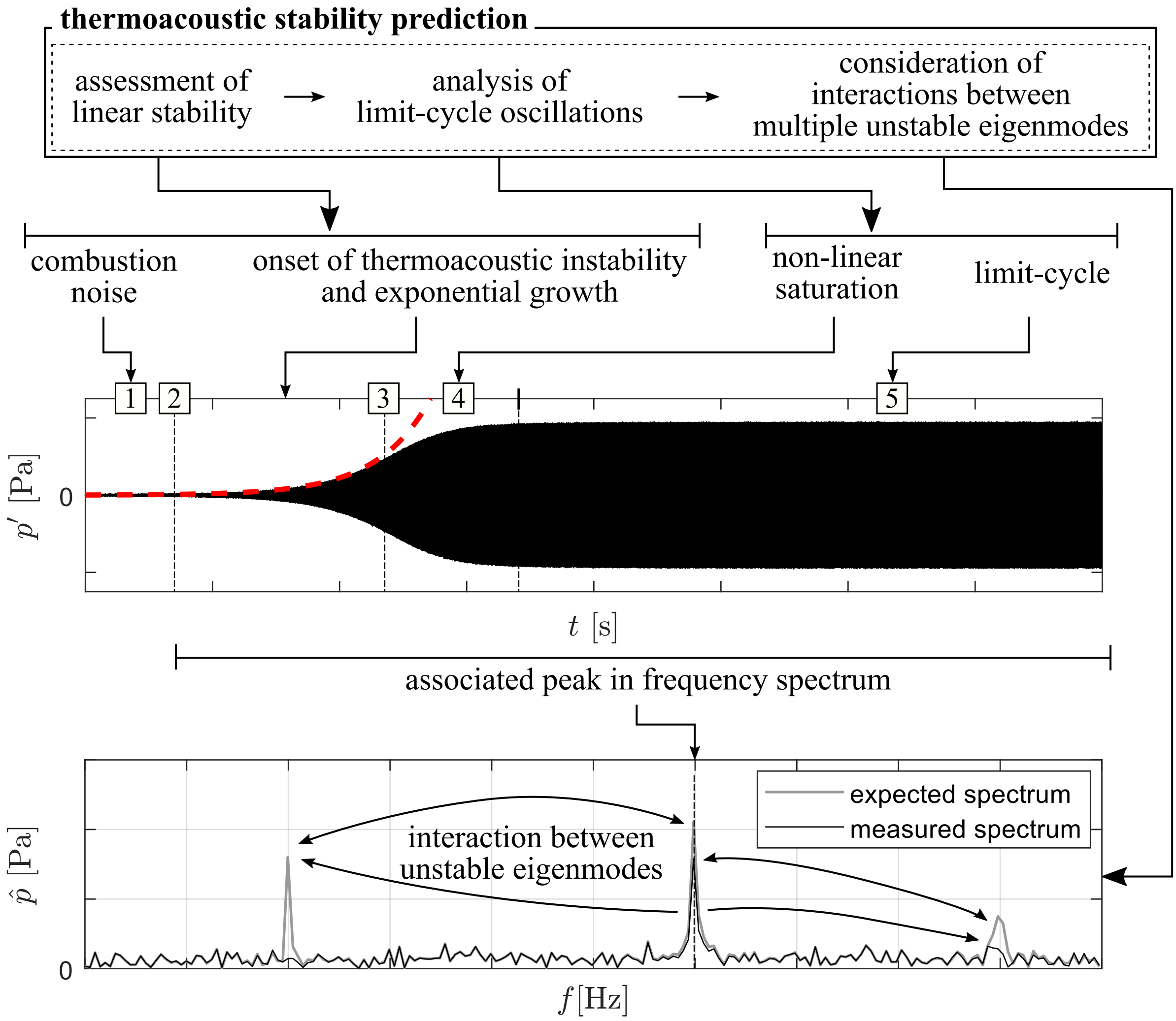

Figure 1.2: *Analysis steps of a complete thermoacoustic stability analysis with characteristic pressure trace and frequency spectrum showing the evolution of a thermoacoustic instability.*

turbine combustor [37, 40, 43, 49, 50]. More specifically, this step provides information about whether the acoustic modulation of the flame leads to the onset of an instability and how fast acoustic and heat release rate amplitudes grow in time. The onset of an instability can be predicted by evaluating Eq. (1.2):

$$W > D_{\mathrm{net,a}}. \tag{1.3}$$

An acoustic eigenmode becomes unstable, if the energy supply W exceeds net acoustic dissipation $D_{\mathrm{net,a}}$, and remains stable if net dissipation dominates. The pressure time trace in Fig. 1.2 shows an example of the evolution of a thermoacoustic instability including the time span, which can be captured by a linear stability analysis: At the beginning, the pressure data only shows stochastic fluctuations (cf. $\boxed{1}$ in Fig. 1.2), which are associated with broadband combustion noise. During this state, the evaluation of Eq. 1.3 reveals that acoustic losses dominate. Acoustic oscillations, which are induced by the combustion noise, are damped and vanish. The system is stable in a thermoacoustic sense. Then, the operating conditions of the combustor are changed, for instance by increasing the thermal power. Due to the corresponding higher heat release rate, acoustic waves induced by the combustion noise now excite stronger heat release rate perturbations $\dot{q}'$. The Rayleigh integral in Eq. (1.3) of one or more eigenmodes becomes greater than the associated net dissipation $D_{\mathrm{net,a}}$. The onset of a thermoacoustic instability occurs (cf. $\boxed{2}$ in Fig. 1.2), which goes along with the exponential growth of acoustic amplitudes (red dashed line in Fig. 1.2) and likewise amplitudes of heat release rate fluctuations. This early stage of an instability can be described by linear perturbation equations [17, 19]. The linear stability analysis step is thus limited to the instant of time, when the amplitude envelope can no longer be approximated by an exponential function without exceeding a predefined threshold error (cf. $\boxed{3}$ in Fig. 1.2).

2. The **analysis of limit-cycle oscillations** with non-linear saturation effects completes the investigation of the pressure time trace of a single unstable eigenmode. Limit-cycle oscillations represent the final state in the evolution of thermoacoustically unstable eigenmodes [44]. As shown in Fig. 1.2, acoustic amplitudes (and heat release rate fluctuations) remain at a constant level (cf. $\boxed{5}$ in Fig. 1.2), which may be unacceptably high when considering the operational limits of the gas turbine. In this state, the left hand side (l.h.s.) equals the right hand side (r.h.s.) of Eq. (1.3). The transition from exponential growth towards zero growth of amplitudes in the limit-cycle (cf. $\boxed{4}$ in Fig. 1.2) is characterized by a non-linear saturation behavior [45, 51–53]. This process is ascribed to two potential scenarios or a combination of them:

   – Non-linear decrease of the energy supply associated with the flame-acoustics interaction, which involves a non-linear decrease of the Rayleigh integral in Eq. (1.2), and/or

– Non-linear increase of dissipative effects.

The first scenario comprises the attenuation of the thermoacoustic feedback loop either by non-linear behavior of heat release or acoustic pressure oscillations [45, 54]. Non-linearity of heat release rate oscillations comprises the relative reduction of flame modulation in the acoustic field and/or a phase-shift relative to the acoustic pressure oscillation. The latter induces a reduction of the constructive interference between acoustic pressure and heat release rate fluctuations. Non-linearity in the acoustic pressure field is often precluded in gas turbine applications, since amplitudes remain small compared to the mean, operating pressure even in the limit-cycle [44]. The second scenario, i.e. the increase of damping effects, implies that dissipative mechanisms non-linearly depend on amplitudes of the acoustic field.
It is a difficult task to identify the entirety of relevant effects, which finally lead to saturation towards the limit-cycle, and may vary for each combustor, operating condition and frequency range of interest. However, knowing whether a thermocacoustic instability occurs or not, and if so, how strong the limit-cycle pulsations are, allows the implementation of the countermeasures introduced in Section 1.1. Additionally, the understanding of non-linear combustor dynamics also represents a crucial aspect for the third analysis step.

3. Analysis steps 1 and 2 only account for the evolution of a single, unstable eigenmode. However, a complete thermoacoustic stability analysis needs to **consider potential interaction phenomena between all eigenmodes** which exhibit a linearly unstable behavior [55]. In theory, multiple unstable eigenmodes may coexist [56, 57] while interacting or some dominant modes provoke the suppression of others [58]. The exemplary frequency spectrum at the bottom of Fig. 1.2 shows three pressure peaks (gray line) that represent three unstable modes. For instance, analysis step 1 revealed that the Rayleigh integral in Eq. (1.3) exceeds net dissipation at these three eigenfrequencies implying the formation of three limit-cycles. However, the measured frequency spectrum (black

line) only contains one peak, which is associated with the pressure trace in Fig. 1.2. The other two peaks in the expected frequency spectrum (gray line) are suppressed and do not appear, which indicates that the surviving eigenmode suppresses the others. This limit-cycle constellation can change if the dominant mode is damped exclusively, for example by Helmholtz resonators. Consequently, the amplitude of one of the other two linearly unstable modes may then grow to an unacceptable level in this new limit-cycle, which would have to be dealt with.
Without considering potential interaction mechanisms between unstable modes, the application of control strategies to avoid thermoacoustic instabilities may fail completely. In the worst case, implemented damping devices or the complete system design could be optimized for only one unstable eigenmode and then promote the existence of limit-cycle oscillations of another acoustic eigenmode.

A precise execution of each single step of the complete thermoacoustic stability analysis reduces the effort and complexity of the next step. Accurately predicting the linearly unstable modes in step #1 may decrease the number of relevant physical effects which need to be considered in the non-linear analysis part of step #2. In addition, identification of the number of eigenmodes interacting with each other can be restricted to the unstable ones in step #3. Finally, the careful preclusion of irrelevant non-linear saturation effects in step #2 may reduce the complexity of interaction phenomena in step #3.

1.3 High-Frequency Thermoacoustic Oscillations

The research of this thesis particularly focuses on thermoacoustic oscillations in the high-frequency regime of lean-premixed gas turbine combustors. These oscillations increasingly often occur after commissioning of modern gas turbine combustors, which is a consequence of the continuous efficiency as well as operation range increase [59, 60]. The high-frequency regime is characterized by the non-compactness of acoustically relevant elements in the combustion system [37, 61]. The denotation *non-compact* refers to the ratio between characteristic length scales of these relevant elements, which are for instance the flame (λ_{f}), geometric features or even single vortices, and the wavelength λ of an acoustic eigenmode. This ratio is denoted as Helmholtz number *He*, for instance $He_{\mathrm{f}} = \frac{\lambda_{\mathrm{f}}}{\lambda}$:

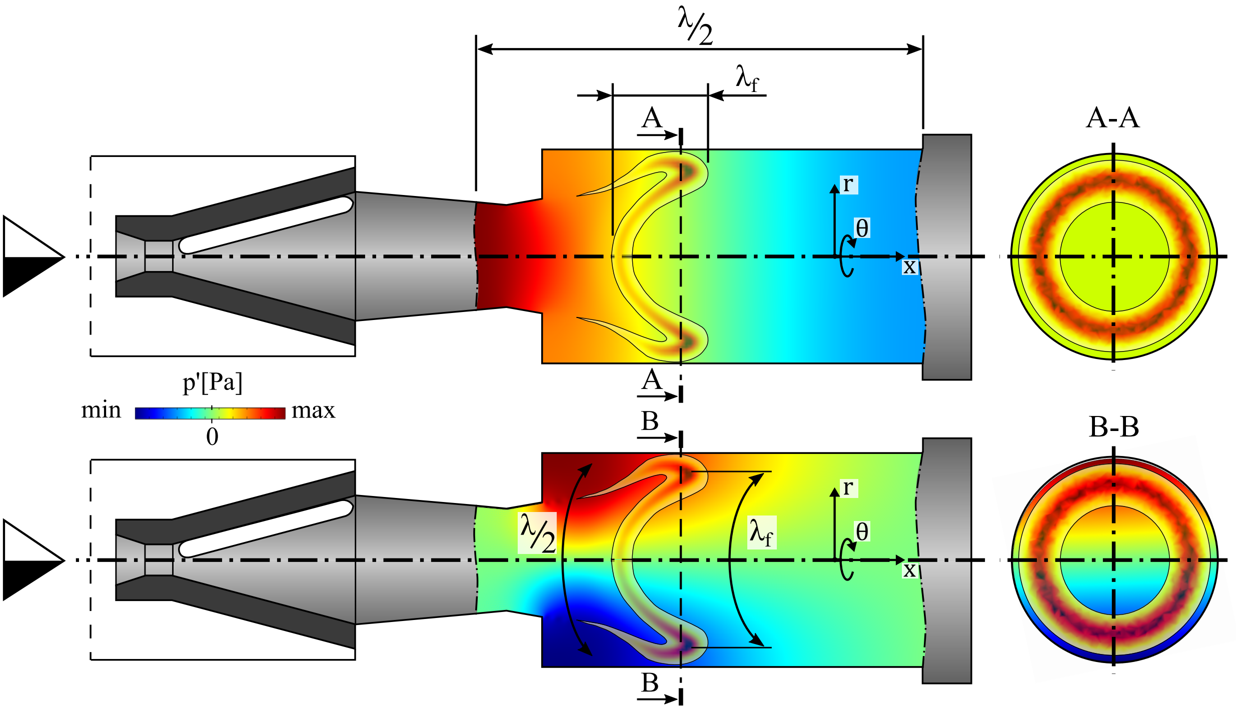

Figure 1.3: *a) Longitudinal acoustic eigenmode with a compact flame; b) first transversal acoustic eigenmode with a non-compact flame.*

- A small value of He number indicates that the acoustic element does not "see" any gradients of the acoustic field, i.e. it is spatially invariant and rendered as *compact*. Then, the element can be assumed to act as a point source. In the context of this work, this situation is associated with the low-frequency range and is illustrated in Fig. 1.3 a). There, the characteristic length scale of the flame λ_{f} is small compared to the acoustic wavelength of the longitudinal eigenmode and thus $He_{\mathrm{f}} \ll 1$

- Contrary to this, in the high-frequency range the length scale of the acoustic element and the wavelength are of same order, i.e. $He \approx 1$. An acoustic element of this type is denoted as a *non-compact* one. This scenario is shown in Fig. 1.3 b), where the flame is now exposed to the oscillating pressure field of the first transversal eigenmode of the combustor. In this case $He_{\mathrm{f}} \approx 1$. Acoustic gradients across the now, vertical characteristic flame length can no longer be treated as negligible, which requires the inclusion of local interactions between the acoustic field and the flame.

The imprecise formulation of "small" and "high" values for the previously introduced He number suggests that the limiting value, which separates compact and non-compact situations, is problem specific. Generally, the denotation "high-frequency" is not restricted to any type of acoustic mode shape. As long as a problem is characterized by non-compactness, associated acoustic oscillations are denoted as high-frequency in this thesis. However, non-compactness of acoustic elements is often associated with multi-dimensional acoustic modes, for instance transversal or radial ones. These modes can only exist, if their oscillation frequency f equals or exceeds the corresponding geometric cut-on frequency $f^{\text{cut-on}}$ in a given combustor [17], i.e.

$$f \geq f^{\text{cut-on}}. \tag{1.4}$$

1.4 Research Goals and Objectives of this Thesis

The main goal of this thesis is to contribute to the design optimization strategy introduced in Section 1.1 by improving the predictability of high-frequency thermoacoustic instabilities from a numerical and theoretical perspective. This comprises the stability analysis concept, which was introduced in Section 1.2, as a whole. Hence, the present work seeks to advance the linear thermoacoustic stability assessment, to identify and understand non-linear saturation effects leading to limit-cycle oscillations in the high-frequency range as well as to model and describe multi-modal interactions. For this purpose, a lean-premixed, atmospheric, swirl-stabilized, lab-scale gas turbine combustor, which is presented in Chapter 3, is used as validation for the developed models and simulations. The high-frequency acoustic eigenmodes of interest in this combustor are the first (T1) and second (T2) transversal modes.

In this thesis, special attention is given to acoustically induced vorticity perturbations and their impact on the evolution of thermoacoustic oscillations. This specific research focus is motivated by the yet barely investigated influence of this perturbation type on transversal eigenmodes in high-frequency thermoacoustic systems. Thematically, this topic completes the classification of this thesis, which was presented in this introduction chapter and is summarized in Fig. 1.4.

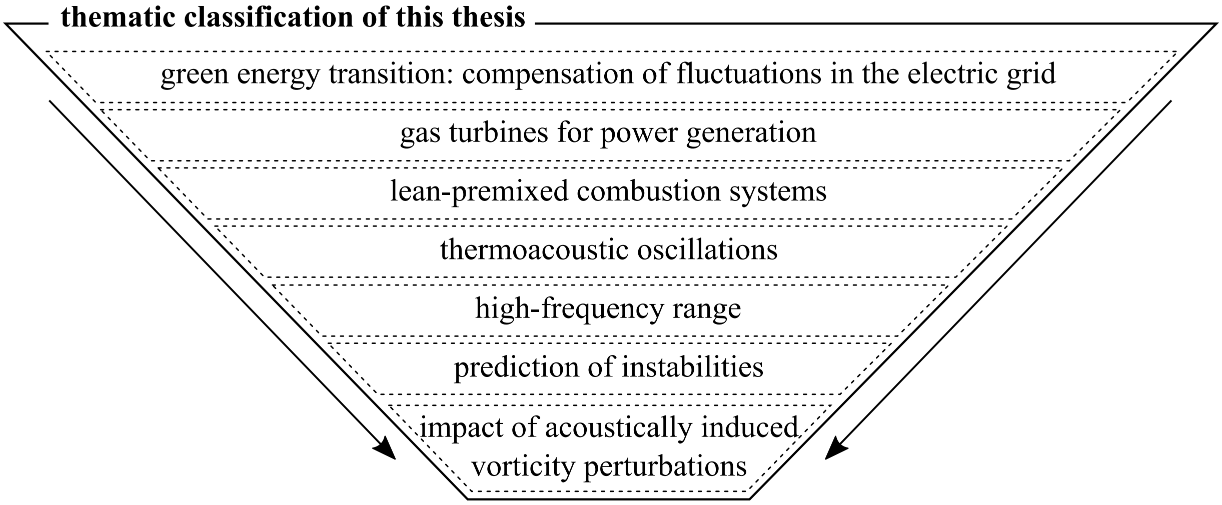

Figure 1.4: *Thematic classification of this thesis.*

Typically, vortex perturbations may significantly contribute to damping. However, they can also contribute to the amplification of acoustics either via vortex-mean flow coupling effects [62, 63] or via modulation of the heat release as indicated in Fig. 1.1. Thus, they must be considered in thermoacoustic stability predictions. While the driving potential of vortex shedding is fairly well understood in the low-frequency range [23–26], Schwing et al. [64] found that vortex perturbations do not (or only weakly) amplify high-frequency thermoacoustic oscillations of the first transversal eigenmode in a lean-premixed, swirl-stabilized combustor. In contrast, Berger et al. [61] revealed in their reheat combustor experiment that vortex perturbations are likely the primary driver of a transversely oscillating acoustic eigenmode. Obviously, their impact is rather case dependent and non-generalizable, which complicates thermoacoustic predictions and thus requires further research effort. Similarly, acoustic damping associated with vorticity disturbances has mostly been investigated for longitudinal modes at rather low frequencies. In this context, Howe [65–68] and Bechert [69] provided fundamental physical insight into the phenomenon of acoustically induced vortex shedding from sharp edges and showed quantitatively that this can contribute to sound attenuation. To the author's knowledge, the dissipative impact of this effect –and of acoustically induced vorticity perturbations in general– on multidimensional eigenmodes at higher frequencies has not yet been addressed in the open literature. These gaps in knowledge yield the following research objectives for the three steps of thermoacoustic stability predictions introduced in Section 1.2 and specify the structure of this thesis:

1. **Linear stability assessment** (Chapters 4 and 5): for this task, a hybrid *Computational Fluid Dynamics/Computational Aero Acoustics* (CFD/CAA) approach is used, which has already been applied in several research projects at the author's institute [37, 49, 50]. However, this analysis framework has yet not reached a sufficiently accurate level in terms of reliable prediction capabilities. Enhancement of the prediction capabilities of the hybrid CFD/CAA methodology unfolds into the following specific research tasks:

   – Development of a numerical method to decompose CAA solution fields computed with linearized disturbance equations into acoustic and vortical parts to perform detailed energetic analyses.

   – Minimization of undesired numerical errors in the computational approach, which are caused by the presence of convectively transported vortices in CAA solutions fields.

   – Adaption of existing acoustics-flame modulation models to incorporate the impact of vortex perturbations in the linear stability analysis framework.

   – Validation of the advanced CFD/CAA framework against experimental data in the frame of a linear stability analysis with the T1 eigenmode.

2. **Non-linear saturation and limit-cycle oscillations** (Chapter 6): the root-cause of limit-cycle oscillations in high-frequency thermoacoustic systems has yet not been identified [70]. This provides the motivation to investigate the influence of vorticity perturbations on the non-linear, dynamical behavior of such systems, which comprises the following tasks:

   – Establishment of a CFD approach to mimic high-frequency, transversal oscillations in gas turbine combustion chambers to observe the amplitude-dependent evolution of the bulk flow.

  - Computation of amplitude-dependent T1 driving and damping rates by adapting the linear analysis framework (cf. research objective #1), where the CFD results serve as the input.
  - Identification of the root-cause of T1 limit-cycle oscillations in the investigated non-compact thermoacoustic system.

3. **Multi-modal interactions** (Chapter 7): to complete the thermoacoustic stability prediction, the interaction of T1 and T2 acoustic eigenmodes is analyzed in the time-domain via extension of an available Reduced-Order-Model (ROM) approach [48]. This comprises the following tasks:
  - Identification and discussion of relevant interaction mechanisms between unstable eigenmodes in the concerned combustion system.
  - Integration of identified non-linear saturation mechanisms (cf. research objective #2) into the ROM framework to enhance its physical correctness.
  - Analyses of the dynamical behavior of the T1 and T2 modes via numerical computations with the ROM.

The present thesis represents the direct continuation of the Ph.D. project of Dr.-Ing. T. Hummel [37], which forms the basis of this work. His thesis also deals with non-compact thermoacoustic systems. It provides information on flame modulation mechanisms and vorticity damping models in the context of linear stability analysis as well as on the ROM approach and non-linear interactions of degenerate acoustic modes. Additionally, a comprehensive summary on recent work and research highlights at the author's institute is presented, which is thus not repeated in this thesis.

2 Theoretical Fundamentals

This chapter introduces the theoretical fundamentals relevant for the research objectives specified in Section 1.4. Starting from the Navier-Stokes Equations (NSE) in Section 2.1, which describe unsteady flow motions in gas turbine combustors in the most general manner, different levels of simplifications are applied to these including their linearization. In Section 2.2 the linearized disturbance equations are transformed into their frequency domain representation. Then, acoustic boundary conditions are introduced in Section 2.4. In the last Section 2.5, insight into the numerical solution of the linearized disturbance equation via the Finite Element Method (FEM) is given.

2.1 Governing Equations of Gas Turbine Flows

Flow problems in gas turbine combustors are commonly captured by conservation equations for a one-species fluid, which is specified by the mass-averaged properties of fuel and oxidizer [17, 19]. Then, the flow dynamics can be captured by the equations of mass and energy conservation , i.e. Eqs. (2.1) and (2.3), together with the ideal gas law $p/\rho = RT$ as well as with the *Navier-Stokes Eqs.* (2.2) (NSE), which ensure momentum conservation[1]

$$\frac{\partial \rho}{\partial t} + \nabla \cdot \left(\rho \mathbf{u}\right) = m_{\rho} \tag{2.1}$$

$$\rho \left(\frac{\partial \mathbf{u}}{\partial t} + \left(\mathbf{u} \cdot \nabla\right) \mathbf{u}\right) + \nabla p = \nabla \cdot \underline{\boldsymbol{\tau}} + \mathbf{m}_{\mathbf{u}} \tag{2.2}$$

$$\frac{\partial p}{\partial t} + \mathbf{u} \cdot \nabla p + \gamma p \nabla \cdot \mathbf{u} = \left(\gamma - 1\right) \left(\dot{q} + \underline{\boldsymbol{\tau}} : \left(\nabla \mathbf{u}\right) + m_{\mathrm{p}}\right). \tag{2.3}$$

Density $\rho(\mathbf{x}, t)$, velocity $\mathbf{u}(\mathbf{x}, t)$ and pressure $p(\mathbf{x}, t)$ are the spatio-temporal solution variables, which are collected in the solution vector $\boldsymbol{\phi} = [\rho, \mathbf{u}, p]^{\mathrm{T}}$. Equation (2.3) captures the volumetric heat release rate $\dot{q}$ associated with the chemical reaction process/combustion. The ratio of specific heats is denoted

[1] For the sake of brevity, the full set of Eqs. (2.1)-(2.3) is denoted as *Navier-Stokes Equations* (NSE).

as γ and $\underline{\boldsymbol{\tau}}$ is the stress tensor defined as

$$\underline{\boldsymbol{\tau}} = \mu\left(\nabla\mathbf{u} + (\nabla\mathbf{u})^{\mathrm{T}} - \frac{2}{3}(\nabla\cdot\mathbf{u})\,\underline{\mathbf{I}}\right), \tag{2.4}$$

where μ is the dynamic viscosity and $\underline{\mathbf{I}}$ the unity matrix. Additional sources of mass, momentum and energy are represented by the terms m_ρ, $\mathbf{m_u}$ and m_p. These are set zero in this thesis, except where otherwise specified (see for instance Chapter 6).

Based on this fundamental system of non-linear, coupled partial differential equations a variety of simplified sets of equations can be derived. Figure 2.1 gives an overview of the ones used in this thesis with the assumptions made to obtain them. The subsequent sections introduce these equations and provide information on their relevance for this work.

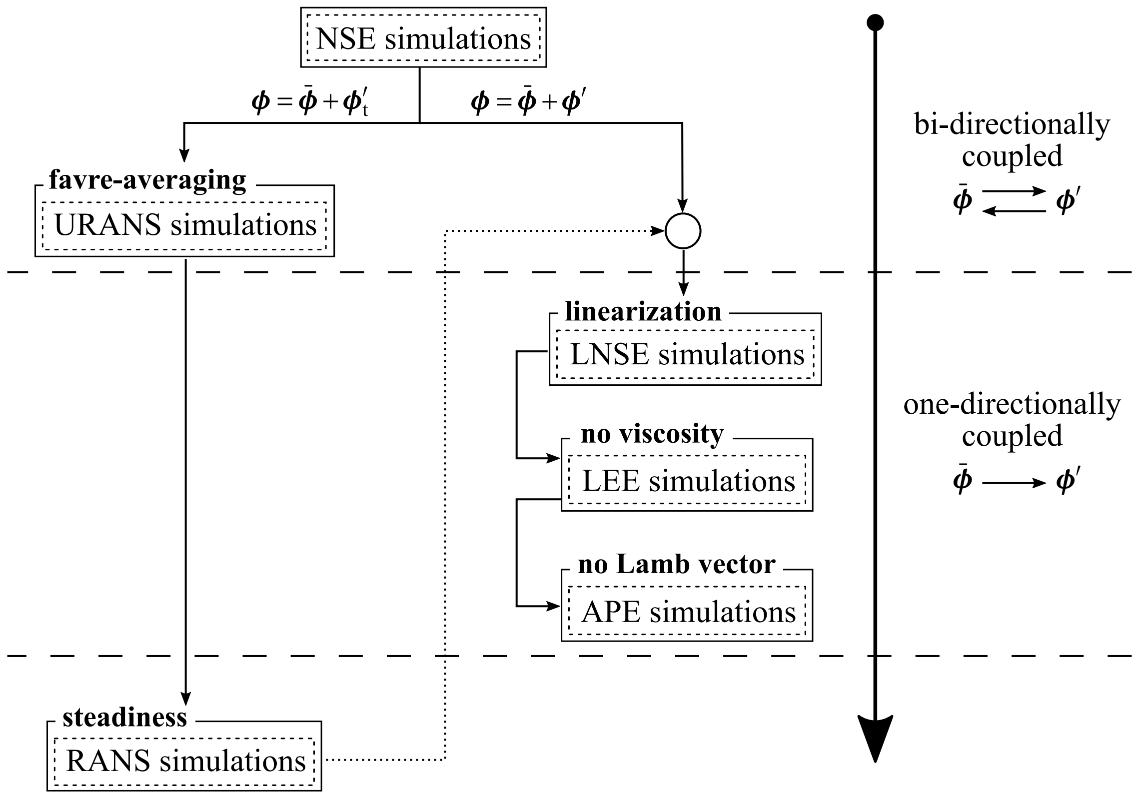

Figure 2.1: *Overview of systems of equations used in this thesis.*

2.1.1 Reynolds-Averaged Equations

Numerically solving the NSE without a combustion model[2] would gain insight into all the physical phenomena of interest at once. However, resolving even the smallest turbulent time and length scales using *Direct Numerical Simulations* (DNS) is connected to a massive computational effort [71]. *Large Eddy Simulations* (LES) reduce computation times of DNS by applying a sub-grid scale model that avoids direct resolution of scales smaller than the threshold [72]. Some examples for LES dealing with thermoacoustic instabilities can be found in Refs. [73–75]. In this work, the effect of turbulence in the bulk flow is fully modeled, which further decreases the computation times. Therefore, the solution vector is decomposed into a time-dependent, mean part $\bar{\boldsymbol{\phi}}(\mathbf{x}, t)$ and a stochastic, turbulent perturbation part $\boldsymbol{\phi}'_{\mathrm{t}}(\mathbf{x}, t)$, i.e.

$$\boldsymbol{\phi} = \bar{\boldsymbol{\phi}} + \boldsymbol{\phi}'_{\mathrm{t}}. \tag{2.5}$$

By inserting this decomposition into Eqs. (2.1)-(2.3) and performing Favre averaging [76], the *Unsteady-Reynolds-Averaged-Navier-Stokes* (URANS) equations are obtained, which allow the computation of the mean part $\bar{\boldsymbol{\phi}}$. The effect of turbulence is fully absorbed within the averaged part and thus, no eddies are resolved. Notice that either species transport equations or a combustion model must be added to Eqs. (2.1)-(2.3) to account for the heat release of the flame in CFD simulations. For the sake of clarity, this is only indictated by $\dot{q}$ in the energy Eq. (2.3). An explicit formulation of the Favre-averaged NSE can be found in Ref. [77]. The consideration of unsteadiness in these equations allows for imposing deterministic fluctuations such as harmonic ones, which mimic acoustic oscillations. For instance, this approach was applied in Ref. [78] to investigate the interaction between combustion of a single injector flame in a rocket engine and transversal velocity oscillations. A similar approach is used in Chapter 6 of the present thesis to analyze the amplitude-dependency of flame and bulk flow as a response to forced oscillations at the T1 resonant frequency in the swirl-stabilized combustor introduced in Chapter 3. With reference to Fig. 2.1, the URANS equations represent a bi-directionally coupled system of equations, which means in the context of this work that the bulk flow and imposed harmonic perturbations

[2] Instead transport equations for each species must be solved together with the compressible, unsteady NSE.

can influence each other.

The steady state of a flow problem, i.e. $\frac{\partial \boldsymbol{\phi}}{\partial t} = \mathbf{0}$, can be computed by *Reynolds-Averaged-Navier-Stokes* (RANS) simulations. As will be explained in Section 2.1.2, this solution can be used as the input for *Linearized Disturbance Equations.*

The (U)RANS equations are commonly employed in Computational Fluid Dynamics (CFD) solvers [79], which represents a standard tool in engineering disciplines. Thus, detailed information on (U)RANS CFD simulations can be found in the literature (e.g. in Ref. [80]) and are not repeated at this point. All (U)RANS CFD simulations are carried out with ANSYS Fluent 18.0 in this thesis.

2.1.2 Linarized Disturbance Equations

Apart from CFD simulations with the URANS equations, so-called *disturbance equations* can be used to calculate the spatio-temporal propagation of coherent disturbances. Instead of decomposing solution variables into mean and turbulent parts (cf. Eq. (2.5)), they are separated into a mean and a deterministic perturbation part $\boldsymbol{\phi}'(\mathbf{x}, t)$ [17, 19], i.e.

$$\boldsymbol{\phi} = \bar{\boldsymbol{\phi}} + \boldsymbol{\phi}'. \tag{2.6}$$

Inserting this approach into Eqs. (2.1)-(2.3) yields a one-directionally coupled system of disturbance equations, which is solved for the perturbation variables $\boldsymbol{\phi}'$ only. These equations underlie the assumption that disturbances do neither influence the mean part $\bar{\boldsymbol{\phi}}$ spatially nor temporally, i.e. the mean flow is invariant with respect to the disturbance flow field. This implies that the mean flow fields need to be provided as input quantities and thus, must a priori be known. One option to obtain them might be experimental data, for instance spatially resolved, time-averaged OH* chemiluminescence [81] and particle image velocimetry recordings to include the distribution of the heat release rate and of the velocity field. However, this is linked to optical accessibility to the combustor and additionally requires high-fidelity measurement techniques. A cost and time efficient method with a high degree of detail is provided by RANS CFD simulations [50]. As introduced before, the RANS equations only provide the steady-state solution of the NSE, which a priori excludes any coupling to time dependent oscillation fields. Performing a CFD RANS simulation followed by an import of the mean flow solution variables $\bar{\boldsymbol{\phi}}$ to a system of disturbance equations represents essentially the CFD/CAA methodology, which is applied in this thesis and is explained in more detail in Section 4.1.

Amplitudes of the flow perturbations observed in gas turbines are small compared to their corresponding mean flow quantities even in the limit-cycle[3] [17, 19, 44], i.e.

$$\rho' \ll \bar{\rho}, \qquad p' \ll \bar{p}, \qquad \|\mathbf{u}'\| \ll \bar{c}. \tag{2.7}$$

This allows negligence of perturbation terms of second (and higher) order and thus of non-linear effects. Inserting Eq. (2.6) into the Eqs. (2.1)-(2.3) and exploiting the linearity assumption of Eq. (2.7) yields a system of linear equations for the disturbance density $\rho'(\mathbf{x}, t)$, velocity $\mathbf{u}'(\mathbf{x}, t)$ and pressure $p'(\mathbf{x}, t)$[4]:

$$\frac{\partial \rho'}{\partial t} + \bar{\mathbf{u}} \cdot \nabla \rho' + \rho' \nabla \cdot \bar{\mathbf{u}} + \mathbf{u}' \cdot \nabla \bar{\rho} + \bar{\rho} \nabla \cdot \mathbf{u}' = 0 \tag{2.8}$$

$$\bar{\rho}\left(\frac{\partial \mathbf{u}'}{\partial t} + (\bar{\mathbf{u}} \cdot \nabla)\,\mathbf{u}' + \left(\mathbf{u}' \cdot \nabla\right)\bar{\mathbf{u}}\right) + \rho'\,(\bar{\mathbf{u}} \cdot \nabla)\,\bar{\mathbf{u}} + \nabla p' = \nabla \cdot \underline{\boldsymbol{\tau}}' \tag{2.9}$$

$$\frac{\partial p'}{\partial t} + \bar{\mathbf{u}} \cdot \nabla p' + \mathbf{u}' \cdot \nabla \bar{p} + \gamma \bar{p} \nabla \cdot \mathbf{u}' + \gamma p' \nabla \cdot \bar{\mathbf{u}} = \left(\gamma - 1\right) \dot{q}' \tag{2.10}$$

Equations (2.8)-(2.10) are denoted as the *Linearized-Navier-Stokes Equations* (LNSE) and describe the amplitude-independent spatio-temporal evolution of flow perturbations around the reference state $\bar{\boldsymbol{\phi}}$. The linearized heat release rate term $\dot{q}'$ quantitatively accounts for the impact of flame dynamics on the disturbance variables [37]. For this purpose, the heat release term in Eq. (2.10) needs to be expressed by local Flame Transfer Functions (FTFs).

Discarding any viscous effects, i.e. $\mu = 0$, which is a commonly applied assumption in thermoacoustics [40], yields the *Linearized-Euler Equations*

[3]Notice that the mean speed of sound represents the characteristic variable to judge the smallness and thus linearity of velocity perturbations.

[4]Viscous heating ($\underline{\boldsymbol{\tau}} : (\nabla \mathbf{u})$) in Eq. (2.10) is neglected in all simulations carried out in this thesis.

(LEE):

$$\frac{\partial \rho'}{\partial t} + \bar{\mathbf{u}} \cdot \nabla \rho' + \rho' \nabla \cdot \bar{\mathbf{u}} + \mathbf{u}' \cdot \nabla \bar{\rho} + \bar{\rho} \nabla \cdot \mathbf{u}' = 0 \tag{2.11}$$

$$\bar{\rho} \left(\frac{\partial \mathbf{u}'}{\partial t} + (\bar{\mathbf{u}} \cdot \nabla) \mathbf{u}' + \left(\mathbf{u}' \cdot \nabla\right) \bar{\mathbf{u}} \right) + \rho' (\bar{\mathbf{u}} \cdot \nabla) \bar{\mathbf{u}} + \nabla p' = \mathbf{0} \tag{2.12}$$

$$\frac{\partial p'}{\partial t} + \bar{\mathbf{u}} \cdot \nabla p' + \mathbf{u}' \cdot \nabla \bar{p} + \gamma \bar{p} \nabla \cdot \mathbf{u}' + \gamma p' \nabla \cdot \bar{\mathbf{u}} = \left(\gamma - 1\right) \dot{q}' \tag{2.13}$$

In a non-homentropic mean flow, the LNSE and LEE describe the propagation of acoustic (subscript a), vorticity (subscript v) and entropy (subscript e) perturbations, which are also denoted as sub-modes, such that the disturbance solution variables satisfy:

$$\rho' = \rho'_{\mathrm{a}} + \rho'_{\mathrm{v}} + \rho'_{\mathrm{e}} \tag{2.14}$$

$$\mathbf{u}' = \mathbf{u}'_{\mathrm{a}} + \mathbf{u}'_{\mathrm{v}} + \mathbf{u}'_{\mathrm{e}} \tag{2.15}$$

$$p' = p'_{\mathrm{a}} + p'_{\mathrm{v}} + p'_{\mathrm{e}} \tag{2.16}$$

This decomposition was introduced by Chu et al. [82] and indicates that there exists a variety of potential interaction processes between the three sub-modes and the bulk flow [17], which affect their individual stability behavior. As introduced in Chapter 1, this thesis particularly focuses on interactions between acoustic and vorticity perturbations. This restriction discards entropy disturbances in the analyses of the present work, which is a justifiable assumption [83–86]: in highly turbulent flows, entropy waves have negligible influence on the combustor dynamics, especially in premixed systems at high frequencies. This applies to the A^2EV combustor introduced in Chapter 3. An approach to avoid entropy sub-modes is to restrict density perturbations to be of isentropic nature. This implies that density perturbations associated with the entropy sub-mode ρ'_{e} are discarded [19]:

$$\rho' = \frac{p'}{\bar{c}^2} + \underbrace{\rho'_{\mathrm{e}}}_{=0} \tag{2.17}$$

Then, the solution variables of Eqs. (2.14)-(2.16) are simplified to:

$$\rho' = \rho'_{\mathrm{a}} + \rho'_{\mathrm{v}} = \frac{p'_{\mathrm{a}} + p'_{\mathrm{v}}}{\bar{c}^2} \tag{2.18}$$

$$\mathbf{u}' = \mathbf{u}'_{\mathrm{a}} + \mathbf{u}'_{\mathrm{v}} \tag{2.19}$$

$$p' = p'_{\mathrm{a}} + p'_{\mathrm{v}}. \tag{2.20}$$

The suppression of entropy disturbances goes along with two beneficial consequences: First, the number of differential equations, which need to be solved, reduces by one due to the algebraic relation of Eq. (2.17). Specifically, the continuity Eqs. (2.8) and (2.11) become redundant and do not need to be considered in thermoacoustic computations as discussed by Romero et al. [87]. Second, spurious entropy produced in lean-premixed systems is avoided. Non-physical entropy occurs in the full set of the LNSE (2.8)-(2.10) and LEE (2.11)-(2.13) due to insufficiently resolved flame dynamics, such as the movement of the flame front in the perturbation field [84]. More detailed information on the spurious entropy production can be found in Ref. [88], where so-called *Linearized Reactive Flow* simulations are performed to correctly account for the unsteady flame dynamics. However, this approach has yet only been applied to a laminar flame anchored in a duct.

A further simplification can be introduced to the isentropic LNSE/LEE by filtering out convectively transported vorticity perturbations. The corresponding equations are denoted as *Acoustic Perturbation Equations* (APE) and were introduced by Ewert et al. [89]. The APE can be derived by applying the vector identity

$$(\bar{\mathbf{u}} \cdot \nabla)\mathbf{u}' + (\mathbf{u}' \cdot \nabla)\bar{\mathbf{u}} = \nabla\left(\bar{\mathbf{u}} \cdot \mathbf{u}'\right) + \left(\bar{\boldsymbol{\Omega}} \times \mathbf{u}'\right) + \left(\boldsymbol{\Omega}' \times \bar{\mathbf{u}}\right) \tag{2.21}$$

to the isentropic LNSE/LEE (2.9)-(2.10)/(2.12)-(2.13), where $\bar{\boldsymbol{\Omega}} = \nabla \times \bar{\mathbf{u}}$ and $\boldsymbol{\Omega}' = \nabla \times \mathbf{u}'$ are the mean and perturbation vorticity, respectively. Removing the terms associated with the vorticity vectors, which are consolidated in the linearized *Lamb vector*, yields the desired form of the isentropic APE:

$$\bar{\rho}\left(\frac{\partial \mathbf{u}'}{\partial t} + \nabla\left(\bar{\mathbf{u}} \cdot \mathbf{u}'\right)\right) + \frac{p'}{\bar{c}^2}\frac{1}{2}\nabla\left(\bar{\mathbf{u}} \cdot \bar{\mathbf{u}}\right) + \nabla p' = \mathbf{0} \tag{2.22}$$

$$\frac{\partial p'}{\partial t} + \bar{\mathbf{u}} \cdot \nabla p' + \mathbf{u}' \cdot \nabla \bar{p} + \gamma \bar{p} \nabla \cdot \mathbf{u}' + \gamma p' \nabla \cdot \bar{\mathbf{u}} = \left(\gamma - 1\right)\dot{q}' \tag{2.23}$$

One of the main outcomes of this thesis is a combined APE and LNSE/LEE computation approach with the *Finite Element Method* (FEM), which allows for an isolated quantification of phenomena associated with acoustically induced vorticity perturbations. This does not only provide physical insight into the contribution of this phenomenon to the thermoacoustic stability but also helps to advance the prediction of instabilities.

Notice that on the isentropic LNSE/LEE and APE, further simplifications can be carried out, for instance by neglecting mean pressure gradients for isobaric conditions, or by assuming a fluid at rest, which would lead to the wave equation. The consequences of the latter simplification is are discussed in Refs. [90, 91].

2.2 Linearized Equations in Frequency-Domain

Numerically solving the linearized systems of equations introduced in Section 2.1 is still connected to a significant computational effort. This is due to the characteristics of the linearized equations, which capture acoustic (propagating at the speed of sound) but also convective phenomena (propagating at the mean flow velocity) and thus are governed by a large disparity of time scales. This may restrict the simulation to small time step sizes potentially leading to considerable computational effort [92]. Additionally, boundary conditions for the disturbance equations generally depend on frequency, which complicates analysis in time domain as disturbances with a wide spectrum of frequencies might be present in practical systems [93].

These problems motivate the transformation of the linear isentropic disturbance equations from the time into the frequency domain. Then, frequency-dependent boundary conditions can be implemented in a straightforward manner and integration in time can be avoided, which drastically reduces the computational costs. Therefore, it is assumed that acoustic and vorticity perturbations harmonically oscillate in time, while the amplitudes of the perturbations can grow or decay exponentially:

$$\boldsymbol{\phi}'(\mathbf{x}, t) = \hat{\boldsymbol{\phi}}(\mathbf{x}, s)\, e^{st}. \tag{2.24}$$

The complex valued frequency-domain solution variables s and $\hat{\boldsymbol{\phi}}(\mathbf{x}, s)$ are related to time-domain variables $\boldsymbol{\phi}'(\mathbf{x}, t)$ by the Laplace transform $\mathscr{L}\left\{\boldsymbol{\phi}'(\mathbf{x}, t)\right\}$

$$\mathscr{L}\left\{\boldsymbol{\phi}'(\mathbf{x}, t)\right\} = \hat{\boldsymbol{\phi}}(\mathbf{x}, s) = \int_0^\infty e^{-st}\boldsymbol{\phi}'(\mathbf{x}, t)\,\mathrm{d}t, \tag{2.25}$$

where $s = s_\mathrm{r} + i s_\mathrm{i}$ is the Laplace variable[5]. Real and imaginary parts of s, i.e. s_r and s_i, denote the growth rate and angular eigenfrequency. $\hat{\boldsymbol{\phi}}(\mathbf{x}, s)$ repre-

[5]Notice that the Laplace transform can be replaced by the Fourier transform if the real part of s is zero.

sents the complex-valued amplitude distribution of pressure $\hat{p}(\mathbf{x}, s)$ and velocity $\hat{\mathbf{u}}(\mathbf{x}, s)$ for a certain Laplace variable. Considering that the Laplace transform of a first order time derivative is $\mathscr{L}\left\{\frac{\partial}{\partial t}\boldsymbol{\phi}'(t)\right\} = s\hat{\boldsymbol{\phi}}(s)$, the isentropic LNSE, LEE and APE can be rewritten as a function of s as well as of $\hat{p}(\mathbf{x}, s)$ and $\hat{\mathbf{u}}(\mathbf{x}, s)$. However, the Laplace variable is usually expressed in terms of a complex-valued angular frequency ω, i.e. $s = i\omega = i(2\pi f - i\nu)$, with ν as the growth rate and f as the oscillating frequency. Then, the isentropic LNSE in frequency-domain are obtained:

$$\bar{\rho}\left(i\omega\hat{\mathbf{u}} + (\bar{\mathbf{u}}\cdot\nabla)\hat{\mathbf{u}} + (\hat{\mathbf{u}}\cdot\nabla)\bar{\mathbf{u}}\right) + \frac{\hat{p}}{\bar{c}^2}\bar{\mathbf{u}}\cdot\nabla\bar{\mathbf{u}} + \nabla\hat{p} = \nabla\cdot\underline{\hat{\boldsymbol{\tau}}} \tag{2.26}$$

$$i\omega\hat{p} + \bar{\mathbf{u}}\cdot\nabla\hat{p} + \hat{\mathbf{u}}\cdot\nabla\bar{p} + \gamma\bar{p}\nabla\cdot\hat{\mathbf{u}} + \gamma\hat{p}\nabla\cdot\bar{\mathbf{u}} = \left(\gamma - 1\right)\hat{\dot{q}}. \tag{2.27}$$

Accordingly, the isentropic LEE (2.12)-(2.13) and APE (2.22)-(2.23) read in frequency domain

$$\bar{\rho}\left(i\omega\hat{\mathbf{u}} + (\bar{\mathbf{u}}\cdot\nabla)\hat{\mathbf{u}} + (\hat{\mathbf{u}}\cdot\nabla)\bar{\mathbf{u}}\right) + \frac{\hat{p}}{\bar{c}^2}\bar{\mathbf{u}}\cdot\nabla\bar{\mathbf{u}} + \nabla\hat{p} = \mathbf{0} \tag{2.28}$$

$$i\omega\hat{p} + \bar{\mathbf{u}}\cdot\nabla\hat{p} + \hat{\mathbf{u}}\cdot\nabla\bar{p} + \gamma\bar{p}\nabla\cdot\hat{\mathbf{u}} + \gamma\hat{p}\nabla\cdot\bar{\mathbf{u}} = \left(\gamma - 1\right)\hat{\dot{q}} \tag{2.29}$$

and

$$\bar{\rho}\left(i\omega\hat{\mathbf{u}} + \nabla\left(\bar{\mathbf{u}}\cdot\hat{\mathbf{u}}\right)\right) + \frac{\hat{p}}{\bar{c}^2}\frac{1}{2}\nabla\left(\bar{\mathbf{u}}\cdot\bar{\mathbf{u}}\right) + \nabla\hat{p} = \mathbf{0} \tag{2.30}$$

$$i\omega\hat{p} + \bar{\mathbf{u}}\cdot\nabla\hat{p} + \hat{\mathbf{u}}\cdot\nabla\bar{p} + \gamma\bar{p}\nabla\cdot\hat{\mathbf{u}} + \gamma\hat{p}\nabla\cdot\bar{\mathbf{u}} = \left(\gamma - 1\right)\hat{\dot{q}}, \tag{2.31}$$

respectively.

Writing the frequency-transformed disturbance equations in matrix notation and rearranging the system matrices in the form of an eigenvalue problem represents the method of choice in this thesis to predict the linear thermoacoustic stability of an eigenmode of interest. Solving the eigenvalue problem gives the eigenfrequency ω_i, which directly provides an answer to the energy balance of Eq. (1.3) in terms of the growth rate ν. More information on this topic is introduced in Chapter 5.

2.3 Disturbance Energy

Coherent perturbation fields inside a given volume V can be associated with a disturbance energy density E. Its volume-integrated, temporal evolution provides information on the stability of the disturbance field and can be described by intensity $\mathbf{I}$ leaving or entering the domain through its surfaces S in boundary normal direction ($\mathbf{n}$ is the boundary normal vector) and the excitation Q as well as dissipation D inside the domain volume [94, 95]:

$$\int_V \frac{\partial E}{\partial t} \mathrm{d}V + \int_S \mathbf{I} \cdot \mathbf{n} \mathrm{S} = \int_V Q \mathrm{d}V - \int_V D \mathrm{d}V, \tag{2.32}$$

Based on the LEE continuity and momentum Eqs. (2.11)-(2.12) together with the isentropicity Eq. (2.17), isentropic formulations for E, $\mathbf{I}$, Q and D can be derived. The conservation Eq. (2.32) for the disturbance energy is obtained by multiplying the continuity Eq. (2.11) and the momentum Eq. (2.12) with $p'/\bar{\rho} + \bar{\mathbf{u}} \cdot \mathbf{u}'$ and $\mathbf{u}' + p/'(\bar{\rho}\bar{c}^2)\bar{\mathbf{u}}$, respectively, adding both results subsequently and applying Eq. (2.17) [96]. The definitions for energy density, intensity, excitation and dissipation in frequency space read:

$$E = \frac{\hat{p}^2}{2\bar{\rho}\bar{c}^2} + \frac{\bar{\rho}\hat{\mathbf{u}}^2}{2} + \hat{\rho}\left(\bar{\mathbf{u}} \cdot \hat{\mathbf{u}}\right) \tag{2.33}$$

$$\mathbf{I} = \underbrace{\left(\frac{\hat{p}}{\bar{\rho}} + \left(\hat{\mathbf{u}} \cdot \bar{\mathbf{u}}\right)\right)}_{=\hat{h}} \underbrace{\left(\bar{\rho}\hat{\mathbf{u}} + \hat{\rho}\bar{\mathbf{u}}\right)}_{=\hat{\mathbf{m}}} \tag{2.34}$$

$$Q = \frac{\gamma - 1}{\bar{\rho}\bar{c}^2} \hat{p}\hat{\dot{q}} \tag{2.35}$$

$$D = \underbrace{\bar{\rho}\Big(\underbrace{\left(\bar{\mathbf{\Omega}} \times \hat{\mathbf{u}}\right) \cdot \hat{\mathbf{u}}}_{=0} + \left(\hat{\mathbf{\Omega}} \times \bar{\mathbf{u}}\right) \cdot \hat{\mathbf{u}}\Big) + \hat{\rho}\left(\bar{\mathbf{\Omega}} \times \bar{\mathbf{u}}\right) \cdot \hat{\mathbf{u}}}_{=D_{\Omega}} + \hat{\mathbf{m}} \cdot \frac{\frac{\hat{p}}{\bar{c}^2}\nabla\bar{p} - \hat{p}\nabla\bar{\rho}}{\bar{\rho}^2}. \tag{2.36}$$

The intensity vector $\mathbf{I}$ in Eq. (2.34) is the product of disturbance enthalpy $\hat{h}$ and fluctuating mass flow $\hat{\mathbf{m}}$. Equation (2.35) captures the effect of the unsteady heat release rate on the temporal evolution of the perturbation field and is proportional to the Rayleigh index introduced in Eq. (1.2). The dissipation of disturbance energy inside the volume of interest is described by Eq. (2.36). The first three terms D_{Ω} in Eq. (2.36) are associated with acoustically induced vorticity perturbations. These volumetric sources/sinks describe interactions between the mean flow or the mean vorticity field, $\bar{\mathbf{u}}$ and $\bar{\mathbf{\Omega}}$ respectively, and the disturbance fields. The last term in Eq. (2.36) is associated with the coupling of isentropic acoustic/vorticity perturbations with the non-homentropic mean flow[6]. Notice that the first term of Eq. (2.36) vanishes identically as $\left(\bar{\boldsymbol{\Omega}} \times \hat{\mathbf{u}}\right)$ gives a vector perpendicular to $\hat{\mathbf{u}}$. Physically, this means that the force vector $\left(\bar{\boldsymbol{\Omega}} \times \hat{\mathbf{u}}\right)$ does not perform work on the disturbance field. However, this term is not simply discarded in Eq. (2.36) as it describes the energy transformation process between acoustic and vortical disturbance fields in shear-layers of the bulk flow (a detailed analysis on these energy transformation processes is provided in Appendix A). Specifically, vortical energy can be created on the expense of acoustics (or vice versa), which would decrease (increase) the acoustic energy density over time. This counteracts (supports) the acoustic energy supply caused by the thermoacoustic feedback loop shown in Fig. 1.1. This transformation process indicates that energy density E, intensity vector $\mathbf{I}$ as well as the excitation and dissipation terms Q and D can be split into contributions associated with acoustics and vorticity (keep in mind that the entropy sub-mode is suppressed). The corresponding decomposition of E, $\mathbf{I}$, Q and D into vortical and acoustic sub-modes is obtained by inserting Eqs. (2.14)-(2.16) into Eqs. (2.33)-(2.36) [17][7]:

$$E = E_\mathrm{a} + E_\mathrm{v}, \tag{2.37}$$

$$\mathbf{I} = \mathbf{I}_\mathrm{a} + \mathbf{I}_\mathrm{v}, \tag{2.38}$$

$$Q = Q_\mathrm{a} + Q_\mathrm{v}. \tag{2.39}$$

$$D = D_\mathrm{a} + D_\mathrm{v}. \tag{2.40}$$

The decomposition of the energy balance of Eq. (2.32) with Eqs. (2.37)-(2.40) into acoustic and vortical parts is one of the main novelties in this thesis as it provides detailed insight into physical but also numerical phenomena. For instance, this method allows detailed analyses of the transformation process between the acoustic and vortical sub-modes and its relevance in thermoacoustic stability predictions with the LNSE/LEE (cf. Appendix A). In Section 5.1.1, the decomposition methodology is applied to assess the impact of numerical stabilization schemes (details in Section 2.5) on the acoustic and vortical sub-modes and in Chapter 6, it is used to identify the root-cause of limit-cycle oscillations in high-frequency thermoacoustic systems. All these investigations demand for a decomposition of velocity and pressure solution fields

[6]This term vanishes for homentropic mean flows, i.e. $\nabla \bar{p} = \bar{c}^2 \nabla \bar{\rho}$.

[7]Inserting Eqs. (2.18)-(2.20) into Eqs. (2.33)-(2.34) additionally yields mixed terms, i.e. $E_{\mathrm{a,v}}$ and $\mathbf{I}_{\mathrm{a,v}}$. However, their physical interpretation is still not fully understood [17] and are thus not considered further in this thesis.

into acoustic and vortical parts to evaluate associated energy density, intensity, amplification and dissipation fields of Eqs.(2.37)-(2.40). This is achieved via a Helmholtz decomposition, which is introduced in Section 4.3.

2.4 Boundary Conditions

Either analytically or numerically, solving linearized disturbance equations in frequency domain represents a boundary value problem. This section introduces acoustic boundary conditions for isentropic disturbance equations to obtain unique solutions for the acoustic sub-mode. Special focus is put on the coexistence of hydrodynamical, vortical (convectively transported by the mean flow) and acoustic perturbations (propagating at the speed of sound) at the boundary conditions.

2.4.1 Impedance Boundary Conditions

The complex-valued impedance $Z(\omega)$ represents the most general way to describe boundary conditions for acoustic disturbances. It relates acoustic pressure to velocity perturbations

$$Z(\omega) = \frac{1}{\bar{\rho}\bar{c}} \frac{\hat{p}}{\hat{\mathbf{u}} \cdot \mathbf{n}}, \tag{2.41}$$

For better comprehensibility, the impedance can be viewed as a measure for the fraction of an incident acoustic wave which is reflected into the domain. Thereby, a reflection coefficient R can be deduced as a function of the impedance Z:

$$R = \frac{Z-1}{Z+1}. \tag{2.42}$$

The characterization of the acoustic reflection behavior at the domain boundaries is difficult as the value of Z is unknown in most practical cases. However, there exist several value pairs for $\hat{p}$ and $\hat{\mathbf{u}} \cdot \mathbf{n}$ which are commonly used to approximate the acoustic behavior at the domain boundaries:

- Slip walls ($\hat{\mathbf{u}} \cdot \mathbf{n} = 0$): then, $Z \to \infty$ and $R = 1$, which means that an incident acoustic wave is fully reflected without a phase shift.
- Pressure boundary ($\hat{p} = 0$): here, $Z = 0$ which means that an incident acoustic wave is fully reflected but with a phase shift of π.

- Anechoic boundary ($\hat{p} = \bar{\rho}\bar{c}\hat{\mathbf{u}}\cdot\mathbf{n}$): an incident acoustic wave is completely absorbed at the boundary, which is recognizable as $R = 0$ or $Z = 1$.
- Energetically neutral boundary ($\hat{\mathbf{m}}\cdot\mathbf{n} = 0$ or $\hat{h} = 0$) [97]: with reference to Eq. (2.34), the acoustic intensity becomes zero, i.e. $\mathbf{I}\cdot\mathbf{n} = 0$, which prevents any intensity to enter or exit the domain. In particular this type of boundary condition is useful, if both, in- and outlet(s) are energetically neutral. Then, acoustic amplification and/or dissipation inside the domain volume is the sole root-cause affecting the temporal change of the acoustic disturbance energy. In this case, the energy balance of Eq. (2.32) reduces to
$$\int_V \frac{\partial E}{\partial t} dV = \int_V Q dV - \int_V D dV \tag{2.43}$$
In other words, this type of boundary condition allows quantification of the thermoacoustic stability without the impact of the domain boundaries.
The zero mass flow and enthalpy conditions can be related to the impedance Z via
$$\hat{\mathbf{m}}\cdot\mathbf{n} = \Big(\bar{\rho}\hat{\mathbf{u}} + \underbrace{\frac{\hat{p}}{\bar{c}^2}}_{=\hat{\rho}}\bar{\mathbf{u}}\Big)\cdot\mathbf{n} = 0 \quad \rightarrow \quad \underbrace{\frac{1}{\bar{\rho}\bar{c}}\frac{\hat{p}}{\hat{\mathbf{u}}\cdot\mathbf{n}}}_{=Z(\omega)} = -\frac{\bar{c}}{\bar{\mathbf{u}}\cdot\mathbf{n}} = -\frac{1}{\mathbf{M}\cdot\mathbf{n}}, \tag{2.44}$$
$$\hat{h} = \frac{\hat{p}}{\bar{\rho}} + \hat{\mathbf{u}}\cdot\bar{\mathbf{u}} = 0 \quad \rightarrow \quad \underbrace{\frac{1}{\bar{\rho}\bar{c}}\frac{\hat{p}}{\hat{\mathbf{u}}\cdot\mathbf{n}}}_{=Z(\omega)} = -\frac{\bar{\mathbf{u}}\cdot\mathbf{n}}{\bar{c}} = -\mathbf{M}\cdot\mathbf{n}, \tag{2.45}$$
where $\mathbf{M}$ is the Mach number vector. Notice that the zero mass flow and enthalpy conditions reduce to slip wall and pressure boundaries respectively only if $\mathbf{M} = \mathbf{0}$. This indicates that $\hat{\mathbf{u}}\cdot\mathbf{n} = 0$ and $\hat{p} = 0$ are not energetically neutral conditions in the presence of a mean flow field.

It is important to emphasize that the impedance boundary condition is only applicable to acoustic oscillations propagating with the speed of sound, but not to convectively transported vorticity (or entropy) disturbances. Attention must thus be given to boundary conditions for the vorticity sub-mode and in particular to the outlet boundary: vortices either enter the computational domain through the inlet or are generated somewhere inside of it[8]. They travel

[8]At the inlet, a zero vorticity condition can be imposed, i.e. $\nabla\times\hat{\mathbf{\Omega}} = \mathbf{0}$.

downstream towards the outlet along the streamlines of the bulk flow. Physically, the vortices are not (partially) reflected but simply exit the domain. Generally, the impedance boundary condition at the outlet cannot reproduce this behavior, which results in non-physical behavior in the vicinity of the outlet. To circumvent this, two strategies are followed in this thesis:

1. Transversal modes considered in this work are cut-off downstream of the flame. This occurs due to an increasing value of the cut-on frequency $f^{\text{cut-on}}$. This characteristic frequency was already introduced in Eq. (1.4) and can play an important role for the specification of boundary conditions. For T1 and T2 eigenmodes in cylindrical combustion chambers, it is
$$f^{\text{cut-on}}_{\text{T1/T2}}(\mathbf{x}) = \frac{s_{\text{T1/T2}}\,\bar{c}(\mathbf{x})}{2\pi R_{\text{c}}(\mathbf{x})}, \tag{2.46}$$
where $s_{\text{T1/T2}}$ is the first/second root of the Bessel function of the first kind. More interestingly, the cut-on frequency increases locally either for an increasing temperature and thus increasing speed of sound $\bar{c}(\mathbf{x})$ or a decreasing combustion chamber radius R_{c}. In regions where the cut-on frequency value exceeds the oscillating frequency of the T1/T2 eigenmode, the acoustic sub-modes can no longer propagate freely and they decay exponentially towards a zero value. In combustor applications, the flame provokes a temperature elevation and thus an increase of the cut-on frequency across it. Transversal modes decay in downstream direction, i.e. towards the outlet, which is visible in Fig. 1.3 b). If the outlet is at a sufficient distance to the flame, the acoustic eigenmode may have been disappeared almost completely, which energetically decouples this boundary from the rest of the acoustic domain. Hence, no acoustic intensity crosses the outlet as $\hat{p}_{\text{a}}$ and $\hat{\mathbf{u}}_{\text{a}}$ are zero anyway. This allows the specification of boundary conditions, which are more appropriate for convectively transported vorticity perturbations without disrupting the acoustic energy balance. In this thesis, a pressure outlet is implemented, i.e. $\hat{p} = 0$, through which the vortices can exit the domain towards the environment at ambient pressure level.

2. Acoustically triggered, convectively transported vortices in high-frequency systems are relatively small compared to the acoustic wavelength. This goes along with sharp velocity gradients, which in turn

provoke fast dissipation, either due to viscous or artificial/numerical diffusion. This is analyzed in more detail in Section 5.1.1.2. If the outlet is at a sufficient distance to the origin of vortex shedding, the vortices have been dissipated before they reach this boundary. This allows the specification of pure acoustic, i.e. impedance boundary conditions, at exits.

2.4.2 Azimuthal Periodicity of Transversal Modes

A three-dimensional simulation with linearized disturbance equations can be reduced to a two-dimensional one if the combustor geometry of interest together with all the corresponding mean flow quantities exhibits continuous rotational symmetry. Then, solution variables of the LNSE/LEE/APE can be written as[9]

$$\hat{\boldsymbol{\phi}}\,(r,\theta,x)\Big|_{\theta_{\mathrm{ref}}} = \hat{\boldsymbol{\phi}}\,(r,x)\,e^{ib\theta}\Big|_{\theta_{\mathrm{ref}}} \tag{2.47}$$

with $|b|$ as the azimuthal mode order. For T1 and T2 modes, $b = \pm 1$ and $b = \pm 2$, respectively[10]. In this thesis $b = -1$ and $b = -2$ in all analyses, which represent the in swirl-direction rotating T1 and T2 modes (details on the loss of degeneracy of transversal modes can be found in Ref. [37]). Inserting Eq. (2.47) into the LNSE/LEE/APE for all disturbance variables and division by $e^{ib\theta}$ yields the simplified systems of equations. Notice that information about pseudo-periodic boundary conditions for combustors with discrete periodicity in circumferential direction is provided in the Appendix B. There, the azimuthal mode order $|b|$ is discussed in more detail, too.

2.5 Finite Element Method for Disturbance Equations

In order to solve complex partial differential equations –such as the linearized disturbance equations in frequency domain– numerical tools are often the method of choice[11]. Due to the capability to resolve complex geometries (which is often the case in practical combustion systems) and to work well with unstructured meshes, the *Finite Element Method* (FEM) is used in this

[9] Spatial derivatives of solution variables in azimuthal direction read $\partial\hat{\boldsymbol{\phi}}(r,\theta,x)/\partial\theta\big|_{\theta_{\mathrm{ref}}} = ib\,\hat{\boldsymbol{\phi}}\,(r,x)\,e^{ib\theta}\big|_{\theta_{\mathrm{ref}}}$.

[10] The sign provides information about the direction of rotation, i.e. clock- or counter clockwise.

[11] Parts of this section were published in Ref. [98]

work to assess the linear stability of thermoacoustic systems, although its application to fluid dynamic problems is less common [99, 100]: The reason for this are numerical instabilities, which arise due to the presence of convective operators. These may lead to node-to-node oscillations, especially in regions of steep gradients of the solution variables. In contrast to structural or static heat transfer problems, where no convective transport is present, the discretization of the convection operator leads to non-symmetric system matrices. Then, the difference between the FEM solution and the exact solution diverges and spurious solutions may occur [99]. The one-dimensional convection diffusion equation is a famous example that demonstrates the weakness of the FEM for convectively dominated equations. For this simplified equation, analytical as well as the corresponding FEM approximation can be obtained by classical "paper and pen" work [99]. The latter is a function of the *Peclet number*

$$Pe = \frac{\bar{u}H}{2d}, \tag{2.48}$$

which relates convective to diffusive effects and may be viewed as an indicator for the occurrence of spurious FEM solutions. In Eq. (2.48), $\bar{u}$ denotes the mean velocity, H the finite element size and d a diffusivity coefficient. For $Pe < 1$, numerical solutions without spurious oscillations can be obtained, i.e. the numerical solutions are stable and vice versa. A comparison between the solution of the standard FEM approximation and the analytical one reveals that the deviation between both is ascribed to an underestimation of diffusion, which originates from the FEM discretization procedure. To avoid unstable solutions, either the mesh element size must be decreased or diffusion must be (artificially) increased to obtain a stable FEM solution, which otherwise would be unstable, i.e. $Pe > 1$.

With reference to the LEE (2.28)-(2.29), it is obvious that artificial diffusion is necessary to obtain non-spurious solutions, since no natural diffusion is considered in the LEE, i.e. $d = 0$ and thus $Pe = \infty$. Even the LNSE (2.26)-(2.27) may need to be stabilized, if the viscosity μ encountered in these equations is not sufficient to produce stable FEM solutions. Interestingly, FEM computations with the APE (2.30)-(2.31) produce stable solutions without the addition of artificial diffusion although they capture the effect of the mean flow on the acoustic field. This can be explained by the absence of convectively transported vortices in APE solutions fields, which is the result of removing the linearized *Lamb* vector terms in these equations.

In this work, a combination of the *Streamline-Upwind-Petrov-Galerkin* (SUPG) [101] and the *Pressure-stabilizing-Petrov-Galerkin* (PSPG) [102] artificial diffusion schemes is employed as part of the FEM setup rendering it as *stabilized Finite Element Method* (sFEM). Application of the stabilization technique to the LNSE/LEE/APE results in the following system of linear equations [103]:

$$\int_V \left[\mathscr{R}_{\hat{\mathbf{u}}}\Big(\psi_{\hat{\mathbf{u}}} + \overbrace{\tau\mathscr{R}_{\hat{\mathbf{u}},\mathrm{stab}}}^{\psi'_{\hat{\mathbf{u}}}}\Big)\right]\mathrm{d}V = \mathbf{0} \tag{2.49}$$

$$\int_V \left[\mathscr{R}_{\hat{p}}\Big(\psi_{\hat{p}} + \underbrace{\tau\mathscr{R}_{\hat{p},\mathrm{stab}}}_{\psi'_{\hat{p}}}\Big)\right]\mathrm{d}V = 0 \tag{2.50}$$

Equations (2.49)-(2.50) represent a stabilized set of linearized, isentropic disturbance equations (in frequency space) in weak formulation, where $\psi_{\hat{\mathbf{u}}}$ and $\psi_{\hat{p}}$ are weighting functions associated with the solution variables $\hat{\mathbf{u}}$ and $\hat{p}$. $\mathscr{R}_{\hat{\mathbf{u}}}$ and $\mathscr{R}_{\hat{p}}$ denote the residuals of LNSE/LEE/APE momentum and energy equations, respectively. For the LNSE (2.26)-(2.27) and LEE (2.28)-(2.29) the SUPG/PSPG stabilization terms (subscript "stab") read[12]

$$\mathscr{R}_{\hat{\mathbf{u}},\mathrm{stab}} = \bar{\rho}\left((\bar{\mathbf{u}}\cdot\nabla)\psi_{\hat{\mathbf{u}}} + (\psi_{\hat{\mathbf{u}}}\cdot\nabla)\bar{\mathbf{u}}\right) + \nabla\psi_{\hat{p}} \tag{2.51}$$

$$\mathscr{R}_{\hat{p},\mathrm{stab}} = \bar{\mathbf{u}}\cdot\nabla\psi_{\hat{p}} + \psi_{\hat{\mathbf{u}}}\cdot\nabla\bar{p} + \gamma\bar{p}\left(\nabla\cdot\psi_{\hat{\mathbf{u}}}\right). \tag{2.52}$$

The stabilization parameter τ in Eqs. (2.49)-(2.50) is defined as [37, 49, 50]

$$\tau = \alpha_\tau \max\left(\frac{H(\mathbf{x})}{\bar{u}(\mathbf{x}) + \bar{c}(\mathbf{x})}\right), \tag{2.53}$$

where α_τ allows global adjustment of the magnitude of artificial diffusion. This tuning variable can be set arbitrarily to achieve the desired impact of numerical stabilization. The local impact of artificial diffusion depends on the respective size of the element H, the mean flow velocity $\bar{u}$ and the speed of sound $\bar{c}$.

In this thesis, computations with the sFEM are performed with COMSOL Multiphysics 5.2a.

[12]The APE momentum stabilization term yields accordingly, i.e. $\mathscr{R}_{\hat{\mathbf{u}},\mathrm{stab}} = \bar{\rho}\nabla\left(\bar{\mathbf{u}}\cdot\psi_{\hat{\mathbf{u}}}\right) + \nabla\psi_{\hat{p}}$

2.6 Acoustically Induced Vortex Shedding

In the previous sections of this chapter, some aspects of acoustically induced vortex shedding have already been introduced. This section provides information on the origin of the convectively transported vorticity perturbations to complete the picture[13].

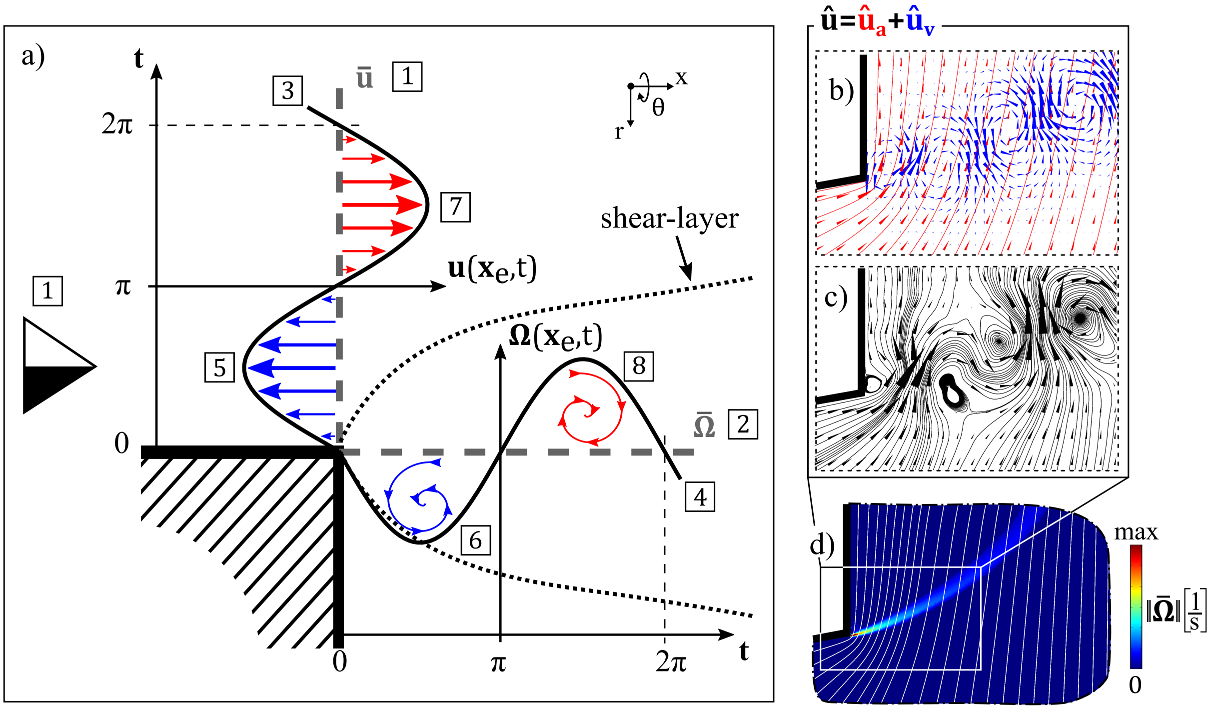

Figure 2.2: *a) Formation process of vortex disturbances; b) acoustic (red) and vortical (blue) velocity streamlines; c) superimposed streamlines; d) interaction between acoustic velocity and the mean shear-layer.*

The periodic shedding of convectively transported vortex disturbances originates from regions of strong mean vorticity. This is particularly the case at sudden area expansions, where the mean flow separates and a shear-layer forms [65]. Figure 2.2 a) explains the formation process of acoustically induced vortex shedding in the time-domain. The schematic shows the temporal evolution of the superimposed velocity $\mathbf{u}(\mathbf{x}=\mathbf{x}_e, t)$ and vorticity $\mathbf{\Omega}(\mathbf{x}=\mathbf{x}_e, t)$ directly at the edge location (subscript e): The starting point is given by an ax-

[13] Parts of this chapter were published in Ref. [104]

ial, steady-state flow $\bar{\mathbf{u}}$ $\boxed{1}$, which passes the corner at $\mathbf{x} = \mathbf{x}_\mathrm{e}$. Intuitively, it separates at the edge and induces a mean vorticity field $\boxed{2}$. The additional presence of acoustic velocity oscillations $\mathbf{u}_\mathrm{a}'$ exposes harmonic perturbations to the steady-state flow in a superimposed manner, i.e. $\mathbf{u}(\mathbf{x}_\mathrm{e}, t) = \bar{\mathbf{u}}(\mathbf{x}_\mathrm{e}) + \mathbf{u}_\mathrm{a}'(\mathbf{x}_\mathrm{e}, t)$ $\boxed{3}$. Consequently, the strength of shed vorticity $\boldsymbol{\Omega}(\mathbf{x}_\mathrm{e}, t) = \bar{\boldsymbol{\Omega}}(\mathbf{x}_\mathrm{e}) + \boldsymbol{\Omega}'(\mathbf{x}_\mathrm{e}, t)$ has to follow the instantaneous harmonic changes of the edge velocity $\boxed{4}$. Within the first half of the period, the acoustic particle velocity points upstream and reduces the total velocity with respect to its mean value $\boxed{5}$. As a response to that, a vortex perturbation is generated, which rotates in opposite (here counter-clockwise (CCW)) direction compared to the induced clockwise (CW) rotating mean velocity $\boxed{6}$. This vortex mutually reduces the superimposed vorticity and associated rotational velocity. Within the second half of the period, the acoustic velocity points downstream and enhances the superimposed velocity at the edge $\boxed{7}$. Now, a CW rotating vortex is shed to increase the overall vorticity $\boxed{8}$. The result is the periodic formation of CCW and CW rotating vortex disturbances. Notice that the length scale of a vortex λ_v can be approximated by

$$\lambda_\mathrm{v} = \frac{1}{2}\frac{\|\bar{\mathbf{u}}\|}{f_\mathrm{a}}, \tag{2.54}$$

and shows that it decreases with increasing acoustic oscillation frequencies.

Figure 2.2 b) displays the disturbed, rotational velocity field $\hat{\mathbf{u}}_\mathrm{v}$ (blue streamlines), which is induced by CW and CCW rotating vortices shed from an area expansion. These vortices are triggered by acoustic velocity oscillations $\hat{\mathbf{u}}_\mathrm{a}$ (red streamlines) of the T1 mode of the swirl-stabilized combustor introduced in Chapter 3 of this thesis[14]. Figure 2.2 c) displays the original, combined velocity solution[15], which can be reconstructed by adding vortical and acoustic velocities, i.e. $\hat{\mathbf{u}} = \hat{\mathbf{u}}_\mathrm{a} + \hat{\mathbf{u}}_\mathrm{v}$. These results are obtained by a Helmholtz decomposition, which can be applied to LNSE/LEE solutions. Detailed information on this procedure are presented in Section 4.3 of this work.

The generation of the vortex disturbances is connected to a conversion of acoustic momentum into rotational momentum resulting in a reduction of acoustic (kinetic) energy and thus pressure amplitudes as well. This can coun-

[14]The streamlines show the real parts of radial and axial velocities.

[15]Obtained from a LEE simulation.

teract thermoacoustic driving and support stable operation of a gas turbine combustor. The region of acoustic energy reduction is mainly restricted to the vicinity of the shear-layer's origin, i.e. downstream of the burner mouth's edge, as Howe stated [65–67]. On the one hand, this is due to an acoustic velocity singularity at the sharp edge. In this context, the (infinitely) sharp edge enforces (infinitely) high amplitudes of acoustic velocity (directly) around the edge. As shown in Fig. 2.2 b), the acoustic velocity (red streamlines) follows the geometry contour inducing large amplitude values directly at the location of the sharp edge. Thus, the magnitude of acoustic velocity is considerably higher near the sharp edge compared to the rest of the flow domain. The high amplitudes of acoustic velocities cause a strong interaction with the mean vorticity field, of which the magnitude is the highest directly downstream of the mean flow separation point as well. The situation is displayed in Fig. 2.2 d). This implies that the transformation of acoustic energy into vortical energy primarily occurs close to the corner. A detailed analysis of the energy transformation process between acoustic and vortical sub-modes caused by vortex shedding is provided in Appendix A.

Notice that the amount of acoustic energy transformed into vortical energy decreases, if the sharp corner is rounded. In this case, the velocity singularity vanishes and acoustic velocity amplitudes decrease, which reduces the interaction with the mean vorticity field in the vicinity of the rounded corner. To establish maximum acoustic dissipation due to vortex shedding, the corner should thus be manufactured as "sharp" as possible. Finally, it is mentioned that the formation of convectively transported vortices is not restricted to shear-layers of the bulk flow only. Generally, vortices can be generated in regions, where the acoustic velocity field is exposed to non-zero values of the mean vorticity field. Next to shear-layers, this can be the case in boundary-layers of the mean flow. However, it can be expected that the amount of acoustic energy consumed to produce the vortices is low compared to the amount consumed in the vicinity of the shear-layer origin. This is constituted by relatively low acoustic velocity magnitudes away from sharp corners.

3 A^{2}EV Combustor

The A^{2}EV swirl-stabilized, lab-scale test rig represents an atmospheric, can-type combustor, which was developed at the Thermodynamics Institute of the Technical University of Munich [37, 61, 105–107]. A schematic of the combustor is displayed in Fig. 3.1 including the geometrical dimensions in millimeters. The corresponding flow fields in the combustion chamber are obtained by reactive RANS CFD simulations. Exemplary distributions for radial, azimuthal and axial velocities as well as for temperature and heat release rate are shown in Fig. 3.1. More detailed information on the CFD simulations is provided in Section 5.2. Notice that the thermoacoustic analysis is restricted to the combustion chamber only.

The perfectly premixed, preheated fuel/oxidizer flow consisting of natural gas and air enters the A^{2}EV swirl generator, after having passed the plenum (not included in the schematic). The counter-clockwise rotating, swirling fluid streams through the mixing tube and enters the optically accessible combustion chamber, where the combustion reaction takes places. Then, the reaction products leave through the exhaust section.

In this work, the following operational conditions are investigated:

- Preheated inlet gas temperature in the range of $423\text{K} \le \bar{T}_{\text{in}} \le 723\text{K}$ in steps of 100K,
- Inlet mass flow between $60\,\text{g/s} \le \bar{\dot{m}}_{\text{in}} \le 120\,\text{g/s}$ in steps of $20\,\text{g/s}$ and
- Air excess ratio between $1 \le \lambda \le 1.8$ in steps of 0.2.

The combination of the latter two parameters allows variation of the thermal power in between the range of $97\text{kW} \le P_{\text{th}} \le 350\text{kW}$. In total, 80 different operational points are deduced by variation of the three parameters. For these, experimental benchmark data is readily available, which provides information about the thermoacoustic stability of the T1 eigenmode of the

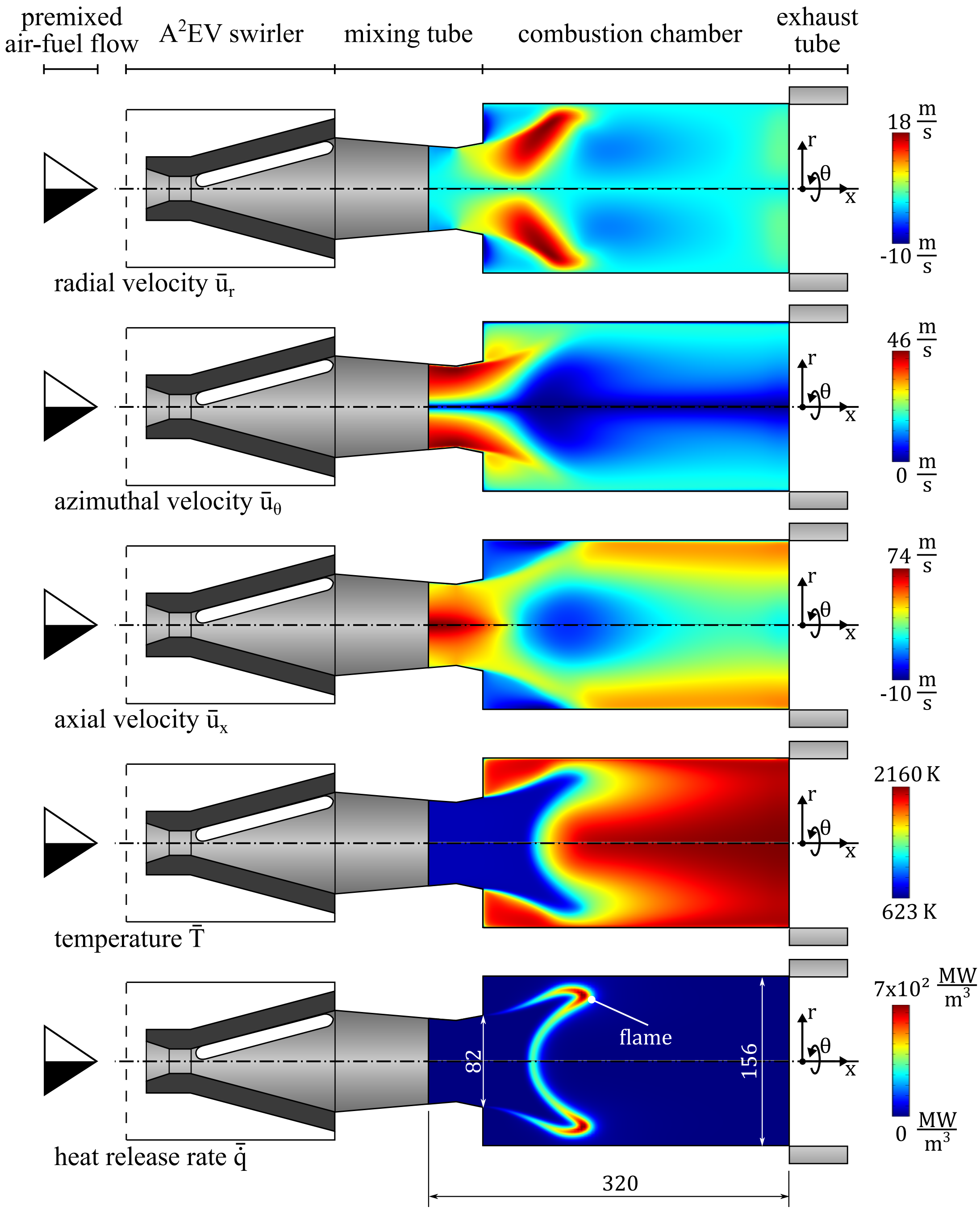

Figure 3.1: *Schematic of the A^2EV swirl-stabilized test rig configuration with exemplary mean flow field in the combustion chamber of (from top to bottom) radial, azimuthal and axial velocities as well as temperature and heat release rate.*

combustor. About half of the operational points undergo a self-excited thermoacoustic instability at this eigenfrequency [22, 81].

Exemplary frequency spectra of time series recorded from a (marginally) stable ($\bar{\dot{m}}_{\mathrm{in}}$ = 120g/s, $\bar{T}_{\mathrm{in}}$ = 623K, λ = 1.8) and a thermoacoustically unstable ($\bar{\dot{m}}_{\mathrm{in}}$ = 120g/s, $\bar{T}_{\mathrm{in}}$ = 623K, λ = 1.2) operational point are presented in Fig. 3.2 a) and b), respectively.

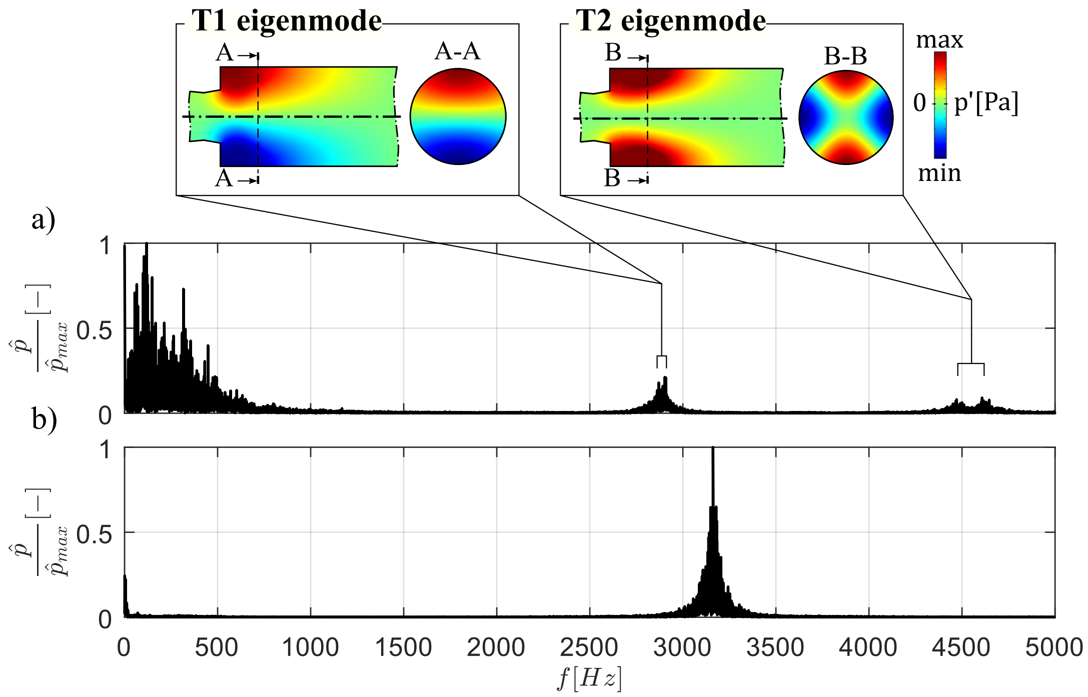

Figure 3.2: *a) Frequency spectrum of a (marginally) stable operational point; b) frequency spectrum of an unstable operational point.*

The stable operational point (Fig. 3.2 a)) reveals four peaks in the high-frequency range :

- The first two peaks are associated with the non-degenerate T1 modes at $f_{\mathrm{T1}} \approx$ 2800Hz. The loss of degeneracy occurs due to the swirling mean flow. The result is two rotating T1 modes. One rotates in the swirl direction, the other in the counter swirl direction. These modes are closely spaced in frequency, which complicates the distinction in the spectrum of Fig. 3.2 a). Typically, the in-swirl rotating mode is associated with the higher frequency [37]. The corresponding mode shape is displayed above.

- The non-degenerate T2 eigenmode pair appears at $f_{\mathrm{T2}} \approx 4500\mathrm{Hz}$. In this case, the frequency gap between the modes is larger. In contrast to the T1 mode, the T2 mode is characterized by four circumferential pressure anti-nodes instead of only two in the case of a T1 mode. The T2 pressure mode shape is displayed in Fig. 3.2 a).

The frequency spectrum of the unstable operational point in Fig. 3.2 b) reveals that only the T1 mode is unstable, specifically the one rotating in swirl-direction [37]. Notice that the frequency shift between unstable and stable operational point occurs due to the temperature increase caused by the lower air excess ratio. The two T2 mode peaks are not visible, which either indicates that it is stable in a thermoacoustic sense or it is unstable but suppressed by the T1 mode due to modal coupling effects.

4 Methods for Thermoacoustic Stability Predictions

The methods introduced in this chapter serve as the fundamental analysis basis for the thermoacoustic stability predictions in Chapters 5-7. First, the CFD/CAA methodology is presented followed by the growth rate equation. Lastly, the Helmholtz decomposition is applied to the field of thermoacoustics, which establishes the possibility to separate LNSE/LEE solutions fields into acoustic and vortical parts. Notice that the provision of such a decomposition method represents one of the research goals of this thesis.

4.1 Computational Fluid Dynamics/Computational Aero Acoustics Methodology

The basic idea and simultaneously the main advantage of the CFD/CAA methodology consists in the sequential computation of different time and length scales, which tremendously reduces computational costs. Using one-directionally coupled systems of equations for the CAA part, as introduced in Section 2.1 with Fig. 2.1, allows effective computation of disturbance scales, which are considerably larger than turbulent length and time scales but smaller than time scales of the ensemble-averaged mean flow. In this sense, the mean flow fields and thus the effect of turbulence are determined in a separated, first computation step via a (U)RANS CFD simulation. This mean flow data serves as the input for the CAA part[1]. Then, a modal analysis in terms of an eigenfrequency simulation with linearized disturbance equations in the frequency domain (cf. Section 2.2) is carried out. This second computation step directly provides information on the stability of an eigenmode in the form of a growth rate. Specifically, discretizing the governing disturbance equations in the context of the sFEM yields system matrices which can be rearranged in

[1] Notice that CFD and FEM meshes can differ.

the form of a generalized eigenvalue problem [37,50], i.e.

$$[i\omega_{\mathrm{i}}\mathbf{E}+(\mathbf{A}+\mathbf{A}_{\mathrm{stab}})]\,\hat{\boldsymbol{\phi}}_{\mathrm{i}}=\mathbf{0}. \tag{4.1}$$

$\mathbf{E}$, $\mathbf{A}$ and $\mathbf{A}_{\mathrm{stab}}$ denote the system matrices associated with temporal and spatial derivatives in the disturbance equations as well as with the SUPG/PSPG stabilization scheme introduced in Section 2.5. Numerically solving Eq. (4.1) gives the eigenvalue $i\omega_{\mathrm{i}}$ and the corresponding eigenvector $\hat{\boldsymbol{\phi}}_{\mathrm{i}}$ of eigenmode i. Eigenvalue and eigenvector in combination represent an eigensolution of Eq. (4.1), where the eigenvector is the characteristic eigenmode shape representing the amplitude distributions of the solution variables $\hat{p}$ and $\hat{\mathbf{u}}$. As mentioned in Section 2.2, the angular eigenfrequency ω_{i} consists of a real and an imaginary part. It hosts information about the oscillating frequency f and the temporal amplitude evolution of the solution variables in terms of the growth rate ν:

$$\omega_{\mathrm{i}}=2\pi f-i\nu. \tag{4.2}$$

With reference to Eq. (2.24), the value of the growth rate determines how fast amplitudes of disturbances solution variables grow (or decay) in time (cf. the red line in Fig. 1.2). Physically, the net growth rate ν consists of driving (β) and damping (α) contributions but also contains the effect of energy fluxes leaving or entering the domain through in- and outlets ($\nu_{\mathbf{I}}$) as well as the non-physical, dissipative impact of the numerical stabilization scheme (ν_{stab}), i.e.

$$\nu=\alpha+\beta+\nu_{\mathbf{I}}+\nu_{\mathrm{stab}}. \tag{4.3}$$

Notice that $\alpha<0$ and $\beta>0$ in this thesis. The sign of the growth rate subtracted by the non-physical part ν_{stab} determines the linear thermoacoustic stability limit of an eigenmode of interest at predefined operational conditions [37,49]:

$$\nu-\nu_{\mathrm{stab}}>0 \;\rightarrow\; \text{unstable} \tag{4.4}$$

$$\nu-\nu_{\mathrm{stab}}\leq 0 \;\rightarrow\; \text{(marginally) stable} \tag{4.5}$$

According to the Eqs. (4.4)-(4.5), three stability states can be identified (cf. Eq. (1.2)):

1. The eigenmode is unstable, if the net supply of disturbance energy exceeds its reduction due to dissipative mechanisms.

2. The eigenmode is marginally stable, if the net supply of disturbance energy is zero.

3. The eigenmode is stable, if dissipative effects dominate the driving mechanisms.

In summary, the task of linear thermoacoustic stability assessments with the CFD/CAA method comes down to consideration of all (relevant) effects which change the acoustic energy in the control volume. In order to retrieve accurate and reliable stability predictions results, the artificial growth rate part originating from the numerical stabilization scheme must either be minimized, i.e. $\nu_{\mathrm{stab}} \rightarrow 0$, or compensated in the analysis by quantification of ν_{stab} and subtraction from the net growth rate, i.e. $\nu - \nu_{\mathrm{stab}}$. Otherwise, the magnitude of thermoacoustic growth rates may be underestimated.

4.2 Growth Rate Equation

Cantrell and Hart [108] introduced an growth rate equation, which represents an alternative way to determine the stability of an eigenmode. It reflects the growth rate in terms of the volume-integrated, period-averaged (denoted by $\langle \ldots \rangle$[2]) and normalized change of the oscillating energy density E of an eigenmode, i.e.

$$\nu = \frac{1}{2} \frac{\int_V \frac{d\langle E \rangle}{\mathrm{d}t} \mathrm{d}V}{\int_V \langle E \rangle \mathrm{d}V}. \tag{4.6}$$

The growth rate Eq. (4.6) can be combined with the energy balance of Eq. (2.32), which allows the decomposition of the growth into three parts associated with sources and sinks inside the computational volume and intensity leaving or entering through the domain boundaries, ν_{Q}, ν_{D} and $\nu_{\mathbf{I}}$ respectively:

$$\nu = \frac{1}{2} \frac{\int_V \langle Q \rangle \mathrm{d}V - \int_V \langle D \rangle \mathrm{d}V - \int_S \langle \mathbf{I} \cdot \mathbf{n} \rangle \mathrm{d}S}{\int_V \langle E \rangle \mathrm{d}V} = \nu_{\mathrm{Q}} + \nu_{\mathrm{D}} + \nu_{\mathbf{I}}. \tag{4.7}$$

Successively inserting the energy Eqs. (2.33)-(2.36) into Eq. (4.7) allows computation of the three growth rate contributions in a separated manner. This is not possible by straightforwardly performing an eigenfrequency analysis with

[2]For practical guidance on the period-averaging of thermoacoustic signals, visit Section 2.7. of Ref. [37].

the CFD/CAA method introduced in Section 4.1 as the resulting growth rate contains the contribution of the intensity inherently. Hence, the main advantage of the growth rate Eq. (4.6) consists of the possibility to distinguish between different phenomena affecting the stability of an eigenmode. This can be exploited to determine individual growth rates for each physical effect. In this thesis, the first three terms $D_{\mathbf{\Omega}}$ of Eq. (2.36) are of particular interest as these are associated with acoustically induced vorticity perturbations. By neglecting the contributions of the excitation term Q, the last term in the dissipation term D and the intensity $\mathbf{I}$ in the energy balance of Eq. (2.32), a growth rate equation is obtained which exclusively describes the dissipative impact of vorticity perturbations on the thermoacoustic stability, i.e.

$$\begin{aligned} \nu =& \frac{1}{2}\frac{\int_V \langle \bar{\rho}\big(\overbrace{\big(\bar{\mathbf{\Omega}} \times \hat{\mathbf{u}}\big) \cdot \hat{\mathbf{u}}}^{=0} + \big(\hat{\mathbf{\Omega}} \times \bar{\mathbf{u}}\big) \cdot \hat{\mathbf{u}}\big) + \hat{\rho}\,\big(\bar{\mathbf{\Omega}} \times \bar{\mathbf{u}}\big) \cdot \hat{\mathbf{u}} \rangle \mathrm{d}V}{\int_V \langle E \rangle \mathrm{d}V} = \\ =& \alpha_{\mathrm{D}_{\mathbf{\Omega}}} = \underbrace{\alpha_{\mathrm{D}_{\mathbf{\Omega}},1}}_{=0} + \alpha_{\mathrm{D}_{\mathbf{\Omega}},2} + \alpha_{\mathrm{D}_{\mathbf{\Omega}},3} \end{aligned} \tag{4.8}$$

The three damping rate parts $\alpha_{\mathrm{D}_{\mathbf{\Omega}},1}$-$\alpha_{\mathrm{D}_{\mathbf{\Omega}},3}$ are related to the three cross-product terms in the numerator of Eq. (4.8). Recall that $\alpha_{\mathrm{D}_{\mathbf{\Omega}},1}$ vanishes identically as shortly explained in Section 2.3. Detailed information on $\alpha_{\mathrm{D}_{\mathbf{\Omega}},1}$ is provided in Appendix A. Ultimately, the decomposed solution variables of Eqs. (2.18)-(2.20) can be inserted into Eq. (4.8) to investigate the stability of acoustic and vortical sub-modes separately as a function of the volumetric sinks/sources $D_{\mathbf{\Omega}}$. Specifically, normalizing the acoustic and vortical dissipation parts with the respective period-averaged, volume-integrated acoustic (E_a) and vortical energy densities (E_v) gives the two corresponding damping rates

$$\alpha_{\mathrm{D}_{\mathbf{\Omega}},\mathrm{a}} = \frac{1}{2}\frac{\int_V \langle D_{\mathbf{\Omega},\mathrm{a}} \rangle \mathrm{d}V}{\int_V \langle E_\mathrm{a} \rangle \mathrm{d}V}, \tag{4.9}$$

$$\alpha_{\mathrm{D}_{\mathbf{\Omega}},\mathrm{v}} = \frac{1}{2}\frac{\int_V \langle D_{\mathbf{\Omega},\mathrm{v}} \rangle \mathrm{d}V}{\int_V \langle E_\mathrm{v} \rangle \mathrm{d}V}. \tag{4.10}$$

For evaluations with the growth rate Eq. (4.8), solution fields for disturbance pressure $\hat{p}$ and velocity $\hat{\mathbf{u}}$ are required. These are straightforwardly obtainable from eigenfrequency simulations with the CFD/CAA approach introduced in Section 4.1. In conclusion, a CFD/CAA eigenfrequency simulation needs to be carried out first. The resulting eigenmode shape consisting of acoustic and vortical parts is used to calculate individual acoustic and/or vortical growth rate parts with the growth rate Eq. (4.8).

In order to access the growth rates of acoustic and vortical sub-modes in Eqs. (4.9)-(4.10), the pressure and velocity disturbance fields need to be split into acoustic and vortical parts as proposed in Eqs. (2.18)-(2.20). This is achieved by a Helmholtz decomposition, which is presented in Section 4.3.

4.3 Helmholtz Decomposition of Disturbance Fields

Helmholtz' decomposition theorem [109] is commonly used in fluid dynamics to compute solenoidal and irrotational parts of velocity fields [110]. In this thesis, it is applied to solution fields of the LNSE/LEE in the frequency domain to obtain explicit access to their acoustic and vortical sub-modes.

For reactive cases with mean density gradients ($\nabla\bar{\rho} \neq \mathbf{0}$), the acoustic velocity field does generally not satisfy the irrotationality condition, i.e. $\nabla \times \hat{\mathbf{u}}_\mathrm{a} \neq \mathbf{0}$. Physically, this can be explained by the refraction of acoustic waves at density gradients in the flame region. This phenomenon induces a rotational component in the acoustic velocity vector $\hat{\mathbf{u}}_\mathrm{a}$ if the mean density gradient and the incident acoustic wave are arranged in angle to each other. Applying the Helmholtz decomposition to the LNSE/LEE velocity vector $\hat{\mathbf{u}}$ with the goal to determine acoustic and vortical parts, is thus incorrect as the acoustic velocity field does not represent the irrotional part of the LNSE/LEE velocity field only. Hence, an alternative disturbance quantity is required which describes acoustic and vortical motions. In addition, the acoustic part of this quantity must be irrotational in the presence of mean density gradients.

With reference to Appendix C, the disturbance mass flow field $\hat{\mathbf{m}}$ satisfies these requirements and thus, represents a suitable quantity to decompose an isentropic LNSE/LEE solution field into its acoustic and vortical sub-modes. Application of Helmholtz' decomposition theorem, which states that any (smooth) vector field is represented by the sum of the gradient of a scalar potential and the curl of a vector potential [110], allows writing of the LNSE/LEE mass flow vector as

$$\hat{\mathbf{m}} = \hat{\mathbf{m}}_{\mathrm{a}} + \hat{\mathbf{m}}_{\mathrm{v}} = \nabla\Phi_{\hat{\mathbf{m}}} + \nabla\times\boldsymbol{\chi}_{\hat{\mathbf{m}}}. \tag{4.11}$$

Acoustic and vortical mass flow parts correspond to the scalar potential $\Phi_{\hat{\mathbf{m}}}$ and the vector potential $\boldsymbol{\chi}_{\hat{\mathbf{m}}}$, respectively. To either solve for the scalar or the vector potential, either the divergence or the curl is applied to Eq. (4.11) yielding the equations

$$\nabla\cdot\hat{\mathbf{m}} = \nabla\cdot\hat{\mathbf{m}}_{\mathrm{a}} = \nabla\cdot\nabla\Phi_{\hat{\mathbf{m}}} = \Delta\Phi_{\hat{\mathbf{m}}} \tag{4.12}$$

$$\nabla\times\hat{\mathbf{m}} = \nabla\times\hat{\mathbf{m}}_{\mathrm{v}} = \nabla\times\nabla\times\boldsymbol{\chi}_{\hat{\mathbf{m}}}. \tag{4.13}$$

In Eqs. (4.12)-(4.13), irrotationality of the acoustic and solenoidality the vortical mass flow field is exploited, i.e.

$$\nabla\times\hat{\mathbf{m}}_{\mathrm{a}} = \nabla\times\nabla\Phi_{\hat{\mathbf{m}}} = \mathbf{0}, \tag{4.14}$$

$$\nabla\cdot\hat{\mathbf{m}}_{\mathrm{v}} = \nabla\cdot\nabla\times\boldsymbol{\chi}_{\hat{\mathbf{m}}} = 0. \tag{4.15}$$

The decomposed solution variables $\hat{\mathbf{m}}_{\mathrm{a}}$ and $\hat{\mathbf{m}}_{\mathrm{v}}$ can be obtained, if either Eq. (4.12) or Eq. (4.13) is solved numerically. Specifying acoustic boundary conditions (cf. Section 2.4.1), which can be explicitly formulated as a function of the scalar potential, allows computation of $\Phi_{\hat{\mathbf{m}}}$ via solving the Poisson Eq. (4.12) [110]. Notice additionally that the determination of the scalar potential goes along with a reduced computational effort compared to the computation of the vector potential $\boldsymbol{\chi}_{\hat{\mathbf{m}}}$: for a three-dimensional case, three equations need to be solved in order to obtain the vector potential, while only one equation is required to obtain the scalar potential. In this thesis, the isentropic LNSE/LEE in combination with the Poisson Eq. (4.12) are solved numerically with the sFEM. This introduces the scalar potential $\Phi_{\hat{\mathbf{m}}}$ as a further solution variable, which is directly coupled to the LNSE/LEE solution fields. The equation for the scalar potential $\Phi_{\hat{\mathbf{m}}}$ in weak formulation reads

$$\int_V \left[(\nabla\cdot\hat{\mathbf{m}})\,\psi_{\Phi_{\hat{\mathbf{m}}}} + \nabla\Phi_{\hat{\mathbf{m}}}\cdot\nabla\psi_{\Phi_{\hat{\mathbf{m}}}}\right]\mathrm{d}V - \int_S (\mathbf{n}\cdot\nabla\Phi_{\hat{\mathbf{m}}})\psi_{\Phi_{\hat{\mathbf{m}}}}\mathrm{d}S = 0, \tag{4.16}$$

where $\int_V \Delta\Phi_{\hat{\mathbf{m}}}\psi_{\Phi_{\hat{\mathbf{m}}}}\mathrm{d}V = -\int_V \nabla\Phi_{\hat{\mathbf{m}}}\cdot\nabla\psi_{\Phi_{\hat{\mathbf{m}}}}\mathrm{d}V + \int_S(\mathbf{n}\cdot\nabla\Phi_{\hat{\mathbf{m}}})\psi_{\Phi_{\hat{\mathbf{m}}}}\mathrm{d}S$ is applied to the second order derivatives of the Poisson Eq. (4.12) [99]. Hence, the Helmholtz decomposition is not treated as a post-processing step, which facilitates and accelerates the computation of acoustic and vortical sub-modes as separated post-processing steps can be avoided.

After having determined $\Phi_{\hat{\mathbf{m}}}$ of a LNSE/LEE solution via numerically solving Eq. (4.12), acoustic and vortical mass flow fields can directly be computed by

$$\hat{\mathbf{m}}_{\mathrm{a}} = \nabla\Phi_{\hat{\mathbf{m}}} = \hat{\mathbf{u}}_{\mathrm{a}}\bar{\rho} + \frac{\hat{p}_{\mathrm{a}}}{\bar{c}^2}\bar{\mathbf{u}} \qquad \rightarrow \qquad \hat{\mathbf{m}}_{\mathrm{v}} = \hat{\mathbf{m}} - \hat{\mathbf{m}}_{\mathrm{a}}. \tag{4.17}$$

The corresponding velocity fields are obtained from Eq. (4.17) and by exploiting Eq. (2.19) i.e.

$$\hat{\mathbf{u}}_{\mathrm{a}} = \frac{\hat{\mathbf{m}}_{\mathrm{a}} - \frac{\hat{p}_{\mathrm{a}}}{\bar{c}^2}\bar{\mathbf{u}}}{\bar{\rho}} \qquad \rightarrow \qquad \hat{\mathbf{u}}_{\mathrm{v}} = \hat{\mathbf{u}} - \hat{\mathbf{u}}_{\mathrm{a}}. \tag{4.18}$$

Finally, the acoustic pressure $\hat{p}_{\mathrm{a}}$, which is also required to compute $\hat{\mathbf{u}}_{\mathrm{a}}$ in Eq. (4.18), and the vortical pressure can be computed via

$$\hat{p}_{\mathrm{a}} = -\left(i\omega\Phi_{\hat{\mathbf{m}}} + \bar{\mathbf{u}}\cdot\nabla\Phi_{\hat{\mathbf{m}}}\right) \qquad \rightarrow \qquad \hat{p}_{\mathrm{v}} = \hat{p} - \hat{p}_{\mathrm{a}}. \tag{4.19}$$

For the derivation of Eq. (4.19), the interested reader is referred to the Appendix C.2.

Figure 4.1 presents decomposed LNSE disturbance fields of the T1 eigenmode of the A^2EV combustor configuration introduced in Chapter 3. Notice that the root-cause of the irregular pattern visible along the shear-layer in the acoustic sub-mode results in the mid column of Fig. 4.1 is caused by the interaction of acoustics and vortices with the non-homentropic mean flow field. As pointed out in Ref. [87], this interaction would generate entropy waves, which are not resolved in this work due to the isentropicity Eq. (2.17). Thus, this irregular pattern reveals regions where "isentropic mass flow" is transformed into "entropy mass flow".

The Helmholtz decomposition of a LNSE/LEE mass flow field provides access to the acoustic part $\hat{\mathbf{m}}_{\mathrm{a}}$. This part is linked to the acoustic pressure $\hat{p}_{\mathrm{a}}$ and velocity $\hat{\mathbf{u}}_{\mathrm{a}}$ through Eq. (4.17). Although the acoustic mass flow field is irrotational (cf. Eq. (4.14)), this does generally not apply to the acoustic velocity field, i.e. $\nabla\times\hat{\mathbf{u}}_{\mathrm{a}} \neq \mathbf{0}$. This is demonstrated in the following by taking the curl of the acoustic mass flow field $\hat{\mathbf{m}}_{\mathrm{a}}$ in Eq. (4.20). Next, Eq.(4.20) is solved for $\nabla\times\hat{\mathbf{u}}_{\mathrm{a}}$,

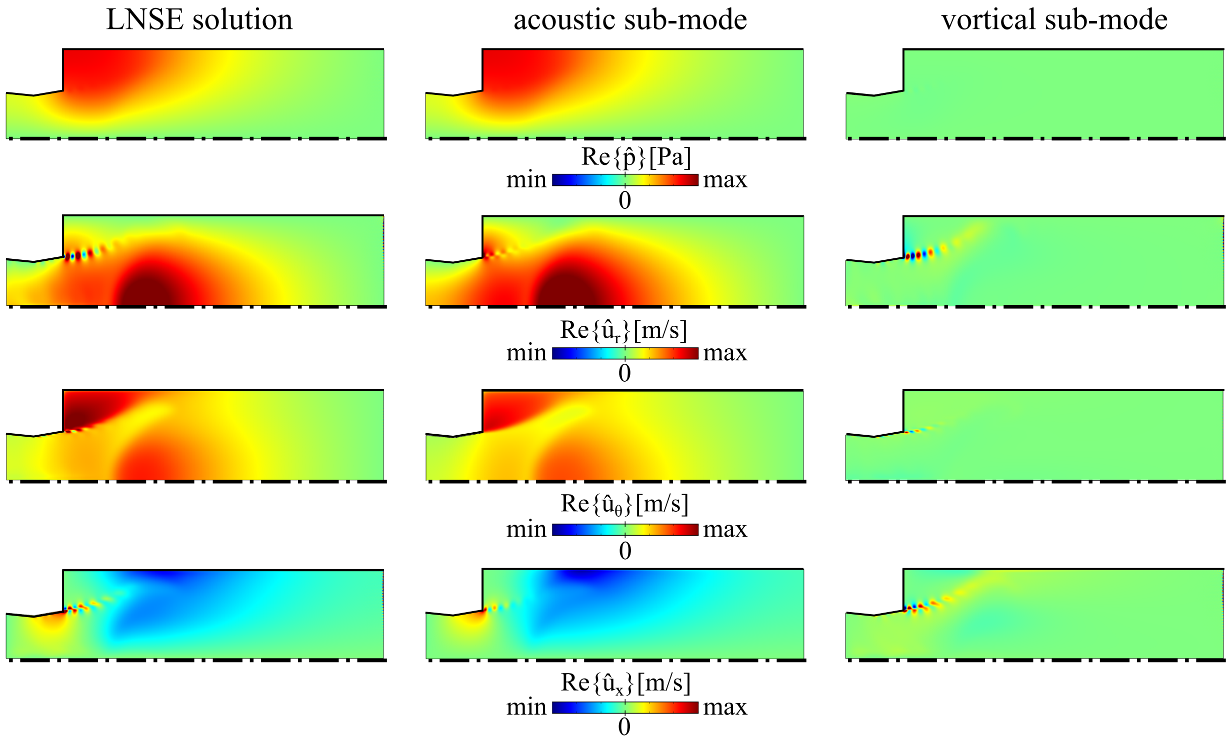

Figure 4.1: *Results of the mass flow Helmholtz decomposition of the T1 eigenmode of the A^2EV combustor: pressure (first row) with radial (second row), azimuthal (third row) and axial (fourth row) velocity distributions for the original LNSE solution (left column) and for the decomposed acoustic (mid column) as well as vortical (right column) sub-modes.*

which gives Eq. (4.21):

$$\nabla \times \hat{\mathbf{m}}_a = \nabla \times \nabla \Phi_{\hat{\mathbf{m}}} = \nabla \times \left(\bar{\rho} \hat{\mathbf{u}}_a + \underbrace{\frac{\hat{p}_a}{\bar{c}^2}}_{=\hat{\rho}_a} \bar{\mathbf{u}} \right) = \mathbf{0} \tag{4.20}$$

$$\rightarrow \quad \nabla \times \hat{\mathbf{u}}_a = \hat{\boldsymbol{\Omega}}_a = -\frac{1}{\bar{\rho}} \left[\nabla \bar{\rho} \times \underbrace{\hat{\mathbf{u}}_a}_{\approx \frac{\nabla \hat{p}_a}{i\omega\bar{\rho}}} + \hat{\rho}_a \underbrace{\nabla \times \bar{\mathbf{u}}}_{=\bar{\boldsymbol{\Omega}}} + \nabla \hat{\rho}_a \times \bar{\mathbf{u}} \right] \tag{4.21}$$

Equation (4.21) confirms that the acoustic velocity field is governed by acoustic vorticity perturbations $\hat{\boldsymbol{\Omega}}_a$, if the angle between the acoustic velocity field and the mean density gradient is non-zero (first term in Eq. (4.21)). This term indicates that rotation is introduced by the baroclinic effect [17], which is recognizable if the acoustic velocity field is expressed as a function of the acoustic pressure[3]. Similarly, rotation is produced, if the acoustic density gradient and the mean velocity vector are not parallel allocated (third term in Eq. (4.21)). Additional rotation is induced, if acoustic density perturbations are exposed to a shear-layer in the bulk flow (second term in Eq. (4.21)). Equation (4.21) reveals that the acoustic velocity field is only irrotational in the absence of mean density gradients[4] and of a bulk flow. Then, Eq. (4.21) becomes the zero vector, which indicates that the acoustic velocity field is irrotational.

For isothermal conditions and low Mach numbers ($M \ll 1$), this implies that mass flow Helmholtz decomposition can be replaced by the Helmholtz decomposition of the LNSE/LEE velocity field $\hat{\mathbf{u}}$ as $\nabla \times \hat{\mathbf{m}}_\mathrm{a} \approx \bar{\rho}\nabla \times \hat{\mathbf{u}}_\mathrm{a} \approx \mathbf{0}$. In this case, the LNSE/LEE velocity vector can be written as

$$\hat{\mathbf{u}} = \hat{\mathbf{u}}_\mathrm{a} + \hat{\mathbf{u}}_\mathrm{v} = \nabla\Phi + \nabla \times \boldsymbol{\chi}, \tag{4.22}$$

with the new scalar and vector velocity potentials Φ and $\boldsymbol{\chi}$. With reference to Eqs. (4.11)-(4.16), Eq. (4.22) can be solved for Φ, which gives the acoustic and vortical velocity and pressure fields of the associated LNSE/LEE solution in a decomposed manner:

$$\hat{\mathbf{u}}_\mathrm{a} = \nabla\Phi \qquad \rightarrow \qquad \hat{\mathbf{u}}_\mathrm{v} = \hat{\mathbf{u}} - \hat{\mathbf{u}}_\mathrm{a} \tag{4.23}$$

$$\hat{p}_\mathrm{a} = -\bar{\rho}\left(i\omega\Phi + \bar{\mathbf{u}}\cdot\nabla\Phi\right) \qquad \rightarrow \qquad \hat{p}_\mathrm{v} = \hat{p} - \hat{p}_\mathrm{a}. \tag{4.24}$$

Notice that the equation for the acoustic pressure $\hat{p}_\mathrm{a}$ in Eq. (4.24) (cf. Refs. [89, 111]) can be deduced from the linearized APE momentum Eq. (2.30) (details in the Appendix C.2).

Notice that all LNSE/LEE solution fields associated with an isothermal mean flow field, i.e. $\nabla\bar{\rho} = \mathbf{0}$, are decomposed by applying the Helmholtz decomposition to the velocity field $\hat{\mathbf{u}}$ in this thesis. An example of LEE decomposition results of the T1 eigenmode of a non-reactive, isothermal A^2EV combustor configuration is presented in Fig. A.3 of Appendix A.1. A comparison between the mass flow and velocity decomposition is provided in Appendix C.

[3] This is justifiable in the case of zero or small Mach numbers.

[4] An exception would be a longitudinal eigenmode in a straight duct with temperature jump. Then $\nabla\bar{\rho} \parallel \hat{\mathbf{u}}_\mathrm{a}$ and thus $\nabla\bar{\rho} \times \hat{\mathbf{u}}_\mathrm{a} = \mathbf{0}$ in Eq. (4.21).

4.4 Model Order Reduction

The CFD/CAA method introduced in Section 4.1 is limited to linear perturbations, which means that is only capable of describing the early stage of a thermoacoustic instability. As illustrated in Fig. 1.2, this early stage ends, when the temporal amplitude evolution can no longer be approximated by an exponential curve (cf. $\boxed{3}$ in Fig. 1.2). The inclusion of non-linear effects to the CFD/CAA method would require convolution operations, which is not straightforward. To avoid this, non-linear saturation effects and limit-cycle oscillations (cf. $\boxed{4}$ and $\boxed{5}$ in Fig. 1.2, respectively) as well as multi-modal interactions are modeled in the time-domain via non-linear equations. In this thesis, the isentropic APE (2.22)-(2.23) in the time domain are expanded to account for non-linear mechanisms. The APE have the advantage over the LEE/LNSE that no artificial diffusion scheme is required to produce stable solutions. The contribution of further dissipative mechanisms (such as of vortex shedding) can be considered by modifying the APE growth rate. Flame driving can be modeled directly in the time domain simulation. More details are provided in Chapter 7.

Directly solving the modified APE in the time domain is theoretically possible and would provide the desired information on the non-linear thermoacoustic dynamics. However, this approach is impractical as the large discrete system sizes of the A^2EV combustor (which result from highly resolved meshes in this thesis, see for instance Fig. 5.7) –and particularly of industrially relevant combustors– deny an efficient numerical computation of the envelope amplitude of the disturbance solution variables. To circumvent this problem, Hummel [37] applied the so-called *modal truncation* theory to non-compact thermoacoustic systems. He developed a *Reduced Order Model* (ROM), which allows efficient computation of non-linear oscillations in combustion chambers with arbitrarily complex geometries. The starting point for the model order reduction is given by the linear state-space system

$$\frac{\mathrm{d}\boldsymbol{\phi}'}{\mathrm{d}t} + \mathbf{E}^{-1}\mathbf{A}\boldsymbol{\phi}' = \mathbf{E}^{-1}\mathbf{B}\mathbf{u} \tag{4.25}$$

$$\mathbf{y} = \mathbf{C}\boldsymbol{\phi}' + \mathbf{D}, \tag{4.26}$$

which describes the dynamical behavior of the full order system in the time-domain. Equation (4.25) can be obtained by inversely Laplace transform the eigenvalue problem of Eq. (4.1) and left-multiplication by the inverse of $\mathbf{E}$. The addition of the input matrix $\mathbf{B}$ allows the incorporation of spatially distributed momentum and energy sources/sinks hosted by the input signal vector $\mathbf{u}$. Output signals $\mathbf{y}$ of the solution variables p' and $\mathbf{u}'$ are retrieved by Eq. (4.26), where $\mathbf{C}$ is the output matrix. $\mathbf{D}$ denotes the feedthrough matrix, which is omitted ($\mathbf{D} = \mathbf{0}$). The four main tasks to obtain the ROM from Eqs. (4.25)-(4.26) comprise:

1. Transformation of the state-space system matrix $\mathbf{E}^{-1}\mathbf{A}$ into its corresponding canonical normal form $\tilde{\mathbf{A}}$. In this equivalent representation, the eigenvalues (or rather the eigenfrequencies $i\omega_{\mathrm{i}}$) form the new diagonal system matrix, i.e. $\tilde{\mathbf{A}} = \mathrm{diag}(i\omega_{\mathrm{i}})$.

2. Projection of the full system matrix in canonical normal form onto a reduced one, i.e. $\tilde{\mathbf{A}} \rightarrow \tilde{\mathbf{A}}_{\mathrm{r}}$, by limiting the eigenspace to the eigenmodes in the frequency range of interest. As a result, the number of degrees of freedom in the ROM reduces to the number of considered eigenmodes.

3. Creation of suitable in- and output matrices to model non-compact flame driving as well as amplitude-dependent acoustic dissipation via feedback loops in step #4.

4. Establishment of (non-)linear feedback loops between the output vector $\mathbf{y}$ and the input vector $\mathbf{u}$ as well as between the output vector $\mathbf{y}$ and the ROM system matrix $\tilde{\mathbf{A}}_{\mathrm{r}}$ to model (non-)linear flame driving and damping in the time-domain simulations, respectively.

The outcome of this procedure is the reduced order state-space model

$$\frac{\mathrm{d}\boldsymbol{\eta}}{\mathrm{d}t} = \tilde{\mathbf{A}}_{\mathrm{r}}\boldsymbol{\eta} + \tilde{\mathbf{B}}_{\mathrm{r}}\mathbf{u} \tag{4.27}$$

$$\mathbf{y} = \tilde{\mathbf{C}}_{\mathrm{r}}\boldsymbol{\eta}, \tag{4.28}$$

where the state vector $\boldsymbol{\eta}$ describes the temporal amplitude evolution of the eigenmodes considered in the reduced eigenspace. $\tilde{\mathbf{B}}_{\mathrm{r}}$ and $\tilde{\mathbf{C}}_{\mathrm{r}}$ are reduced in- and output matrices originating from the ROM creation process. Equations (4.27)-(4.28) serve as the basis for thermoacoustic computations in the time domain in Chapter 7. In the frame of this work, #4 of the ROM creation process is adapted to account for the pressure amplitude-dependency of the mean flow investigated in Chapter 6. This modification seeks to advance the physical accuracy and ultimately the predictive capabilities of the ROM with regard to limit-cycle oscillations and interactions between multiple unstable acoustic eigenmodes. This translates into the task to express the ROM system matrix $\tilde{\mathbf{A}}_{\mathrm{r}}$ and the input vector $\mathbf{u}$ as a non-linear function of the ROM output vector, i.e. $\tilde{\mathbf{A}}_{\mathrm{r}} = \tilde{\mathbf{A}}_{\mathrm{r}}(\mathbf{y})$ and $\mathbf{u} = \mathbf{u}(\mathbf{y})$.

To validate the modifications, the non-linear interaction between the in-swirl direction rotating T1 and the T2 modes of the A^2EV combustor are investigated and compared with measurements. Notice that the reduced system matrix $\tilde{\mathbf{A}}_{\mathrm{r}}$ is a [2x2] diagonal matrix made up of the T1 and T2 eigenvalues in this case. In contrast to this, the corresponding (full order) system matrices $\mathbf{E}$ and $\mathbf{A}$ of the fully discretized computational domain in Eq. (4.1) have the size $[n\mathrm{x}n]$. n is the number of degrees of freedom and depends on the mesh resolution, the spatial descretization order and the number of governing equations. Typical values of n are in the range of 10^4 to 10^6 degrees of freedom, which stresses the performance improvement with the ROM.

For more detailed information on the derivation of the ROM and on the theory of *modal truncation* the interested reader is referred to the dissertation of Hummel [37] and to Lunze [112], respectively.

5 Linear Stability Assessment

As pointed out in Section 1.2, a crucial aspect of the design, operation and control of a thermoacoustic system is given by the prediction of its linear stability limits. One approach to describe linear amplifying flame- as well as damping mean flow-acoustics interactions might be the utilization of linear, one-dimensional network models with compact elements characterized by one-dimensional transfer functions [29, 113]. However, for high-frequency oscillations this approach fails due to the non-compactness ascribed to the multi-dimensional wave propagation. In consequence, two- or three-dimensional simulations with the LNSE or LEE, which inherently account for any thermoacoustic non-compactness, have moved into the focus recently [49, 50].[1] Specifically, eigenfrequency analyses have been expected to yield the desired thermoacoustic stability information in terms of growth rates [37, 50, 114]. However, the predictive capabilities of this hybrid *Computational Fluid Dynamics/Computational Aero Acoustics* (CFD/CAA) methodology have not yet reached a sufficient level and are thus improved as part of this work. In this context, the present thesis seeks to provide a reliable and time-efficient thermoacoustic stability prediction tool. Furthermore, the tool must be applicable to industrially relevant combustor configurations and must solely use numerical computation approaches to avoid expensive, experimental investigations for the realization of thermoacoustic control and/or retrofit strategies.

To achieve this goal, the existing CFD/CAA tool is extended. The impact of the SUPG/PSPG numerical stabilization scheme on acoustics and on hydrodynamic vortices is investigated in Section 5.1.1. Based on these investigations, a methodology is introduced to eliminate the non-physical part ν_{stab} in LNSE/LEE growth rates (cf. Eq. (4.3)), which is caused by artificial diffusion. In Section 5.1.2, a local flame transfer function (FTF) is proposed to model the

[1] A detailed discussion about, and an analysis on the suitability of these equations for thermoacoustic stability predictions is provided in Appendix A.

thermoacoustic driving potential of vortex-flame interactions. In Section 5.2 of this chapter, the performance of the advanced CFD/CAA model is judged from the comparison of thermoacoustic stability prediction results with experimental observations. In addition, a methodology is established, which allows a detailed assessment of specific physical effects with respect to their relevance for the thermoacoustic stability.

5.1 Extension of the Thermoacoustic Prediction Tool

This section introduces the elimination method as well as the vortex-flame FTF to improve the predictive capabilities of the existing CFD/CAA tool for thermoacoustic stability analyses [37, 50].

5.1.1 Quantification and Elimination of Numerical Damping

The necessity for numerical stabilization (subscript "*stab*") with artificial diffusion represents one main shortcoming of CAA simulations with the sFEM[2]. Specifically, the growth rate ν obtained from eigenfrequency analyses with the LEE/LNSE hosts a non-physical contribution ν_{stab} originating from the artificial diffusion scheme in addition to the physically meaningful damping, driving and growth rates, α, β and $\nu_{\mathbf{I}}$ (see Eq. (4.3)). The quantification of the undesired, but necessary part ν_{stab} is not straightforward and represents the main goal of this section. As will be shown, the contribution of both rates, α and ν_{stab}, to the overall growth rate ν can be of the same order of magnitude. This may lead to a drastic overestimation of dissipation in the system and thus to a potentially incorrect thermoacoustic stability assessment.

The study in the present section seeks to advance the understanding on how the SUPG/PSPG stabilization scheme influences eigensolutions of the isentropic LEE and LNSE. The Helmholtz decomposition (see Section 4.3) of eigenmode shapes into acoustic and convectively transported vortical components reveals the impact of the SUPG/PSPG stabilization scheme on each perturbation field separately. Then, a methodology is presented to quantify the effect of numerical stabilization on the disturbance field in terms of the

[2] Parts of this section were published in Ref. [98]

growth rate ν_{stab}. This result can be subtracted from the original, "polluted" LEE/LNSE growth rate ν yielding a corrected growth rate ν_{corr}. The latter represents the "physical" part only which is associated with damping and driving inside the domain volume as well as with energy fluxes crossing the domain boundaries (cf. Eq. (4.3)), i.e.

$$\nu_{\mathrm{corr}} = \alpha + \beta + \nu_{\mathbf{I}} = \nu - \nu_{\mathrm{stab}}. \tag{5.1}$$

For reasons of clarity, the following analyses are conducted with the LEE instead of the LNSE as the utilization of the LNSE would result in a "mixture" of artificial and physically meaningful diffusion. As will be shown in Section 5.2, the extraction of the damping rate associated with the physical diffusion part from the overall, "polluted" LNSE growth rate requires an additional computational step. This step can be omitted in the case of LEE simulations.

5.1.1.1 Numerical Setup

In order to analyze the effect of artificial diffusion on acoustic and vortical sub-modes, the atmospheric and isothermal ($\bar{T}$ = 298K, $\bar{p}$ = 101325Pa, M_{in} = 0.2) experiment of Ronneberger [115] is numerically investigated instead of the A^2EV combustor. The advantage over transversal eigenmodes in the A^2EV combustor is that the principal direction of acoustic wave propagation and convection of vortices occurs in axial direction. Then, complex, multi-dimensional evaluations can be avoided, which facilitates analyses on the effect of artificial diffusion. Furthermore, the isothermal, non-reactive conditions are predestined for this proof-of-concept study as any effect of combustion on acoustic and vortical sub-modes can a priori be excluded. Finally, vortex shedding and vorticity-mean flow interaction remain the sole physical mechanisms inside the combustor volume affecting the stability of the acoustic sub-mode next to the non-physical one attributed to the numerical stabilization scheme:

$$\nu_{\mathrm{corr}} = \alpha_{\mathrm{D}_{\boldsymbol{\Omega}}} + \nu_{\mathbf{I}} = \nu - \nu_{\mathrm{stab}}. \tag{5.2}$$

However, notice that the subsequently proposed quantification and elimination method is applicable to reactive cases with mean density gradients as well. This will be demonstrated in Section 5.2 by application of the method to the linear stability assessment of the T1 mode of the A^2EV combustor.

A schematic of the setup of the experiment of Ronneberger is shown in Fig. 5.1. This rather simple area jump geometry consisting of two axisymmetric pipes is optimum to investigate longitudinal eigenmode shapes.

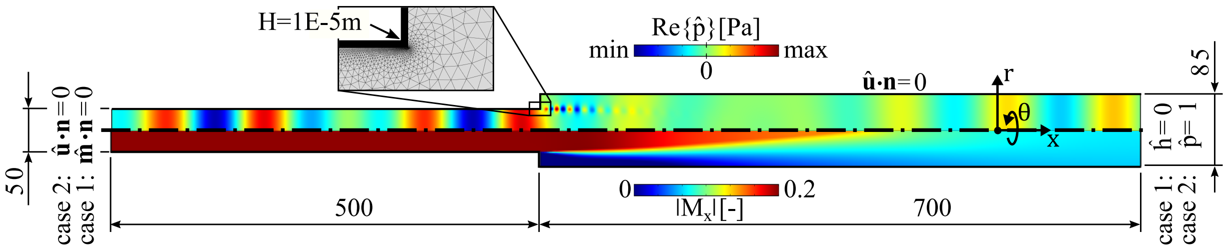

Figure 5.1: *Computational domain hosting the investigated longitudinal eigenmode shape in terms of pressure (upper half) for* $\alpha_\tau = 20$ *with corresponding boundary conditions and the underlying mean velocity field (lower half - dimensions in [mm]).*

The upper half of Fig. 5.1 shows the longitudinal pressure mode shape analyzed in this section together with the boundary conditions. For this proof-of-concept study, two sets of boundary conditions are used:

1.) In- and outlet boundary conditions are energetically neutral (cf. Section 2.4.1). This is achieved by specifying $\hat{\mathbf{m}} \cdot \mathbf{n} = 0$ at the inlet and $\hat{h} = 0$ at the outlet (case 1 in Fig. 5.1).

2.) The system is excited at the outlet and is closed at the inlet. This is achieved by specifying $\hat{p} = 1$ at the outlet and $\hat{\mathbf{u}} \cdot \mathbf{n} = 0$ at the inlet (case 2 in Fig. 5.1)[3].

Boundary case 1 is used for the eigenfrequency analyses in Sections 5.1.1.3-5.1.1.4. The absence of intensity $\mathbf{I}$ (cf. Eq. (2.34)) at in- and outlets leaves damping due to artificial diffusion (ν_{stab}) and vortex shedding as well as vorticity-mean flow interactions ($\alpha_{\mathrm{D}_\Omega}$) as the sole contributions to the LEE growth rate in Eq.(5.2). This is exploited to demonstrate that the LEE growth

[3]The system is excited (either at one or multiple locations) at a frequency f of interest (in this case, the frequency of interest exactly matches the eigenfrequency of the longitudinal eigenmode shown in Fig. 5.1, i.e. $f = \mathrm{Re}\{\omega_i\}/2\pi$). Mathematically this can be achieved by introducing a load vector $\mathbf{B}$ on the r.h.s. of Eq. (4.1), i.e. $i\omega\mathbf{E}\hat{\boldsymbol{\phi}} + [\mathbf{A} + \tau\mathbf{A}_{\text{stab}}]\hat{\boldsymbol{\phi}} = \mathbf{B}$.

rate is composed of these two growth rate parts in an additive manner.

Boundary case 2 is used in the frame of a forced frequency response analysis in Section 5.1.1.2 to study the effect of numerical damping on LEE eigenmode shapes. This is done by investigating the acoustic and vortical intensity $\mathbf{I}_{a/v}$ along the axis, which provides information on the axial transport of disturbance energy E. The closed inlet prevents the decay of the acoustic intensity $\mathbf{I}_a$ from the outlet towards a zero value at the inlet, which facilitates the interpretation of results.

The close-up view in Fig. 5.1 shows the FEM mesh in the vicinity of the area jump. The grid in the corner region is highly refined. The eigenmode shape shown in the upper half of Fig. 5.1 is obtained by solving the eigenvalue problem of Eq. (4.1) with the stabilized LEE ($\alpha_\tau = 20$) and boundary case 1. In accordance with the CFD/CAA methodology, the mean flow fields are determined in a separate steady-state, incompressible RANS CFD simulation. The resulting flow fields serve as the input to the isentropic LEE (2.28)-(2.29). The lower half of the axisymmetric configuration displays the absolute value of the mean velocity field, which amounts to $M_{\text{in}} = 0.2$ at the inlet. Notice that slip-walls are assumed in the CFD simulation to avoid mean vorticity production in the boundary-layer along the walls.

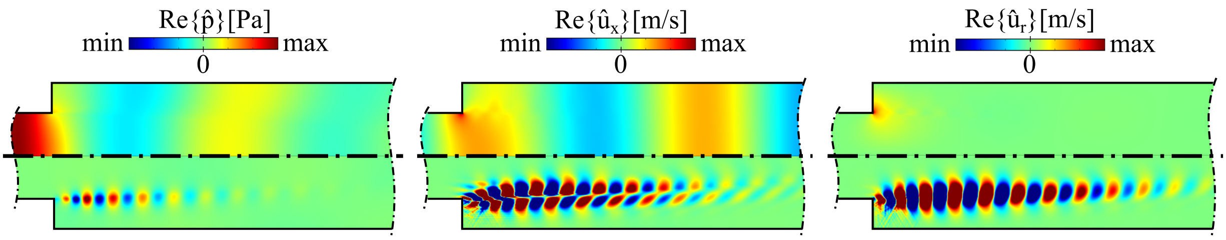

Figure 5.2: *Decomposed acoustic (upper halves) and vortical (lower halves) disturbance fields for* $\alpha_\tau = 20$.

Applying the velocity Helmholtz decomposition to the overall LEE field in Fig. 5.1 leads to the sub-modes presented in Fig. 5.2: the top half represents the pure acoustic part and the lower half the complementary vortical part. The original LEE pressure field in Fig. 5.1 can be reconstructed by adding up the acoustic and vortical pressure fields shown on the left side of Fig. 5.2. In Section 5.1.1.2, this decomposed eigenmode shape is used to analyze the impact of the numerical stabilization scheme on the acoustic and the convective, vortical sub-mode. In addition, the subsequently presented methodology to quantify the damping rate due to artificial diffusion is applied to this eigensolution as well.

5.1.1.2 Impact of Artificial Diffusion on Acoustic and Vortical Sub-Modes

In this section the impact of artificial diffusion on eigensolutions of the LEE is analyzed from a global perspective via investigating the dependency of acoustic and vortical intensity (cf. Eq. (2.38)) on the tuning variable α_τ. Recall that this parameter allows adjustment of the amount of artificial diffusion introduced to the LEE.

Inserting the vortical-acoustic decomposition approaches of Eqs. (2.15)-(2.16) into the eigenvalue problem of Eq. (4.1) gives

$$i\omega_{\mathrm{i}}\mathbf{E}(\hat{\boldsymbol{\phi}}_{\mathrm{i,a}}+\hat{\boldsymbol{\phi}}_{\mathrm{i,v}})+\left[\mathbf{A}(\hat{\boldsymbol{\phi}}_{\mathrm{i,a}}+\hat{\boldsymbol{\phi}}_{\mathrm{i,v}})+\tau\mathbf{A}_{\mathrm{stab}}(\hat{\boldsymbol{\phi}}_{\mathrm{i,a}}+\hat{\boldsymbol{\phi}}_{\mathrm{i,v}})\right]=\mathbf{0}. \tag{5.3}$$

Equation (5.3) indicates that the employed stabilization scheme acts separately on acoustic and vortical sub-modes. This allows analysis of its impact on each of the sub-modes and implies a decomposition of the artificial diffusion growth rates into

$$\nu_{\mathrm{stab}}=\nu_{\mathrm{stab,a}}+\nu_{\mathrm{stab,v}} \tag{5.4}$$

with $\nu_{\mathrm{stab,a}}$ and $\nu_{\mathrm{stab,v}}$ acting on acoustic and vortical sub-modes only.

The decomposed solution fields shown in Fig. 5.2 are used to compute the period-averaged, axial acoustic and vortical intensities, $\langle I_{\mathrm{a,x}}\rangle$ and $\langle I_{\mathrm{v,x}}\rangle$ (cf. Eq. (2.34)):

$$\langle I_{\mathrm{a,x}}\rangle=\left\langle\left[\frac{\hat{p}_{\mathrm{a}}}{\bar{\rho}}+\hat{\mathbf{u}}_{\mathrm{a}}\cdot\bar{\mathbf{u}}\right]\left[\bar{\rho}\,\hat{u}_{\mathrm{a,x}}+\hat{\rho}_{\mathrm{a}}\bar{u}_{\mathrm{x}}\right]\right\rangle, \tag{5.5}$$

$$\langle I_{\mathrm{v,x}}\rangle=\left\langle\left[\frac{\hat{p}_{\mathrm{v}}}{\bar{\rho}}+\hat{\mathbf{u}}_{\mathrm{v}}\cdot\bar{\mathbf{u}}\right]\left[\bar{\rho}\,\hat{u}_{\mathrm{v,x}}+\hat{\rho}_{\mathrm{v}}\bar{u}_{\mathrm{x}}\right]\right\rangle. \tag{5.6}$$

Eqs. (5.5)-(5.6) describe the axial acoustic and vortical energy flux density or in other words, the transport of acoustic and vortical energy E_{a} and E_{v} in axial direction. Figure 5.3 a) presents the spatial distribution of axial acoustic (upper half) and vortical (lower half) energy flux densities in response to the downstream, acoustic excitation ($\hat{p} = 1$, boundary condition case 2). The flux density fields in Fig. 5.3 a) are radially integrated. The integrated result of $\langle I_{a,x} \rangle$ and $\langle I_{v,x} \rangle$ are plotted against the axial coordinate x in Fig. 5.3 b) for three different values of the global stabilization parameter α_τ. Reddish and bluish lines represent acoustic and vortical energy density fluxes, respectively.

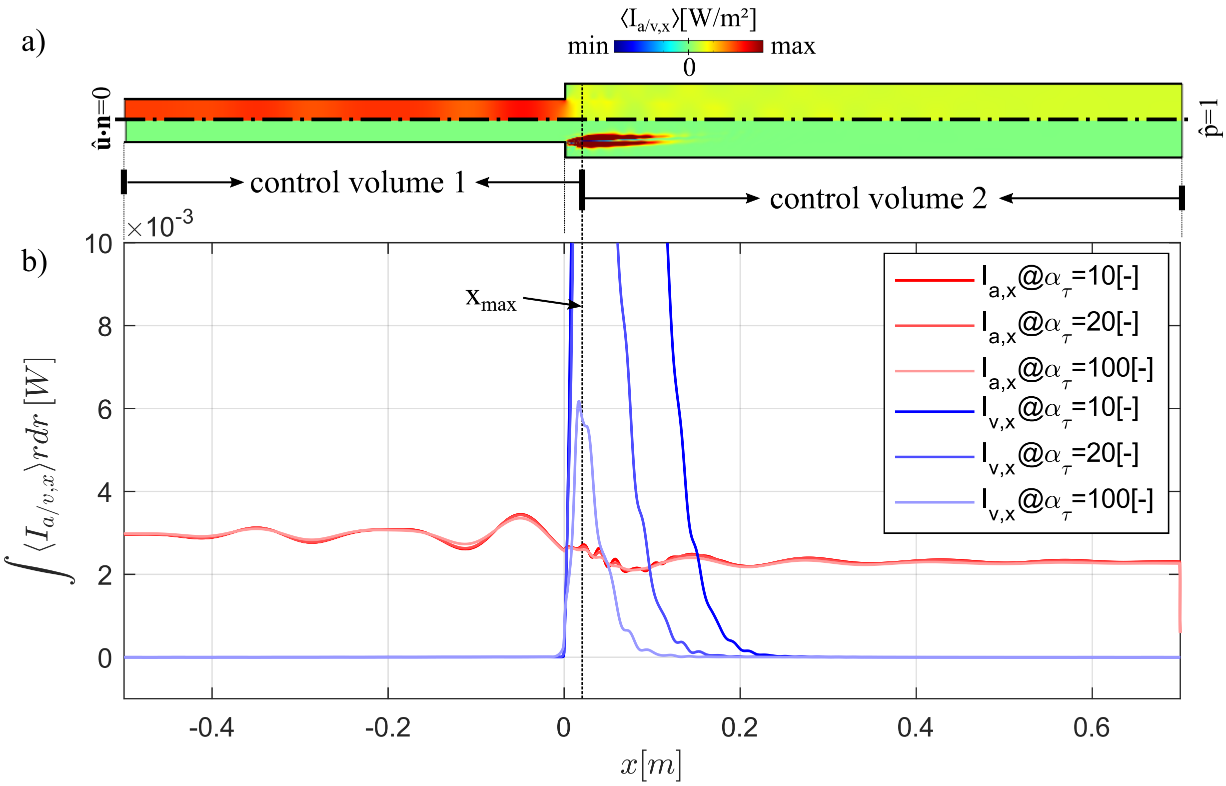

Figure 5.3: *a) Acoustic (upper half) and vortical (lower half) energy flux densities for a global tuning parameter value of $\alpha_\tau = 20$; b) integrated fluxes along the axis.*

Acoustic energy is transported by the mean flow through the inlet into the domain. This is possible because the inlet boundary is not specified to be energetically neutral. Due to the absence of mean vorticity inside the smaller, upstream pipe (promoted by slip walls in the CFD simulation), i.e. $-0.5\text{m} \leq x \leq 0\text{m}$, no vorticity perturbations and thus vortical energy is transported. At the area jump ($x = 0\text{m}$), the mean flow separates and a shear-layer develops. The acoustic field couples with the shear-layer, which provokes the consumption of acoustic energy to generate the convectively transported vortex perturbations. This explains the decrease of the acoustic energy flux (reddish lines in Fig. 5.3) over the area jump and the transport of vortical energy for $x \geq 0$m in downstream direction. The decrease of the acoustic energy flux is (almost) equal for the three α_τ values revealing that the transformation process from acoustic into vortical energy is (almost) unaffected by the numerical stabilization scheme. The bluish lines in Fig. 5.3 b) reveal that the vortical energy flux vanishes completely while convecting downstream through the computational domain. Increasing α_τ values accelerate the dissipation process, which demonstrates that numerical damping is responsible for the decay of the vortical perturbations. From an energetically point of view, this implies that the energy supplied by the acoustic field to generate/shed the vortices is fully dissipated by numerical damping. To illustrate this, the energy balances for the vortical sub-mode in the control volumes 1 (V_1) and 2 (V_2) displayed in Fig. 5.3 are given in Eqs. (5.7)-(5.8). Notice that the border plane between the control volumes is placed at the location of the maximum vortical flux density value, i.e. $\max\left(\int \langle I_{\mathrm{v,x}}\rangle r dr\right) \rightarrow x_{\mathrm{max}}$, which is also depicted in Fig. 5.3:

$$\left[\langle I_{\mathrm{v,x}}\rangle\right]_{x=0}^{x=x_{\mathrm{max}}} + \int_{V_1} D_{\mathbf{\Omega},\mathrm{v}} + D_{\mathrm{stab,v}} \mathrm{d}V_1 = 0, \tag{5.7}$$

$$\left[\langle I_{\mathrm{v,x}}\rangle\right]_{x=x_{\mathrm{max}}}^{x=0.7} + \int_{V_2} \underbrace{D_{\mathbf{\Omega},\mathrm{v}}}_{\approx 0} + D_{\mathrm{stab,v}} \mathrm{d}V_2 = 0, \tag{5.8}$$

In control volume 1 (cf. Eq. (5.7)), the vortical energy flux at $x = 0$ is zero. The volumetric source $D_{\mathbf{\Omega},\mathrm{v}}$ describes the vortical energy supplied by the acoustic field through energy transformation and by the bulk flow through the interaction of shed vortices with the mean velocity field. In control volume 1, a small fraction of the vortical energy is dissipated by artificial diffusion (cf. the term with $D_{\mathrm{stab,v}}$ in Eq. (5.7)). The larger portion leaves control volume 1 towards control volume 2. In control volume 2 (cf. Eq. (5.8)), no vortical energy is supplied ($D_{\mathbf{\Omega},\mathrm{v}} \approx 0$), but only dissipated by numerical diffusion. Remember that the transformation from acoustic into vortical energy primarily occurs in the vicinity of the sharp corner. Combining Eqs. (5.7)-(5.8) shows that the energy supply from the acoustic and the mean flow field is dissipated by the numerical stabilization scheme, i.e.

$$\int_{V_1} D_{\mathbf{\Omega},\mathrm{v}} + D_{\mathrm{stab,v}} \mathrm{d}V_1 + \int_{V_2} \underbrace{D_{\mathbf{\Omega},\mathrm{v}}}_{\approx 0} + D_{\mathrm{stab,v}} \mathrm{d}V_2 = 0 = \int_V \frac{\partial \langle E_{\mathrm{v}}\rangle}{\partial t} \mathrm{d}V \tag{5.9}$$

Thus, the temporal change of vortical energy density $\langle E_\mathrm{v}\rangle$ is zero in the total computational domain. As a result, the LEE growth can be written as

$$\nu = \nu_\mathrm{a} + \underbrace{\nu_\mathrm{v}}_{=0} = \alpha_{\mathrm{D}_{\boldsymbol{\Omega}},\mathrm{a}} + \nu_{\mathrm{stab,a}} + \nu_{\mathbf{I},\mathrm{a}} + \underbrace{\alpha_{\mathrm{D}_{\boldsymbol{\Omega}},\mathrm{v}} + \nu_{\mathrm{stab,v}}}_{=0}. \tag{5.10}$$

where $\nu_{\mathrm{stab,a}}$ is the artificial diffusion growth rate, which acts on acoustics only. The growth rate $\nu_{\mathbf{I},\mathrm{a}}$ is associated with acoustic energy fluxes leaving or entering the domain through in- and outlets. Recall that this growth rate vanishes for energetically neutral in- and outlet boundary conditions. In order to determine the physically meaningful acoustic growth rate $\nu_{\mathrm{corr}} = \alpha_{\mathrm{D}_{\boldsymbol{\Omega}},\mathrm{a}} + \nu_{\mathbf{I},\mathrm{a}}$ from a LEE growth rate ν, the quantification of $\nu_{\mathrm{stab,a}}$ is required.

5.1.1.3 Quantification of Numerical Damping

The task of this section comprises the quantification of the non-physical growth rate $\nu_{\mathrm{stab,a}}$ in eigenfrequency analyses with the LEE. The goal of the quantification approach is to determine the corrected LEE growth rate ν_{corr} by subtraction of $\nu_{\mathrm{stab,a}}$ from the "polluted" LEE growth rate ν. In the present and the following Section 5.1.1.4, the boundary condition case 1 is applied. This simplifies Eq. (5.10) to

$$\nu = \alpha_{\mathrm{D}_{\boldsymbol{\Omega}},\mathrm{a}} + \nu_{\mathrm{stab,a}}. \tag{5.11}$$

since $\nu_{\mathbf{I},\mathrm{a}} = 0$.

The proposed quantification methodology is based on the combination of eigenfrequency simulations with the source-free, isentropic LEE and APE. Recall that the APE solely describe the acoustic propagation while the convectively transported, vortical sub-mode is suppressed. In other words, the source-free APE are equivalent to the LEE without considering the mechanism of acoustically induced vortex shedding. Hence, the growth rates computed with the LEE and APE are expected to solely differ by the impact of the cross-product terms $\bar{\rho}[(\bar{\boldsymbol{\Omega}} \times \hat{\mathbf{u}}) + (\hat{\boldsymbol{\Omega}} \times \bar{\mathbf{u}})]$ and $\hat{\rho}(\bar{\boldsymbol{\Omega}} \times \bar{\mathbf{u}})$ (cf. Eq. (2.21)), if numerical stabilization is identical in both systems of equations. This is assumed to be fulfilled, if

- the boundary conditions and mean flow fields are the same for both systems of equations,

- mesh topology and size remain identical,
- the tuning variable α_τ is equal and
- the cross-product terms only weakly perturb the (natural) acoustic LEE sub-mode.

The first condition seeks to keep the numerical LEE and APE setups identical. The second and third conditions enforce equal distributions of the stabilization parameter $\tau(\mathbf{x})$ of the SUPG/PSPG stabilization scheme. The last requirement establishes similarity between the acoustic solution fields of LEE and APE and is fulfilled if $f \gg \alpha_{\mathrm{D}_\Omega,\mathrm{a}}$ in LEE eigenfrequency simulations. Then, the vorticity terms barely affect the acoustic LEE mode shape, which thus resembles the APE mode shape.

The LEE and APE growth rates can be written as

$$\nu_{\mathrm{LEE}} = \alpha_{\mathrm{D}_\Omega,\mathrm{a}} + \nu_{\mathrm{stab,a}} \tag{5.12}$$

$$\nu_{\mathrm{APE}} = \nu_{\mathrm{stab,a}}. \tag{5.13}$$

By satisfying the four conditions, the numerical stabilization part $\nu_{\mathrm{stab,a}}$ can be assumed to be equal in Eqs. (5.12) and (5.13). Then, the corrected LEE growth rate ν_{corr} can simply be determined by

$$\nu_{\mathrm{corr}} = \alpha_{\mathrm{D}_\Omega,\mathrm{a}} = \nu_{\mathrm{LEE}} - \nu_{\mathrm{APE}}. \tag{5.14}$$

5.1.1.4 Verification of the Quantification Method

The goal of this study is to demonstrate the validity of the proposed quantification method. Therefore, the method is applied to the longitudinal eigenmode shape of the area jump setup shown in Fig. 5.1. For the following eigenfrequency analyses, energetically neutral in- and outlets are specified (boundary conditions case 1).

Two mesh configurations are investigated to judge the influence of the spatial grid resolution on the computed growth rates. The fine mesh setup consists of 4.23×10^5 elements and is shown in the close-up window of Fig. 5.1. The maximum element size in the coarse mesh setup is constant in the entire computational domain. Thus, the sharp corner is not highly resolved. The number of elements is reduced by a factor of approximately ten to 4.7×10^4. Figure 5.4 shows the growth rate results, which are computed for a range of $0 \leq \alpha_\tau \leq 80$. Squares, crosses and dots represent the growth rates of "polluted"

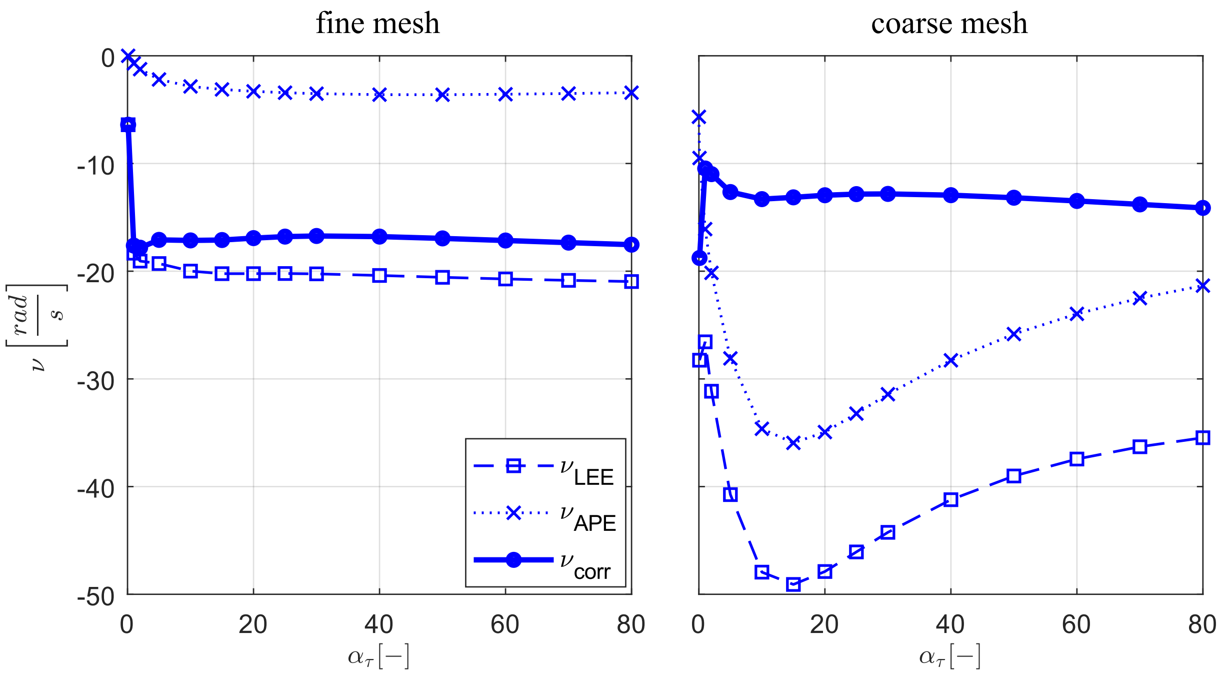

Figure 5.4: *Growth rates plotted against increasing α_τ values for the fine and coarse meshes.*

LEE, APE and corrected LEE growth rates for several values of the stabilization parameter α_τ, respectively. As stated in Eq. (5.14), the corrected rates (dots) are simply obtained by subtracting the APE (crosses) from the "polluted" LEE rates (squares). The following conclusions can be drawn, which hold for the fine and coarse mesh configuration:

- The impact of artificial diffusion on APE growth rates (crosses) tends to vanish in the limit of $\alpha_\tau \to 0$. This confirms that the source-free, isentropic APE do neither capture acoustically induced vortex shedding nor any other physically meaningful, dissipative effects[4] but solely comprise the impact of the SUPG/PSPG stabilization scheme. This is also in agreement with the observation that the APE growth rate values are always higher than the polluted LEE growth rates in Fig. 5.4.

[4]Notice that this holds only for homentropic mean flow conditions.

- For both meshes, LEE (squares) and APE (crosses) growth rates show a consistent trend for increasing values of α_τ. This observation confirms that the four conditions introduced in Section 5.1.1.3 are fulfilled. Similarity between the isentropic LEE and APE is established and the numerical stabilization scheme acts (nearly) equally in both systems of equations.

- The almost constant corrected LEE growth rates (dots) computed for both meshes reveal independence of the proposed methodology on the specified α_τ values and thus on the numerical stabilization scheme (but not on the mesh; details below). With reference to Eq. (5.12), this verifies that "polluted" LEE growth rates consist of two parts, which can be add up: one part ($\nu_{\mathrm{stab,a}}$) represents the artificial damping originating from the SUPG/PSPG stabilization scheme, while the other part ($\alpha_{\mathrm{D}_\Omega,\mathrm{a}}$) provides information on the physically meaningful damping associated with the cross-product terms in the LEE.

The comparison of the results obtained with the two meshes reveals the following:

- The dependency of LEE and APE growth rates on numerical stabilization is stronger in the coarse mesh case. This corresponds to the expectations as the stabilization parameter $\tau(\mathbf{x})$ is proportional to the local mesh size H. In addition, the finer mesh case is more stable in a numerical sense and thus, requires naturally less artificial diffusion to produce non-spurious eigensolutions. This can be explained with reference to the Peclet number in Eq. (2.48), which becomes smaller the higher the mesh resolution is.

- In the coarse mesh case, the growth rate curves of the APE (crosses) and "polluted" LEE (squares) monotonically decrease towards a minimum at $\alpha_\tau \approx 17$. After having passed the minimum, growth rates increase again, which implies that less acoustic energy is dissipated by artificial diffusion. The three regions, i.e. the (i) growth rate decrease, (ii) growth rate minimum and (iii) growth rate increase, can be associated with (i) underdamped, (ii) ideally damped and (iii) over-damped oscillator behavior.
  A similar trend cannot be observed in the fine mesh case, which indi-

cates that the effect of numerical damping is weak and the sensitivity of numerical damping to variations of α_τ is low.

- Quantitatively, numerical stabilization causes a growth rate of $\nu_{\mathrm{stab,a}} \approx -3\frac{\mathrm{rad}}{\mathrm{s}}$ for the fine mesh (cf. crosses in Fig. 5.4). Subtracting this value from the "polluted" LEE growth rate yields a corrected rate of $\nu_{\mathrm{corr}} = \alpha_{\mathrm{D}_\Omega,\mathrm{a}} \approx -17\frac{\mathrm{rad}}{\mathrm{s}}$, which represents the damping due to vortex shedding. Hence, numerical stabilization falsifies the physically meaningful growth rate part by $\approx 18\%$. This error drastically increases for the coarse mesh configuration. In the worst case ($\alpha_\tau \approx 17$), dissipation is overestimated by approximately 250% relative to the dissipation due to vortex shedding.

- The computations with the LEE and APE with the two mesh cases produce slightly different corrected growth rates due to vortex shedding ($\Delta\nu_{\mathrm{corr}} \approx 4\frac{\mathrm{rad}}{\mathrm{s}}$). This indicates that the coarse mesh has not reached a sufficient resolution to correctly capture the acoustical/vortical energy transformation process. This observation emphasizes that the presented quantification approach can only establish independence of the numerical stabilization scheme, but no mesh independence. The utilization of a coarsely resolved computational domain may lead to an inaccurate resolution of physically relevant effects –such as the vortex shedding mechanism. This numerical error cannot be compensated by the method proposed in this section. A classical grid convergence study is thus recommended in any case to judge the mesh independence of the growth rates. Notice that the fine mesh case shows the converged growth rate results.

In Section 5.2, the proposed quantification method is applied to the A^2EV combustor configuration introduced in Chapter 3. It is demonstrated that the impact of numerical stabilization can also be eliminated in a fully discretized, three-dimensional domain. This will confirm that the proposed method is applicable to practical and reactive cases, too.

5.1.2 Modeling of Vortex-Flame Interactions

In the work of Zellhuber [116], Schwing [106], Hummel [37] and Berger [61], the displacement and deformation of the flame was found to be the main driver of the thermoacoustic instabilities at the T1 eigenfrequency in the

A^2EV combustor. Recent work of Berger [61] revealed a further mechanism, which drives the T1 eigenmode in a reheat combustor: in the shear-layers of the *High Frequency Transverse Reheat Combustor* (HTRC), he observed an alternating pattern of positive and negative fluctuations of the OH*-chemiluminescence intensity, which can be related to heat release rate fluctuations. These pockets originate at the area expansion of the combustion chamber inlet and convect downstream with the mean flow velocity. Together with the measured length scale of these pockets, which resembles the vortical length scale λ_v in Eq. (2.54), it is likely that that the intensity disturbances are related to acoustically induced vortices.

This section seeks to incorporate the thermoacoustic driving potential of acoustically induced vortices to the existing CFD/CAA framework. Therefore, a FTF is developed and included to the pressure equation to model local heat release rate fluctuations induced by the interaction of the convectively transported vortices with a premixed flame. Therefore, the vortex-flame FTF is expressed as a function of the isentropic solution variables $\mathbf{u}'$ and p'. The main novelty of this model consists of the integration of the mass flow Helmholtz decomposition to the modeling task. Recall that this decomposition provides exclusive access to the rotational velocity component $\mathbf{u}'_\mathrm{v}$ associated with the convectively transported vortices.

The proposed model is based on the idea that the acoustically induced vortices periodically alter the local flame speed. This is assumed to take place as the vortices induce a rotational velocity field $\mathbf{u}'_\mathrm{v}$ around the vortex core. The rotational velocity field can be described by the Rankine vortex model [117]: this model assumes a rigid-body rotational flow in the vortex core region and irrotational flow outside of the core region. With respect to the angular velocity this means that it is constant in a certain radius r from the vortex center. After having passed this critical radius it converges towards a zero value in the environment for $r \to \infty$. A street of clock- and counterclockwise rotating vortices induces thus an oscillating velocity field $\mathbf{u}'_\mathrm{v}$ along the shear-layer, such as displayed in Fig. 5.5.
The modeling task comprises the extension of the existing flame displacement and deformation FTFs introduced in Ref. [37] by an additional term, which de-

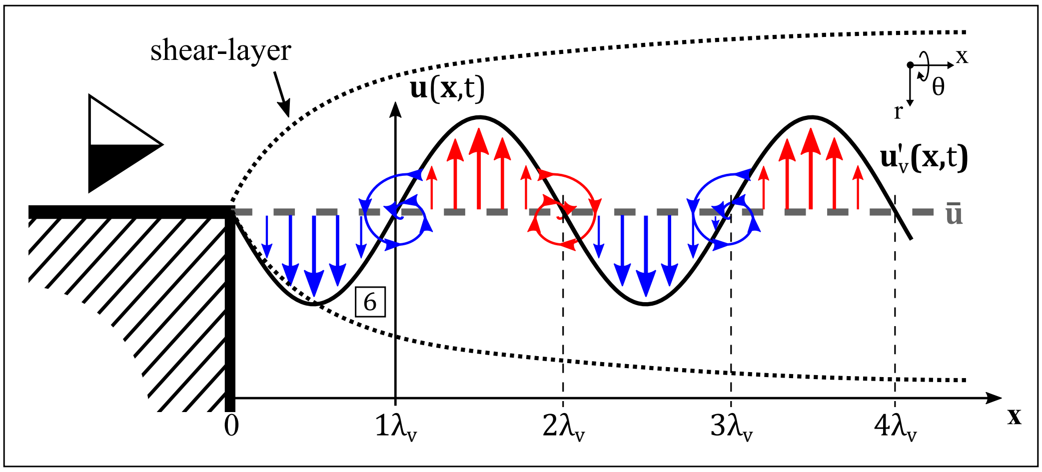

Figure 5.5: *Rotational velocity along the shear-layer caused by acoustically induced vortices.*

scribes heat release rate disturbances as a function of the local, rotational velocity $\hat{\mathbf{u}}_\mathrm{v}$. The starting point is given by the expression for the volume-specific local heat release rate

$$\dot{q}\,(\mathbf{x},t) = Y_\mathrm{f} H_\mathrm{f} \rho_\mathrm{u} s\,(\mathbf{x},t)\,\sigma\,(\mathbf{x},t)\,, \tag{5.15}$$

where Y_f denotes the fuel mass fraction, H_f the lower heating value, ρ_u the density of the unburned air-fuel mixture and $s\,(\mathbf{x},t)$ the local flame speed. $\sigma\,(\mathbf{x},t)$ is the flame surface density, i.e. the flame surface per unit volume. For premixed flames, Y_f and ρ_u are constant.

Phenomenologically, the shed vortices perturb the flame front, which modulates the heat release rate. In this work, the heat release rate modulation by vortices is described by fluctuations of the flame speed $s'\,(\mathbf{x},t)$, which are induced by the vortical velocity field $\mathbf{u}'_\mathrm{v}$. $\sigma = \sigma\,(\mathbf{x})$ is temporally constant and represents the laminar flame surface density. Hence, linearization of Eq. (5.15) results in

$$\dot{q}\,(\mathbf{x},t) = Y_\mathrm{f} H_\mathrm{f} \rho_\mathrm{u} \sigma\,(\mathbf{x}) \left(\bar{s}\,(\mathbf{x}) + s'\,(\mathbf{x},t)\right) = \bar{\dot{q}}\,(\mathbf{x}) + \dot{q}'_\mathrm{s}\,(\mathbf{x},t)\,. \tag{5.16}$$

where $\dot{q}'_\mathrm{s}$ are heat release rate fluctuations associated with fluctuations of the flame speed. This modeling framework implies that any change in the rotational flow velocity $\mathbf{u}'_\mathrm{v}$ must translate into an in- or decrease of the flame speed

s to prevent the deformation and displacement of the laminar flame surface area by convectively transported vortices. Then, the flame front remains at rest, i.e. it is quasi-steady with respect to temporal fluctuations in the rotational velocity field $\mathbf{u}'_\mathrm{v}$. Notice that this approach is in accordance with the CFD/CAA methodology, which cannot describe temporal changes of the flame surface area without the introduction of an additional transport equation for $\sigma(\mathbf{x}, t)$. The quasi-steadiness assumption implies to write

$$s'(\mathbf{x}, t) = \mathbf{u}'_{\mathrm{v,n}} = \mathbf{n}_\mathrm{f} \cdot \mathbf{u}'_\mathrm{v} = -\frac{\nabla\Theta}{\|\nabla\Theta\|} \cdot \mathbf{u}'_\mathrm{v}, \tag{5.17}$$

where $\mathbf{u}'_{\mathrm{v,n}}$ is the part of the rotational velocity, which is orthogonal to the flame front. This quantity is obtained by scalar multiplication of $\mathbf{u}'_\mathrm{v}$ with the flame normal vector $\mathbf{n}_\mathrm{f}$[5], which is equivalent to the negative, normalized gradient of the progress variable Θ [118]. Hence, heat release rate perturbations caused by flame speed fluctuations can be expressed as a function of $\mathbf{u}'_\mathrm{v}$, i.e.

$$\dot{q}'_\mathrm{s} = -Y_\mathrm{f} H_\mathrm{f} \rho_\mathrm{u} \sigma(\mathbf{x}, t) \frac{\nabla\Theta}{\|\nabla\Theta\|} \cdot \mathbf{u}'_\mathrm{v}. \tag{5.18}$$

Notice that this quasi-steady modeling approach was also proposed in Refs. [25, 119] to describe the impact of vortices on the thermoacoustic stability. However, the main difficulty, for instance in the work of Hirsch et al. [119], was the determination of the vortical velocity field $\mathbf{u}'_{\mathrm{v,n}}$. They used analytical calculations based on the *Biot-Savart* law together with simplifying assumptions for the flow path of the vortices to access the desired (but simplified) velocity field $\mathbf{u}'_\mathrm{v}$. This analytical approach can be circumvented by applying the mass flow Helmholtz decomposition, which directly yields the rotational velocity field associated with the convectively transported vortices. Hence, the combination of the existing quasi-steady approach with the Helmholtz decomposition tremendously simplifies the application of the quasi-steadiness vortex-flame interaction model. In addition, the degree of detail enhances as the Helmholtz decomposition provides access to any rotational velocity field of arbitrary complexity without the need of simplifications.

The final task comprises the integration of the FTF in Eq. (5.18) to the

[5] Pointing from the product to the educt side.

CFD/CAA framework. This is achieved by rearranging Eq.(5.16) to

$$\dot{q}(\mathbf{x},t) = \underbrace{Y_\mathrm{f} H_\mathrm{f} \rho_\mathrm{u} \sigma(\mathbf{x})\, \bar{s}(\mathbf{x})}_{=\bar{\dot{q}}(\mathbf{x})} \left(1 + \frac{s'(\mathbf{x},t)}{\bar{s}(\mathbf{x})}\right) = \bar{\dot{q}}(\mathbf{x}) + \bar{\dot{q}}(\mathbf{x}) \frac{s'(\mathbf{x},t)}{\bar{s}(\mathbf{x})}, \tag{5.19}$$

where the mean flame speed $\bar{s}$ is obtainable from CFD simulations. Inserting Eq. (5.17) into Eq. (5.19), transformation into the frequency domain and adding the disturbance part to the existing displacement and deformation FTFs [37], $\hat{\dot{q}}_\Delta$ and $\hat{\dot{q}}_\rho$, gives the overall heat release rate fluctuation

$$\hat{\dot{q}} = \Bigg(\underbrace{-\bar{\dot{q}} \frac{\frac{\nabla\Theta}{\|\nabla\Theta\|} \cdot \hat{\mathbf{u}}_\mathrm{v}}{\bar{s}}}_{\hat{\dot{q}}_\mathrm{s}} \underbrace{- \nabla\bar{\dot{q}} \cdot \frac{\hat{\mathbf{u}}_\mathrm{a}}{i\omega}}_{\hat{\dot{q}}_\Delta} \underbrace{+ \bar{\dot{q}} \frac{\hat{p}_\mathrm{a}}{\bar{\rho}\bar{c}^2}}_{\hat{\dot{q}}_\rho} \Bigg). \tag{5.20}$$

The first term in Eq. (5.20) allows for the inclusion of heat release rate perturbations caused by vortex induced flame speed fluctuations to the linear thermoacoustic stability analysis framework. Successively replacing the heat release rate term $\hat{\dot{q}}$ in the energy Eq. (2.27) by the three FTFs $\hat{\dot{q}}_\mathrm{s}$, $\hat{\dot{q}}_\Delta$ and $\hat{\dot{q}}_\rho$ allows determination of the associated driving rates β_s, β_Δ and β_ρ via eigenfrequency analyses (see Section 5.2).

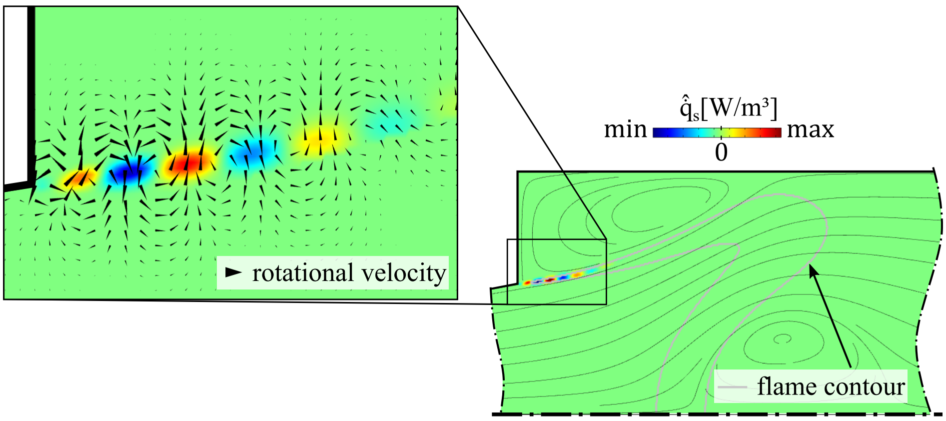

Figure 5.6: *Computed heat release rate fluctuations $\hat{\dot{q}}_s$ caused by acoustically induced vortices in the A^2EV combustor.*

Figure 5.6 presents the application of the vortex-flame FTF $\hat{\dot{q}}_\mathrm{s}$ for representative operational conditions (see the mean fields in Fig. 3.1). The heat release rate fluctuations in Fig. 5.6 are produced by vortices, which are triggered by the T1 eigenmode in the A^2EV combustor. The spatial extent of the heat release rate fluctuations and thus of the vortex street is essentially determined by viscosity. Hence, viscous dissipation of vortices is an important factor to account for the thermoacoustic driving potential of these heat release rate fluctuations in a physically meaningful manner. Artificial diffusion would erroneously shorten or elongate the vortex street depending on the value of the stabilization parameter α_τ. This disqualifies the LEE for the task of modeling vortex-flame interactions. Instead, the LNSE are used to prevent the non-physical influence of the stabilization scheme on the dissipation of vortices. With reference to the *Peclet* number of Eq. (2.48), this indirectly implies the need of a FEM mesh, which is resolved sufficiently high to produce a stable FEM solution without the addition of artificial diffusion on top of the physical one.

In Section 5.2, the impact of the heat release rate fluctuations $\hat{\dot{q}}_s$ on the linear thermoacoustic stability of the T1 eigenmode in the A^2EV combustor is computed in terms of driving rates for 80 operational points.

Notice that Romero [87] proposes the complementary vortex-flame driving model, which is based on the modulation of the flame surface density σ by coherent vortices while the flame speed is assumed to be constant. He expresses flame surface density disturbances σ' as a function of fluctuations in the progress variable, i.e. $\sigma' = f(\Theta')$. Therefore, an additional transport equation for Θ' must be solved. In comparison to the quasi-steady vortex-flame model proposed in this section, this increases the computational effort but might be more accurate from a physical point of view. A detailed comparison between the two models and their performance in thermoacoustic stability analyses is pending and must be addressed as part of future research.

5.2 Linear Stability of the T1 Eigenmode in the A^{2}EV Combustor

This section presents the CFD/CAA model, which incorporates the findings and methods of Section 5.1. The outcome of this model is thermoacoustic growth rates, which can be decomposed into the following contributions

$$\nu_{\mathrm{T1}} - \nu_{\mathrm{stab,a}} = \nu_{\mathrm{T1,corr}} = \alpha_{\mathrm{D}_{\boldsymbol{\Omega}},\mathrm{a}} + \alpha_{\nabla\bar{s}} + \alpha_{\mu} + \alpha_{\mathrm{BL}_{\mu/\mathrm{th}}} + \beta_{\Delta} + \beta_{\rho} + \beta_{\mathrm{s}} \tag{5.21}$$

with

- the numerical stabilization part $\nu_{\mathrm{stab,a}}$, which must be eliminated in the analysis as it is associated with non-physical artificial diffusion introduced by the SUPG/PSPG stabilization scheme (see Section 5.1.1),
- the damping rate $\alpha_{\mathrm{D}_{\boldsymbol{\Omega}},\mathrm{a}}$ caused by the cross product terms $\boldsymbol{\Omega} \times \mathbf{u}$ in the LNSE/LEE,
- the damping rate $\alpha_{\nabla\bar{s}}$ describing the interaction of acoustics with the non-homentropic mean flow field (cf. the last term in Eq. (2.36)) [87],
- the damping rate α_{μ} associated with viscosity inside the domain (cf. the term $\nabla \cdot \underline{\hat{\boldsymbol{\tau}}}$ in Eq. (2.26)),
- the damping rate $\alpha_{\mathrm{BL}_{\mu/\mathrm{th}}}$ associated with visco-thermal losses in the acoustic boundary layer [120],
- the driving rates β_{Δ} and β_{ρ} due to flame displacement and deformation introduced by Hummel [22, 37] and
- the driving rate β_{s} associated with flame speed fluctuations (see Section 5.1.2).

Knowledge about the individual relevance of these contributions for the stability of a thermoacoustic system allows the validation and specific application of design optimization strategies to systematically mitigate or reinforce single driving or damping mechanisms, respectively.

Each contribution in Eq. (5.21) can be computed via a difference approach similar to the methodology proposed in Section 5.1.1.3 to eliminate the impact of numerical stabilization in LEE growth rates. In this section, LNSE, LEE and APE eigenfrequency simulations are jointly used to determine the individual growth, driving and damping rates in Eq. (5.21). Each rate is associated with a characteristic simulation setup. For demonstration, the subsequently applied notation is explained for the following example:

$$\nu = \nu_{\mathrm{LNSE}}\Big|_{\hat{\dot{q}}=\hat{\dot{q}}_{\mathrm{s}}}^{\alpha_\tau=0} \tag{5.22}$$

Equation (5.22) indicates that the growth rate ν is obtained from an LNSE eigenfrequency simulation. In this simulation, $\alpha_\tau = 0$, which implies that the numerical stabilization scheme is deactivated. If no indication with respect to the value of α_τ is given, it is non-zero and the numerical stabilization scheme is active. In the subsequent Section 5.2.1, values of $\alpha_\tau = 1$ and $\alpha_\tau = 0.1$ are used for a two- and a three-dimensional computational setup. Furthermore, driving due to vortex-flame interactions is considered via the local FTF $\hat{\dot{q}}_{\mathrm{s}}$. Two other options for $\hat{\dot{q}}$ are the flame displacement and deformation FTFs $\hat{\dot{q}}_\Delta$ and $\hat{\dot{q}}_\rho$. Notice that $\hat{\dot{q}} = 0$ highlights that the flame is assumed to be passive.

Next, the computation of the single contributions in Eq. (5.21) is presented:

- For reactive cases such as the A^2EV combustor, the growth rate associated with the effect of numerical damping on the acoustic sub-mode $\nu_{\mathrm{stab,a}}$ must be determined via two APE eigenfrequency simulations. This procedure is necessary as the APE capture the dissipation of acoustics due to the interaction with the non-homentropic mean flow in addition to the non-physical damping caused by artificial diffusion[6]. In both simulations, the flame is assumed to be passive, i.e. $\hat{\dot{q}} = 0$. In the first simulation, the SUPG/PSPG stabilization scheme is activated recognizable as no indication with respect to the value of α_τ is given in Eq. (5.23). In the second computation step, $\alpha_\tau = 0$ is imposed, which yields the damping rate $\alpha_{\nabla\bar{s}}$ due to the non-homentropicity of the mean flow only. Subtraction of the two corresponding growth rates gives the numerical stabilization part $\nu_{\mathrm{stab,a}}$:

$$\nu_{\mathrm{stab,a}} = \nu_{\mathrm{APE}}\Big|_{\hat{\dot{q}}=0} - \nu_{\mathrm{APE}}\Big|_{\hat{\dot{q}}=0}^{\alpha_\tau=0} = \nu_{\mathrm{APE}}\Big|_{\hat{\dot{q}}=0} - \alpha_{\nabla\bar{s}}. \tag{5.23}$$

  Recall that numerically stable APE solutions are obtained even if $\alpha_\tau = 0$. This is possible as convectively transported vortices are absent in the APE solutions fields.

[6]Recall that only one simulation is required in the case of isothermal conditions. This is possible as acoustic dissipation caused by non-homentropicity is absent in these cases.

- The vorticity damping rate can be computed according to Eq. (5.14):

$$\alpha_{\mathrm{D}_{\mathbf{\Omega}},\mathrm{a}} = \nu_{\mathrm{LEE}}\Big|_{\hat{\dot{q}}=0} - \nu_{\mathrm{APE}}\Big|_{\hat{\dot{q}}=0} = \nu_{\mathrm{LEE}}\Big|_{\hat{\dot{q}}=0} - \nu_{\mathrm{stab,a}} - \alpha_{\nabla\bar{s}} \tag{5.24}$$

  Two independent eigenfrequency simulations with the LEE and APE are carried out, where the value of α_τ is identical in both simulations. No unsteady heat release model is considered, i.e. $\hat{\dot{q}} = 0$. Remember that this is possible as the APE and LEE solely differ by the absence of the vorticity cross-product terms in the APE.

- The growth rate of the LNSE with a passive flame ($\hat{\dot{q}} = 0$) and a non-zero value of α_τ adds up from the superposition of the vorticity damping rate $\alpha_{\mathrm{D}_{\mathbf{\Omega}},\mathrm{a}}$, the damping rate associated with non-homentropic mean flow $\alpha_{\nabla\bar{s}}$, the damping rate α_μ caused by viscous dissipation inside the domain and of the non-physical part $\nu_{\mathrm{stab,a}}$. In order to compute α_μ, the remaining three contributions are subtracted from the overall LNSE growth rate[7]:

$$\alpha_\mu = \nu_{\mathrm{LNSE}}\Big|_{\hat{\dot{q}}=0} - \nu_{\mathrm{stab,a}} - \alpha_{\mathrm{D}_{\mathbf{\Omega}},\mathrm{a}} - \alpha_{\nabla\bar{s}}. \tag{5.25}$$

- In a post-processing step, the damping rate associated with visco-thermal losses in the acoustic boundary-layer is computed based on the approach of Searby [120]: the period-averaged rate of change of the acoustic energy density $\langle\frac{\mathrm{d}E_\mathrm{a}}{\mathrm{d}t}\rangle$ for an APE eigenmode is expressed in terms of viscous (subscript μ) and thermal (subscript th) acoustic energy flux densities leaving the domain walls. Specifically, they read

$$\begin{aligned}\left\langle\frac{\mathrm{d}E_\mathrm{a}}{\mathrm{d}t}\right\rangle &= \langle\left(\mathbf{I}_{\mu,\mathrm{a}} + \mathbf{I}_{\mathrm{th,a}}\right)\cdot\mathbf{n}\rangle = \\ &= \left\langle\frac{1}{2}\left(\hat{\mathbf{u}}\cdot\hat{\mathbf{u}}\right)\sqrt{\frac{\omega_\mathrm{a}\bar{\rho}\mu}{2}} + \frac{1}{2}\left(\gamma-1\right)\frac{\hat{p}^2}{\gamma\bar{p}}\sqrt{\frac{\omega_\mathrm{a}\lambda_{\mathrm{th}}}{c_\mathrm{p}\bar{\rho}2}}\right\rangle,\end{aligned} \tag{5.26}$$

  where c_p is the specific heat capacity and λ_{th} the thermal conductivity of the gas mixture. The corresponding damping rate is obtained by applying the growth rate equation introduced in Section 4.2. Specifically, integration of Eq. (5.26) along the walls and normalizing the result by the

[7]Alternatively, the stress tensor term could be added to the APE momentum Eq. (2.22), while $\alpha_\tau = 0$. The difference in growth rates appearing in two eigenfrequency simulations corresponding to an active ($\mu \neq 0$) and an inactive ($\mu = 0$) stress tensor term gives α_μ.

volume-integrated acoustic energy density gives the damping rate $\alpha_{\mathrm{BL}_{\mu/\mathrm{th}}}$, which is associated with visco-thermal losses in the acoustic boundary-layer:

$$\alpha_{\mathrm{BL}_{\mu/\mathrm{th}}} = \frac{1}{2} \frac{\int_S \langle \left(\mathbf{I}_{\mu,\mathrm{a}} + \mathbf{I}_{\mathrm{th,a}} \right) \cdot \mathbf{n} \rangle \mathrm{d}S}{\int_V \langle E_\mathrm{a} \rangle \mathrm{d}V}. \tag{5.27}$$

- The displacement and deformation rates can be computed via APE eigenfrequency simulations, where the impact of numerical damping is set to zero by specifying $\alpha_\tau = 0$. The unsteady heat release rate in the energy equation is modeled by the FTFs [22, 37]

$$\hat{\dot{q}} = \hat{\dot{q}}_\Delta + \hat{\dot{q}}_\rho = -\nabla \bar{\dot{q}} \cdot \frac{\hat{\mathbf{u}}_\mathrm{a}}{i\omega} + \bar{\dot{q}} \frac{\hat{p}_\mathrm{a}}{\bar{\rho} \bar{c}^2}. \tag{5.28}$$

  To extract the corresponding driving rates from an APE growth rate, the damping rate associated with the non-homentropic mean flow must be subtracted:

$$\beta_\Delta = \nu_{\mathrm{APE}} \Big|_{\hat{\dot{q}} = \hat{\dot{q}}_\Delta}^{\alpha_\tau = 0} - \alpha_{\nabla \bar{s}} \tag{5.29}$$

$$\beta_\rho = \nu_{\mathrm{APE}} \Big|_{\hat{\dot{q}} = \hat{\dot{q}}_\rho}^{\alpha_\tau = 0} - \alpha_{\nabla \bar{s}}. \tag{5.30}$$

- The vortex-flame driving rate can be determined by two LNSE eigenfrequency simulations. In the first computation, the unsteady heat release rate in the energy equation is modeled via the FTF introduced in Section 5.1.2

$$\hat{\dot{q}} = \hat{\dot{q}}_\mathrm{s} = \bar{\dot{q}} \frac{-\frac{\nabla \Theta}{\|\nabla \Theta\|} \cdot \hat{\mathbf{u}}_\mathrm{v}}{\bar{s}}. \tag{5.31}$$

  In the second step, no unsteady heat release is considered, i.e. $\hat{\dot{q}} = 0$. Subtraction of the LNSE growth rate which does not contain the effect of the vortex-flame FTF from the growth rate which does, provides the driving rate β_s:

$$\beta_\mathrm{s} = \nu_{\mathrm{LNSE}} \Big|_{\hat{\dot{q}} = \hat{\dot{q}}_\mathrm{s}}^{\alpha_\tau = 0} - \nu_{\mathrm{LNSE}} \Big|_{\hat{\dot{q}} = 0}^{\alpha_\tau = 0}. \tag{5.32}$$

Finally, it is emphasized that the proposed difference methodology is only valid and applicable, if the single driving and damping mechanisms do only weakly perturb the natural, unaffected acoustic sub-mode[8]. Otherwise, the acoustic (sub-)mode shapes in the independent LNSE/LEE/APE eigenfrequency simulations may not be similar, which would prohibit the additive superposition of growth rates. The applicability of the difference method can be justified if the condition

$$2\pi f_{\mathrm{i,ref}} \gg \nu. \tag{5.33}$$

is satisfied. Interpretatively, Eq. (5.33) states that growth rates can be subtracted if the oscillating frequency of the unperturbed, reference eigenmode i is large compared to the damping/driving rate of the perturbed case.

The mean flow fields required to compute the damping and driving rates of Eq. (5.21) are obtained by reacting, steady-state, RANS CFD simulations. In order to increase the spatial resolution in the combustion chamber, the RANS CFD simulations comprise two steps:

1. First, each operational point is simulated for isothermal conditions. A quarter of the entire combustor geometry including the A^2EV swirler, mixing section, combustion chamber and exhaust tube is simulated. The isothermal profiles of axial, radial and azimuthal velocities as well as turbulent kinetic energy and dissipation are extracted at the inlet plane to the combustion chamber.

2. The extracted profiles serve then as inlet velocity boundary condition for a second, quasi-two dimensional and highly resolved reactive CFD simulation consisting of one cell in azimuthal direction. Notice that rotational symmetry of the profiles is assumed, which was found to be a justifiable simplification. Combustion is modeled by an extended version of the *Flamelet Generated Manifold* (FGM) approach [77, 121] with the GRI 3.0 kinetics mechanism [122].

Details on the RANS CFD simulations as well as on the mesh convergence study are presented in Appendix D.

[8]The unperturbed acoustic sub-mode is represented by the APE solution with $\alpha_\tau = 0$ in this case.

5.2.1 T1 Growth Rate Results

In this section, the linear thermoacoustic stability behavior of the T1 eigenmode in the A^2EV combustor is computed for the 80 operational points introduced in Chapter 3. For each operational point, experimental data is available in a binary manner, i.e. whether it was observed to be thermoacoustically stable or unstable. According to Section 5.2, the decomposed contributions of Eq. (5.21) to the overall T1 growth rate of one operational point is obtained by two LNSE, one LEE and four APE eigenfrequency simulations. In total, 560 eigenfrequency simulations are carried out to retrieve the linear thermoacoustic stability limits across the entire operational range, which are presented in this section.

5.2.1.1 Methodological Improvements

The linear stability assessment of the T1 mode of the A^2EV combustor with the CFD/CAA method was already addressed in the dissertation of Hummel [37]. The next few sentences highlight the advancements of the CFD/CAA model introduced in this thesis with respect to the legacy version used by Hummel:
In the work of Hummel [37], measured OH*-chemiluminescence images were used to obtain the mean heat release input fields. This approach has been replaced by reactive CFD RANS computations. Now, consistent mean flow velocity, temperature and heat release rate fields, i.e. all coming from the same simulation, are available for the CAA part. Compared to the work of Hummel [37], driving rates associated with flame deformation and displacement are computed with the APE instead of a Helmholtz-type system of equations, which neglects the effect of the mean flow velocity. However, it was found that the mean flow has a negligible impact on these driving rates. Additionally, viscothermal losses in the acoustic boundary-layer as well as acoustic dissipation due to viscosity inside the domain are now included in the linear stability analysis of this thesis. Furthermore, the effect of the non-homentropic mean flow field is considered, which was not addressed before. The new vortex-flame FTF presented in Section 5.1.2 now incorporates the thermoacoustic driving potential of acoustically induced vortices. Significant modifications and improvements have been introduced for the computation of damping rates asso-

ciated with acoustically induced vorticity perturbations and their interaction with the mean flow. In the dissertation of Hummel [37], they were obtained by a modeling approach based on reflection coefficient computations with the Helmholtz equation as no method was available to eliminate the impact of numerical stabilization in the growth rates of LEE eigenfrequency computations. The introduction of the methodology to eliminate the effect of numerical damping (cf. Section 5.1.1.3) raised the predictive performance of LEE eigenfrequency computations to a satisfactory level and allowed replacement of the reflection coefficient method. The advanced CFD/CAA framework presented in Section 5.2 improves thus the predictive capabilities of linear thermoacoustic stability analyses by the physically correct inclusion of a variety of relevant effects, while numerical errors are minimized.

5.2.1.2 Computational Setup

In order to demonstrate the applicability of the CFD/CAA method to practical cases, the thermoacoustic stability analysis for the T1 eigenmode is performed twice: The first analysis comprises a simplified two-dimensional domain of the A^2EV combustor. As explained in Section 2.4.2, a three-dimensional domain can be reduced to a two-dimensional one, if the combustor geometry of interest together with all the corresponding mean flow quantities exhibits continuous rotational symmetry. This allows a drastic decrease of the mesh element size H for given computational resources. The susceptibility of this numerical setup to produce spurious solutions and the impact of the employed artificial diffusion scheme mutually decrease. The values of the *Peclet* number in Eq. (2.48) and of the stabilization parameter in Eq. (2.53) reduce with smaller values of H. The highly resolved analysis with the two-dimensional domain represents the reference case as it is barely affected by numerical stabilization. However, it has little industrial relevance, as real combustors often exhibit complex geometries, where no simplifications concerning rotational symmetry of the geometry can be exploited. In these cases, available computational resources often limit the mesh resolution. Then, numerical stabilization is responsible for a significant part of the resulting growth rates as shown in Fig. 5.4. To demonstrate the applicability of the advanced CFD/CAA setup for practical cases, the stability analysis for the T1 mode in the A^2EV combustor is repeated. In this analysis, the azimuthal periodicity simplification is dropped and the fully discretized, three-dimensional domain is considered. Both, highly and weakly resolved cases, are subjected to the elimination procedure proposed in Section 5.1.1.3 to exclude the non-physical growth rate ascribed to the SUPG/PSPG artificial diffusion scheme. The stability results of both numerical setups are compared with each other to validate the predictive capabilities of the stability assessment framework for technically relevant, i.e. fully discretized, applications.

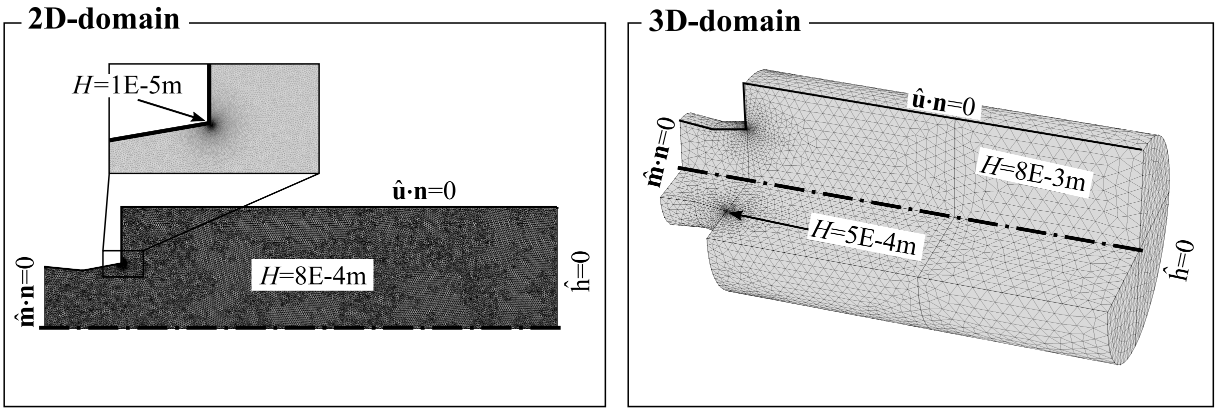

Figure 5.7: *Two- and three-dimensional computational domains with mesh sizes and boundary conditions.*

Figure 5.7 presents the two configurations and provides information about mesh element sizes as well as the specified boundary conditions for the solution variables $\hat{\mathbf{u}}$ and $\hat{p}$. In- and outlet are specified to be energetically neutral ($\hat{\mathbf{m}} \cdot \mathbf{n} = \hat{h} = 0$) precluding any acoustic energy fluxes through these boundaries. The walls are of slip wall type ($\hat{\mathbf{u}} \cdot \mathbf{n} = 0$). The mesh resolution at the area jump, i.e. where the acoustically induced generation of vortices physically occurs, significantly influences the quality of LNSE and LEE solutions. An insufficient resolution of this region leads to an inaccurately resolved energy transformation process between acoustic and vortical perturbation fields. To provide optimal starting conditions for the thermoacoustic stability analysis, most of the available computational resources are invested in the sharp area jump region, shown in Fig. 5.7. The total number of mesh elements amounts to approximately $102 \cdot 10^3$ and $730 \cdot 10^3$ for the two- and three-dimensional cases, respectively. The values for the stabilization parameter are set to $\alpha_\tau = 1$ for eigenfrequency analyses with the two-dimensional domain and to $\alpha_\tau = 0.1$

for simulations with the three-dimensional domain.

5.2.1.3 Thermoacoustic Stability Results

The thermoacoustic stability behavior predicted with the two (left column)- and three dimensional (right column) domains in Fig. 5.7 is compared with each other in Fig. 5.8. The individual contributions to the net growth rate $\nu_{\mathrm{T1,corr}}$ are plotted for the 80 operational points against an increasing power density (see Chapter 3). Recall that variations of the power density are caused by changes of the mean inlet mass flow and the air excess ratio. Experimental data for each of the operational points is available, which provides information about the thermoacoustic stability of the T1 mode in a binary manner: the filled circles in Fig. 5.8 indicate stable, the open circles unstable operation.

The **blue damping rate clouds** in the first row represent the dissipation of acoustic energy associated with acoustically induced vorticity perturbations. Mathematically, they correspond to the cross-product terms in the dissipation Eq. (2.36). This effect significantly contributes to acoustic damping and thus counteracts thermoacoustic driving mechanisms. Physically, the (linear) increase of dissipation with power density appears due to an increase of the inlet mass flow rate $\bar{\dot{m}}_{\mathrm{in}}$ and a decrease of the air excess ratio λ. Higher inlet mass flow rates lead to increased mean flow velocities in the A^2EV combustor, which mutually increases the strength of the mean vorticity field. In turn, this induces a stronger interaction of acoustic and vorticity perturbations with the mean flow, which ultimately results in an increase of acoustic damping. Lower air excess ratios, i.e. richer air-fuel mixtures, lead to a radial flame contraction towards the axis. In Chapter 6, the sensitivity of the damping rate $\alpha_{\mathrm{D}_\Omega,\mathrm{a}}$ is investigated with respect to a radial flame contraction[9]. It is shown that a stronger radial flame contraction leads to stronger acoustic dissipation, which explains the increase of dissipation for richer operational conditions.

The **magenta-colored damping rate clouds** in the second row are associated with interactions between the acoustic disturbance field and the non-homentropic mean flow field. Similar as for the blue dots, acoustic

[9]In Chapter 6, a single operational point is investigated only. There, the flame contraction is caused by the pulsation-amplitude dependency of the mean flow field instead of variations of the air excess ratio.

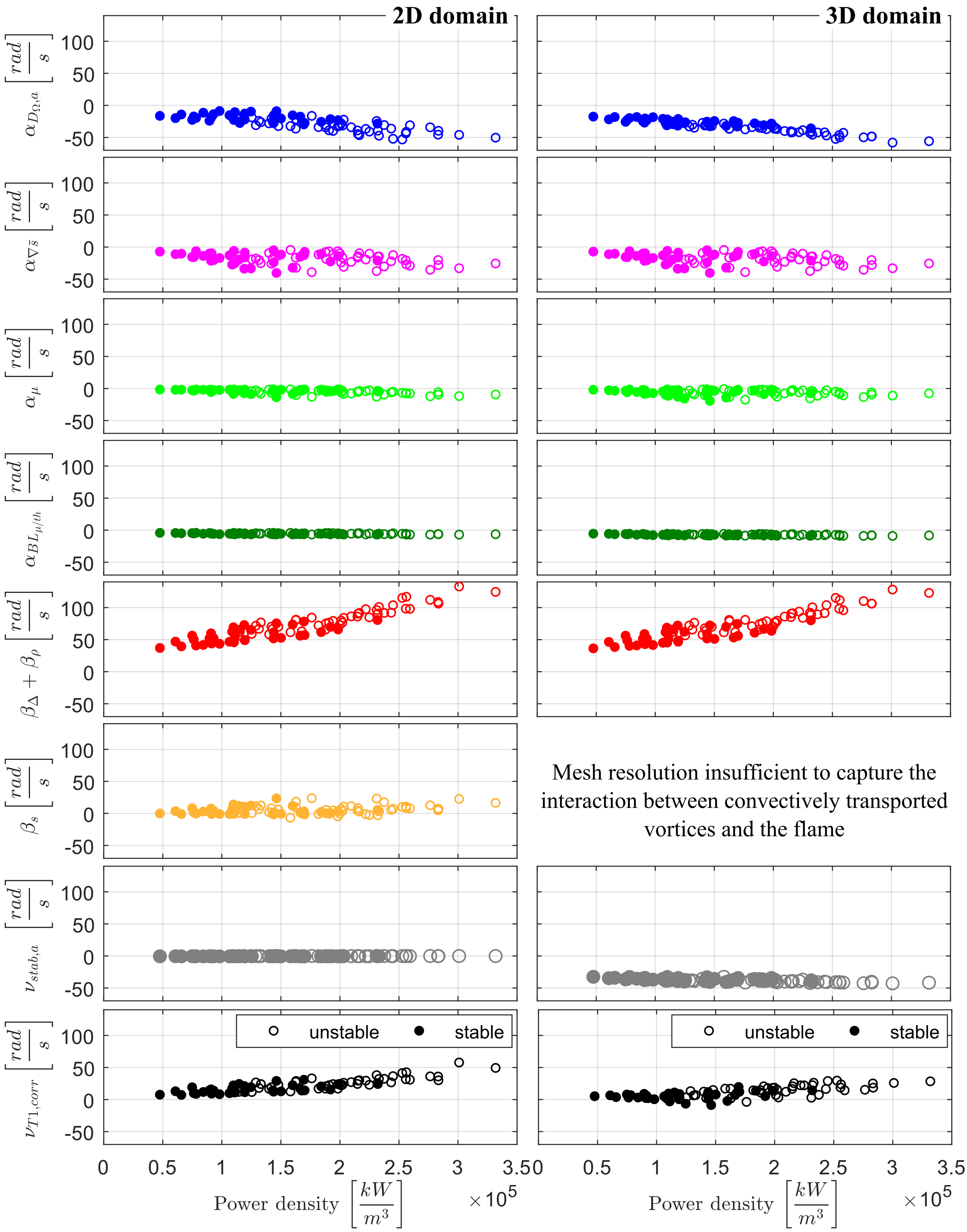

Figure 5.8: *Computed T1 growth rates. Open and closed circles indicate the thermoacoustic stability behavior observed in the experiment.*

dissipation increases with power density, which is caused by the increasing temperature across the flame. However, the gradient is weaker compared to the trend of the blue dots. As this thesis focuses on acoustically induced vorticity perturbation and their impact on the thermoacoustic stability, a detailed analysis is skipped at this point. Further information can be found in Refs. [49, 87].

Light and **dark green dots** provide information on the impact of viscous losses inside the domain and of visco-thermal losses in the acoustic boundary-layer on the thermoacoustic stability. Compared with blue and magenta-colored damping rate clouds, their trends are nearly constant with thermal power. Their relevance in terms of absolute value is lower compared to the previous two effects; however, both effects should be considered in precise stability analyses as they might be relevant for other eigenmodes or combustion systems, such as for the HTRC, for instance [87].

The **red dots** represent the sum of driving rates of flame displacement and deformation. These rates increase with power density, which is intuitive as the FTFs $\hat{\dot{q}}_\Delta$ and $\hat{\dot{q}}_\rho$ directly depend on the mean heat release rate in the chamber and its gradient, which also increases for higher power densities. A detailed comparison between these driving rates, which are based on numerically computed heat release fields, and driving rates based on experimentally measured OH*-chemiluminescence images is presented in Appendix D.3.

The **orange** dots are the driving rates associated with the heat release rate modulation caused by convectively transported vortices (see Section 5.1.2). Their thermoacoustic driving potential is lower than the one of flame displacement and deformation. This has two reasons: Firstly, the mean heat release rate in the outer shear-layer of the A^2EV combustor almost vanishes completely as shown in Fig. 5.9. Heat losses and flame stretch reduce the reactivity of the gas mixture in this region, which results in a weak interaction between shed vortices and the flame.
Secondly, the length scale λ_v of shed vortices is small due to the relatively low mean flow velocities and the high T1 oscillation frequency (cf. Eq. (2.54)). This results in a pattern of small, positive and negative valued heat release

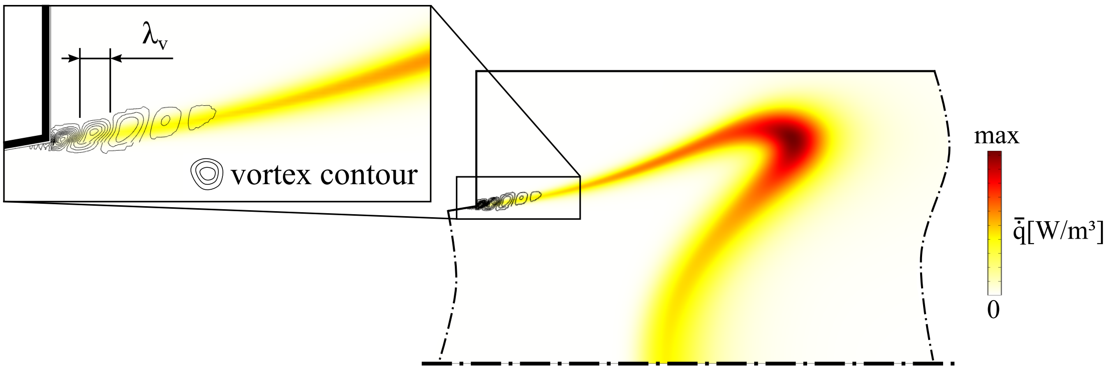

Figure 5.9: *Interaction between shed vortices and the heat release rate.*

rate fluctuations (cf. Fig. 5.6), which sum up to weak driving in an integral sense. Notice that this observation does not generally apply to high-frequency systems. Berger [61] and Romero [87] experimentally and numerically showed in the HTRC experiment that vortex-flame interaction can dominate thermoacoustic driving of transverse acoustic eigenmodes.
As explained in the corresponding modeling Section 5.1.2, the application of the proposed FTF is linked to highly resolved meshes. The fully discretized, three-dimensional A^2EV combustor (see Fig. 5.7) does not have a sufficient mesh quality[10] to resolve the small-scale vortices. This explains the lack of these driving rates in Fig. 5.8.

The **gray dots** represent the non-physical growth rate caused by the SUPG/PSPG stabilization scheme. These growth rates were subtracted from the LEE and LNSE growth rates to obtain the damping rates $\alpha_{\mathrm{D}_{\mathbf{\Omega}},\mathrm{a}}$ (blue dots) and α_μ (light green dots). The impact of the numerical stabilization scheme on computed growth rates strongly depends on the mesh resolution. This was discussed in more detail in Section 5.1.1. In the two-dimensional reference case, artificial diffusion growth rates take values close to zero. Thus, the numerical stabilization scheme does (almost) not falsify the thermoacoustic stability analysis. In this case, the proposed elimination procedure (see Section 5.1.1.3) could be avoided without falsifying the thermoacoustic stability results drastically. In contrast to this, the utilization of the "polluted"

[10]A further mesh refinement was not possible as available computational resources restricted the analysis to the three-dimensional mesh presented in Fig. 5.7.

LEE and LNSE growth rates obtained with the fully discretized domain must be seen –at least– critical. Here, artificial dissipation falsifies thermoacoustic growth rates by approximately $40 - 50\,\mathrm{rad}/\mathrm{s}$ depending on the operational point. This value is of the same order of magnitude as the physically meaningful damping rate $\alpha_{\mathrm{D}_{\Omega},\mathrm{a}}$. Without the elimination of this non-physical contribution, acoustic dissipation is tremendously overestimated due to the SUPG/PSPG stabilization scheme. This would lead to a wrong interpretation of the thermoacoustic stability. The comparison study in Fig. 5.8 demonstrates that even eigenfrequency simulations with fully-discretized domains governed by a relatively low mesh resolution can yield reasonable results, if the proposed quantification method is applied. However, remember that numerical errors due to an insufficient resolution of physical effects caused by a coarse mesh can still mitigate the validity of these results. This must be considered in interpretations of the thermoacoustic growth rates.

The **black dots** represent the overall thermoacoustic growth rates of the T1 mode, which are corrected by the non-physical impact of artificial diffusion. Each black dot is computed according to Eq. (5.21) and represents the sum of the individually determined damping and driving rates. Regarding Fig. 5.8 this means that each black dot is obtained by adding up the colored dots above at the same level of power density (but not the gray dots as these are the non-physical numerical damping growth rates). Notice that the growth rates computed with the two- and three-dimensional domains differ by the vortex-flame driving rates (orange dots), which are not considered in the three-dimensional case. Recall that the filled and open circles indicate whether the T1 mode was observed to be stable or unstable in the experiment. In the two-dimensional case, the thermoacoustic stability analysis predicts unstable behavior for all operational points. This can be recognized by the net growth rate clouds (black dots in the left column of Fig. 5.8), which are above the zero line. However, experimental observations revealed that a thermoacoustic instability occurs only for about half of the operational points. In the three-dimensional case, which lacks the vortex-flame driving rates, several filled circles are below the zero line, which indicates agreement with the experiment. Nevertheless, the measured stability trend is reproduced consistently meaning that the unstable operational points (open circles in Fig. 5.8) are associated with higher thermoacoustic growth rates than the stable ones (filled circles in Fig. 5.8). From this observation it can be concluded that the overall driving rate $\beta_{\mathrm{T1}} = \beta_{\mathrm{s}} + \beta_{\Delta} + \beta_{\rho}$ increases stronger than the the overall damping rate $\alpha_{\mathrm{T1}} = \alpha_{\mathrm{D_\Omega,a}} + \alpha_{\nabla\bar{s}} + \alpha_{\mu} + \alpha_{\mathrm{BL}_{\mu/\mathrm{th}}}$ (cf. Eq. (5.21)). Furthermore, it is emphasized that the individual damping and driving rates in Eq. (5.21) exhibit absolute values up to approximately $150\,\mathrm{rad/s}$ but add up to overall growth rates (black dots in Fig. 5.8) close to the stability limit. This indicates that the CFD/CAA model proposed in this thesis almost reaches satisfactory predictive capabilities; however, with a small discrepancy to the experiment. From a technical perspective, the T1 growth rates in Fig. 5.8 can be viewed as conservative thermoacoustic stability prediction results with a small safety buffer. The found discrepancy or rather safty buffer might be due to the lack of physical effects, which have yet not been considered in the analysis: Firstly, the interplay between acoustic and vortical disturbances with entropy waves across the premixed flame is precluded because of the isentropicity assumption of Eq. (2.17). To incorporate these interactions physically correct, the isentropicity assumption must be dropped and the movement of mean flow field in the flame region must be considered in linearized disturbance equations. Otherwise, spurious entropy is generated [84, 88]. Secondly, detailed geometrical features (e.g. grooves, small pockets,...), which are not captured by the idealized computational domain of the combustion chamber, might increase acoustic dissipation. Notice that an overestimation of driving due to flame displacement and deformation caused by inaccurate CFD simulations can be excluded as a potential source of error as net the driving rates associated with computed and measured flame brushes are (nearly) identical (see Appendix D.3). However, a similar validation approach to judge the suitability of the CFD heat release rate field for the computation of flame-vortex driving has not yet been conducted and is left to future work at this point.

5.3 Summary and Future Work

In this chapter, the predictive capabilities of a hybrid *Computational Fluid Dynamics/Computational Aero Acoustics* method are enhanced. This is achieved by a correct incorporation of acoustic dissipation to the modal analysis framework, which is caused by acoustically induced vorticity perturbations. The main results and findings are summarized in the following:

- A methodology is established to eliminate the non-physical contribution of the SUPG/PSPG numerical stabilization scheme in growth rates obtained by eigenfrequency studies with the *Linearized Navier-Stokes Equations* and *Linearized Euler Equations*. The results are corrected growth rates, which solely contain the physical part associated with dissipation due to acoustically induced vortex disturbances. The application of this methodology overcomes a main shortcoming of the CFD/CAA approach with the *stabilized Finite Element Method* and significantly improves its predictive capabilities for thermoacoustic stability analyses.

- A local flame transfer function is developed to compute driving rates, which describe the effect of vortex-flame interactions on the thermoacoustic stability.

- Detailed insight into the growth rate results is provided by decomposing the net thermoacoustic growth rate into its individual contributions. This allowed assessment of the relevance of each growth rate part.

- It is demonstrated that the improved CFD/CAA method is applicable to industrial relevant gas turbine combustors.

- From the comparison of computed thermoacoustic growth rates of the T1 eigenmode in the A^2EV combustor with the experimentally observed stability behavior, it is concluded that the predictive capabilities of the CFD/CAA method almost reached a satisfactory level. However, a small mismatch compared with the experiments remains. This gap must be closed in future work packages by identification of further relevant effects affecting the thermoacoustic stability.

6 Non-Linear Saturation and Limit-Cycle

The non-linear saturation mechanism has been subject to research in the thermoacoustics community for many years[1]. In 1997, Dowling [44] extended the linear flame response model of Bloxsidge et al. [124], which is based on velocity perturbations at the flame holder of a blow-down combustor experiment, by non-linear effects to reproduce limit-cycle amplitudes measured by Langhorne [125]. In 2002, Lieuwen et al. [52] experimentally studied the non-linear flame response of a premixed combustor as a function of the amplitude of imposed pressure oscillations. Balachandran et al. [54] used different measurement methods to investigate the non-linear increase of heat release rate perturbations as a response to acoustic velocity forcing at the inlet of a bluff body combustor. All methods showed deviations from a linear trend even for moderate amplitudes and saturation towards a constant level for higher amplitude levels. Noiray et al. [45] used this data to show that the saturation of the heat release rate fluctuations $\dot{q}'_{\mathrm{NL}}$ can be approximated by a hyperbolic tangent pressure function multiplied by a constant calibration factor κ. For the sake of simplicity, they used the third order Taylor expansion of the hyperbolic tangent, which yields a cubic heat release rate saturation term as a function of acoustic pressure p', i.e.

$$\dot{q}'_{\mathrm{NL}}(t) \propto -\kappa p'^{3}(t) \tag{6.1}$$

This term has been established in the thermoacoustics community in past years to model the limit-cycle. For instance, Ghirardo et al. [47] and Moeck et al. [46] applied the cubic function in their work to model limit-cycle oscillations of spinning and standing azimuthal as well as synchronized azimuthal and axisymmetric acoustic modes in an annular combustor, respectively. The same function was adopted by Hummel et al. [48] in their ROM to describe non-compact thermoacoustic oscillations of the T1 eigenmode in the A^2EV combustor. Although the utilization of the saturation term in all these analyses yielded reasonable results and unlocked fundamental

[1] Parts of this chapter were published in Ref. [123].

physical understanding of various non-linear phenomena in thermoacoustic systems, its practical and physical significance should not be overestimated. Specifically, without having benchmark data available, the calibration factor κ can be set arbitrarily to achieve any limit-cycle amplitude. Hence, the reliable prediction of amplitude-levels is precluded and a precise application of countermeasures to mitigate limit-cycle oscillations is not possible. Additionally, the transfer of the perception of heat release saturation as the root-cause for limit-cycle oscillations to high-frequency, non-compact thermoacoustic systems has not yet been verified. It has only been proven for compact flames exposed to longitudinal modes at rather low-frequencies (see e.g. Refs. [52–54, 125]). Instead, recent work of Berger et al. [70] at the author's institute revealed a constant flame response in terms of amplitude-independent T1 flame driving rates in the A^2EV combustor system. They separately investigated the flame displacement and deformation modulation mechanisms [22, 81] and identified corresponding non-linear contributions to the driving rates for each of them. The non-linear behavior appears due to an amplitude-dependent, radial flame contraction. More specifically, a decrease of deformation and an increase of displacement driving rates was observed for increasing pressure amplitudes. However, the superposition of both trends balanced out to constant flame driving. This observation contradicts the state-of-the-art perception of heat release rate saturation and indicates alternative paths to the formation of high-frequency limit-cycle oscillations in the A^2EV combustor.

The motivation of this chapter is identification of these alternative paths. Hence, the perception of saturation of the flame driving potential is not followed in this thesis. Instead, the research focus is put on the amplitude-dependent increase of its counter-player, namely the impact of dissipative effects. In the context of this thesis, the generation of acoustically induced vorticity perturbations and their coupling with the mean flow is numerically investigated at several acoustic pressure amplitude levels. A qualitative comparison of the flame's driving behavior computed in this work with the results of Berger et al. [70] validates the presented analysis framework.

The chapter is structured as follows: First, the analysis strategy with some details on the numerical setup is presented. In the results section, the flame contraction is analyzed and its root-cause is identified. Then, amplitude-dependent driving and damping rates are computed and discussed. Finally, the effect mainly responsible for the increase of acoustic damping is revealed and analyzed.

6.1 Analysis Strategy for Non-Linear Oscillations

The proposed analysis strategy is based on the hybrid CFD/CAA approach, which was introduced in Section 4.1. In this chapter, it is adapted to compute amplitude-dependent damping and driving rates. Specifically, computations with the URANS equations replace the RANS simulations. With reference to Fig. 6.1, the conceptual framework is explained in the following three subsections.

6.1.1 CFD Simulations

The starting point for the investigations is a compressible CFD simulation with the URANS equations (information on the operational conditions: $\bar{\dot{m}}_{\mathrm{in}} = 120\,\mathrm{g/s}$, $\bar{T}_{\mathrm{in}} = 623\mathrm{K}$, $\lambda = 1.2$). Perfectly premixed, lean combustion is captured by the extended version of the *Flamelet Generated Manifold* model developed by Klarmann et al. [77, 121, 126], which includes effects of flame stretch and heat losses. Due to the circumferential variability of the T1 mode, axisymmetry cannot be exploited to reduce computational costs in time-domain CFD simulations. Hence, the chamber is fully discretized by a structured mesh (see Appendix E). The computation consists of two phases (cf. the diagram in Fig. 6.1).

Phase I: a steady-state solution is obtained via an URANS simulation after 250 time steps. Notice that the steady-state can alternatively be computed via a RANS simulation.

Phase II: at time step 251 the source term function

$$m_{p'}(r,\theta,x,t) = A_{p'}(t - t_{\mathrm{ref}})\,\delta_{p'} \sin\left[2\pi f_{\mathrm{T1}}(t - t_{\mathrm{ref}}) + \theta_{\mathrm{rot}}\right] \tag{6.2}$$

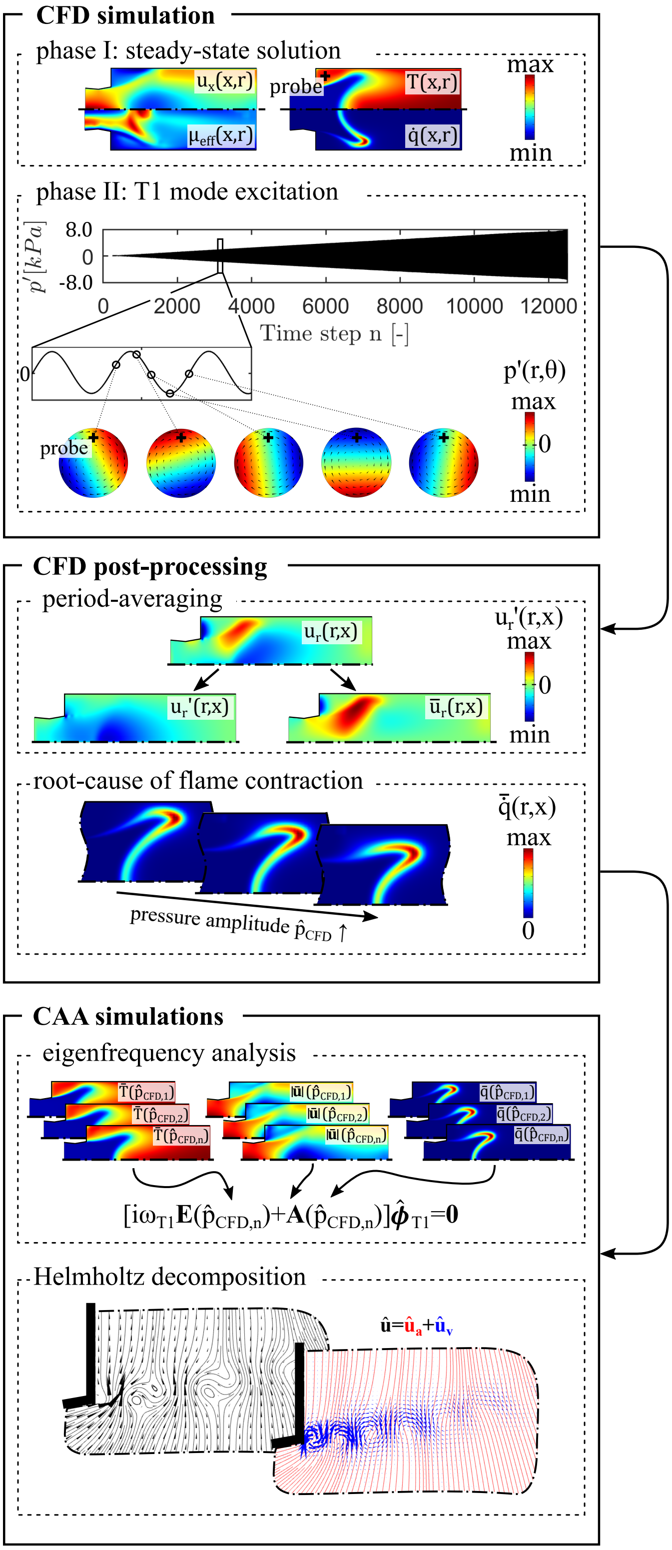

Figure 6.1: *Computational framework.*

is activated in the energy equation (cf. Eq. (2.3)), which produces harmonic pressure oscillations at the chamber's T1 resonance frequency f_{T1}. The spatial distribution function $\delta_{p'} = f(r,x)$ indicates that the source term acts in a restricted volume only and is zero elsewhere (cf. Fig. E.1 in Appendix E). Its amplitude linearly increases with time starting from a zero value, which is realized by the term $(t - t_{\mathrm{ref}})$. $A_{p'}$ denotes the constant gradient and can be set arbitrarily to produce any desired envelope amplitude. In this study, the source term in Eq. (6.2) produces maximum T1 pressure pulsations in between -8.0kPa and 8.0kPa within 12500 time steps, which is equivalent to a physical time span of 0.125s. The corresponding pressure time trace is displayed in the second dashed box of Fig. 6.1. Notice that this gradient is similar to those measured in the A^2EV combustor (cf. Fig. 5 in Ref. [70]). To mimic the T1 mode's rotation in swirl direction, which occurs in the real combustor due to the swirling flow and the associated loss of degeneracy [127], circumferential variability of the source term must be included. This is achieved by the azimuthal phase angle θ_{rot} in the sine-function, where $\theta_{\mathrm{rot}} \in [-\pi, \pi]$. In the second dashed box of Fig. 6.1, snapshots of the rotating pressure field at individual time steps within one oscillating period are presented. Notice that the T1 resonance frequency f_{T1} is determined in a pre-study via a frequency response analysis. For this purpose, a modified source term similar to the one in Eq. (6.2) is used, which allows simultaneous excitation at several frequencies with a constant forcing amplitude (see Eq. (E.1) in Appendix E). The resulting T1 resonance frequency appears as a peak in the corresponding frequency spectrum at $f_{\mathrm{T1}} = 2750\mathrm{Hz}$. This frequency value in combination with the time step size of $\Delta t = 0.00001\mathrm{s}$ yields a temporal resolution of ${}^{T_{P_{\mathrm{T1}}}}/_{\Delta t} \approx 36$ time steps per oscillation period $T_{P_{\mathrm{T1}}}$ for the simulation analyzed in this study. Details on the frequency response analysis and on the URANS CFD mesh are provided in the Appendix E.

6.1.2 CFD Post-Processing: Period-Averaging

Relevant CFD solutions fields $\boldsymbol{\phi}(r, x, t)$ are period-averaged in one $r - x$ plane to access slowly varying mean as well as oscillating quantities at a certain time step n, $\bar{\boldsymbol{\phi}}_{\mathrm{n}}(r, x, t)$ and $\boldsymbol{\phi}'_{\mathrm{n}}(r, x, t)$ respectively:

$$\boldsymbol{\phi}'_{\mathrm{n}}(r, x, t) = \boldsymbol{\phi}_{\mathrm{n}}(r, x, t) - \underbrace{\frac{\Delta t}{T_{P_{T1}}} \sum\nolimits_{k=\mathrm{n}-\frac{T_{P_{T1}}}{\Delta t}}^{\mathrm{n}} \boldsymbol{\phi}_{\mathrm{k}}(r, x, t)}_{=\bar{\boldsymbol{\phi}}_{\mathrm{n}}(r,x,t)} \tag{6.3}$$

The decomposition of the radial velocity field into its mean and fluctuating part is shown in the third dashed box of Fig. 6.1. The bulk flow and perturbation fields are used to explain the physical root-cause of the amplitude-dependent flame contraction, which is reproduced in the CFD simulation (cf. the fourth dashed box in Fig. 6.1) in accordance with OH*-chemiluminescense images measured by Berger et al. [70]. Notice that data extraction in one representative $r - x$ cut plane is sufficient to fully reconstruct the oscillating as well as the period-averaged fields in the chamber. This is possible due to the continuous rotational symmetry of the mean fields, which was found to be a valid assumption.

6.1.3 CAA Simulations

To perform CAA simulations, period-averaged velocity, temperature, heat release rate and viscosity CFD fields at several pressure amplitude levels are successively interpolated on the two-dimensional computational grid shown in Fig. 5.7. The corresponding linear eigenvalue problem of Eq. (4.1) based on linearized disturbance equations in the frequency domain is solved numerically with the FEM for each of the mean flow data sets. The governing equations in this study are the isentropic LNSE (2.26)-(2.27). These are solved in a highly resolved, two-dimensional mesh, which allows computation of stable FEM solution without the addition of artificial diffusion (cf. Section 2.5). Hence, optimum numerical conditions are established to fundamentally investigate the amplitude-dependent acoustic dissipation potential of acoustically induced vorticity perturbations.

Conceptually, the presented approach is similar to the well-known "*Flame Describing Function*" framework applied by Noiray et al. [128] to a compact thermoacoustic system. They express the flame response not only as a function of frequency, which is commonly referred to as the "*Flame Transfer Function*", but also as a function of the acoustic velocity amplitude at a reference position in the combustor. Then, the describing function is used to compute amplitude-dependent eigenfrequencies. Their study follows the generally accepted perception that flame saturation is the root-cause of limit-cycle oscillations; however, this perception is dropped in this work and the focus is set on the amplitude-dependent increase of damping in a non-compact thermoacoustic system. Hence, a term like "*Damping Describing Function*" framework would be more appropriate to classify the presented framework although the "*Damping Describing Function*" is not explicitly available. Instead, it is inherently included in the mean field data extracted from the CFD simulation at j distinct pressure amplitude levels. These fields are used to parameterize the eigenvalue problem in Eq. (4.1) as a function of the URANS CFD pressure amplitude $\hat{p}_{\mathrm{CFD}}$ determined at the probe location shown in the first and second two dashed boxes of Fig. 6.1, i.e.

$$\left[i\omega_{\mathrm{T1,j}} \mathbf{E}\left(\hat{p}_{\mathrm{CFD,j}}\right) + \mathbf{A}\left(\hat{p}_{\mathrm{CFD,j}}\right)\right] \hat{\boldsymbol{\phi}}_{\mathrm{T1,j}} = \mathbf{0}. \tag{6.4}$$

Mathematically, the parameter $\hat{p}_{\mathrm{CFD}}$ non-linearly modifies the system matrices **E** and **A** of Eq. (6.4) in an a priori unknown manner, which thus requires benchmark data at several fixed points to approximate the behavior. In the context of this study, the benchmark data is represented by the period-averaged CFD fields at some T1 pressure amplitude levels, which are the *j* fixed points.

In order to compute the desired thermoacoustic driving and damping rates of Eq. (6.4) individually at each fixed point, $\beta_\mathrm{j} = \beta_{\Delta,\mathrm{j}} + \beta_{\rho,\mathrm{j}}$ and $\alpha_{\mathrm{D}_{\mathbf{\Omega}},\mathrm{a},\mathrm{j}}$ respectively, the methodology introduced in Section 5.2 is applied. For this study, three independent eigenfrequency analyses are carried out:

1. The first simulation is performed with the isentropic LNSE (2.26)-(2.27), where the flame is assumed to be passive ($\hat{\dot{q}} = 0$).

2. Then, an eigenfrequency computation is performed with the isentropic APE, where unsteady heat release is now modeled by the flame displacement and deformation FTFs, $\hat{\dot{q}}_\Delta$ and $\hat{\dot{q}}_\rho$ respectively (cf. Eq. (5.28)). In this study, the stress tensor is added to the r.h.s. of the APE momentum equation, i.e.

$$\bar{\rho}\left(i\omega\hat{\mathbf{u}} + \nabla\left(\bar{\mathbf{u}}\cdot\hat{\mathbf{u}}\right)\right) + \hat{\rho}\left(\frac{1}{2}\nabla\left(\bar{\mathbf{u}}\cdot\bar{\mathbf{u}}\right)\right) + \nabla\hat{p} = \nabla\cdot\hat{\boldsymbol{\tau}}. \tag{6.5}$$

   Consequently, the APE momentum Eq. (6.5) contains the effect of viscosity on the acoustic velocity field[2].

3. A final simulation is performed with Eqs. (6.5) and (2.31), where no unsteady heat release is considered in the latter equation, i.e. $\hat{\dot{q}} = 0$.

With reference to Section 5.2, the damping rate $\alpha_{\mathrm{D}_{\mathbf{\Omega}},\mathrm{a}}$ as well as the driving

[2]For the sake of clarity, the flame-vortex FTF $\hat{\dot{q}}_\mathrm{s}$ (see Section 5.1.2) is not considered in this study. Recall that the focus of this chapter is put on the amplitude-dependent increase of acoustic dissipation as well as on displacement and deformation driving rates for which experimental results of Berger et al. [70] are available.

rates β_Δ and β_ρ are obtained by subtraction (cf. Eq. (5.22)), i.e.

$$\alpha_{\mathrm{D}_{\boldsymbol{\Omega}},\mathrm{a}} = \nu_{\mathrm{LNSE}}\Big|_{\hat{\dot{q}}=0}^{\alpha_\tau=0} - \nu_{\mathrm{APE}}\Big|_{\hat{\dot{q}}=0}^{\alpha_\tau=0}, \tag{6.6}$$

$$\alpha_{\mathrm{rest}} = \alpha_{\nabla\bar{s}} + \alpha_\mu = \nu_{\mathrm{APE}}\Big|_{\hat{\dot{q}}=0}^{\alpha_\tau=0}, \tag{6.7}$$

$$\beta_\Delta = \nu_{\mathrm{APE}}\Big|_{\hat{\dot{q}}=\hat{\dot{q}}_\Delta}^{\alpha_\tau=0} - \nu_{\mathrm{APE}}\Big|_{\hat{\dot{q}}=0}^{\alpha_\tau=0}, \tag{6.8}$$

$$\beta_\rho = \nu_{\mathrm{APE}}\Big|_{\hat{\dot{q}}=\hat{\dot{q}}_\rho}^{\alpha_\tau=0} - \nu_{\mathrm{APE}}\Big|_{\hat{\dot{q}}=0}^{\alpha_\tau=0}. \tag{6.9}$$

6.2 Results and Discussion

This section presents the results obtained by following the analysis strategy introduced in the previous Section 6.1.3. First, the amplitude-dependent flame contraction is analyzed and its root-cause is identified, which was not possible in the frame of the experiments of Berger et al. [70]. Next, driving rates based on the flame displacement and deformation source terms of Eq. (5.28) are computed at several pressure amplitude levels. The trends are discussed with respect to experimental results. This seeks to validate the numerical framework and to justify the computational approach as well as the analysis of amplitude-dependent damping rates, which is discussed in the subsequent step.

Notice that measured line-of-sight OH*-chemiluminescence images of the A^2EV combustor for various T1 pressure amplitudes and corresponding driving rates can be found in the work of Berger et al. [70] and are thus not repeated in this thesis. These experiments are based on low- and high-swirl configurations of the A^2EV combustor, while a medium-swirl configuration is analyzed in this study. However, the results of this study are expected to be extrapolable to the low and high swirl configurations.

6.2.1 Root-Cause of Non-Linear Flame Contraction

The period-averaged heat release rate distributions at five T1 pressure amplitude levels are shown in the upper halves of the plots in Fig. 6.2 a). In the lower halves, difference images are displayed, which are obtained by subtracting the steady-state field at 0kPa from each of the five fields, i.e. $\Delta\bar{\dot{q}}_{\mathrm{j}} = \bar{\dot{q}}\left(\hat{p}_{\mathrm{CFD,j}}\right) - \bar{\dot{q}}\,(0\mathrm{kPa})$. Visual inspection of Fig. 6.2 a) already reveals that the heat release maximum $\bar{\dot{q}}_{\mathrm{max}}$, which is marked by crosses, contracts towards the chamber's axis for increasing pressure amplitudes. At the same time, the flame root $\bar{\dot{q}}_{\mathrm{root}}$, which is marked by vertical dashed lines, shifts further downstream. Notice that the measured OH*-chemiluminescence images of low- and high-swirl configurations of the A^2EV combustor in Ref. [70] show a similar contraction. Additionally, Schimeck et al. [129] reported a reduction of the flame angle for increasing acoustic amplitudes in their swirl-stabilized combustor experiments while the axial flame extent increased. This exactly resembles the trends of Fig. 6.2 a).

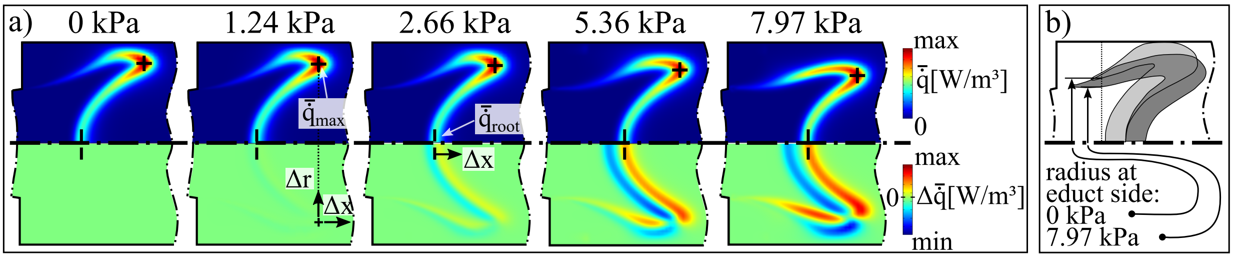

Figure 6.2: *a) Period-averaged heat release fields at several pressure amplitude levels (upper halves) and difference images (lower halves); b) flame contour with radii of cross-sectional areas at the educt side.*

The downstream shift of the flame root and heat release maximum is a consequence of the radial contraction and can illustratively be explained by inspecting the gray shaded flame contour planes in Fig. 6.2 b). Due to the flame contraction, the radius of the cross-sectional area reduces at the educt side, which is indicated by the two arrows. As period-averaged mass flow and density do not change, the educt bulk flow must accelerate to compensate for the decrease of the cross-sectional area. The increased axial flow momentum pushes the stagnation point, and thus the flame, further downstream.

The root-cause of the flame contraction itself can be identified in the vicinity of the combustion chamber's inlet, where the bulk flow separates from the area jump and creates a shear-layer. Figure 6.3 a) shows three snapshots of the total axial velocity $u_{\mathrm{x}} = \bar{u}_{\mathrm{x}} + u'_{\mathrm{x}}$ at different instants of time within one oscilla-

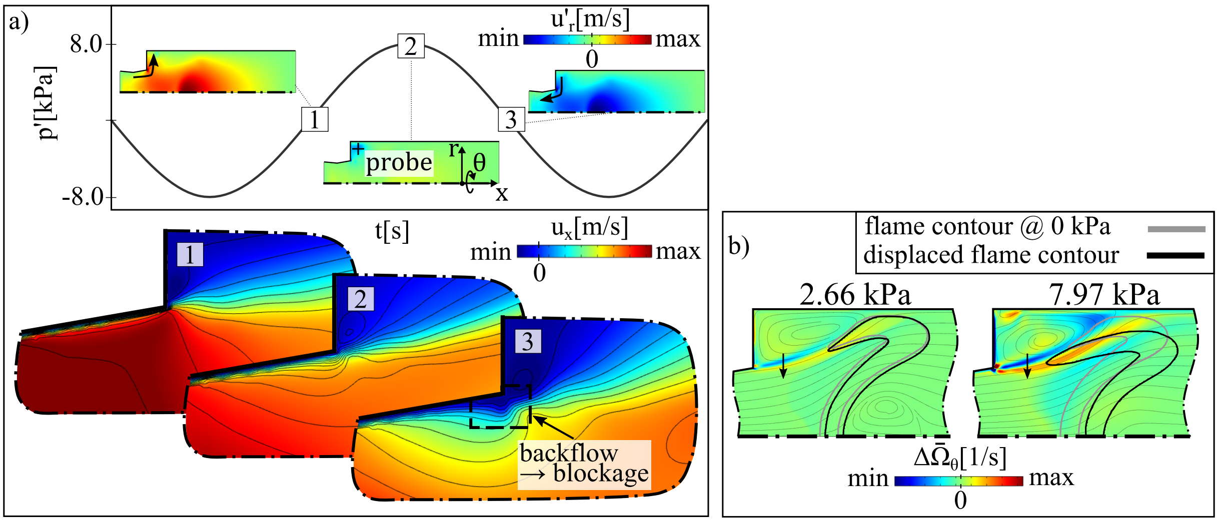

Figure 6.3: *a) Formation of a backflow zone within one oscillation period near the combustion chamber inlet; b) difference images of the azimuthal mean vorticity vector component.*

tion period. At instant $\boxed{1}$, the pressure at the probe location is zero, while the radial acoustic velocity is maximum and positive in the upper half of the $r-x$ plane. In this situation, acoustics flows from the mixing tube around the corner of the area jump into the combustion chamber, which is indicated by the little arrow in the graph of Fig. 6.3 a). The total axial velocity u_x thus, increases. At instant $\boxed{2}$, the pressure is maximum and the radial acoustic velocity is zero yielding $u_x = \bar{u}_x$. At instant $\boxed{3}$, the pressure is zero again, but the radial acoustic velocity is now negative and points towards the axis. The perturbed fluid flows from the chamber upstream into the mixing tube and decreases the total axial velocity. The high perturbation velocity in the vicinity of the corner of the area jump in combination with the relatively low bulk flow velocity in the boundary layer promotes the occurrence of backflow zones directly upstream of the edge, which is clearly visible in snapshot $\boxed{3}$ of Fig. 6.3 a). The bubble with negative axial velocities leads to blockage, which forces the flow to separate from the wall and to redirect towards the axis. As a consequence, the flow detachment angle deviates as the flow can no longer leave the wall contour tangentially. This blockage appears periodically but only within one half of an oscillation period. Within the other half (cf. instant $\boxed{1}$ in Fig. 6.3 a)), the flow is only accelerated, but not redirected. In a period-averaged sense, this leads to a mean deviation of the detachment angle with respect to the steady-state situation, i.e. at $\hat{p}_{\mathrm{CFD}} = 0$ kPa. The impact of this mechanism on the period-averaged fields becomes stronger with increasing pressure amplitudes as the acoustic velocity mutually increases. This, in turn leads to a spatial expansion of the backflow bubble and enlarges the blocked zone. Figure 6.3 b) displays the resulting detachment angle deviation via difference images of the mean shear-layer at two pressure amplitude levels. Specifically, the images are obtained via evaluating the period-averaged azimuthal vorticity fields for the two amplitude values and by subsequently subtracting the steady-state field at zero pressure amplitude, i.e. $\Delta\bar{\Omega}_{\theta,\mathrm{j}} = |\bar{\Omega}_{\theta}\left(\hat{p}_{\mathrm{CFD,j}}\right)| - |\bar{\Omega}_{\theta}\,(0\mathrm{kPa})\,|$. From left to right and thus, for increasing amplitude values, the shear-layer shifts further in the direction of the axis, which goes along with the observed flame contraction illustrated by the gray and black contours.

6.2.2 Amplitude-Dependent Driving and Damping Rates

The amplitude-dependent driving and damping rates are computed according to Section 6.1.3 and are plotted against increasing pressure amplitude values in Fig. 6.4 a). With reference to Eqs. (6.6)-(6.9), the green line with dots in magenta represents the growth rate α_{rest} of effects that can neither be attributed to flame displacement (red dotted line, β_{Δ}) and deformation (red dashed line, β_{ρ}) nor to the generation of acoustically induced vorticity perturbations and their coupling with the mean flow (blue line, $\alpha_{\mathrm{D}_{\Omega},\mathrm{a}}$). Specifically, α_{rest} contains the effects of viscosity (light green dots in Fig. 5.8) and the non-homentropic mean flow field (magenta-colored dots in Fig. 5.8). The red continuous line is the net driving rate β, which is the superposition of red dashed and dotted lines.

The deformation driving rates reduce slightly by approximately $6\,\mathrm{rad}/\mathrm{s}$ while the displacement rates reveal an increasing trend of approximately $7\,\mathrm{rad}/\mathrm{s}$ across the investigated pressure amplitude range. In total, the deviations compensate each other, which finally leads to constant driving. The red line in Fig. 6.4 b) shows the percentage deviation of the net driving rates relative to the acoustically unperturbed case at 0kPa and confirms that flame driving remains almost constant for all amplitude levels. This agrees with the

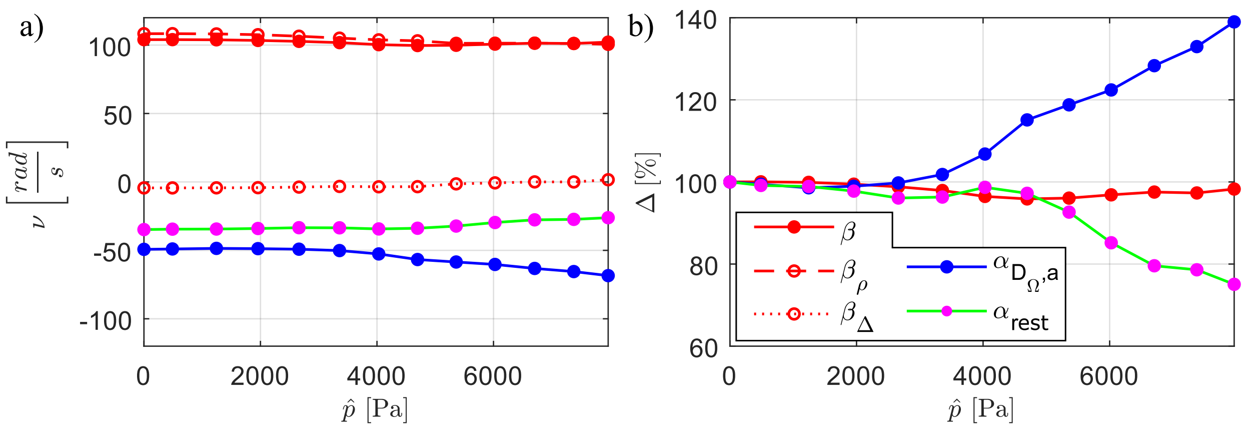

Figure 6.4: *a) Absolute and b) relative evolution of vorticity damping rates (blue line), flame driving rates (red lines) and remaining growth rate contributions (green-magenta colored line) vs. increasing amplitudes.*

experimental results of Berger et al. [70] and thus validates the computational framework of this study. This also indicates once more that flame saturation is not the root-cause of high-frequency, thermoacoustic limit-cycle oscillations in this combustor. Instead, the blue curve in Fig. 6.4 a) reveals significantly decreasing damping rates and thus increasing dissipation of acoustic energy associated with the *Lamb* vector terms in Eq. (2.36). With reference to Fig. 6.4 b), the damping rate magnitudes increase by approximately 40% within the inspected pressure amplitude spectrum. The remaining effects due to the non-homentropic mean flow and viscous stresses act in a dissipative manner on T1 oscillations, which can be seen by the corresponding negative damping rate values of the green-magenta-colored curve in Fig. 6.4 a). For increasing amplitude levels, their dissipative impact attenuates by approximately 22% (cf. Fig. 6.4 b)), which counteracts but cannot compensate the damping increase associated with the acoustically induced vorticity perturbations. This observation infers that limit-cycle oscillations of the unstable T1 mode in the A^2EV combustor might be the result of an overall growth of acoustic dissipation.

Figure 6.5 a) shows the eigenfrequency map of the parameterized eigenvalue problem given by Eq. (6.4). Each point in this graph represents an eigenfrequency at a certain pressure amplitude, which is composed of the oscillation frequency f and the net T1 growth rate $\nu = \alpha_{\text{rest}} + \alpha_{\text{D}_\Omega,\text{a}} + \beta_\rho + \beta_\Delta$. After a slight increase, the net growth rate monotonously decreases from $\nu \approx 20\,\text{rad/s}$ towards a value of $\nu \approx 9\,\text{rad/s}$ at $\hat{p}_{\text{CFD}} \approx 5.36\text{kPa}$. At the same time, the T1 oscillation frequency reduces by approximately 49Hz. Then, the eigenfrequency "turns a loop", i.e. the growth rate and frequency values grow before they decrease again towards a value of $\nu = 7.58\,\text{rad/s}$ and $f = 2718\text{Hz}$ at $\hat{p}_{\text{CFD}} \approx 8.0\text{kPa}$. However, limit-cycle oscillations are characterized by a net growth rate of $\nu = 0\,\text{rad/s}$, which could not fully be reproduced. Notice that the inclusion of losses in the acoustic boundary layer, which produce a damping rate of $\alpha_{\text{BL}_{\mu/\text{th}}} \approx 4\,\text{rad/s}$ according to Fig. 5.8, does still not lead to the expected zero growth rate value, but to a value very close to it. Nevertheless, the evident decrease of the net growth rate reveals that amplitude-dependent-dissipation mechanisms may play a major role to explain the formation process of limit-cycle oscillations in high-frequency thermoacoustic systems.

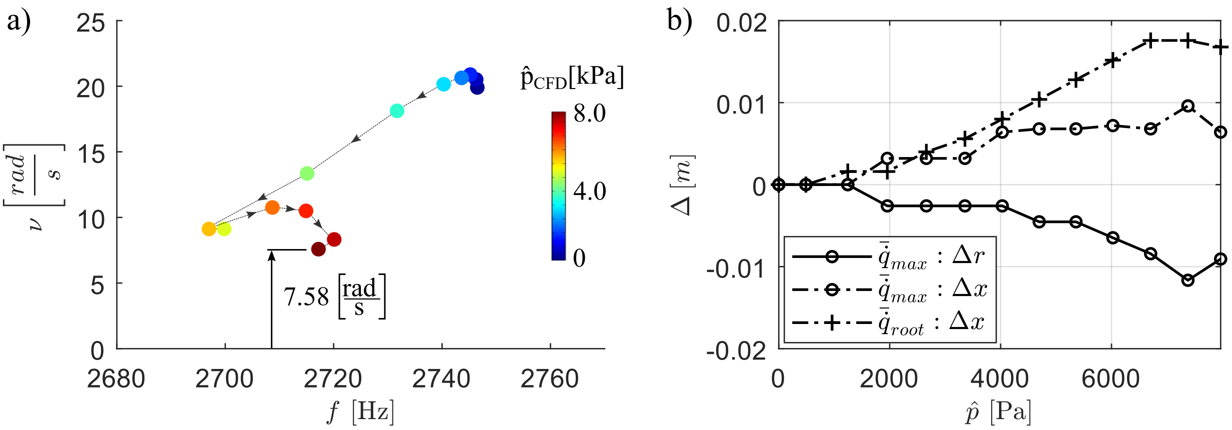

Figure 6.5: *a) Eigenfrequency map of the parameterized eigenvalue problem of Eq.* (6.4)*; b) heat release rate maximum and root displacement vs. increasing amplitudes.*

Next, particular attention is given to the root-cause of the amplitude-dependent dissipation increase associated with the cross-product terms $(\mathbf{\Omega} \times \mathbf{u})$ in the LNSE, i.e. the evolution of the blue curve in Fig. 6.4 a). A discussion on the effects represented by the green-magenta colored curve is left to future work at this point and the reason for constant driving was already addressed in the work of Berger et al. [70]. First however, the focus is briefly on the drop of the T1 oscillation frequency f displayed in Fig. 6.5 a). Notice that a frequency reduction of similar order was measured in the experiment of Ref. [70]. Three pressure ranges can be distinguished:

- 0kPa-3.35kPa: The slight frequency decrease can be related to the flame shift quantified in Fig. 6.5 b). Heat release maximum (dashed line in Fig. 6.5 b)) and flame root (dotted line in Fig. 6.5 b)) equally shift downstream, while the radial contraction (continuous line in Fig. 6.5 b)) remains small. From this, it can be deduced that the period-averaged flame brush acts like a rigid body as it simply moves downstream without significant deformation. In consequence, the T1 mode can propagate further downstream as the cut-on region increases (cf. Eq. (2.46)). This in turn reduces the axial wave number which ultimately leads to the observed frequency decrease.

- 3.35kPa-6.02kPa: As can be seen in Fig. 6.5 b), the heat release rate maximum remains at the same axial position while the cold fresh gas flow keeps pushing the flame root further downstream. Due to this spatial compression, the radially averaged temperature decreases in this region. This reduces the speed of sound and thus the cut-on frequency, which allows the T1 mode to propagate further downstream. Again, the axial wave number diminishes leading to the relatively strong frequency drop.

- 6.02kPa-7.97kPa: The frequency increase occurs due to the radial flame contraction, which compensates the decrease associated with the axial flame shift. The radial displacement results in an enlargement of the outer recirculation zone, which is filled with hot combustion products. This leads to rising radially averaged temperatures in between the flame root and the position of heat release rate maximum. This mutually results in an elevation of the cut-on frequency $f^{\text{cut-on}}$, which finally yields the increasing T1 oscillation frequencies.

6.2.2.1 Discussion on Acoustic Dissipation Caused by Vorticity Disturbances

As explained in Section A.2, acoustic dissipation associated with the blue curve in Fig. 6.5 a) and thus with the *Lamb* vector term ($\mathbf{\Omega} \times \mathbf{u}$) is caused by the interaction of vorticity $\mathbf{\Omega} = \bar{\mathbf{\Omega}} + \hat{\mathbf{\Omega}}$ with the velocity field $\mathbf{u} = \bar{\mathbf{u}} + \hat{\mathbf{u}}$. With reference to Eqs. (2.21) and (2.36), the three terms related to vorticity occurring in the LNSE (2.26) read:

$$\left[\rho\left(\mathbf{\Omega}\times\mathbf{u}\right)\right]' \approx \left[\bar{\rho}(\bar{\mathbf{\Omega}}\times\hat{\mathbf{u}}) + \bar{\rho}(\hat{\mathbf{\Omega}}\times\bar{\mathbf{u}}) + \hat{\rho}(\bar{\mathbf{\Omega}}\times\bar{\mathbf{u}})\right] e^{i\omega_{\mathrm{T1}}t} \tag{6.10}$$

Recall that the first term describes the transformation of acoustic energy into rotational kinetic one and vice versa (see Section 2.6 and Appendix A for details). This appears primarily near the sharp area jump corner at the combustion chamber inlet as both, magnitudes of the mean vorticity and of velocity perturbations are high relative to rest of the combustion chamber. The absolute value of the period-averaged vorticity vector (at 0kPa) is shown in the lower half of Fig. 6.6 and confirms that the highest values are allocated in the outer shear-layer near the chamber inlet.

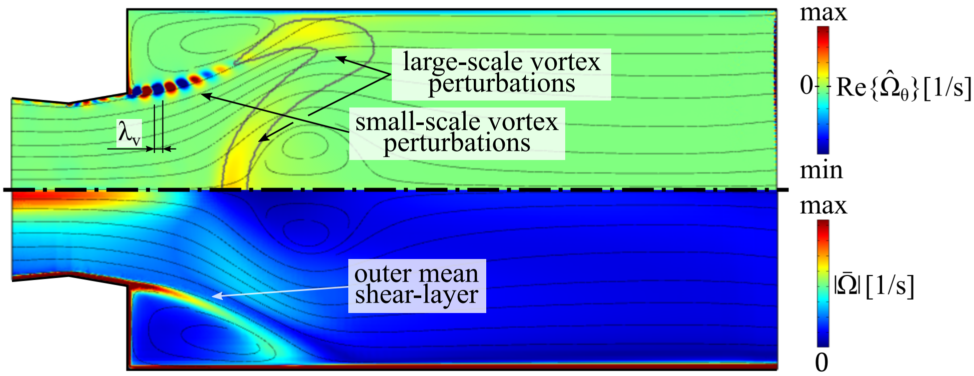

Figure 6.6: *Azimuthal component of the vorticity perturbation vector (upper half) and absolute value of the period-averaged vorticity vector (lower half) with streamlines of the bulk flow and flame contour (gray contour line) at 0kPa CFD pressure amplitude.*

The result is the acoustically induced shedding of the small-scale, clock- and counterclockwise rotating vortices illustrated in the upper half of Fig. 6.6. These are shed from the corner, convect downstream with the bulk flow velocity and finally dissipate due to viscous effects. The second term $\bar{\rho}(\hat{\mathbf{\Omega}}\times\bar{\mathbf{u}})$ describes the interaction of generated vorticity perturbations with the bulk flow velocity. The third cross-product term $\hat{\rho}(\bar{\mathbf{\Omega}}\times\bar{\mathbf{u}})$ produces a rotational acceleration of acoustic density fluctuations. The impact of the latter term on the LNSE eigensolution, i.e. eigenfrequency and -vector, is negligibly small due to its second order dependency on the small Mach numbers in this combustion chamber. However, these three terms do not explain the large-scale vorticity perturbation visible in the upper half of Fig. 6.6. It appears only in the flame region and originates from another vorticity source, namely by the baroclinic effect. This can easily be shown revisiting the APE (2.30), where the cross-product terms are absent. Taking the curl of Eq.(2.30) and applying the vector identity $\nabla \times \nabla(...) = \mathbf{0}$ yields the corresponding vorticity perturbation equation

$$i\omega\hat{\mathbf{\Omega}} = i\omega\hat{\mathbf{\Omega}}_{\text{l-s}} = i\omega\hat{\mathbf{\Omega}}_{\text{a}} = -\frac{\nabla\bar{\rho} \times \nabla\hat{p}}{\bar{\rho}^2}. \tag{6.11}$$

The r.h.s. of Eq.(6.11) represents the baroclinic effect, which is equally present in the LNSE momentum Eq. (2.26). Obviously, this type of vorticity is acoustically triggered by pressure gradient fluctuations and only occurs in regions where the mean density changes. For isothermal conditions, this type of vorticity is thus absent as $\nabla\bar{\rho} = \mathbf{0}$. It is oscillating with the frequency f but is not transported by the bulk flow as any convection terms are absent in Eq. (6.11) although the corresponding momentum Eq. (2.30) does consider translation by convection via the term $\nabla(\bar{\mathbf{u}} \cdot \hat{\mathbf{u}})$. The two latter characteristics can easily be confirmed by visual inspection of the upper half of Fig. 6.6: large-scale vortices are solely present in the flame region (gray contour), i.e. in regions of strong mean density gradients, but not downstream of the flame. For reactive cases with mean density gradients, this confirms that the acoustic velocity field does generally not satisfy the irrotationality condition of Eq. (4.14), i.e. $\nabla \times \hat{\mathbf{u}}_{\text{a}} \neq \mathbf{0}$ as stated in Section 4.3. This also explains why the mass flow Helmholtz decomposition must be applied to reactive cases instead of the velocity Helmholtz decomposition. The generation of baroclinic, acoustic vorticity $\hat{\mathbf{\Omega}}_{\text{a}}$ in Eq. (6.11) can illustratively be explained by the non-uniform in-/decrease of the speed of sound across mean density gradients, which can lead to the refraction of acoustic waves. This induces a rotational component in the acoustic velocity field $\hat{\mathbf{u}}_{\text{a}}$, if the acoustic velocity vector (which can be rewritten in terms of the gradient of the acoustic pressure $\nabla\hat{p}_{\text{a}}$) is not aligned with the mean flow density gradients. In conclusion, vorticity disturbances in reactive cases are not only generated by the "classical" shedding mechanism from sharp edges (cf. Section 2.6), but also by refraction of acoustic waves at density gradients. Both vorticity types are fundamentally different as the first type is a classical, hydrodynamic vortex, which convects downstream with the mean flow, while the second type is of acoustic nature.

Although the generation of the large-scale vorticity in the acoustic velocity field is not linked to the cross-product ($\mathbf{\Omega} \times \mathbf{u}$) but to the baroclinic effect described by Eq. (6.11), this type of vorticity can interact with the mean flow in the LNSE (2.26) via the second term on the r.h.s. of Eq. (6.11), i.e. $\bar{\rho}([\hat{\mathbf{\Omega}}_{\text{s-s}} + \hat{\mathbf{\Omega}}_{\text{l-s}}] \times \bar{\mathbf{u}})$. This affects the T1 damping rate $\alpha_{\mathrm{D}_\Omega,\mathrm{a}}$ and thus the thermoacoustic stability behavior. Now, there is the question of how the three cross-product terms and more specifically, which vorticity perturbation type, i.e. small-scale hydrodynamic or large-scale acoustic one, contribute to the net damping rate $\alpha_{\mathrm{D}_\Omega,\mathrm{a}}$. This knowledge would reveal the physical phenomenon responsible for the amplitude-dependent increase of dissipation. To gain insight, the growth rate Eq. (4.9) is used. The numerator in Eq. (4.9) is replaced by D_a, which reads in the context of the present study

$$D_\mathrm{a} = -\underbrace{\bar{\rho}\left(\bar{\mathbf{\Omega}} \times \hat{\mathbf{u}}_\mathrm{v}\right) \cdot \hat{\mathbf{u}}_\mathrm{a}}_{\text{Term 1}} - \underbrace{\bar{\rho}\left(\hat{\mathbf{\Omega}}_{\text{s-s}} \times \bar{\mathbf{u}}\right) \cdot \hat{\mathbf{u}}_\mathrm{a}}_{\text{Term 2}} - \underbrace{\bar{\rho}\left(\hat{\mathbf{\Omega}}_{\text{l-s}} \times \bar{\mathbf{u}}\right) \cdot \hat{\mathbf{u}}_\mathrm{a}}_{\text{Term 3}} - \underbrace{\hat{\rho}\left(\bar{\mathbf{\Omega}} \times \bar{\mathbf{u}}\right) \cdot \hat{\mathbf{u}}_\mathrm{a}}_{\text{Term 4}}. \tag{6.12}$$

Notice that the subscripts a and v on the r.h.s. of Eq. (6.12) denote acoustic and hydrodynamic, vortical velocity fields. The latter is associated with convectively transported vortices but not with the acoustic type of vorticity $\hat{\mathbf{\Omega}}_\mathrm{a}$. Remember that these velocity fields are the direct outcome of the mass flow Helmholtz decomposition introduced in Section 4.3. The four terms in Eq. (6.12) allow individual quantification of the dissipation of acoustic energy associated with Eq. (6.10). After having evaluated the acoustic energy density E_a

$$E_\mathrm{a} = \frac{\hat{p}_\mathrm{a}^2}{2\bar{\rho}\bar{c}^2} + \bar{\rho}\frac{\hat{\mathbf{u}}_\mathrm{a}^2}{2} + \hat{\rho}_\mathrm{a}\left(\bar{\mathbf{u}} \cdot \hat{\mathbf{u}}_\mathrm{a}\right), \tag{6.13}$$

four damping rates corresponding to terms 1-4 in Eq. (6.12) can be computed. These are presented in Fig. 6.7:

The net damping rate $\alpha_{\mathrm{D}_\Omega,\mathrm{a}}$ (see also in Fig. 6.4 a)) is represented by the thick, continuous line with the circle markers. It is the sum of the values of the four thin lines. The close-up view reveals that terms 1,2 and 4 do contribute with less than $\pm 5\,\mathrm{rad/s}$ to overall damping. As mentioned before, term 4 (triangles in Fig. 6.7) is of second order dependency on the Mach number, which is low everywhere in this combustor. As expected, its dissipative impact is negligibly small. Terms 1 and 2 are both associated with the "classical", small-scale vortices shed from the area jump edge (see Section 2.6 and Appendix A). The

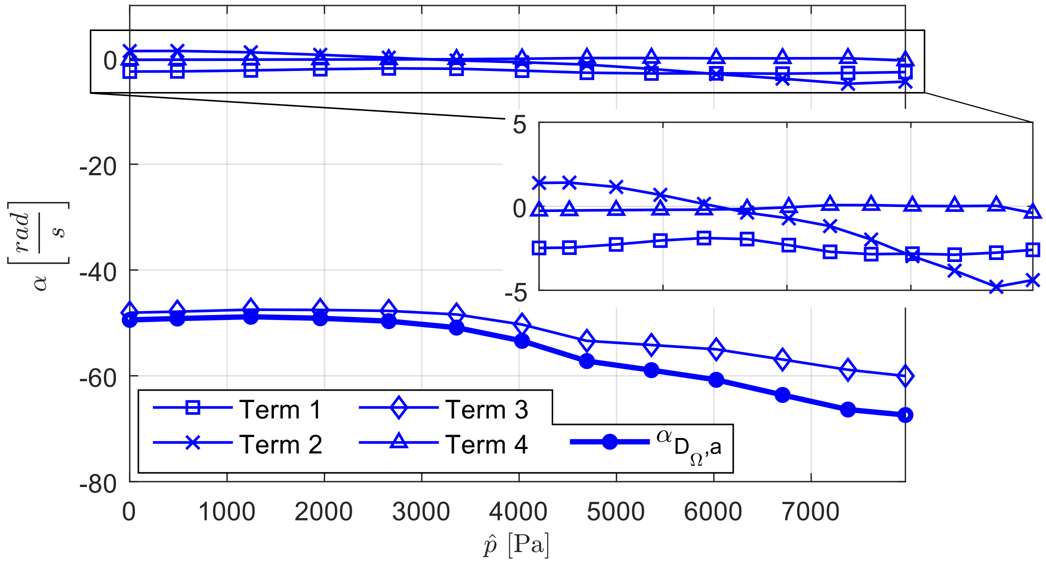

Figure 6.7: *Decomposed damping rates computed with Eq.* (6.12) *vs. increasing CFD pressure amplitudes.*

reason for their low contribution can be explained by the small scale of the vortices themselves: as shown in Fig. 2.2 a), the vortex street consists of clock- and counter-clockwise rotating regions. This alternating pattern is mutually reflected in terms 1 and 2 as of acoustic energy dissipation and supply regions. In an integral sense, they sum up to a value close to zero. Notice that this observation cannot be generalized or simply transferred to another combustion system or acoustic mode but must be validated for the respective case. The characteristic length scale λ_v of one of these small vortices can be approximated by Eq. (2.54). Hence, high mean flow values at the area jump corner or low oscillation frequencies lead to larger vortices and a "coarser" alternating pattern, which may sum up to a relevant damping contribution [61, 66]. If the mean flow velocity is kept constant, this comes down to a low-pass filter behavior towards higher frequencies of these convectively transported vortices. With reference to Fig. 6.6, the small vortex length scale of $\lambda_v \approx 6.3$mm associated with the T1 mode in the A^2EV combustor obviously results in low corresponding damping rate contributions as presented in Fig. 6.7. The following two conclusions are drawn:

- The "classical" vortex shedding mechanism (squares and crosses in Fig. 6.7), which is mainly responsible for acoustic dissipation in low-frequency systems [66], has a minor influence on the thermoacoustic stability of the studied high-frequency combustor.

- In the A^2EV combustor, large-scale vorticity perturbations, which are produced in the acoustic velocity field by the baroclinic effect, and their interaction with the period-averaged velocity field (term 3 in Fig. 6.7) are the main source of acoustic dissipation with respect to the four cross-product terms of vorticity and velocity in Eq. (6.12). For increasing acoustic pressure amplitudes, this effect becomes stronger, which explains the growth rate decrease observed in the eigenfrequency map presented in Fig. 6.5 a). Notice that this implies that the baroclinic vorticity disturbances are the main contributors to the damping rates $\alpha_{\mathrm{D}_\Omega,\mathrm{a}}$ in the simulated 80 operating points of Section 5.2.1 (cf. the blue dots in Fig. 5.8).

6.2.2.2 Investigation of the Amplitude-Dependent Dissipation Increase

The root-cause of the amplitude-dependent dissipation increase can be attributed to the radial flame contraction as well as to its axial shift in downstream direction: physically, $-\bar{\rho}(\hat{\mathbf{\Omega}}_{\mathbf{l\text{-}s}} \times \bar{\mathbf{u}}) = -\bar{\rho}\boldsymbol{\mathscr{L}}_{\text{l-s}}$ represents a volume-specific force vector performing work in the acoustic velocity field $\hat{\mathbf{u}}_\mathrm{a}$. No work is performed, if both vectors are perpendicular to each other. In contrast, the acoustic flow is accelerated, i.e. energy is supplied, or decelerated, i.e. energy is reduced/dissipated, if the vector points in the same or in the opposite direction as the acoustic velocity vector, respectively. Mathematically, this is described by the scalar product $D_{\mathrm{a,Term\,3}} = -\bar{\rho}\boldsymbol{\mathscr{L}}_{\text{l-s}} \cdot \hat{\mathbf{u}}_\mathrm{a}$ in Eq. (6.12), which provides information on the angle constellation between the vectors $-\boldsymbol{\mathscr{L}}_{\text{l-s}}$ and $\hat{\mathbf{u}}_\mathrm{a}$. In the A^2EV combustor, the amplitude-dependent flow field evolution provokes a re-alignment of these two vectors towards a stronger opposite orientation, which results in the observed increase of acoustic dissipation. Explicitly writing the scalar product in cylinder coordinates

$$D_{\mathrm{a,Term\,3}} = -\bar{\rho}\boldsymbol{\mathscr{L}}_{\text{l-s}} \cdot \hat{\mathbf{u}}_\mathrm{a} = \underbrace{-\bar{\rho}\mathscr{L}_{\text{l-s,r}}\hat{u}_{\mathrm{a,r}}}_{\text{Term 3,r}} \underbrace{-\bar{\rho}\mathscr{L}_{\text{l-s},\theta}\hat{u}_{\mathrm{a},\theta}}_{\text{Term 3},\theta} \underbrace{-\bar{\rho}\mathscr{L}_{\text{l-s,x}}\hat{u}_{\mathrm{a,x}}}_{\text{Term 3,x}} \tag{6.14}$$

and visualizing its period-average in Fig. 6.8 a) (upper halves of the plots shown on the left) demonstrates that the region of acoustic losses (blue areas) enlarges with increasing amplitude levels. This can especially be observed in the outer shear-layer, while the center region at the flame root remains almost unaffected.

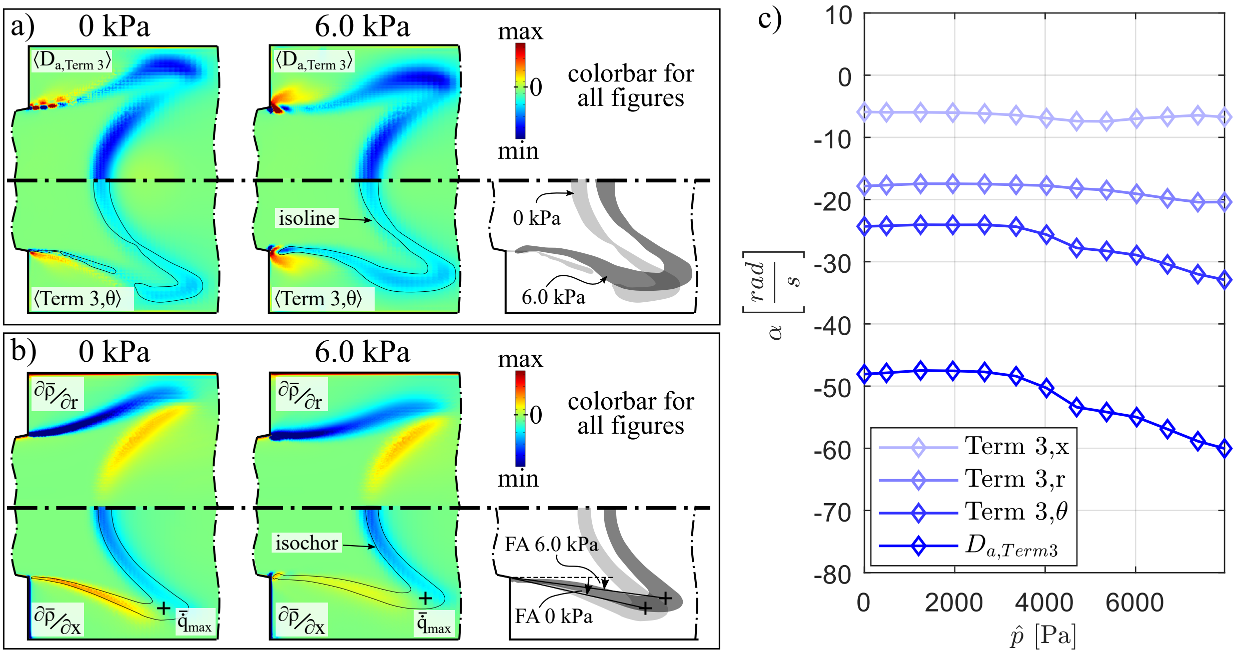

Figure 6.8: *a) Regions of acoustic dissipation associated with large-scale vorticity perturbations (upper halves) and its azimuthal contribution (lower halves) with isolines; b) radial (upper halves) and axial (lower halves) derivatives of the mean density lines with isochors for two pressure amplitude levels; c) individual contributions of the three vector components in Eq.* (6.14) *to the damping rate associated with large-scale vorticity perturbations.*

Analyzing each term individually in Eq. (6.14) and plotting the corresponding damping rates in Fig. 6.8 c) reveals that the azimuthal term is mainly responsible for the increase of dissipation in this combustor ("Term 3,θ" in Fig. 6.8 c)). Visual inspection of the lower halves of the plots in Fig. 6.8 a) with the isolines indicates this, too. Further inspection of the corresponding *Lamb* vector component yields

$$\mathscr{L}_{\text{l-s},\theta} = \hat{\Omega}_{\text{l-s,x}}\bar{u}_{\text{r}} - \hat{\Omega}_{\text{l-s,r}}\bar{u}_{\text{x}} = \frac{1}{i\omega_{\text{T1}}\bar{\rho}^2}\left(\frac{\partial\bar{\rho}}{\partial r} - \frac{\partial\bar{\rho}}{\partial x}\right)\frac{1}{r}\frac{\partial\hat{p}}{\partial\theta}, \tag{6.15}$$

where the vorticity Eq. (6.11) is exploited. Equation (6.15) shows that the azimuthal component of the volume specific force vector $-\bar{\rho}\mathscr{L}_{\text{l-s}}$ depends on the difference between radial and axial derivatives of the period-averaged density. Three scenarios are possible:

1. $(\frac{\partial\bar{\rho}}{\partial r} - \frac{\partial\bar{\rho}}{\partial x}) > 0$: the force component $-\bar{\rho}\mathscr{L}_{\text{l-s},\theta}$ points in the opposite direction as the azimuthal acoustic velocity component $\hat{u}_{\text{a},\theta}$. Acoustic energy is decreased/dissipated.

2. $(\frac{\partial\bar{\rho}}{\partial r} - \frac{\partial\bar{\rho}}{\partial x}) = 0$: the force component $-\bar{\rho}\mathscr{L}_{\text{l-s},\theta}$ does not affect the azimuthal acoustic velocity component $\hat{u}_{\text{a},\theta}$. The acoustic energy is remains unaffected.

3. $(\frac{\partial\bar{\rho}}{\partial r} - \frac{\partial\bar{\rho}}{\partial x}) < 0$: the force component $-\bar{\rho}\mathscr{L}_{\text{l-s},\theta}$ points in the same direction as the azimuthal acoustic velocity component $\hat{u}_{\text{a},\theta}$. Acoustic energy is supplied.

In conclusion, the higher the positive difference between radial and the axial density derivatives is (case 1), the stronger is the azimuthal contribution to acoustic damping. With reference to Fig. 6.8 b), where radial (upper halves) and axial (lower halves) density gradients are presented for two pressure amplitudes, this can be observed in the A^2EV combustor for growing acoustic amplitude levels as the axial density gradient drops in the outer shear-layer, while the radial one remains almost unaffected. This occurs due to the flame contraction, which results in a decrease of the flame angle (FA) depicted in the right plot of Fig. 6.8 b).

6.3 Summary and Future Work

The numerical reconstruction of the amplitude-dependent flame contraction, which was measured for the first transversal eigenmode of the A^2EV combustion system, provided detailed insight into the root-cause of this phenomenon and into the associated impact on thermoacoustic driving and damping rates. The following conclusions can be drawn:

- The flame contraction appears due to the occurrence of a backflow region directly upstream of the combustion chamber inlet, which is created periodically each time the oscillating flow velocity and the bulk flow motion point in opposite direction. This provokes the re-directing of the flow towards the chamber center in a period-averaged sense leading to the observed mean flame contraction. This mechanism reinforces with increasing acoustic pressure, and thus velocity amplitudes, as the backflow region enlarges.

- Associated computed flame driving rates resemble the amplitude-independent behavior observed in the A^2EV experiments. This disqualifies the perception of heat release rate saturation as the root-cause of limit-cycle oscillations in this high-frequency thermoacoustic system.

- Acoustic dissipation associated with acoustically induced vorticity perturbations reveals a significant amplitude-dependent increase, explaining the formation of a limit-cycle in the investigated system.

- Large-scale, acoustically induced vorticity perturbations, which are generated by the baroclinic effect, are found to be mainly responsible for the amplitude-dependent increase of acoustic dissipation. The "classical" vortex shedding mechanism from sharp edges has a weak influence on the stability of the investigated transversal eigenmode.

Future work could comprise the identification of further amplitude-dependent damping mechanisms to deepen the understanding of the origin of limit-cycle oscillations in high-frequency thermoacoustic systems.

- Special focus shall be put on the amplitude-dependent increase of acoustic dissipation caused by the non-homentropic mean flow field. This analysis was skipped in this thesis but might provide deeper insight into the root-cause of the limit-cycle.

- In addition, acoustic damping caused by non-linear shedding of convectively transported vortices should be addressed. This may become important, if acoustic velocity amplitudes are of the same order of magnitude as the bulk flow velocity, i.e. $\|\hat{\mathbf{u}}_a\|/\|\bar{\mathbf{u}}\| \geq 1$. This non-linearity cannot be captured by the analysis approach presented in this chapter as linear disturbance equations are not capable of describing the non-linear behavior by nature. Instead simulation with the so-called *Perturbed Non-conservative Non-linear Euler* equations can be carried out to determine the relevance of this phenomenon in thermoacoustic systems.

Additionally, the proposed analysis method needs to be applied to other combustion chamber geometries, for instance rectangular or annular ones, to verify the transferability of the results of this thesis to other combustor types.

7 Multi-Modal Interactions

The frequency spectrum of a time series recorded from a thermoacoustically unstable operational point often exhibits only one distinct peak despite the presence of multiple (linearly) unstable modes [55]. The implication from this observation is the existence of modal energy transfer and competition mechanisms, which lead to the suppression of all remaining modes by the dominant one. However, in theory even multiple unstable modes can coexist if they synchronize. Synchronization of self-sustained oscillators is a well-known and extensively studied field in non-linear dynamics and also occurs in the field of thermoacoustics [46, 130, 131]. A comprehensive summary on the phenomenon of synchronization is provided in Ref. [132]. In the context of thermoacoustics, two (or more) coupled acoustic modes oscillating at different frequencies f_1 and f_2 synchronize towards a common oscillation frequency $f_1 \neq f_{1,\mathrm{sync}} = f_{\mathrm{sync}} = f_{2,\mathrm{sync}} \neq f_2$, which is different to the ones of the uncoupled modes. With reference to Section 1.2, the third and last step of a comprehensive thermoacoustic stability analysis comprises the consideration of non-linear interactions between linearly unstable acoustic eigenmodes. Knowledge about the non-linear coupling mechanisms provides a complete picture of the dynamics of thermoacoustic systems and allows the application of well-suited countermeasures, such as retrofit strategies or the implementation of Helmholtz resonators, to avoid instabilities in the frequency band of interest.

In the frequency spectrum of the stable operational point of the A^2EV combustor in Fig. 3.2 a), the T1 and T2 modes appear as potential interaction partners[1]. By decreasing the air excess ratio from $\lambda = 1.8$ to $\lambda = 1.2$, the T1 mode becomes unstable and appears as the sole peak in the frequency spectrum of Fig. 3.2 b). This observation implies that the T2 mode is either linearly stable for $\lambda = 1.2$ or it is unstable but suppressed by the T1 mode.

[1] In this thesis, the focus is set on the non-degenerate modes rotating in the swirl direction. Details and explanations on the non-degeneracy of transversal modes can be found in Ref. [37].

The frequency spectrum in Fig. 3.2 b) does not allow the distinction between these two options, which prevents the experimental assessment of the linear thermoacoustic stability of the T2 mode. This means that synchronization of the T1 and T2 modes is either irrelevant, if the T2 mode is unstable but suppressed by the T1 mode, or it would be a relevant phenomenon but does not appear because the T2 mode is linearly stable. In the frame of this thesis, the assessment of the relevance of T1/T2 synchronization in the A^2EV combustor is limited to the following theoretical discussion:
Synchronization of two acoustic modes most likely occurs, if their oscillation frequencies are closely spaced in the frequency spectrum [132], i.e. $f_1 \approx f_2$. Then, so-called $1:1$ synchronization may occur, which was observed by Moeck. et al. [46] for azimuthal and axisymmetric acoustic modes in an annular combustor. However, so-called *higher-order synchronization* can occur as well. This can provoke the synchronization of acoustic modes, which are largely spaced in the frequency spectrum. An example for *higher-order synchronization* would be the synchronization of two modes where $f_1 \approx 2f_2$. In this case, the oscillation frequency of mode 1 is approximately twice as high as the one of mode 2. The synchronized state can then be characterized by $f_1 \neq f_{1,\mathrm{sync}} = 2f_{2,\mathrm{sync}} \neq f_2$. More generally, any rational number $\mathbb{Q} = {}^{l}/_{m}$, i.e. synchronization order, is possible. With reference to Fig. 3.2 a), synchronization of order ${}^{l}/_{m} = {}^{3}/_{5}$, i.e. $5f_{\mathrm{T1}} \approx 5 \cdot 2800\mathrm{Hz} \approx 3 \cdot 4500\mathrm{Hz} \approx 3f_{\mathrm{T2}}$ would be conceivable in the case of the T1 and T2 modes of the A^2EV combustor. However, any other synchronization order is more unlikely to occur than $\mathbb{Q} = 1$, i.e $f_1 \approx f_2$ [132][2]. This implies that it is hard to observe higher-order synchronization in real applications as shown for instance in Ref. [133]. In the author's opinion and with reference to the literature (e.g. Refs. [46, 132, 133]), it is very unlikely to observe synchronization phenomena with the frequency gap between T1 and T2 mode in the A^2EV combustor. In consequence, the modeling and analysis of modal interactions between T1 and T2 modes in the A^2EV combustor focuses on suppression processes or in other words, the "mode competition".

[2] Quantitatively, this can be assessed by the so-called *Arnold tongues*. *Arnold tongues* reveal the synchronization region of two coupled oscillators, i.e. the frequency range in which they can synchronize, as a function of the coupling strength of the oscillators. For more information, the interested reader is referred to Ref. [132] at this point.

In this chapter, the ROM, which was introduced in Section 4.4 [37], is modified. Specifically, modal suppression effects between T1 and T2 eigenmodes of the A^2EV combustor are described through the integration of the non-linear, pressure amplitude-dependent dissipation mechanisms identified in Chapter 6.

7.1 Modification of the Reduced Order Model

As explained in Section 4.4, the ROM framework is based on the APE (2.30)-(2.31) in the frequency domain with a numerical stabilization parameter of $\alpha_\tau = 0$. Recall that this is possible as convective perturbations, which are primarily responsible for the occurrence of numerical instabilities, are absent in the APE. Hence, the non-physical effect of the SUPG/PSPG stabilization scheme is precluded in the following ROM simulations.

In order to model modal interactions between T1 and T2 eigenmodes in the A^2EV combustor for the operational point in Fig. 3.2 b) ($\bar{\dot{m}}_{\mathrm{in}} = 120 \, ^{g}/_{s}$, $\bar{T}_{\mathrm{in}} = 623K$ and $\lambda = 1.2$), a ROM is created according to the four steps introduced in Section 4.4. Next, the ROM is modified to account for the non-linear phenomena associated with the radial flame contraction investigated in Chapter 6. This comprises the inclusion of the spatial flame contraction and its impact on the amplitude-dependent thermoacoustic driving and damping behavior into the ROM. In this context, damping and driving rate data as well as heat release rate fields are available as a function of the pressure amplitude at a reference position in the A^2EV combustor. This data is used to express the ROM system matrix $\tilde{\mathbf{A}}_{\mathrm{r}}$ and the input vector $\mathbf{u}$ as a non-linear function of the ROM output vector $\mathbf{y}$, i.e. $\tilde{\mathbf{A}}_{\mathrm{r}} = \tilde{\mathbf{A}}_{\mathrm{r}}(\mathbf{y})$ and $\mathbf{u} = \mathbf{u}(\mathbf{y})$. Figure 7.1 presents the modified APE state-space model, in which acoustic waves are constantly excited by white noise indicated by box $\boxed{1}$. The state vector $\boldsymbol{\eta}$ describes the temporal amplitude evolution of the in-swirl direction rotating T1 and T2 modes of the A^2EV combustor. The diagonal system matrix $\tilde{\mathbf{A}}_{\mathrm{r}}$ hosts the corresponding eigenfrequencies. The reduced input matrix $\tilde{\mathbf{B}}_{\mathrm{r}}$ allows the placement of spatially distributed volumetric sources/sinks with the input vector $\mathbf{u}$, while the reduced output matrix $\tilde{\mathbf{C}}_{\mathrm{r}}$ allows the extraction of acoustic pressure, velocity and displacement signals at multiple locations of interest.

The extracted data is collected in the output vector **y**.

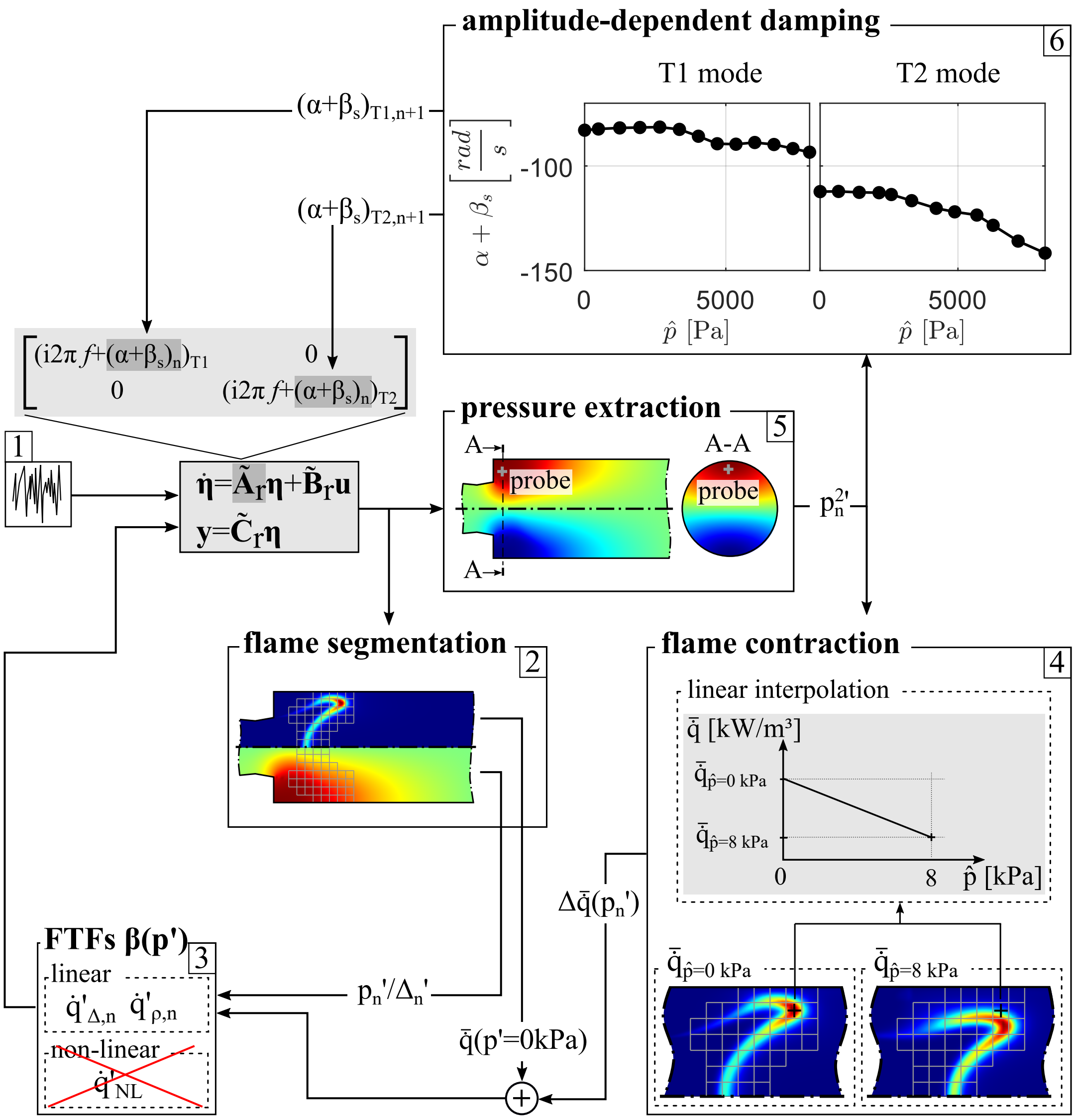

Figure 7.1: *Amplitude-dependent state-space model.*

In- and output matrices are used for the creation of local feedback loops to model non-compact thermoacoustic driving with the flame displacement and deformation FTFs [37]. This is illustrated by the boxes $\boxed{2}$ and $\boxed{3}$ in Fig. 7.1: The flame is split into acoustically compact segments indicated by the grid in box $\boxed{2}$. For each of these segments an individual feedback loop is established. Acoustic pressure p'_n and displacement Δ'_n signals as well as the mean heat release rate $\bar{\dot{q}}$ (and its gradient $\nabla\bar{\dot{q}}$)[3] are extracted from each segment to compute the local displacement and deformation FTFs, $\dot{q}'_{\Delta,\mathrm{n}}$ and $\dot{q}'_{\rho,\mathrm{n}}$, at time step n in box $\boxed{3}$. Notice that the mean heat release rate field in box $\boxed{2}$ represents the acoustically unaffected distribution at $p' = 0\mathrm{kPa}$. The local FTF values serve as the state-space system input at the locations of the respective flame segments, which closes each local feedback loop. The pulsation-amplitude dependency of the mean flow on the FTFs in frame $\boxed{3}$ is captured by box $\boxed{4}$ together with box $\boxed{5}$. The period-averaged heat release rate fields obtained from the URANS CFD simulation in Chapter 6 serve as the modeling basis. Their amplitude-dependency is known as a function of the pressure amplitude at the probe location shown in box $\boxed{5}$. Two heat release rate distributions at two reference pressure amplitudes are used to approximate the radial flame contraction in the A^2EV combustor: The first heat release rate distribution represents the acoustically unaffected case for $\hat{p} = 0\mathrm{kPa}$. The second one is associated with a pressure amplitude of $\hat{p} = 8\mathrm{kPa}$, which represents the maximum amplitude in the URANS CFD simulation presented in Chapter 6. Again, the flame segmentation approach is applied to the two heat release rate fields as indicated by the rectangular pattern in box $\boxed{4}$ of Fig. 7.1. Based on the current ROM pressure amplitude determined at the probe position shown in box $\boxed{5}$, the heat release rate difference $\Delta\bar{\dot{q}}_\mathrm{n} = \bar{\dot{q}}_{\hat{p}=0\mathrm{kPa}} - \bar{\dot{q}}_\mathrm{n}$ at time step n is computed for each flame segment via linear interpolation. This difference value serves as the input for the FTFs in box $\boxed{3}$ of Fig. 7.1.

Notice that the flame contraction computed for increasing T2 pressure amplitudes in the A^2EV combustor showed a similar behavior as for T1 oscillations. This justifies to perform the calculation of the heat release rate difference $\Delta\bar{\dot{q}}_\mathrm{n}$ independent of the mode shape in this case. However, the flame contraction behavior is generally different for each acoustic mode. If no simplification can be made, the heat release rate difference $\Delta\bar{\dot{q}}_\mathrm{n}$ must be determined depending on which eigemode dominates and has the highest amplitude values in the combustion system. This complicates the setup of the amplitude-dependent state-space model but might be realized by implementing band-pass filters

[3]Notice that the heat release rate gradient is required to compute the displacement FTF. For reasons of clarity, the gradient field is not shown in Fig. 7.1.

and pressure amplitude queries to evaluate the current amplitude of each mode considered in the ROM.

Furthermore, it is emphasized that the flame contraction feature in box $\boxed{4}$ of Fig. 7.1 cannot account for changes of the acoustic mode shape, which inherently occur as a result of the flame contraction. In other words this means that the FTFs in box $\boxed{3}$ are calculated for a spatially constant acoustic mode shape, while the heat release rate field varies in response to the current pressure amplitude. Despite the enhancement of the physical accuracy of the ROM by considering changes of the heat release rate field, this inconsistency can produce errors in the FTF calculation as changes of the acoustic pressure and velocity mode shapes do affect the FTF calculation as well. The amplitude-dependent variation of the acoustic mode shape in run-time has yet not been realized in the ROM, but would further enhance the physical accuracy of the ROM. The assessment of the impact of this inconsistency on the flame displacement and deformation driving potential in the ROM is difficult. It might be estimated by investigating the shift in oscillation frequency Δf_{i} of mode i, which is caused by the flame contraction (cf. Fig. 6.5 a)), with respect to the acoustically unaffected oscillation frequency at $\hat{p} = 0\mathrm{kPa}$, i.e. $f_{\mathrm{i},\hat{p}=0\mathrm{kPa}}$. The condition $\Delta f_{\mathrm{i}} \ll f_{\mathrm{i},\hat{p}=0\mathrm{kPa}}$ might be used as an indicator to judge similarity between perturbed and unperturbed mode shapes. With reference to Fig. F.2 c), the frequency shift for T1 and T2 modes amounts to $\Delta f_{\mathrm{T1}} \approx \Delta f_{\mathrm{T2}} \approx 50\mathrm{Hz}$, which is small compared to the respective oscillation frequencies $f_{\mathrm{T1},\hat{p}=0\mathrm{kPa}} \approx 2750\mathrm{Hz}$ and $f_{\mathrm{T2},\hat{p}=0\mathrm{kPa}} \approx 4580\mathrm{Hz}$. Hence, the error caused by the inconsistency is assumed to be small in the present study.

Finally, driving due to flame displacement and deformation is found to behave almost amplitude-independent (cf. Fig. F.2 a) and b)). This observation implies that the amplitude-dependent variation of the heat release rate field modeled in box $\boxed{4}$ of Fig. 7.1 barely affects the flame dynamics in the A^2EV combustor but might be important for other eigenmodes or combustor types. The cubic heat release rate term $\dot{q}'_{\mathrm{NL}}$ of Eq. (6.1) represents one option to produce limit-cycle oscillation and to couple acoustic eigenmodes in the ROM [37]. However, in Chapter 6, it is identified that heat release rate saturation is not the root-cause of limit-cycle oscillations in the A^2EV combustor. Hence, this saturation term is removed from the ROM, which is indicated by the red cross in box $\boxed{3}$. Instead amplitude-saturation and modal coupling is modeled by the adaption of the ROM system matrix $\tilde{\mathbf{A}}_\mathrm{r}$ during run-time. As shown in Appendix G, this is achieved by decreasing the damping rates of T1 and T2 modes (α_T1 and α_T2) on the diagonal entries of $\tilde{\mathbf{A}}_\mathrm{r}$ as a function of the current ROM pressure p'_n. For this purpose, the available damping and driving rates of Chapters 5 and 6 as well as of Appendix F are used as benchmark data. This data includes acoustic damping rates associated with acoustically induced vorticity perturbations ($\alpha_{\mathrm{D}_{\boldsymbol{\Omega}},\mathrm{a}}$), visco-thermal losses in the acoustic boundary layer ($\alpha_{\mathrm{BL}_{\mu/\mathrm{th}}}$), viscosity effects inside the chamber volume (α_μ) and the non-homentropic mean flow ($\alpha_{\nabla\bar{s}}$) (cf. Eq. (5.21)). Driving due to vortex-flame interactions is considered by the driving rate (β_s). Adding up all contributions, i.e.

$$\beta_\mathrm{s} + \alpha(p') = \beta_\mathrm{s} + \alpha_{\mathrm{D}_{\boldsymbol{\Omega}},\mathrm{a}}(p') + \alpha_{\mathrm{BL}_{\mu/\mathrm{th}}} + \alpha_\mu(p') + \alpha_{\nabla\bar{s}}(p'), \tag{7.1}$$

gives the T1 and T2 damping rate curves in the plots of box $\boxed{6}$ of Fig. 7.1. Equation (7.1) indicates that pressure-dependent data is yet not available for $\alpha_{\mathrm{BL}_{\mu/\mathrm{th}}}$ and β_s, which are thus assumed to be constant for increasing pressure amplitudes. Keep in mind that thermoacoustic driving caused by flame displacement and deformation is directly modeled in the ROM via local feedback loops in box $\boxed{3}$, which translates into the driving rate $\beta(p')$. This explains the absence of the corresponding driving rates β_Δ and β_ρ in Eq. (7.1). The overall growth rate of the ROM can be written as

$$\nu(p') = \beta_\Delta(p') + \beta_\rho(p') + \beta_\mathrm{s} + \alpha(p') = \Big(\beta(p') + \underbrace{\beta_\mathrm{s} + \alpha_{p'=0\mathrm{kPa}} - \alpha_{p'=0\mathrm{kPa}}\epsilon p'^2}_{=\beta_\mathrm{s}+\alpha(p')}\Big). \tag{7.2}$$

The sum of the constant vortex-flame driving rate β_s and the pressure amplitude-dependent damping rates $\alpha(p')$ in Eq. (7.1) is approximated by a quadratic function through fitting of the non-linearity coefficient ϵ in Eq. (7.2) to the benchmark damping and driving rate data of T1 and T2 modes. Details on the T2 damping and driving rates are provided in the Appendix F. The quadratic pressure dependency in Eq. (7.2) is based on the *Van-der-Pol* oscillator Eq. (G.6) derived for the ROM in the Appendix G and allows extrapolation of the damping rate curves in the plots of box $\boxed{6}$ of Fig. 7.1 towards higher pressure amplitude values. In practice (see Fig. 7.1), the current pressure value at time step n is used to determine the corresponding T1 and T2 damping rates from $\alpha(p')$ in Eq. (7.2). In the next time step $n+1$, the updated damping rate $\alpha_{\mathrm{n+1}}$ replaces the old one α_{n} in the system matrix $\tilde{\mathbf{A}}_{\mathrm{r}}$. The damping rates of T1 and T2 modes, $\alpha_{\mathrm{T1}}(p')$ and $\alpha_{\mathrm{T2}}(p')$, increase until the amplification due to the linear FTF feedback loop is compensated and a limit-cycle forms.

7.2 Non-Linear Coupling between T1 and T2 Modes

In this section, the modified ROM of Fig. 7.1 is analyzed. The overall pressure amplitude-dependent T1 and T2 growth rates can be computed according to Eq. (7.2). However, as driving due to flame displacement and deformation is inherently captured by the local feedback loops in the ROM, the pressure-dependency of the corresponding driving rates $\beta(p')$ is a priori unknown. Therefore, constant T1 and T2 displacement and deformation driving rates are assumed to estimate the T1 and T2 growth rate evolution in the state-space system of Fig. 7.1. The constant driving rates correspond to the acoustically unaffected cases, i.e. $\beta = \beta(p' = 0\mathrm{kPa})$, which are known from Chapters 5 and 6. Notice that this simplification can be justified by the weak pressure dependency of displacement and deformation driving rates ($\beta(p') \approx$ const.) identified in Chapter 6. Dashed and dotted lines in Fig. 7.2 show the expected amplitude-dependent T1 and T2 growth rate behavior of the state-space system presented in Fig. 7.1. This behavior is the result of the (almost) constant flame displacement (β_Δ) and deformation (β_ρ) driving rates considered by the local feedback loops (boxes $\boxed{2}$-$\boxed{4}$) and the amplitude-dependent acoustic dissipation increase modeled by the adaption of the ROM system matrix in run-time (box $\boxed{6}$) with the quadratic damping rate function $\beta_{\mathrm{s}} + \alpha(p')$ in Eq. (7.2). In Fig. 7.2, circles and squares represent the overall T1 and T2 benchmark growth rates obtained from the URANS CFD/CAA approach presented in Chapter 6.

The computed growth rates in Fig. 7.2 reveal that T1 and T2 modes are linearly unstable at $\hat{p} = 0\mathrm{kPa}$. Specifically, T1 and T2 growth rates amount to $\nu_{\mathrm{T2},\hat{\mathrm{p}}=0\mathrm{kPa}} \approx 21^{\mathrm{rad}}/_{\mathrm{s}}$ and $\nu_{\mathrm{T2},\hat{\mathrm{p}}=0\mathrm{kPa}} \approx 10^{\mathrm{rad}}/_{\mathrm{s}}$, respectively. These values indicate that the T1 mode is amplified stronger by $\Delta\nu_{\hat{p}=0\mathrm{kPa}} \approx 11^{\mathrm{rad}}/_{\mathrm{s}}$. Transferred to the measured frequency spectrum in Fig. 3.2 b) this would imply that T1 and T2 modes are linearly unstable in the experiment for the operational

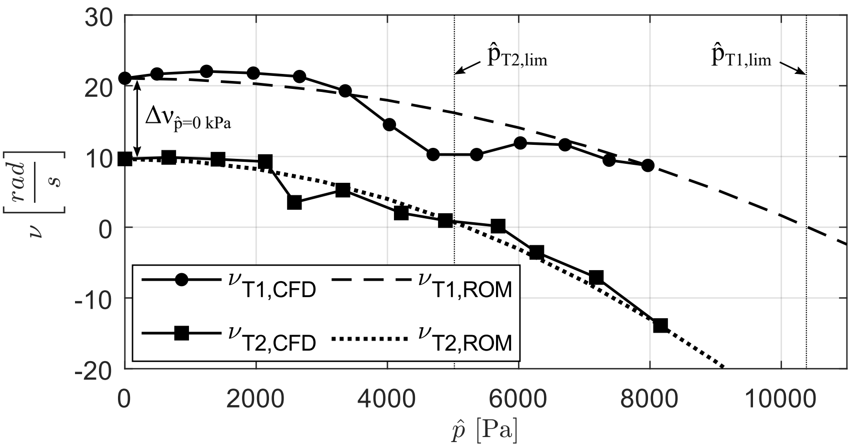

Figure 7.2: *Amplitude-dependent growth rate data of T1 (circles) and T2 (squares) modes, which is approximated by quadratic functions in the ROM.*

point with an air excess ratio of $\lambda = 1.2$. However, only one distinct peak at the T1 eigenfrequency is visible in the frequency spectrum. From this observation in combination with the computed growth rates in Fig. 7.2 it can be concluded that the T2 mode is apparently suppressed by the T1 mode. The two parabolas, which approximate the amplitude-dependency of T1 (dashed line in Fig. 7.2) and T2 (dotted line in Fig. 7.2) modes, cross the zero line at $\hat{p}_{\mathrm{T1,lim}} \approx 10.2$kPa and $\hat{p}_{\mathrm{T2,lim}} \approx 5.0$kPa. For these pressure amplitudes $\nu_{\mathrm{T1}} = \nu_{\mathrm{T2}} = 0^{\mathrm{rad}}/_{\mathrm{s}}$, which suggests that T1 and T2 limit-cycle oscillations of approximately 10.2kPa and 5.0kPa can be expected in the following ROM simulations, if both modes are investigated in an uncoupled sense.

The growth rate constellation between T1 and T2 modes presented in Fig. 7.2 is predestined to investigate modal coupling effects. Each of the modes is linearly unstable, which makes each of them a potential candidate to produce limit-cycle oscillations. First, both modes are analyzed individually in Fig. 7.3. Therefore, a ROM must created for each of the modes, where the respective other mode is absent.

The time series of T1 and T2 modes in Fig. 7.3 are extracted at the probe location shown above the respective plots. Notice that this location is identical to the probe position in box $\boxed{5}$ of Fig. 7.2. The computed limit-cycle amplitudes of T1 and T2 eigenmodes are $\hat{p}_{\mathrm{T1,lim}} \approx 10.2$kPa and $\hat{p}_{\mathrm{T2,lim}} \approx 5.0$kPa,

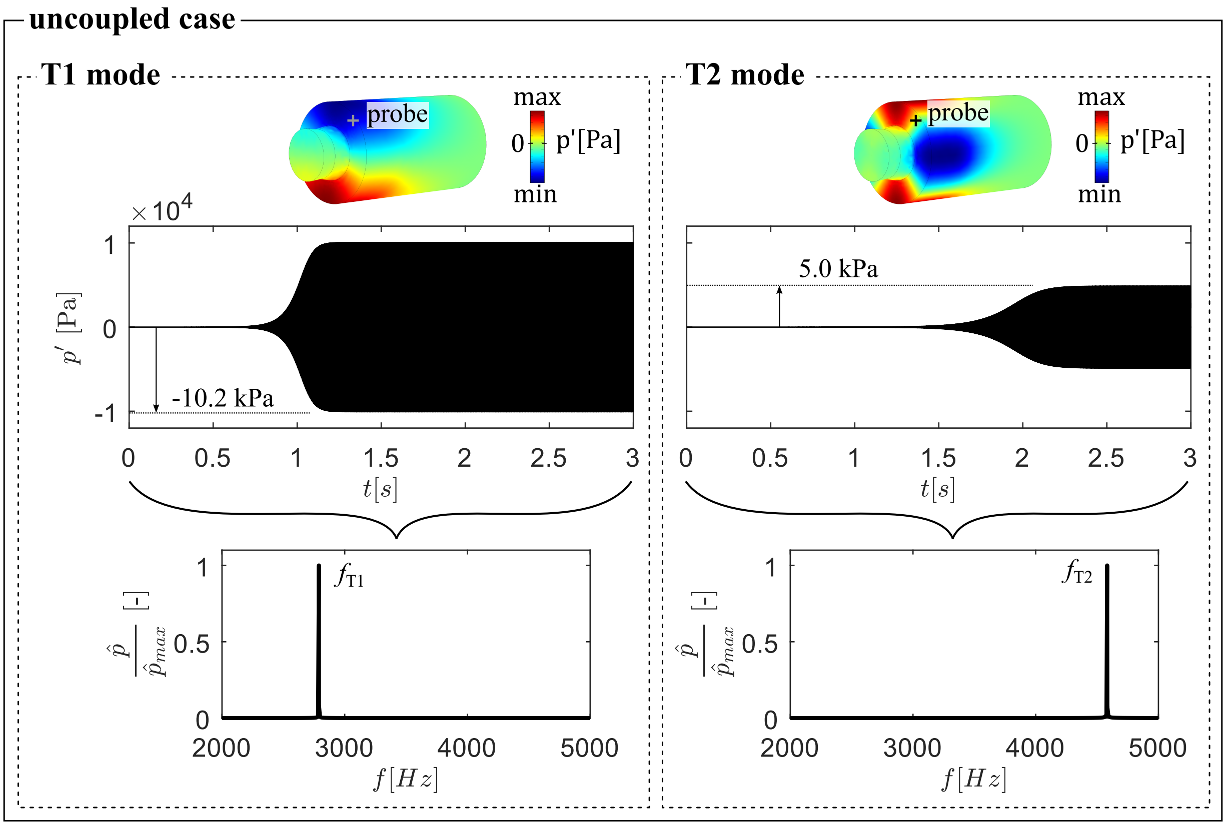

Figure 7.3: *Computed time series with the corresponding frequency spectra for uncoupled T1 (left) and T2 (right) eigenmodes.*

which reflects the expected values in Fig. 7.2. The corresponding, normalized frequency spectra reveal single peaks at the T1 and T2 eigenfrequencies.

Next, the ROM of Fig. 7.1 is investigated, where T1 and T2 modes are coupled. Figure 7.4 presents the time series recorded at the identical probe position as in the top plot of Fig. 7.3.

The upper time series in Fig. 7.4 seems to be identical to the one on the left side of Fig. 7.3 for the T1 mode. However, closer inspection of the time span between $0s \le t \le 0.25s$ in detail B shows a pressure trace consisting of more than one harmonic signal. The normalized frequency spectrum for the time between $0.0s \le t \le 0.25s$ reveals that the pressure signal consists of a superposition of T1 and T2 oscillations, i.e. $p'(t) = p'_{\mathrm{T1}} + p'_{\mathrm{T2}}$. The green T1 and blue T2 lines in Fig. 7.4 present the respective envelope amplitudes and are obtained by bandpass-filtering the raw pressure signal. Green and

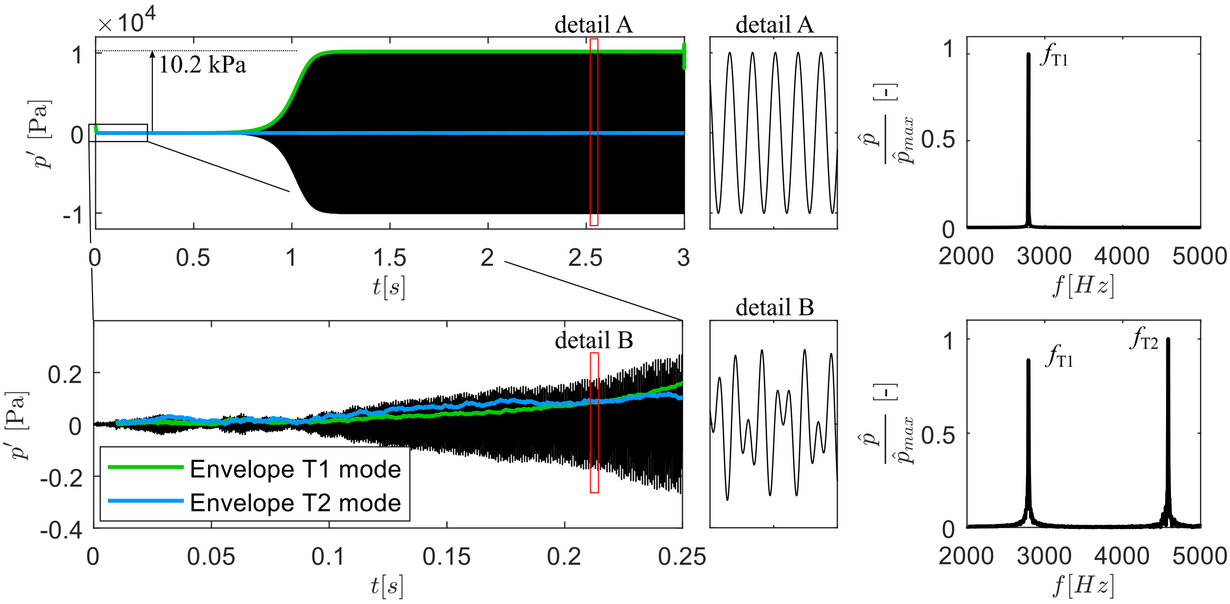

Figure 7.4: *Computed time series with frequency spectra for a time span at the onset of the instability and in the limit-cycle.*

blue curves in the close-up view confirm that both modes are simultaneously present during the onset of the thermoacoustic instability. Of course, this is not the case in the T1 mode time trace of Fig. 7.3. Finally, the amplitude of the T1 mode increases and saturates towards oscillation amplitudes of $\hat{p}_{\mathrm{T1,lim}} \approx 10.2$kPa in the limit-cycle. The frequency spectrum of the limit-cycle oscillations confirms a single frequency dominance at the T1 eigenfrequency f_{T1}, which explains the harmonic pressure oscillations in detail A. The envelope amplitude of the T2 mode remains near the zero line although the T2 mode is linearly unstable up to pressure amplitudes of $\hat{p}_{\mathrm{T2,lim}} \approx 5.0$kPa (cf. Fig. 7.2). Hence, the T2 mode is suppressed by the T1 mode, which is the "survivor" of the mode competition. The non-linear coupling between the modes is established by the amplitude-dependent modification of ROM system matrix $\tilde{\mathbf{A}}_{\mathrm{r}}$. This is highlighted in the Appendix G, where it is shown analytically that the T1 and T2 modes in the ROM illustrated in Fig. 7.1 can be interpreted as coupled *Van-der-Pol* oscillators. Notice that the limit-cycle amplitude of the T1 mode in Fig. 7.4 is equal to the uncoupled case on the left side of Fig. 7.3 and amounts to $\hat{p}_{\mathrm{T1,lim}} \approx 10.2$kPa. The conclusion from this comparison is that either modal energy transfer processes between T1 and T2 modes are irrelevant in the investigated scenario or the ROM is yet not able of capturing these type non-linear coupling phenomenon. This discussion and the corresponding investigations are left to future work. Nevertheless, the single frequency dominance in the limit-cycle of Fig. 7.4 is in agreement with the measurements of Fig. 3.2 b) and demonstrates the applicability of the modified ROM for analyses of modal suppression mechanisms.

To emphasize the importance of interactions between multiple unstable modes as part of the complete thermoacoustic prediction strategy presented in the introduction Section 1.2, the following hypothetical scenario is considered: After commissioning of a novel gas turbine, a pressure time trace is measured, which indicates the single frequency dominance of the unstable T1 mode in its combustion chamber. To suppress this T1 instability, an active control system particularly designed to damp the T1 oscillations is planned to be implemented to the gas turbine. The control system is activated automatically as soon as (with some time delay) a certain pressure amplitude threshold value is exceeded in the chamber. Before realizing the expensive control system in the real gas turbine, the stability analysis framework proposed in this thesis is applied:

1. Linear stability analyses with the advanced CFD/CAA method presented in Chapter 5 are performed for various eigenmodes in the vicinity of the unstable T1 eigenfrequency. Indeed, the T1 mode is predicted to be linearly unstable. However, one further eigenmode, namely the T2 mode, is identified to be linearly unstable, too.

2. Through application of the numerical analysis methodology introduced in Chapter 6, acoustically induced vorticity perturbations and their interaction with the bulk flow were identified to be the root-cause of limit-cycle oscillation of these two high-frequency modes.

3. The modified ROM proposed in this chapter is created for these two modes. In addition, the active control system is virtually incorporated to the ROM. To mimic the real application, a pressure query is included to the ROM. After having exceeded a certain T1 pressure amplitude value plus a certain time delay, the T1 damping rate is increased in the ROM system matrix, which mimics the effect of the, now activated control system in the real combustor.

The outcome of this procedure is shown in Fig. 7.5, where it is assumed that the A^2EV combustor represents the real engine.

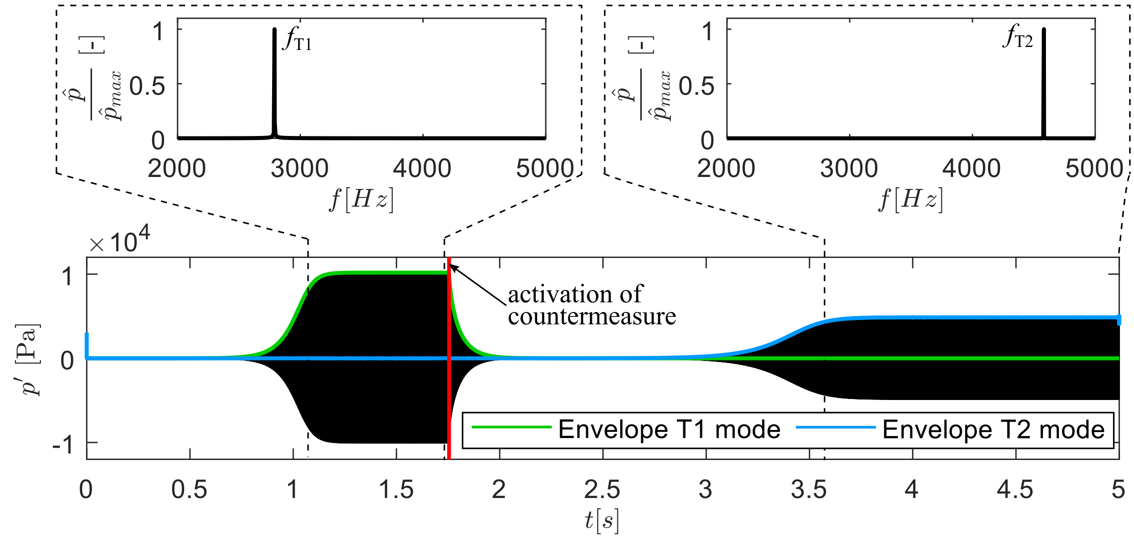

Figure 7.5: *Modeling of an active thermoacoustic control system to suppress T1 oscillations, while the T2 mode is linearly unstable.*

Similarly as in the real gas turbine, pressure amplitudes of the T1 mode (green line in Fig. 7.5) start to grow exponentially, saturate and settle in the limit cycle. The corresponding frequency spectrum gives the misleading impression that the T1 mode is sole unstable mode in the combustor –exactly as in the real engine. Indicated by the red, vertical line in Fig. 7.5, the active control system is activated shortly after the T1 instability has appeared. In consequence, the T1 mode vanishes, i.e. it becomes linearly stable. However, this gives rise to oscillations of the unstable T2 mode, which has yet not been considered in the design of the control system. This finding implies to re-design the active control system to suppress T2 oscillations as well. Without the utilization of the numerical prediction framework of this thesis, the expensive realization of the original active control strategy would have produced unsatisfactory stability results caused by an unexpected, dynamical thermoacoustic system behavior.

Admittedly, this scenario is of rather theoretical nature. Nevertheless, it stresses the importance of receiving a complete picture of the dynamics of a thermoacoustic system reaching from the knowledge about its linear stability limits to non-linear modal interactions. In particular, this might be important for gas turbine combustors, which are characterized by a large number of unstable modes closely spaced in frequency. In such complex cases, the identification of the dominant mode is not as straightforward as for the A^2EV combustor, where only two potential interaction partners are present. Theoretically, even multiple dominant modes may coexist although they do not synchronize. This might be the case, if the interaction volume, or in other word the coupling strength, of the unstable modes is weak.

8 Summary, Conclusions and Future Work

This thesis deals with high-frequency thermoacoustic instabilities in lean-premixed gas turbine combustion systems. These instabilities increasingly often occur after commissioning of modern gas turbine combustors and may lead to hardware damage and/or decrease the operational window of the gas turbine. The research objective of this work represents the qualitative and quantitative prediction of thermoacoustic instabilities from a numerical and theoretical perspective. This allows systematic application of countermeasures to avoid or mitigate unstable behavior. The approach to predict thermoacoustic instabilities is separated into three steps which comprise

1.) the determination of the linear thermoacoustic stability limits,

2.) the identification of non-linear saturation mechanisms leading to the formation of limit-cycle oscillations and

3.) the consideration of modal suppression phenomena between linearly unstable eigenmodes.

The goal of this thesis is to improve the predictability of high-frequency thermoacoustic instabilities by the accurate consideration of the influence of acoustically induced vorticity perturbations on the thermoacoustic stability behavior in the three analysis steps. This is achieved by providing new computational methods and models and by advancing existing ones. Additionally, fundamental numerical studies are carried out to enhance the understanding of the influence of vorticity perturbations on high-frequency thermoacoustic oscillations in general.

To judge the performance of the computational tools and to validate numerical investigations, a lab-scale, swirl-stabilized combustor is used as benchmark system. For the first transversal (T1) eigenmode of this combustor extensive experimental data is available.
Step #1 of the thermoacoustic stability prediction approach is based

on a hybrid *Computational Fluid Dynamics/Computational Aero Acoustics* (CFD/CAA) method. Eigenfrequency simulations with linearized disturbance equations in the frequency domain, which are solved with the *stabilized Finite Element Method* (sFEM), provide information on the thermoacoustic stability in terms of growth rates. To improve the predictive capabilities of step #1, the following research tasks are dealt with:

- The Helmholtz decomposition is applied to thermoacoustic systems. This provides access to acoustic and vortical solution fields in a separated manner. The decomposed fields are used to perform energetic analyses, which provide detailed insight into the thermoacoustic stability behavior.

- A methodology is established to eliminate the non-physical impact of numerical stabilization schemes on thermoacoustic growth rates. This allows the physically correct incorporation of acoustic dissipation caused by acoustically induced vorticity perturbations to the CFD/CAA method.

- A model is developed to describe the effect of interactions between shed vortices and the flame on the thermoacoustic stability.

- The overall thermoacoustic growth rate is decomposed into its individual contributions. This provides detailed physical insight into the contribution of individual effects to the linear thermoacoustic stability behavior.

The main findings of the linear stability assessment are summarized in the following:

- The elimination of numerical damping in thermoacoustic growth rates overcomes one of the main shortcomings of the CFD/CAA method on the basis of the sFEM. It is demonstrated that reasonable linear stability results can be retrieved from fully discretized, three-dimensional domains, which proofs the applicability of the CFD/CAA method for practical gas turbine combustion systems.

- The stability results revealed that acoustically induced vortices are one of the main sources of acoustic damping.

- From comparison to experiments, it is shown that the CFD/CAA approach consistently reproduces the measurements. For increasing thermal power densities, thermoacoustic driving grows faster than acoustic dissipation.

- The expected stability limit is predicted accurately. However, a small discrepancy to the experiment remains.

To close this gap, it is suggested to assess the errors in the individual contributions of the overall growth rate which occur by using CFD solution fields as the input for thermoacoustic stability analysis instead of experimental data. Additionally, entropy waves, which are precluded from all analysis in this work, should be incorporated physically correct to the CFD/CAA tool in the future.

Step #2 of the thermoacoustic stability prediction approach focuses on the identification of non-linear saturation mechanisms, which lead to limit-cycle oscillations in high-frequency thermoacoustic systems. A fundamental numerical study based on the CFD/CAA approach is carried out to individually compute thermoacoustic damping and driving rates for various acoustic amplitude levels at the T1 eigenfrequency of the benchmark combustor. The study revealed the following findings:

- Driving due to flame-acoustics interactions exhibits almost no amplitude-dependency, which agrees with prior experimentally based studies at the author's institute. This contradicts the concept of heat release saturation as the root-cause for limit-cycle oscillations at least for the high-frequency benchmark system investigated in this thesis.

- Instead, a significant increase of acoustic dissipation is identified for increasing pressure amplitudes in this numerical study, which explains the formation of the limit-cycle.

- The dissipation mechanism responsible for the amplitude-dependent dissipation increase can be related to the interaction of vorticity perturbations induced by the refraction of acoustic waves at mean density gradients with the mean velocity field.

- The increase of acoustic dissipation associated with the refraction of acoustic waves is caused by an amplitude-dependent flame contraction, which was also observed in the benchmark experiment.

- On the contrary, the "classical" phenomenon of acoustically induced vortex shedding from sharp corners, which is mainly responsible for acoustic damping in low-frequency systems, is found to barely affect to stability of the investigated high-frequency thermoacoustic system.

The following investigations are suggested for future work:

- The transferability of the findings gathered in step #2 of the thermoacoustic stability prediction approach to other combustion systems must be analyzed and demonstrated.

- Further research should focus on the identification of other amplitude-dependent damping mechanisms. This might include investigations of the amplitude-dependent increase of acoustic damping caused by the non-homentropic mean flow field and the effect of non-linear vortex shedding.

In step #3 of the thermoacoustic stability prediction approach, interactions between unstable acoustic eigenmodes are studied. Modal coupling effects are investigated in the time domain with a *Reduced Order Model* (ROM), which is based on the *modal truncation* theory. This method allows the efficient simulation of the non-linear dynamical behavior of multiple unstable acoustic eigenmodes in arbitrarily complex geometries. The ROM is modified to consider the amplitude-dependent increase of acoustic dissipation, which was identified as the root-cause of limit-cycle oscillations in step #2. Then, the interaction between linearly unstable first and second transversal modes of the benchmark combustor is analyzed, which yielded the following findings:

- The single frequency dominance of the T1 mode measured in the benchmark combustor is reproduced in the ROM. This demonstrates that the modified ROM correctly captures suppression mechanisms between unstable modes.

- It is found that both transversal eigenmodes can be interpreted as two coupled *Van-der-Pol* oscillators, which explains the modal suppression processes from a theoretical point of view.

In the future, the application of the modified ROM to thermoacoustic systems with a large number of unstable modes closely spaced in frequency is expected to unveil fundamental physical understanding of complex modal interaction phenomena. However, this demands for the incorporation of additional modal coupling effects to the ROM next to the suppression mechanism. This comprises the consideration of (higher-order) synchronization of, and the modal energy transfer between multiple unstable acoustic eigenmodes through physically motivated modeling approaches.

A Energy Transformation Processes between Acoustic and Vortical Sub-Modes

As illustrated in Fig. A.1, the co-existence of acoustic and convective, vortical disturbance types in LNSE/LEE eigenmodes implies that the eigensolutions obtained by directly solving the eigenvalue problem of Eq. (4.1) are not of pure acoustic nature, but capture the evolution of the convectively transported, vortical sub-mode in a superimposed manner as well, i.e. $\hat{\boldsymbol{\phi}}_\mathrm{i} = \hat{\boldsymbol{\phi}}_\mathrm{i,a} + \hat{\boldsymbol{\phi}}_\mathrm{i,v}$[1][2]. Mathematically, the eigenvalues are linked to the eigenvectors, which implies that the corresponding growth rates contain the contributions of acoustic and vortical sub-modes, i.e. $\nu = \nu_\mathrm{a} + \nu_\mathrm{v}$, as hypothesized in Ref. [37]. However, a thermoacoustic stability assessment requires the quantification of the acoustic part only as this part provides information on whether a thermoacoustic instability occurs or not. Notice that the oscillating frequency f is identical for both sub-modes, since the convectively transported vortices are triggered by the acoustic sub-mode.

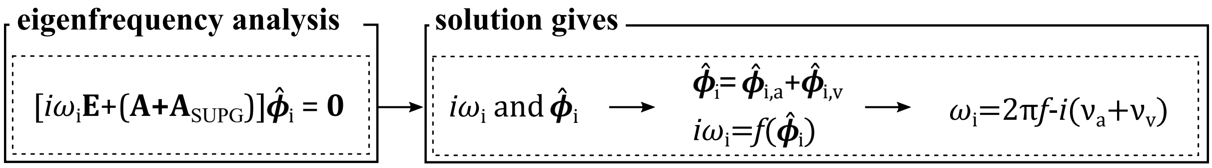

Figure A.1: *Implication of the co-existence of acoustic and vortical sub-modes on eigensolutions of the LNSE/LEE.*

The objective of this appendix comprises the clarification, whether LNSE/LEE growth rates obtained by directly solving the eigenvalue problem of Eq. (4.1) can be used for a thermoacoustic stability analysis, although they are composed of acoustic and vortical parts. This goes along with a theoretical/numerical investigation of the energy transformation processes between

[1] Parts of this chapter were published in Ref. [134]

[2] This appendix refers to Chapters 4-6 in the main part of this thesis.

acoustic and vortical sub-modes, which finally seeks to extract the unambiguous, pure acoustic net growth rate from a direct LNSE/LEE eigensolution by using the growth rate Eq. (4.6). A comparison of the extracted, pure acoustic net growth rate with the one computed by solving the eigenvalue problem of Eq. (4.1) with the sFEM provides an answer to this question.

The numerical setup used for the theoretical study in Appendix A.2 is introduced in Appendix A.1. Next, the term responsible for vortex shedding is identified in the LEE and the region of vortex generation is identified. Then, the energy transformation process between acoustic and vortical sub-modes is discussed. A connection between the energy equation for disturbance quantities derived by Myers (see Eqs. (2.33)-(2.36)) [94, 95] and the equation to quantify the pure acoustic dissipation due to vortex shedding provided by Howe [66] is established. The latter is used to extract the pure acoustic net damping rates $\alpha_{\mathrm{D}_\Omega,\mathrm{a}}$ (cf. Eq. (4.9)) from the LEE. These damping rates are compared to the corresponding LEE growth rates, which are obtained by solving the eigenvalue problem of Eq. (4.1). Finally, a conclusion is drawn concerning the applicability of these direct LEE growth rates for a thermoacoustic stability assessment.

A.1 Numerical Setup

For the purpose of this study, an isothermal configuration of the A^{2}EV swirl configuration is used, which is similar to the reactive one of Chapter 3 but differs by a nozzle termination. A schematic with geometrical dimensions of the combustion chamber with representative mean flow velocity fields is given in Fig. A.2.

For this configuration, the operational condition is fixed to an

- inlet air temperature of $\bar{T}_{\mathrm{in}} = 293K$ and an
- inlet mass flow of $\bar{\dot{m}}_{\mathrm{in}} = 120 \, g/s$.

The nozzle termination provokes an axial attenuation of transversal acoustic modes towards zero at the outlet. This prevents acoustic fluxes through this boundary. As explained in Section 2.4.1, this is caused by an increase of the cut-on frequency in downstream direction as the radius of the chamber

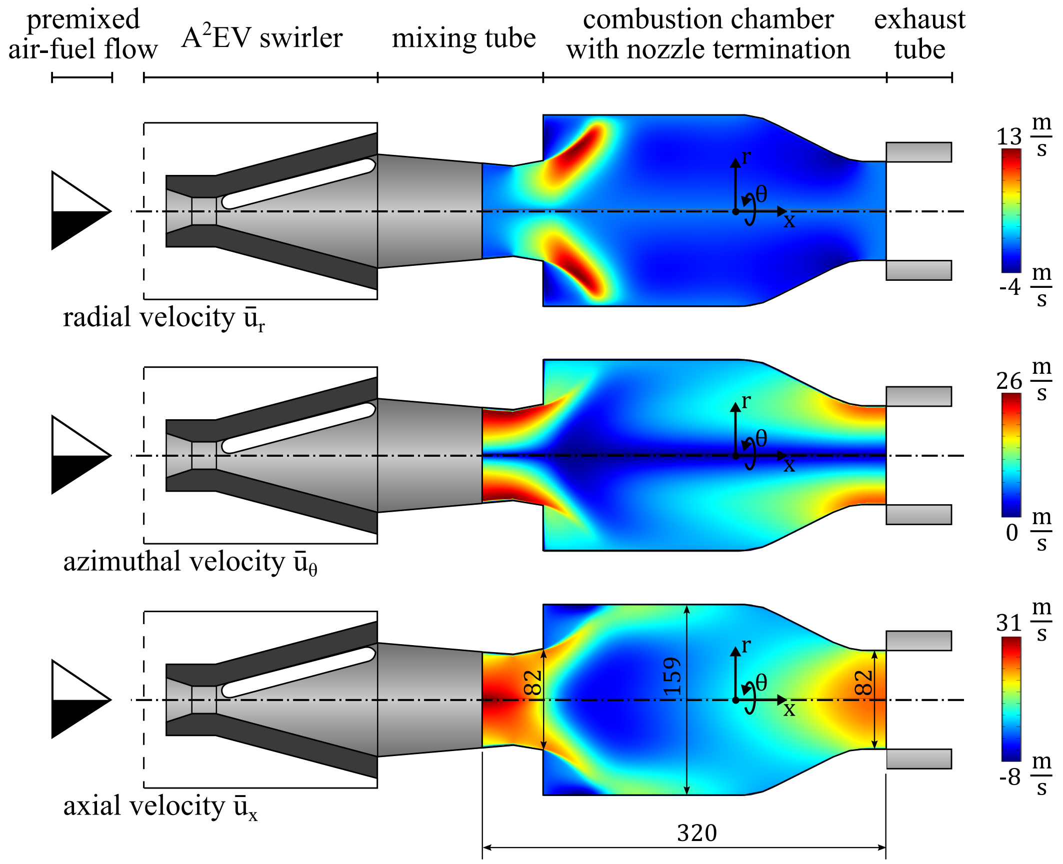

Figure A.2: *Schematic of the isothermal A^2EV swirl-stabilized test rig configuration with mean flow fields in the combustion chamber of (from top to bottom) radial, azimuthal and axial velocities.*

R_c decreases. The absence of combustion in this case is optimum for this analysis as thermoacoustic driving is precluded, i.e. $\beta = 0$. Additionally, baroclinic vorticity generation at density gradients (for details see Chapter 6 and Appendix C) is neglected. Hence, the acoustically triggered generation of hydrodynamic, convectively transported vortices and their subsequent interaction with the mean flow remain the sole mechanisms affecting the LEE growth rate. Remind that LNSE and LEE only differ by the absence of viscous losses in the latter, which implies that all findings presented in this appendix are also transferable to the LNSE.

The T1 eigenmode is the acoustic mode of interest in the study of this appendix. Figure A.3 presents the decomposed LEE disturbance fields, which are obtained by the velocity Helmholtz decomposition introduced in Section 4.3. Remember that this is possible due to the isothermal mean flow fields and the low Mach number in this combustor setup. The first column displays the superimposed LEE solution variables, i.e. pressure $\hat{p}$, radial $\hat{u}_{\mathrm{r}}$, azimuthal $\hat{u}_{\theta}$ and axial velocity $\hat{u}_{\mathrm{x}}$. The second and third columns show the corresponding decomposed acoustic and vortical fields, respectively.

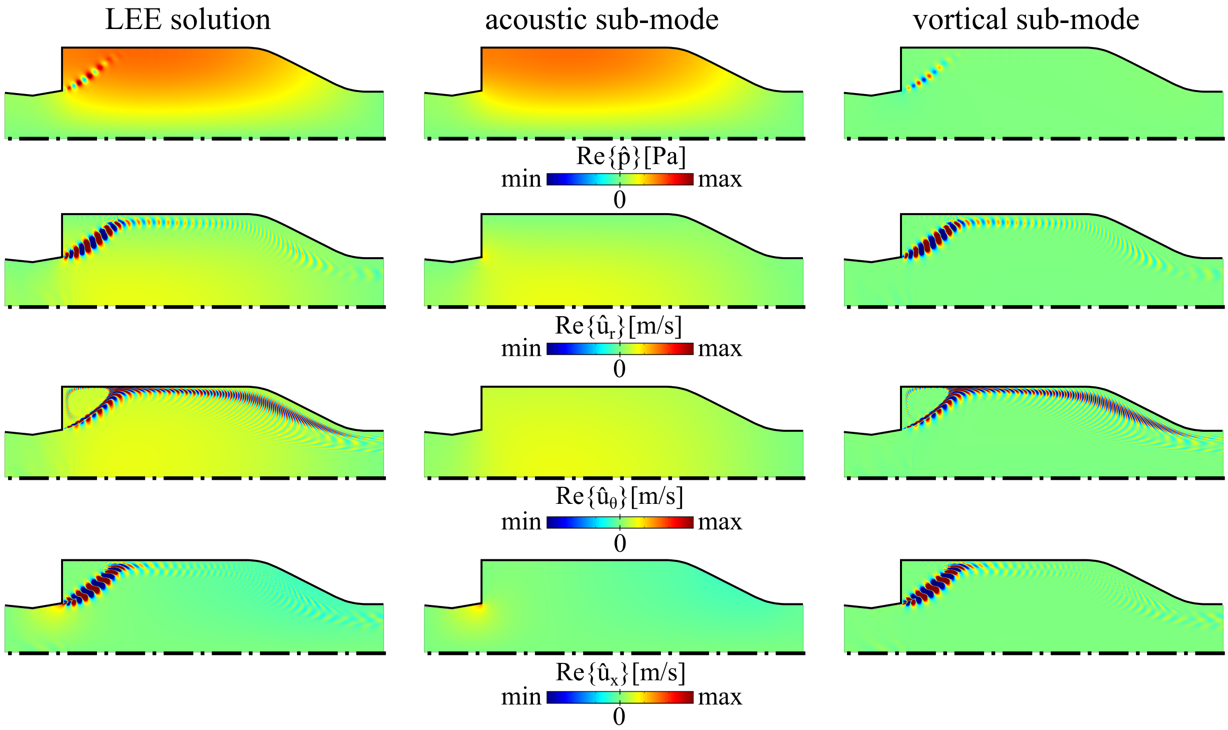

Figure A.3: *Results of the Helmholtz decomposition for the T1 eigenmode of the isothermal A² EV combustor configuration: pressure (first row) with radial (second row), azimuthal (third row) and axial (fourth row) velocity distributions for the original LEE solution (left) as well as decomposed acoustic (middle) and vortical (right) sub-modes.*

The damping rate results presented in Appendix A.3 correspond to the LEE eigenmode shapes displayed in Fig. A.3. These are computed with the two-dimensional numerical setup shown in Fig. A.4.

The close-up view displays the unstructured, triangular mesh in the vicinity of the area expansion. The maximum element size directly at the edge is constantly set to $\max(H) = 10^{-5}$m. The maximum element size of the remain-

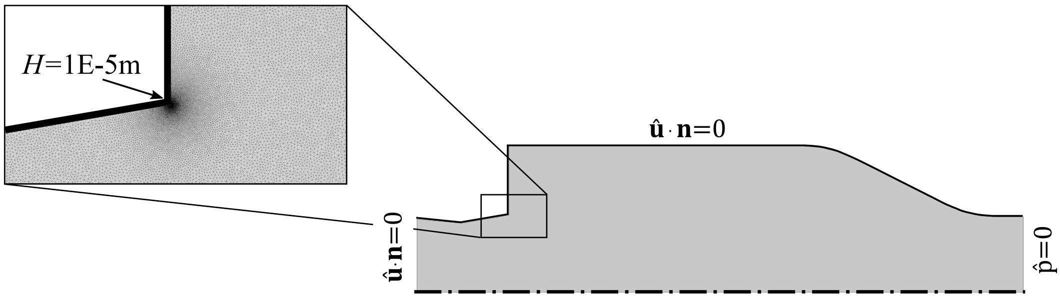

Figure A.4: *Computational domain with boundary conditions and inspection window showing the mesh in the vicinity of the area expansion.*

ing domain is varied in the range of $3 \cdot 10^{-4}\mathrm{m} \leq \max(H) \leq 10^{-3}\mathrm{m}$. The inlet is specified as a closed boundary condition, i.e. $\hat{\mathbf{u}} \cdot \mathbf{n} = 0$. In this case, the specification of the inlet boundary condition is of minor importance and does not influence the final results, which is ascribed to the evanescence of acoustic amplitudes towards a value close to zero at the inlet. Recall that this is caused by the the decreasing radius R_{c} at the chamber inlet, which increases the cut-on frequency $f^{\text{cut-on}}$ (cf. Eq. (2.46)). The outlet is characterized by a vanishing pressure, i.e. $\hat{p} = 0$. Due to the nozzle termination, the acoustic T1 mode shape decays towards a zero value at the outlet. However vortices can reach the outlet, which leads to a vortical energy density flux exiting the domain through it. Combustor walls are treated as slip walls, where $\hat{\mathbf{u}} \cdot \mathbf{n} = 0$.

A.2 Acoustic-Vortical Interactions in the Linearized Euler Equations

The LEE (and LNSE) capture linear interactions between mean flow quantities and an acoustic field including the acoustically triggered shedding of vortex perturbations as well[3]. As explained in Section 2.6, this phenomenon is caused by a shear-layer in the underlying, steady-state flow field. Its interaction with the acoustic field results in a transformation of acoustic into vortical momentum (see Fig. 2.2 d)) [66]. The conversion of momentum is connected to a shift of kinetic energy from the acoustic towards the vortical

[3]This section of the appendix seeks to provide more detailed information on the vortex shedding mechanism introduced in Section 2.6. Furthermore, it supports the discusion about the impact of the SUPG/PSPG stabilization scheme on acoustic and vortical sub-modes in Section 5.1.1.2.

perturbation mode. This involves a decrease of energy in the acoustic field and an energization of the vortical sub-mode. In turn, the generated vortices interact with the mean flow, which may damp or amplify acoustics. However, if the reduction of acoustic energy due to the vortex formation exceeds the potential excitation due to the subsequent mean flow-vortex coupling (vortex sound), a net damping of acoustic oscillating amplitudes results [66]. Concerning the linear stability of thermoacoustic systems, the generation and advection of vortex disturbances can thus counteract flame driving and may turn a thermoacoustic system into stable operation [37].

In order to identify this aeroacoustic interaction as part of the LEE, the momentum Eq. (2.28) is rewritten in an equivalent form by using the vector identity of Eq. (2.21). Combining the resulting equation with the decomposition approaches of Eqs. (2.19)-(2.20) and rearranging the terms yields the momentum equation

$$\begin{aligned} &\bar{\rho}\left[i\omega_{\mathrm{a}}\hat{\mathbf{u}}_{\mathrm{a}} + \nabla\left(\bar{\mathbf{u}}\cdot\hat{\mathbf{u}}_{\mathrm{a}}\right)\right] + \nabla\hat{p}_{\mathrm{a}} = \\ &-\bar{\rho}\,i\omega_{\mathrm{v}}\hat{\mathbf{u}}_{\mathrm{v}} - \bar{\rho}\nabla\left(\bar{\mathbf{u}}\cdot\hat{\mathbf{u}}_{\mathrm{v}}\right) - \nabla\hat{p}_{\mathrm{v}} - \left[\bar{\rho}\left(\hat{\boldsymbol{\Omega}}\times\bar{\mathbf{u}}\right) + \bar{\rho}\left(\bar{\boldsymbol{\Omega}}\times\hat{\mathbf{u}}_{\mathrm{v}}\right) + \bar{\rho}\left(\bar{\boldsymbol{\Omega}}\times\hat{\mathbf{u}}_{\mathrm{a}}\right)\right], \end{aligned} \tag{A.1}$$

where the term $(\hat{\rho}\bar{\mathbf{u}}\cdot\nabla\bar{\mathbf{u}})$ in Eq. (2.12) is neglected. This can be justified by the combination of its second order dependence on the mean flow velocity and the low Mach numbers in this combustor configuration, which results in a negligible small impact of this term on LEE eigensolutions (cf. Fig. 6.7 in Chapter 6). The l.h.s. of Eq. (A.1) is equal to the APE (2.30) and describes the propagation and evolution of the acoustic velocity in the presence of a mean flow [89]. The second term on the r.h.s. of Eq. (A.1) describes the irrotational transport by convection of incompressible vortex perturbations. The fourth and fifth terms capture interactions between existing vorticity perturbations and the mean flow, while the sixth term in Eq. (A.1) is the one responsible for the generation of convectively transported vortices. This can be shown by taking the curl of Eq. (A.1) and applying the vector identities $\nabla\times(\boldsymbol{\Omega}\times\mathbf{u}) = \boldsymbol{\Omega}\nabla\cdot\mathbf{u} + \mathbf{u}\nabla\cdot\boldsymbol{\Omega} + (\mathbf{u}\cdot\nabla)\boldsymbol{\Omega} - (\boldsymbol{\Omega}\cdot\nabla)\mathbf{u}$ with $\nabla\cdot\boldsymbol{\Omega} = \nabla\cdot(\nabla\times\mathbf{u}) = \mathbf{0}$ and $\nabla\times\nabla(\ldots) = \mathbf{0}$. For isothermal conditions[4], the following vorticity transport equation is obtained

$$\begin{aligned}\bar{\rho}\big[i\omega\hat{\mathbf{\Omega}} + \overbrace{(\bar{\mathbf{u}}\cdot\nabla)\hat{\mathbf{\Omega}} - \big(\hat{\mathbf{\Omega}}\cdot\nabla\big)\bar{\mathbf{u}}}^{=\nabla\times(\hat{\mathbf{\Omega}}\times\bar{\mathbf{u}})} + \overbrace{(\hat{\mathbf{u}}_{\mathrm{v}}\cdot\nabla)\bar{\mathbf{\Omega}} - \big(\bar{\mathbf{\Omega}}\cdot\nabla\big)\hat{\mathbf{u}}_{\mathrm{v}}}^{=\nabla\times(\bar{\mathbf{\Omega}}\times\hat{\mathbf{u}}_{\mathrm{v}})} + \ldots \\ \ldots + \underbrace{\bar{\mathbf{\Omega}}\nabla\cdot\hat{\mathbf{u}}_{\mathrm{a}} + (\hat{\mathbf{u}}_{\mathrm{a}}\cdot\nabla)\bar{\mathbf{\Omega}} - \big(\bar{\mathbf{\Omega}}\cdot\nabla\big)\hat{\mathbf{u}}_{\mathrm{a}}}_{=\nabla\times(\bar{\mathbf{\Omega}}\times\hat{\mathbf{u}}_{\mathrm{a}})}\big] = \mathbf{0}.\end{aligned} \tag{A.2}$$

Notice that irrotationality of the acoustic velocity field ($\nabla\times\hat{\mathbf{u}}_{\mathrm{a}} = \hat{\mathbf{\Omega}}_{\mathrm{a}} \approx \mathbf{0}$) is assumed, which is valid for isothermal and low Mach number cases as explained in Section 4.3. Furthermore, incompressibility of the isothermal mean flow field, i.e. $\nabla\cdot\bar{\mathbf{u}} = 0$, and of convectively transported vortical velocity disturbances (see Eq. (4.15)) was exploited to obtain Eq. (A.2). The vorticity Eq. (A.2) reveals that the cross-product term ($\bar{\mathbf{\Omega}}\times\hat{\mathbf{u}}_{\mathrm{a}}$) in the decomposed LEE momentum Eq. (A.1) interconnects the mean vorticity field with the acoustic sub-mode. It is responsible for the generation of convectively transported vortices trough dilatational $\bar{\mathbf{\Omega}}\nabla\cdot\hat{\mathbf{u}}_{\mathrm{a}}$, convective $(\hat{\mathbf{u}}_{\mathrm{a}}\cdot\nabla)\bar{\mathbf{\Omega}}$ and stretching/bending $(\bar{\mathbf{\Omega}}\cdot\nabla)\hat{\mathbf{u}}_{\mathrm{a}}$ effects [17]. In Section 2.6 it is shown that these mechanisms are the strongest directly downstream of the sharp corner at the combustion chamber inlet, which explains the location of vortex generation in Fig. A.3.

The amount of acoustic energy transformed into vortical energy can indirectly be quantified by evaluating the force which shed vortices exert on the acoustic velocity field. In order to quantify this energy transformation process in terms of a damping rate, the growth rate Eq. (4.7) with Eqs. (2.37)-(2.40) can be used. For isothermal and homentropic mean flow conditions, the decomposed relations for E, $\mathbf{I}$ and D read ($Q = 0$ as combustion is absent):

$$E = \frac{\big(\hat{p}_{\mathrm{a}} + \hat{p}_{\mathrm{v}}\big)^2}{2\bar{\rho}} + \frac{\bar{\rho}\,(\hat{\mathbf{u}}_{\mathrm{a}} + \hat{\mathbf{u}}_{\mathrm{v}})^2}{2} + \big(\hat{\rho}_{\mathrm{a}} + \hat{\rho}_{\mathrm{v}}\big)\,\bar{\mathbf{u}}\cdot(\hat{\mathbf{u}}_{\mathrm{a}} + \hat{\mathbf{u}}_{\mathrm{v}})\,, \tag{A.3}$$

$$\mathbf{I} = \Big[\frac{\hat{p}_{\mathrm{a}} + \hat{p}_{\mathrm{v}}}{\bar{\rho}} + (\hat{\mathbf{u}}_{\mathrm{a}} + \hat{\mathbf{u}}_{\mathrm{v}})\cdot\bar{\mathbf{u}}\Big]\big[\bar{\rho}\,(\hat{\mathbf{u}}_{\mathrm{a}} + \hat{\mathbf{u}}_{\mathrm{v}}) + \big(\hat{\rho}_{\mathrm{a}} + \hat{\rho}_{\mathrm{v}}\big)\,\bar{\mathbf{u}}\big], \tag{A.4}$$

$$D = \bar{\rho}\big[\underbrace{\big(\bar{\mathbf{\Omega}}\times(\hat{\mathbf{u}}_{\mathrm{a}} + \hat{\mathbf{u}}_{\mathrm{v}})\big)\cdot(\hat{\mathbf{u}}_{\mathrm{a}} + \hat{\mathbf{u}}_{\mathrm{v}})}_{=0} + \big(\hat{\mathbf{\Omega}}\times\bar{\mathbf{u}}\big)\cdot(\hat{\mathbf{u}}_{\mathrm{a}} + \hat{\mathbf{u}}_{\mathrm{v}})\big]. \tag{A.5}$$

In Eq. (A.5), terms of second order dependence on the mean flow velocity (i.e. $\hat{\rho}\bar{\mathbf{u}}\cdot\nabla\bar{\mathbf{u}} = \mathcal{O}(\mathrm{M}^2)$) are neglected again due to the low Mach number

[4]For reactive conditions with temperature gradients, a baroclinic vorticity source term appears. This is discussed in more detail in Chapter 6.

assumption.

In the following, the impact of each term in Eqs. (A.4)-(A.5) (starting with Eq. (A.5)) on the net growth rate ν is discussed and the corresponding pure acoustic contribution is extracted. In the subsequent Appendix A.3, the acoustic, net damping rates are computed and compared to the ones obtained by solving the eigenvalue problem of Eq. (4.1) with the LEE. Finally, it is shown that the latter approach is able to reproduce the pure acoustic part as well, although the eigensolutions contain the contribution of the convectively transported, vortical sub-mode.

The first term in the dissipation Eq. (A.5) captures the vortex generation process. The contribution of this term to the net dissipation D vanishes identically per definition due to the vector identity $(\mathbf{\Omega} \times \mathbf{u}) \cdot \mathbf{u} = 0$. Mathematically, this occurs as the cross product $(\mathbf{\Omega} \times \mathbf{u})$ gives a vector which is perpendicular to $\mathbf{\Omega}$ and $\mathbf{u}$. Thus, the vortex generation process does not influence the LEE net growth rate ν, as the corresponding damping rate $\alpha_{\mathrm{D}_{\Omega},1}$ gives a zero value:

$$\alpha_{\mathrm{D}_{\Omega},1} = \frac{1}{2} \frac{-\int_V \bar{\rho} \langle \left(\bar{\mathbf{\Omega}} \times (\hat{\mathbf{u}}_{\mathrm{a}} + \hat{\mathbf{u}}_{\mathrm{v}}) \right) \cdot (\hat{\mathbf{u}}_{\mathrm{a}} + \hat{\mathbf{u}}_{\mathrm{v}}) \rangle \mathrm{d}V}{\int_V \langle E \rangle \mathrm{d}V} = 0. \tag{A.6}$$

This infers that the vortex generation process represents an energy conserving transformation process as the work performed by the shed vortices in the acoustic field is equal to the work performed by the acoustic field to generate the vortices. Notice that this confirms the hypothesis stated in the dissertation of Hummel [37]. Expanding the numerator of Eq. (A.6) to

$$\left(\bar{\mathbf{\Omega}} \times \hat{\mathbf{u}}_{\mathrm{v}} \right) \cdot \hat{\mathbf{u}}_{\mathrm{a}} + \left(\bar{\mathbf{\Omega}} \times \hat{\mathbf{u}}_{\mathrm{a}} \right) \cdot \hat{\mathbf{u}}_{\mathrm{v}} = 0, \tag{A.7}$$

where $\left(\bar{\mathbf{\Omega}} \times \hat{\mathbf{u}}_{\mathrm{a}} \right) \cdot \hat{\mathbf{u}}_{\mathrm{a}} = \left(\bar{\mathbf{\Omega}} \times \hat{\mathbf{u}}_{\mathrm{v}} \right) \cdot \hat{\mathbf{u}}_{\mathrm{v}} = 0$ is already considered, shows that the interaction between mean vorticity and acoustic velocity field (second term in Eq. (A.7)), which provokes the shedding of vortex perturbations, performs work in the vortical velocity disturbance field $\hat{\mathbf{u}}_{\mathrm{v}}$. This amplification of the vortical, convectively transported sub-mode is compensated by the work of the interaction between mean vorticity and the instantaneously generated rotational velocity disturbances (first term in Eq. (A.7)) performed in the acoustic field. In other words, this means that the energization of the vortical sub-mode is achieved on the expense of the acoustic perturbation field, while the total energy is conserved. The damping rate associated with the dissipation of acoustics caused by vortex generation $\alpha_{\mathrm{D}_{\Omega},1,\mathrm{a}}$ can thus be determined via the first term of Eq. (A.7), while the acoustic part of the disturbance energy density

$$E_{\mathrm{a}} = \frac{\hat{p}_{\mathrm{a}}^2}{2\bar{\rho}\bar{c}^2} + \bar{\rho}\frac{\hat{\mathbf{u}}_{\mathrm{a}}^2}{2} + \hat{\rho}_{\mathrm{a}}\left(\bar{\mathbf{u}}\cdot\hat{\mathbf{u}}_{\mathrm{a}}\right) \tag{A.8}$$

is considered only. The desired acoustic dissipation term appears in Eq. (A.6) after having removed the term $\left(\bar{\mathbf{\Omega}}\times\hat{\mathbf{u}}_{\mathrm{a}}\right)\cdot\hat{\mathbf{u}}_{\mathrm{v}}$ in the integral of the numerator:

$$\alpha_{\mathrm{D}_{\Omega},1,\mathrm{a}} = \frac{1}{2}\frac{-\int_V \bar{\rho}\langle\left(\bar{\mathbf{\Omega}}\times\hat{\mathbf{u}}_{\mathrm{v}}\right)\cdot\hat{\mathbf{u}}_{\mathrm{a}}\rangle \mathrm{d}V}{\int_V\langle E_{\mathrm{a}}\rangle\mathrm{d}V} \tag{A.9}$$

The second term in the dissipation Eq. (A.5) describes the interaction of the generated disturbance vorticity $\hat{\mathbf{\Omega}}$ with the mean flow. In contrast to the LEE damping rate $\alpha_{\mathrm{D}_{\Omega},1}$ of the vortex generation process (cf. Eq. (A.6)), the LEE growth rate associated with this term takes generally non-zero values and thus changes the energetic state of both, acoustic and vortical sub-modes:

$$\alpha_{\mathrm{D}_{\Omega},2} = \frac{1}{2}\frac{-\int_V \bar{\rho}\langle\left(\hat{\mathbf{\Omega}}\times\bar{\mathbf{u}}\right)\cdot(\hat{\mathbf{u}}_{\mathrm{a}}+\hat{\mathbf{u}}_{\mathrm{v}})\rangle \mathrm{d}V}{\int_V\langle E_{\mathrm{a}}\rangle\mathrm{d}V} = \alpha_{\mathrm{D}_{\Omega},2,\mathrm{a}} + \alpha_{\mathrm{D}_{\Omega},2,\mathrm{v}} \neq 0. \tag{A.10}$$

Hence, the term $(\hat{\mathbf{\Omega}}\times\bar{\mathbf{u}})$ does not describe an energy conserving transformation process. It can be interpreted as a source or sink of acoustic and vortical energy, which originates from the coupling of the generated vortices with the steady bulk flow. Physically, this term represents a force, which can both, increase (energy supply) or decrease (energy reduction) the acoustic $\hat{\mathbf{u}}_{\mathrm{a}}$ as well as the rotational velocity field $\hat{\mathbf{u}}_{\mathrm{v}}$. The impact of this term on the acoustic stability in terms of the acoustic damping rate $\alpha_{\mathrm{D}_{\Omega},2,\mathrm{a}}$ can be determined by only considering the acoustic part of Eq. (A.10), i.e.

$$\alpha_{\mathrm{D}_{\Omega},2,\mathrm{a}} = \frac{1}{2}\frac{-\int_V \bar{\rho}\langle\left(\hat{\mathbf{\Omega}}\times\bar{\mathbf{u}}\right)\cdot\hat{\mathbf{u}}_{\mathrm{a}}\rangle \mathrm{d}V}{\int_V\langle E_{\mathrm{a}}\rangle\mathrm{d}V}. \tag{A.11}$$

The conclusions and findings are summarized in the following:

- From a theoretical point of view, the LEE growth rate does not provide the pure acoustic damping rate. Instead, it describes the stability behavior of acoustic and vortical sub-modes in a superimposed manner. Specifically, the LEE growth rate consists of an acoustic and a vortical contribution, which are both associated with the coupling of vorticity perturbations with the mean flow:

$$\alpha_{\mathrm{D}} = \alpha_{\mathrm{D}_{\mathbf{\Omega}},1} + \alpha_{\mathrm{D}_{\mathbf{\Omega}},2} = 0 + (\alpha_{\mathrm{D}_{\mathbf{\Omega}},2,\mathrm{a}} + \alpha_{\mathrm{D}_{\mathbf{\Omega}},2,\mathrm{v}}). \tag{A.12}$$

- The generation of convectively transported vortices through the interaction of the acoustic velocity field with the mean vorticity field represents an energy conserving transformation process. This mechanism has a zero contribution to the stability of a LEE system since $\alpha_{\mathrm{D}_{\mathbf{\Omega}},1} = 0$.
- The acoustic growth rate of the LEE system associated with dissipation inside the concerned volume is obtained by combining Eqs. (A.9) and (A.11), i.e.

$$\alpha_{\mathrm{D}_{\mathbf{\Omega}},\mathrm{a}} = \alpha_{\mathrm{D}_{\mathbf{\Omega}},1,\mathrm{a}} + \alpha_{\mathrm{D}_{\mathbf{\Omega}},2,\mathrm{a}}. \tag{A.13}$$

  The sum of the argument of the numerator in Eqs. (A.9) and (A.11), i.e. $D_{\mathrm{a}} = \bar{\rho}\langle(\bar{\mathbf{\Omega}} \times \hat{\mathbf{u}}_{\mathrm{v}}) \cdot \hat{\mathbf{u}}_{\mathrm{a}} + (\hat{\mathbf{\Omega}} \times \bar{\mathbf{u}}) \cdot \hat{\mathbf{u}}_{\mathrm{a}}\rangle$, is similar to the formulation derived by Howe [66]. Thus, Howe's energy expression can be seen as a special case of Myer's general formulation for disturbance energy [94], which only accounts for the dissipation of the acoustic sub-mode.

Finally, keep in mind that these findings are not only valid for the LEE but are also transferable to the LNSE as the cross-product terms ($\bar{\mathbf{\Omega}} \times \hat{\mathbf{u}}$) and ($\hat{\mathbf{\Omega}} \times \bar{\mathbf{u}}$) are present in both systems of equations.

Up to now, only the contribution of the dissipation term D given by Eq. (A.5) to the stability of a LEE system was investigated. To complete the energetic analysis, the growth rate $\nu_{\mathbf{I}}$ in Eq. (4.7) associated with intensity fluxes crossing in- and outlet, is accounted for. First, the acoustic intensity flux $\mathbf{I}_{\mathrm{a}}$ is discussed, which consists only of products of acoustic quantities in Eq. (A.4). As explained in Section 2.4.1, the specification of energetically neutral in- and outlet boundaries would prevent any acoustic energy fluxes entering or leaving the domain. In this case, the associated growth rate yields $\nu_{\mathbf{I},\mathrm{a}} = 0$. However, recall that this special type of impedance boundary condition is only applicable for acoustic oscillations but not for convectively transported disturbances. The nozzle termination of the isothermal A^2EV configuration provokes yet a similar energetic decoupling effect of the acoustic sub-mode from the outlet. It results in the attenuation of high-frequency modes towards zero acoustic pressure and velocity amplitudes at the outlet. This appears due to the decreasing chamber diameter and ultimately due to the increasing cut-on frequency. In consequence, an open outlet boundary condition can be specified as the acoustic intensity flux is unaffected anyway. This allows the convectively transported vortices to escape through the outlet. In consequence, all the vortical energy generated inside the domain vanishes through the outlet boundary. Then, the energy balance for convectively transported vorticity perturbation reads

$$\int_S \mathbf{I}_\mathrm{v} \cdot \mathbf{n} dS = -\int_V D_\mathrm{v} dV. \tag{A.14}$$

The net LEE growth rate ν given by Eq. (4.7) can finally be decomposed into:

$$\nu = \underbrace{\nu_{\mathbf{I},\mathrm{a}}}_{=0} + \underbrace{\nu_{\mathbf{I},\mathrm{v}} + \alpha_{\mathrm{D,v}}}_{=0} + \alpha_{\mathrm{D,a}} = \alpha_\mathrm{a} = \nu_\mathrm{a}. \tag{A.15}$$

Equation (A.15) implies that LEE growth rates obtained by directly solving the eigenvalue problem of Eq. (4.1) can indeed provide the desired acoustic damping rate required for a thermoacoustic stability analysis. The complete evolution of the energy transfer between acoustic and vortical sub-modes is illustrated in Fig. A.5.

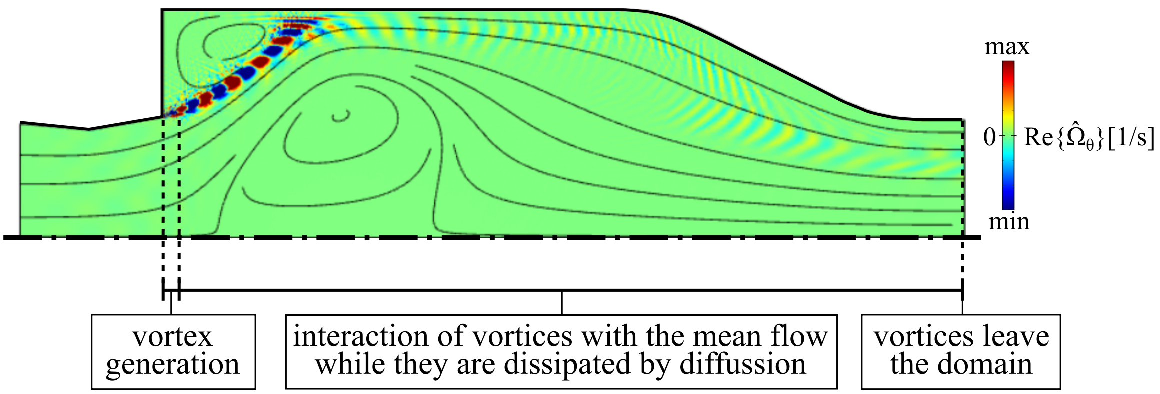

Figure A.5: *Evolution of vortex disturbances.*

One factor, which has not been considered in this study, is the impact of numerical stabilization schemes (subscript "*stab*") on acoustic and vortical sub-modes. Artificial diffusion can adopt a role similar as the open outlet, if it provokes the complete dissipation of the convectively transported vortices before they reach the outlet, while the acoustic intensity flux is (nearly) not affected. Again, only the pure acoustic damping rate would be represented by the LEE net growth rate[5]; however, falsified by a part $\nu_{\mathrm{stab,a}}$ associated with the stabilization scheme:

$$\nu = \underbrace{\nu_{\mathbf{I},\mathrm{a}}}_{=0} + \underbrace{\nu_{\mathbf{I},\mathrm{v}}}_{=0} + \underbrace{\alpha_{\mathrm{D}\Omega,\mathrm{v}} + \nu_{\mathrm{stab,v}}}_{=0} + \nu_{\mathrm{stab,a}} + \alpha_{\mathrm{D}\Omega,\mathrm{a}} = \nu_{\mathrm{a}}. \tag{A.16}$$

Investigations on the impact of numerical stabilization on acoustic and vortical sub-modes are subject of Section 5.1.1 in the main part of this thesis. There, it is revealed that the convectively transported vortices are completely dissipated by diffusive mechanisms before they reach the outlet (cf. Fig. 5.3.). In consequence, the evolution of the acoustic sub-mode remains the sole contribution in the LEE net growth rate, i.e. $\nu = \nu_{\mathrm{a}}$.

A.3 Results: Comparison of LEE Growth Rates

In this section, the pure acoustic damping rates $\alpha_{\mathrm{D}\Omega,\mathrm{a}}$ calculated via Eq. (A.13) are compared with the ones obtained by numerically solving the eigenvalue problem of Eq. (4.1) with the LEE. An agreement of these two rates, i.e. $\alpha_{\mathrm{D}\Omega,\mathrm{a}} = \nu$, legitimates the utilization of LEE growth rates for a thermoacoustic stability assessment.

Figure A.6 summarizes the computed growth rate results of the target eigenmode, which is the T1 mode in this study, in terms of a grid convergence study (increasing mesh element number from left to right). Additionally, the α_τ-sweep reveals the impact of the SUPG/PSPG stabilization scheme on the results for the three mesh configurations. The change of the acoustic damping rate $\alpha_{\mathrm{D}\Omega,\mathrm{a}}$ with mesh resolution and stabilization parameter is used to judge convergence of the solution. With reference to Fig. A.6, convergence is assumed to be reached for values of $\alpha_\tau \geq 15$ independent of the mesh configuration. This was found to be justifiable as the relative deviation is less than $\approx \pm 1\,\mathrm{rad/s}$ with respect to the mean LEE growth rate value in between $15 \leq \alpha_\tau \leq 50$ (cf. the black dashed lines in Fig. A.6). Notice that these results correspond to the in-swirl direction rotating T1 mode.

[5]Notice that this is also valid for the LNSE.

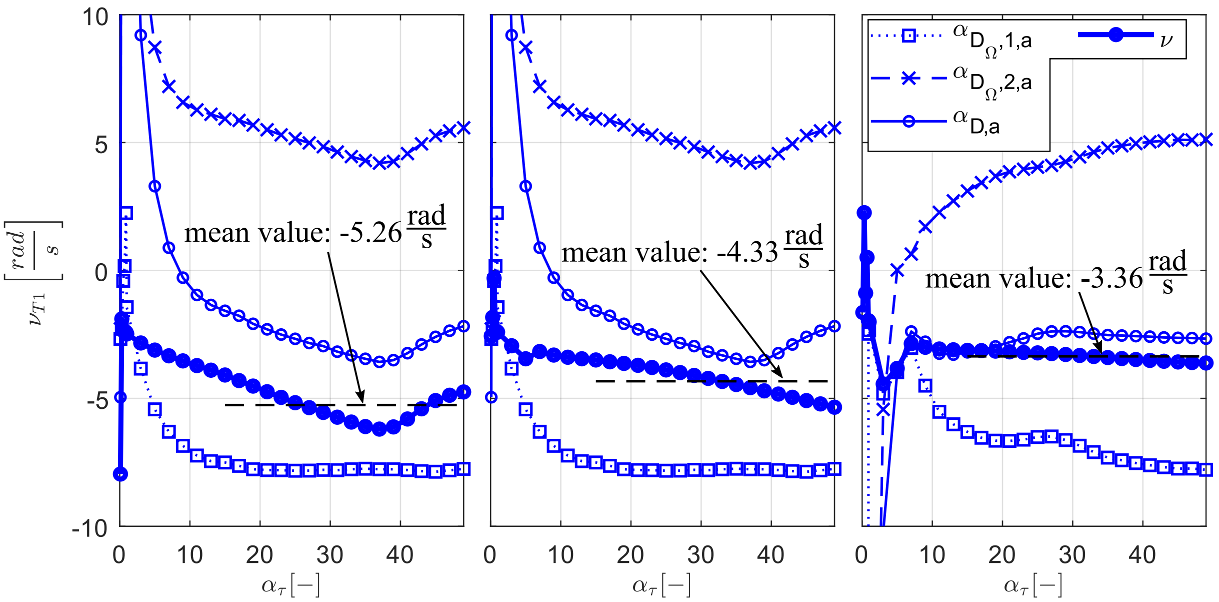

Figure A.6: *Computed T1 growth rates for maximum mesh element sizes of 1E-3m (left), 5E-4m (middle) and 3E-4m (right) in the range of* $0 \leq \alpha_\tau \leq 50$. *Squares and crosses show the acoustic damping rates associated with the vortex generation process and the interaction of vortices with the bulk flow,* $\alpha_{D_\Omega,1,a}$ *and* $\alpha_{D_\Omega,2,a}$ *respectively. The open circles represent the acoustic damping rate* $\alpha_{D,a} = \alpha_{D_\Omega,1,a} + \alpha_{D_\Omega,2,a}$. *The filled circles are the damping rates computed by solving the eigenvalue problem of Eq.* (4.1).

In Fig. A.6, the open circles represent the pure acoustic damping rates $\alpha_{\mathrm{D}_\Omega,\mathrm{a}}$ of the LEE system. These are obtained by evaluating Eq. (A.13) with the decomposed T1 eigenmode shapes of Fig. A.3 at the predefined mesh and tuning parameter configurations. This damping rate is composed of the contributions of the vortex generation process (squares) and the subsequent interaction of the shed vortices with the mean flow (crosses), i.e. $\alpha_{\mathrm{D}_\Omega,1,\mathrm{a}}$ (cf. Eq. (A.9)) and $\alpha_{\mathrm{D}_\Omega,2,\mathrm{a}}$ (cf. Eq. (A.11)), respectively. The former mechanism reveals negative damping rate values indicating that acoustic energy is reduced/consumed to generate the vortices. On the contrary, the latter contribution shows positive damping rates, which implies a supply of acoustic energy due to the vortex-mean flow coupling. The sum of squares and crosses in the plots of Fig. A.6 yields the line with the open circles. Thus, this line represents the pure acoustic damping rate $\alpha_{\mathrm{D}_\Omega,\mathrm{a}} = \alpha_{\mathrm{D}_\Omega,1,\mathrm{a}} + \alpha_{\mathrm{D}_\Omega,2,\mathrm{a}} = \nu_\mathrm{a}$. Remind that the acoustic energy density fluxes through in- and outlet are zero. The filled circles show the growth rates, which are obtained by directly solving the eigenvalue problem of Eq. (4.1) with the LEE. Both, acoustic damping rate and LEE growth rates take positive values in the converged range indicating that the eigenmode is acoustically stable.

The good match of acoustic damping rates with the directly obtained LEE growth rates shows that eigenfrequency analyses with the LEE (and LNSE) do reflect the stability of the acoustic sub-mode only. The implicit impact of the vortical sub-mode on the directly obtained LEE growth rates is thus either compensated by the outlet boundary condition, which allows the vortices to leave the domain but prohibits acoustic intensity fluxes to cross it, or/and by the dissipation of the vortices by (numerical) diffusion. In conclusion, the acoustic growth rate part remains the sole contribution in the LEE growth rates of this study. This shows that the LNSE and LEE are thus suitable systems of equations to assess the thermoacoustic stability of the acoustic eigenmodes of interest.

The deviation between open and filled circles can be explained by the presence of the SUPG/PSPG artificial diffusion scheme acting on the acoustic sub-mode: In the LEE growth rates ν (closed circles), the impact of numerical stabilization is inherently included. This effect is absent in the acoustic damping rates $\alpha_{\mathrm{D}_\Omega,\mathrm{a}}$ obtained by the growth rate Eq. (4.6). The incorporation of acoustic damping caused by (artificial) diffusion in this post-processing analysis is not straightforward and has not yet been achieved. In conclusion, the lower LEE growth rate values can be related to a numerical damping contribution, which falsifies the physically correct result. Figure A.6 reveals that this error reduces for an increasing mesh resolution. Notice that the impact of the numerical stabilization scheme can be eliminated in the LEE growth rates by applying the correction method proposed in Section 5.1.1.3.

B Bloch-Wave Theory for Thermoacoustic Systems

This appendix provides information on how to implement pseudo-periodic boundary conditions in systems with rotational symmetry and highlights difficulties arising in the presence of vortices. Additionally, this appendix presents a workaround for the vortex-problem in systems with continuous rotational symmetry which leads to Eq. (2.47) introduced in Section 2.4.2 of the main part of this thesis.

Combustion chambers often exhibit discrete periodicity in circumferential direction. Then, the so called *Bloch-wave* theory can be employed to represent acoustic modes, which significantly reduces the computational effort not only in the frequency [135], but also in the time domain [136]. Specifically, the computational domain can be decreased to one unit cell, i.e. $1/N$ of the entire domain, where N is the degree of rotational symmetry of the system. According to the *Bloch-wave* theory [137], the acoustic mode shape of the solution variables $\hat{\boldsymbol{\phi}}_{\mathrm{a}}$ can be expressed as

$$\hat{\boldsymbol{\phi}}_{\mathrm{a}}(r,\theta,x,\omega) = \hat{\boldsymbol{\phi}}_{\mathrm{a,N}}(r,\theta,x,\omega)\, e^{ib\theta}, \tag{B.1}$$

where r, θ and x denote radial, azimuthal and axial coordinate direction, respectively. The first multiplicator $\hat{\boldsymbol{\phi}}_{\mathrm{a,N}}$ in Eq. (B.1) hosts information on the acoustic amplitude distribution in the N repeating sectors. It is identical in each of them and continuous between interfaces, i.e.

$$\hat{\boldsymbol{\phi}}_{\mathrm{a,N}}\left(r,\theta_{\mathrm{ref,N}} - \frac{\pi}{N}, x,\omega\right) = \hat{\boldsymbol{\phi}}_{\mathrm{a,N}}\left(r,\theta_{\mathrm{ref,N}} + \frac{\pi}{N}, x,\omega\right). \tag{B.2}$$

$\theta_{\mathrm{ref,N}}$ is the azimuthal reference angle associated with the bisector plane of each of the N unit cells. The second multiplicator in Eq. (B.1) defines the complex phase in circumferential direction and thus, describes the azimuthal variability of $\hat{\boldsymbol{\phi}}_{\mathrm{a,N}}$ with $|b|$ as the azimuthal mode order. If the unit cell exhibits reflectional symmetry, the sign of b only specifies the direction of rotation of azimuthal acoustic modes. These modes are also known as degenerate modes [58, 138]. If $b = 0$, any circumferential variability is precluded, which only allows longitudinal or radial mode shape solutions. If N is an even number and $b = N/2$, so-called *push-pull* modes occur, which exhibit alternating signs in adjacent sectors [138].

In summary, Eqs. (B.1) and (B.2) allow the reconstruction of the acoustic amplitude distribution in the full domain via mapping the amplitude solution of one sector to the others, while adapting its complex phase according to the Bloch-number. This implies restricting computations to only one unit cell, which results in the desired reduction of the computational domain by the factor $1/N$. Therefore, the interfaces to the adjacent sectors need to be defined by boundary conditions. Specifically, inserting Eq. (B.1) into Eq. (B.2) interconnects both interfaces of one representative sector by the pseudo-periodic boundary condition

$$\hat{\boldsymbol{\phi}}_{\mathrm{a}}\left(r,\theta_{\mathrm{ref}}+\frac{\pi}{N},x,\omega\right)=\hat{\boldsymbol{\phi}}_{\mathrm{a}}\left(r,\theta_{\mathrm{ref}}-\frac{\pi}{N},x,\omega\right)e^{-ib\frac{2\pi}{N}}. \tag{B.3}$$

Figure B.1 a) shows the T1 pressure distribution in a cross-section of the A^2EV combustor. As an example, the combustion chamber is split into $N = 8$ identical sectors. Instead of solving the full domain, the simulation can be restricted to the highlighted sector marked by the bisector θ_{ref}. The plane view of the cross section in Fig. B.1 b) shows the pseudo-periodic boundary conditions of Eq. (B.3) to couple the interfaces at $\theta = \theta_{\mathrm{ref}} + \frac{\pi}{N}$ and $\theta = \theta_{\mathrm{ref}} - \frac{\pi}{N}$.

The Bloch-wave theory only applies to (purely) acoustic modes (subscript a in all former equations of this section). As indicated by the vortices in Fig. B.1 b), convectively transported, hydrodynamic vortex perturbations (subscript v) occurring in LEE or LNSE solutions cannot be described physically correct by the pseudo-periodic Bloch boundary condition given by Eq. (B.3). For instance, in a case without swirling mean flow, the interfaces would need to be defined as symmetry boundary condition, instead of a pseudo-periodic one. However, the definition of interface boundary conditions, which act separately on acoustic and vortical perturbations is not straightforward. This can be circumvent by directly inserting the Bloch-wave function (B.1) into the governing equations and computing $\hat{\boldsymbol{\phi}}_{\mathrm{a,N}}(r,\theta,x,\omega)$ at $\theta = \theta_{\mathrm{ref}}$ instead of prescrib-

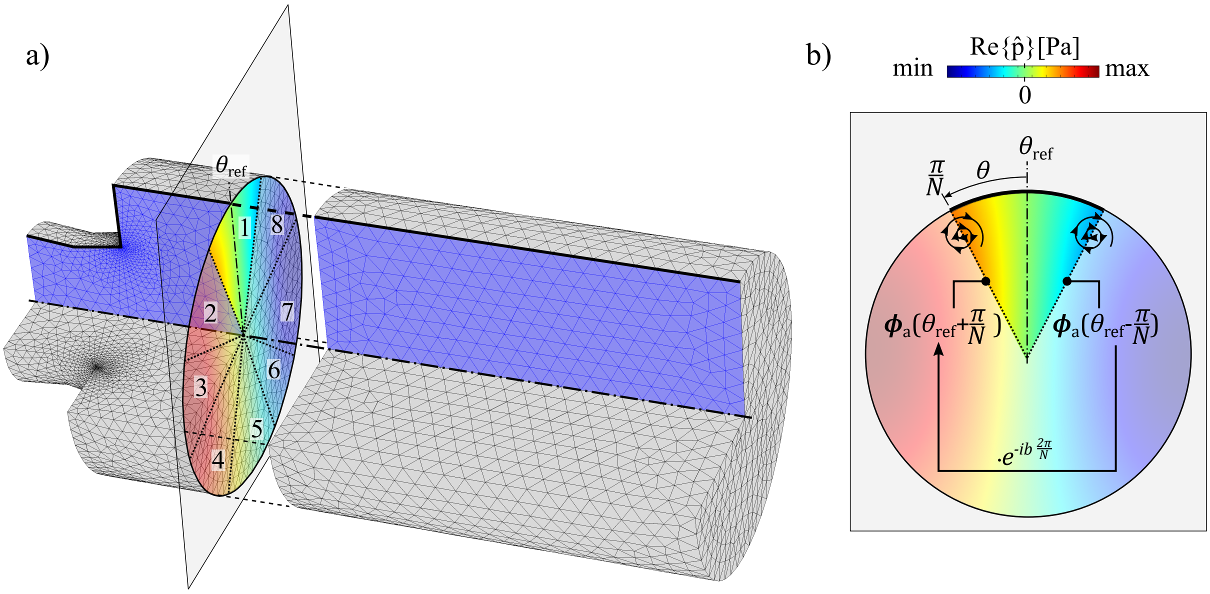

Figure B.1: *a) Separation of the A^2EV combustor into eight unit cells; b) pseudo-periodic boundary conditions for transversal acoustic modes.*

ing circumferential periodicity via the pseudo-periodic boundary condition of Eq. (B.3). However, this is only possible if the geometry of interest together with all the corresponding mean flow quantities exhibit continuous rotational symmetry. Then, $N \rightarrow \infty$, which reduces the three-dimensional problem to a two-dimensional one at the θ_{ref}-plane, as illustrated by the blue plane in Fig. B.1 a). In this case, solution variables of the LNSE/LEE/APE can be written as

$$\hat{\boldsymbol{\phi}}(r,\theta,x)\Big|_{\theta_{\text{ref}}} = \hat{\boldsymbol{\phi}}(r,x)\, e^{ib\theta}\Big|_{\theta_{\text{ref}}}. \tag{B.4}$$

Consequently, spatial derivatives of solution variables in azimuthal direction become

$$\frac{\partial\hat{\boldsymbol{\phi}}(r,\theta,x)}{\partial\theta}\Bigg|_{\theta_{\text{ref}}} = ib\,\hat{\boldsymbol{\phi}}(r,x)\, e^{ib\theta}\Bigg|_{\theta_{\text{ref}}}. \tag{B.5}$$

Equation (B.4) (with Eq. (B.5)) is the equation presented in Section 2.4.2.

C Details on the Helmholtz Decomposition

This appendix seeks to provide details on the Helmholtz decomposition of LNSE/LEE solution fields introduced in Section 4.3.

C.1 Comparison between Mass Flow and Velocity Helmholtz Decomposition

In Section 4.3, the disturbance velocity $\hat{\mathbf{u}}$ is identified to be an inappropriate quantity to decompose LNSE/LEE mode shapes of reacting mean flow fields into acoustic and vortical sub-modes via the Helmholtz decomposition. This appears as the underlying acoustic velocity field $\hat{\mathbf{u}}_\mathrm{a}$ is not irrotational, which will be shown in the following: For demonstrative purposes, it is assumed that $\bar{\mathbf{u}} = \mathbf{0}$. As a result, the isentropic LEE momentum Eq. (2.28) simplifies to

$$\bar{\rho} i\omega \hat{\mathbf{u}} + \nabla \hat{p} = \bar{\rho} i\omega \hat{\mathbf{u}}_\mathrm{a} + \nabla \hat{p}_\mathrm{a} = \mathbf{0} \tag{C.1}$$

Equation (C.1) is of pure acoustic nature as any convective effects are absent. By taking the curl of Eq. (C.1), the corresponding vorticity equations is obtained

$$i\omega\hat{\mathbf{\Omega}} = i\omega\hat{\mathbf{\Omega}}_\mathrm{a} = -\frac{\nabla\bar{\rho} \times \nabla\hat{p}_\mathrm{a}}{\bar{\rho}^2}, \tag{C.2}$$

where the r.h.s. of Eq. (C.2) describes the vorticity production by the baroclinic effect. Equation (C.2) confirms that the acoustic velocity field $\hat{\mathbf{u}}_\mathrm{a}$ is governed by a rotational part, if $\nabla\bar{\rho} \neq \mathbf{0}$; even in the limit of a vanishing mean flow velocity. This observation disqualifies LNSE/LEE velocity fields to serve as the input for the Helmholtz decomposition at least for reacting cases.

To circumvent this, Eq. (C.1) is written in its equivalent conservative form:

$$i\omega\hat{\mathbf{m}} + \nabla \hat{p} = i\omega\hat{\mathbf{m}}_\mathrm{a} + \nabla \hat{p}_\mathrm{a} = \mathbf{0} \tag{C.3}$$

where $\hat{\mathbf{m}}$ is the disturbance mass flow. Taking the curl of Eq. (C.3) reveals

$$i\omega\nabla \times \hat{\mathbf{m}} = i\omega\nabla \times \hat{\mathbf{m}}_{\mathrm{a}} = \mathbf{0}, \tag{C.4}$$

which shows that the acoustic disturbance mass flow is irrotational despite the presence of mean density gradients. This indicates that the disturbance mass flow represents a suitable quantity for the determination of acoustic and vortical sub-modes via the Helmholtz decomposition.

The plots shown in Fig. C.1 compare mass flow (top halves of mid and right columns) with velocity (lower halves of mid and right columns) Helmholtz decomposition results of the T1 eigenmode shape with each other. The original LNSE solution fields in the left column of Fig. C.1 are obtained for reactive conditions in the A^2EV combustor. Visual inspection of the acoustic solution fields obtained by the mass flow Helmholtz decomposition in the top halves of the mid column reveals good agreement with the original LNSE solution fields. Subtraction of these acoustic fields from the LNSE fields gives the vortical fields in the top halves of the right column, which are associated with convectively transported vortices. Erroneously using the LNSE velocity field as the input for the Helmholtz decomposition leads to inaccurate results for both, acoustic and vortical sub-modes. This can be seen by comparing the plots in the lower halves of the mid column with the original LNSE fields. The acoustic sub-mode is not reproduced correctly. Subtraction of these incorrect acoustic decomposition results from the original LNSE solution fields does not only give the convectively transported vortices but also an acoustic part which is erroneously attributed to the vortical fields (cf. the lower halves of the plots in the the right column of Fig. C.1).

C.2 Relation between Scalar Potential and Acoustic Pressure

This appendix presents the derivation of Eqs. (4.19) and (4.24) introduced in Section 4.3. The appendix starts with the derivation of Eq. (4.24).

For isothermal conditions and low Mach numbers, the velocity Helmholtz decomposition can be used to extract acoustic and vortical solution fields as explained in Section 4.3. In this case, the acoustic pressure $\hat{p}_{\mathrm{a}}$ is linked to the

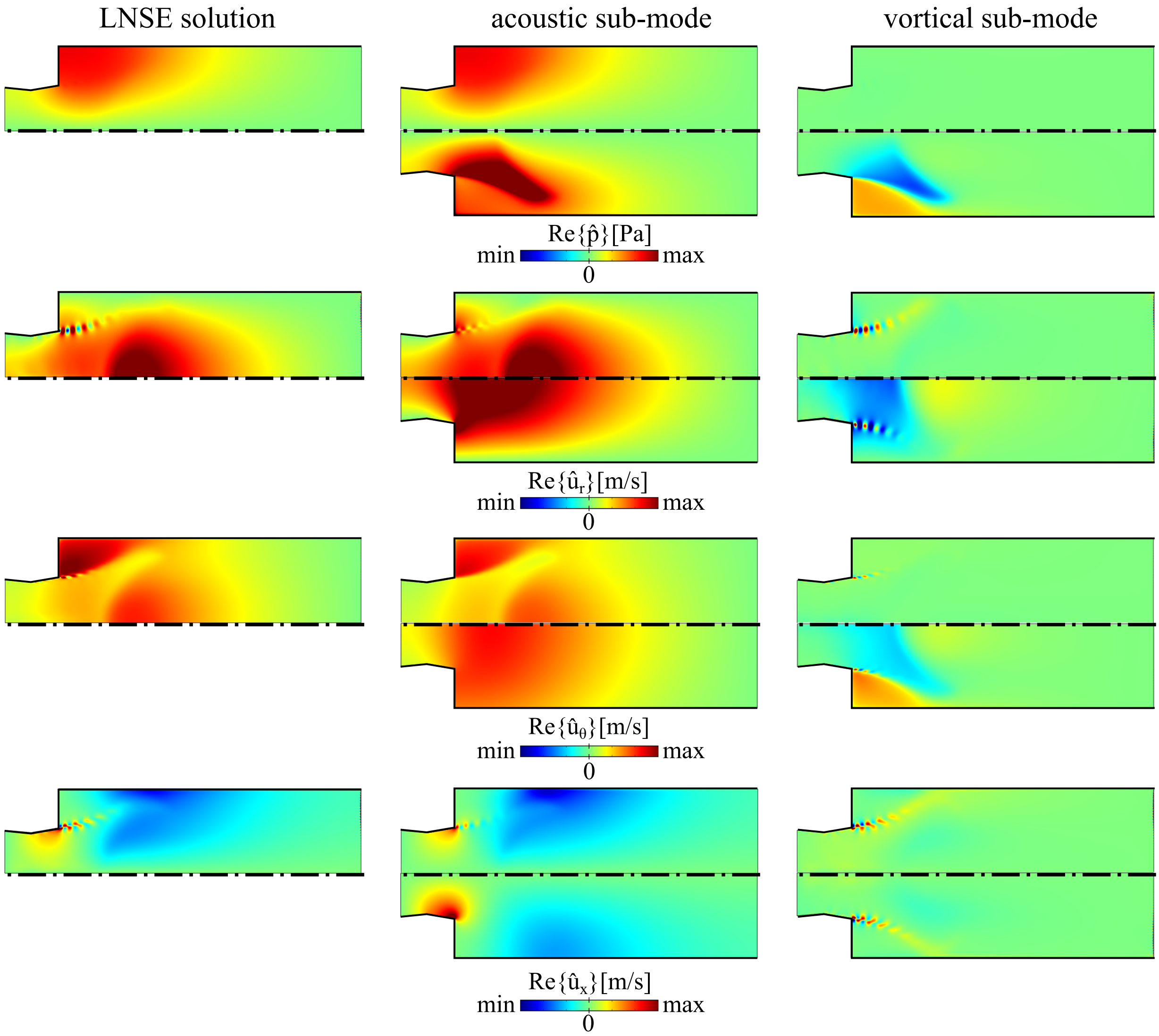

Figure C.1: *Results of the mass flow (top halves) and velocity vector (lower halves) Helmholtz decomposition for the T1 eigenmode of the reactive A^2EV combustor configuration: pressure (first row) with radial (second row), azimuthal (third row) and axial (fourth row) velocity distributions for the original LNSE solution (left) and decomposed acoustic (middle) and vortical (right) sub-modes.*

scalar velocity potential Φ by [111] (cf. Eq. (4.24))

$$\hat{p}_{\mathrm{a}} = -\bar{\rho}\,(i\omega\Phi + \bar{\mathbf{u}}\cdot\nabla\Phi) \tag{C.5}$$

The relation in Eq. (C.5) can be derived from the APE momentum Eq. (2.30), i.e.

$$\bar{\rho}\left(i\omega\hat{\mathbf{u}}+\nabla\left(\bar{\mathbf{u}}\cdot\hat{\mathbf{u}}\right)\right)+\nabla\hat{p}=\mathbf{0}. \tag{C.6}$$

Notice that the term $\hat{p}/\bar{c}^2 \frac{1}{2}\nabla\left(\bar{\mathbf{u}}\cdot\bar{\mathbf{u}}\right)$ is neglected in Eq. (C.6), which can be justified by its second order dependency on the mean flow velocity and the low-Mach number assumption. Writing Eq. (C.6) in terms of the velocity potential, i.e. $\hat{\mathbf{u}}=\hat{\mathbf{u}}_{\mathrm{a}}=\nabla\Phi$ gives (recall that $\nabla\bar{\rho}=\mathbf{0}$)

$$\nabla\left(\bar{\rho}\left(i\omega\Phi+\left(\bar{\mathbf{u}}\cdot\nabla\Phi\right)\right)+\hat{p}_{\mathrm{a}}\right)=\mathbf{0}, \tag{C.7}$$

where linearity of the gradient operator is exploited. The trivial solution of Eq. (C.7) is given by Eq. (C.5).

To obtain the relation between acoustic pressure and the mass flow potential $\Phi_{\hat{\mathbf{m}}}$, the APE momentum equation in conservative form is required. Starting point for its derivation is the linearized LEE momentum equation in conservative form, i.e.

$$i\omega\hat{\mathbf{m}}+\nabla\cdot\left(\hat{\mathbf{m}}\otimes\bar{\mathbf{u}}\right)+\nabla\cdot\left(\bar{\mathbf{m}}\otimes\hat{\mathbf{u}}\right)+\nabla\hat{p}=\mathbf{0}, \tag{C.8}$$

with $\hat{\mathbf{m}}=\bar{\rho}\hat{\mathbf{u}}+\hat{\rho}\bar{\mathbf{u}}$ and $\bar{\mathbf{m}}=\bar{\rho}\bar{\mathbf{u}}$. Applying $\nabla\cdot\left(\mathbf{m}\otimes\mathbf{u}\right)=\mathbf{u}\nabla\cdot\mathbf{m}+\left(\mathbf{m}\cdot\nabla\right)\mathbf{u}$ to Eq. (C.8) gives

$$i\omega\hat{\mathbf{m}}+\bar{\mathbf{u}}\nabla\cdot\hat{\mathbf{m}}+\hat{\mathbf{u}}\underbrace{\nabla\cdot\bar{\mathbf{m}}}_{=0}+\left(\hat{\mathbf{m}}\cdot\nabla\right)\bar{\mathbf{u}}+\left(\bar{\mathbf{m}}\cdot\nabla\right)\hat{\mathbf{u}}+\nabla\hat{p}=\mathbf{0} \tag{C.9}$$

Notice that the divergence of the mean flow mass flow is zero. Next, the vector identity $(\hat{\mathbf{m}}\cdot\nabla)\bar{\mathbf{u}}+(\bar{\mathbf{m}}\cdot\nabla)\hat{\mathbf{u}}=\nabla\left(\hat{\mathbf{m}}\cdot\bar{\mathbf{u}}\right)+\left(\bar{\mathbf{\Omega}}\times\hat{\mathbf{m}}\right)+\left(\left(\nabla\times\hat{\mathbf{m}}\right)\times\bar{\mathbf{u}}\right)$ is used to re-write to Eq. (C.9):

$$i\omega\hat{\mathbf{m}}+\nabla\left(\hat{\mathbf{m}}\cdot\bar{\mathbf{u}}\right)+\nabla\hat{p}=-\bar{\mathbf{u}}\nabla\cdot\hat{\mathbf{m}}-\left(\bar{\mathbf{\Omega}}\times\hat{\mathbf{m}}\right)-\left(\left(\nabla\times\hat{\mathbf{m}}\right)\times\bar{\mathbf{u}}\right). \tag{C.10}$$

Taking the curl of Eq. (C.10) reveals that the terms on the r.h.s. introduce rotation to the mass flow field. Removing these terms gives an irrotational, acoustic momentum equation[1], i.e.

$$i\omega\hat{\mathbf{m}}_{\mathrm{a}}+\nabla\left(\hat{\mathbf{m}}_{\mathrm{a}}\cdot\bar{\mathbf{u}}\right)+\nabla\hat{p}_{\mathrm{a}}=\mathbf{0}, \tag{C.11}$$

which is denoted as the APE momentum equation in conservative form in this thesis. The irrotational mass flow field $\hat{\mathbf{m}}_{\mathrm{a}}$ in Eq. (C.11) can now be expressed

[1] Recall that $\nabla\times\nabla(\ldots)=\mathbf{0}$.

by the gradient of the scalar potential, i.e. $\hat{\mathbf{m}} = \hat{\mathbf{m}}_\mathrm{a} = \nabla\Phi_{\hat{\mathbf{m}}}$. Exploiting linearity of the gradient operator results in

$$\nabla\left(i\omega\Phi_{\hat{\mathbf{m}}} + (\nabla\Phi_{\hat{\mathbf{m}}}\cdot\bar{\mathbf{u}}) + \hat{p}_\mathrm{a}\right) = \mathbf{0}. \tag{C.12}$$

Equation (C.12) is fulfilled if

$$\hat{p}_\mathrm{a} = -\left(i\omega\Phi_{\hat{\mathbf{m}}} + (\nabla\Phi_{\bar{\mathbf{u}}\cdot\hat{\mathbf{m}}})\right). \tag{C.13}$$

Equation (C.13) is the relation between the scalar mass flow potential $\Phi_{\hat{\mathbf{m}}}$ and the acoustic pressure $\hat{p}_\mathrm{a}$ which is introduced in Eq. (4.19) in Section 4.3 of the main part of this thesis.

D RANS CFD Simulations of the A^2EV Combustor

D.1 Additional Information on the RANS CFD Simulations

boundary conditions	isothermal	reactive
$\bar{T}_\infty$	300K	
$\bar{T}_{\mathrm{in}}$	$423\mathrm{K} \leq \bar{T}_{\mathrm{in}} \leq 723\mathrm{K}$	
$\bar{\dot{m}}_{\mathrm{in}}$	$60\frac{\mathrm{g}}{\mathrm{s}} \leq \bar{\dot{m}}_{\mathrm{in}} \leq 120\frac{\mathrm{g}}{\mathrm{s}}$	
λ	/	$1 \leq \lambda \leq 1.8$
α_{wall}	$0\frac{\mathrm{W}}{\mathrm{m^2K}}$	$75\frac{\mathrm{W}}{\mathrm{m^2K}}$
CFD		
domain	3D (quarter)	quasi 2D
turbulence model	$k-\epsilon$ Realizable	
pressure-velocity coupling	SIMPLE	
spatial discretization	second order upwind	
mesh size	$9.67 \cdot 10^5$ cells	$8.13 \cdot 10^4$ cells
mesh type	struct. cut-cell	struct. hexa
outlet type	outflow	
convergence criteria	four decades	four decades
combustion model	/	FGM extension [77, 121]
kinetics	/	GRI 3.0 [122]

Table D.1: *Information on the RANS CFD simulations used for the linear thermoacoustic stability analysis.*

Table D.1 presents the settings for the RANS CFD simulations used in Section 5.2 to compute the linear thermoacoustic stability limits of the T1 eigenmode in the A^2EV combustor. These simulation were performed to obtain the mean flow fields associated with the 80 operational points introduced in Chapter 3.

D.2 Mesh Independence Study

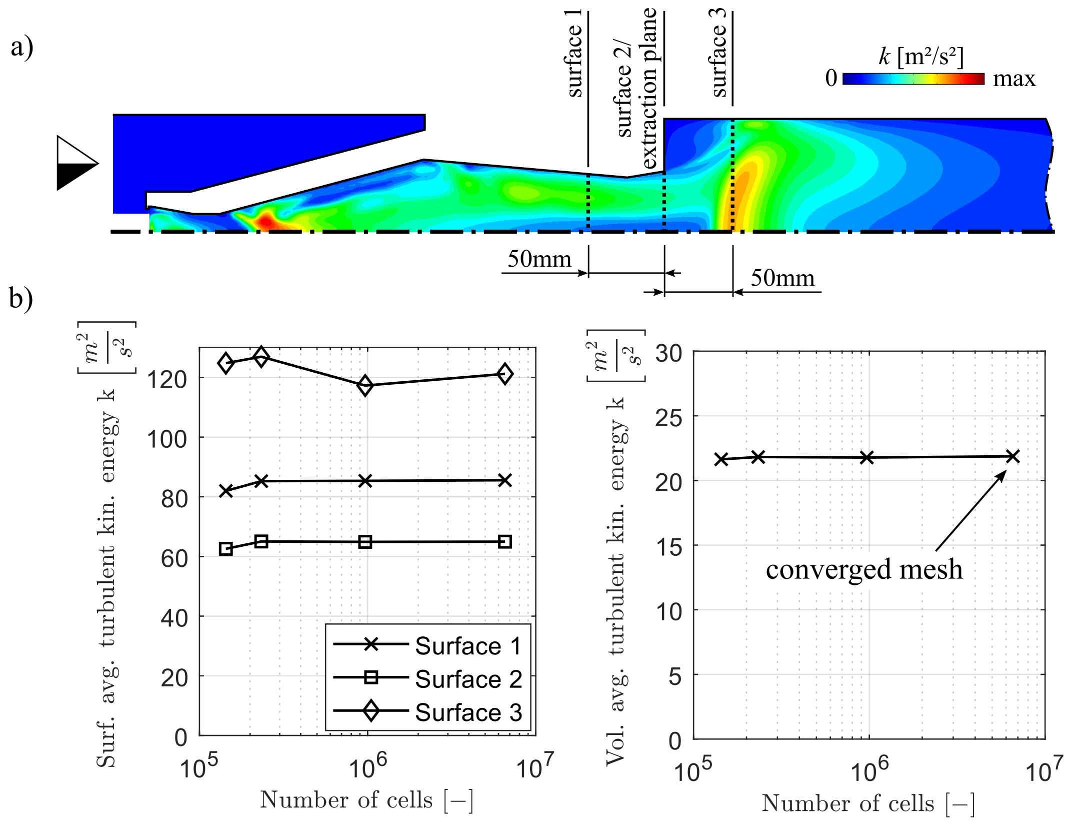

Figure D.1: *a) Turbulent kinetic energy in the complete A^2EV combustor benchmark system obtained by an isothermal RANS CFD simulation; b) mesh independence study in terms k.*

Mesh independence of the isothermal RANS CFD simulations was judged by evaluating the surface- and volume-averaged turbulent kinetic energy in three cross-sectional planes and in the complete computational domain, respectively. An exemplary distribution ($\bar{\dot{m}}_{\text{in}} = 120 g/s$, $\bar{T}_{\text{in}} = 623 K$) of the turbulent kinetic energy simulation is presented in Fig. D.1 a). Figure D.1 b) presents the results of the mesh independence study.
To establish mesh independence in the second, reactive RANS CFD simulation of the combustion chamber only, the volume-averaged turbulent kinetic

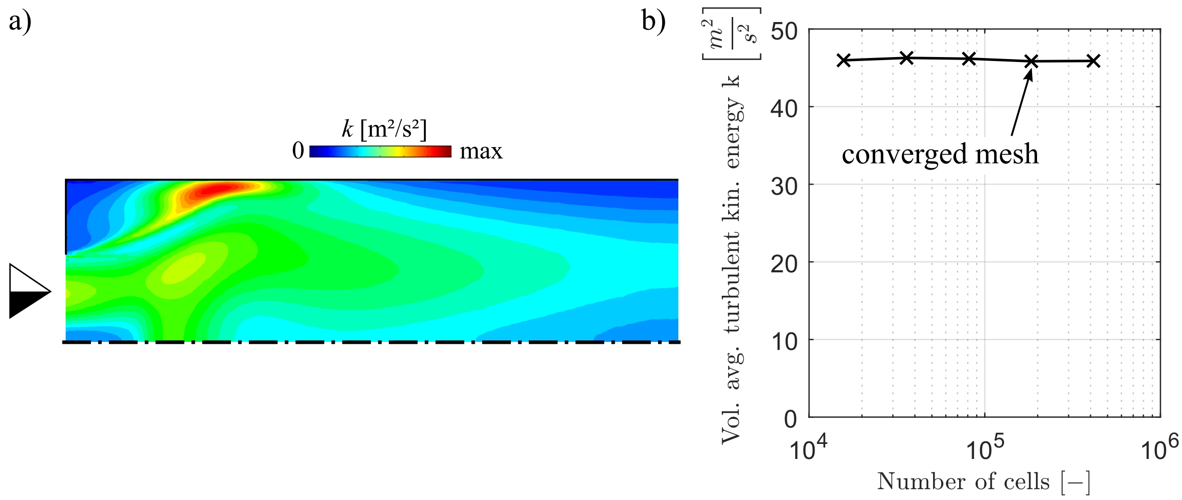

Figure D.2: *a) Turbulent kinetic energy in the A^2EV combustor chamber obtained by a reactive RANS CFD simulation; b) mesh independence study in terms k.*

energy is evaluated for different mesh refinement steps. As an example, Fig. D.2 shows the turbulent kinetic energy distribution for the operational point with $\bar{\dot{m}}_{\text{in}} = 120\,\text{g/s}$, $\bar{T}_{\text{in}} \leq 623\text{K}$ and $\lambda = 1.2$. Figure D.2 presents the mesh independence results in terms of the volume-averaged turbulent kinetic energy.

D.3 Performance of the FGM Extension in Thermoacoustic Stability Analyses

In past work [37], the mean heat release rate distributions $\bar{\dot{q}}$ of the 80 operational points of the A^2EV combustor were obtained by OH*-chemiluminescence measurements, which was possible due to the optical access of the combustion chamber [81][1][2]. In this study, the mean heat release rate distributions are determined with a combustion model and the Gri-Mech 3.0 kinetics mechanism [122]. An extended version of the FGM reaction model proposed by Klarmann et. al. [77, 121] is used, which includes the effects of heat losses and flame stretch on the reaction progress source term. Specifically, in regions of high heat loss and/or stretch, the fuel consump-

[1]Parts of this appendix were published in Ref. [139]

[2]This appendix refers to the flame displacement and deformation driving rates represented by the red dots in Fig. 5.8.

tion speed and thus the reaction progress source term value decrease. As a result, the heat release rate in the outer shear-layers of theA^2EV combustor drops significantly. The application of the FGM extension represents an essential prerequisite for an accurate incorporation of flame dynamics to a thermoacoustic stability analysis as the measured OH*-distributions of the premixed flame do not show strong emissivity in these regions. A comprehensive comparison of the FGM extension to other combustion models can be found in Ref. [121]. In the plots of Fig. D.3 a), normalized measured (upper halves) and computed (lower halves) mean heat release rate distributions of two representative operational points –one thermoacoustically stable, the other unstable– are qualitatively compared with each other. For the purpose of better comparability, the contours (white lines) of the computed ones are projected into the experimentally obtained heat release images [81]. Figure D.3 b) contains the computed deformation (top) and displacement (middle) driving rates β_ρ and β_Δ, respectively, for the T1 eigenmode in the A^2EV combustor. Each circle represents one of the 80 operational points (cf. Chapter 3). The third plot shows the net driving rate $\beta = \beta_\rho + \beta_\Delta$. Red and black dots indicate whether the driving rates are computed with numerically (red) or experimentally obtained (black) flame brushes. Filled and open circles provide information in a binary manner on whether an operational point was stable or unstable in the experiments, respectively. Notice that the driving rate results in Fig. D.3 b) are determined with the three-dimensional computational domain (cf. Fig. 5.7). All eigenfrequency analyses were carried out with the APE and a numerical stabilization parameter value of $\alpha_\tau = 0$ according to Eqs. (5.29)-(5.30). With respect to the experimental benchmark data, the following observations can be deduced concerning the applicability of the reactive CFD simulations and the resulting errors in the corresponding growth rates:

For all 80 operational points, driving due to flame deformation is predicted stronger by the CFD based approach recognizable by the displaced red dots in the top plot of Fig. D.3 b). This is constituted by the following reasons: The main heat release of the computed flame brush is allocated near the combustor wall, whereas the measured location is placed near the axis for both, thermoacoustically stable and unstable operational points visible in

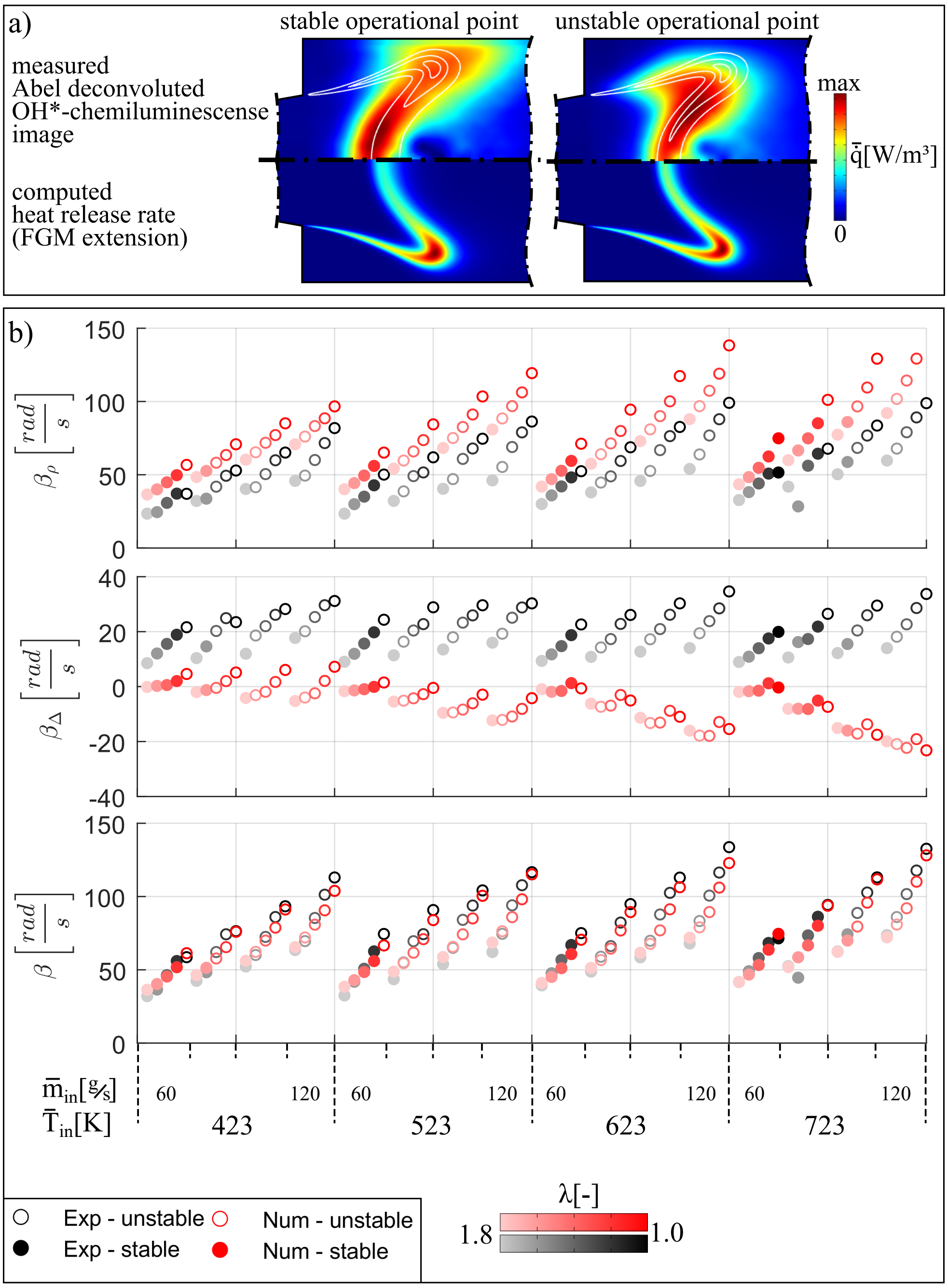

Figure D.3: *a) Comparison between measured (upper halves) and computed (lower halves) heat release rate distributions for a stable and an unstable operational point; b) comparison of deformation (top), displacement (middle) and net (bottom) T1 driving rates computed with simulated (red) and measured (black) flame brushes.*

Fig. D.3 a). With reference to Eq. (5.28), the amplitude of heat release rate oscillations associated with flame deformation $\hat{\dot{q}}_\rho$ is proportional to the product of mean heat release rate $\bar{\dot{q}}$ and acoustic pressure $\hat{p}_\mathrm{a}$ of the T1 mode. Thus, the interaction between computed flame brush and the transversal pressure mode leads to an overestimation of deformation driving rates compared to the measurement-based ones. Regarding the unstable cases, the measured flame brush occurs to be more radially contracted than the computed one. The flame dynamics for unstable, non-compact thermoacoustic systems was investigated experimentally in past work by Berger et. al. [70] and numerically in Chapter 6 of the present thesis. In both studies a pulsation amplitude-dependent flame contraction is identified. Specifically, it was observed that the flame radially contracts for increasing T1 limit-cycle amplitudes. However, this effect cannot be accounted for in the steady-state RANS CFD simulations explaining this source of deviation. Instead, the associated driving rates are based on acoustically unaffected flame shapes, where any feedback from acoustics to the mean flow is excluded. The RANS simulations give thus the real zero amplitude mean flame shapes as theoretically required for a linear stability analysis.

Contrary, driving due to flame displacement (middle plot in Fig. D.3 b)) is underestimated by the CFD simulation based results and even tends to stabilize the thermoacoustic system. This deviation mainly appears due to the reduced heat release rate in the chamber center of the computed flame brush. The resulting generation of heat release rate oscillations due to flame displacement, which depends on the acoustic velocity (cf. Eq. (5.28)), is predicted too weak in this region.

The net driving rates (bottom plot in Fig. D.3 b)) obtained with computed and measured flame shapes show good agreement. However, this is because the former errors in displacement and deformation driving rates compensate each other. This behavior was theoretically discussed in Refs. [70, 140].

In summary, the displacement and deformation driving rates determined with the extended FGM combustion model show acceptable agreement with the measurement-based results. Although the flame deformation and displacement driving rates individually are predicted incorrectly, their net driving potential is almost in perfect agreement with their counterparts based on OH*-measurements. This allows utilization of the corresponding driving rates for the thermoacoustic stability assessment of the T1 eigenmode of the A^2EV combustor and eliminates the RANS CFD simulations as a potential source of error.

E URANS CFD Simulations of the A^{2}EV Combustor

E.1 Details on the Numerical Setup and Mesh Independence

The analysis of Chapter 6 is performed with the mesh shown in Fig. E.1. The gray shaded areas show the regions where the spatial distribution function $\delta_{p'}$ in Eq. (6.2) is non-zero.

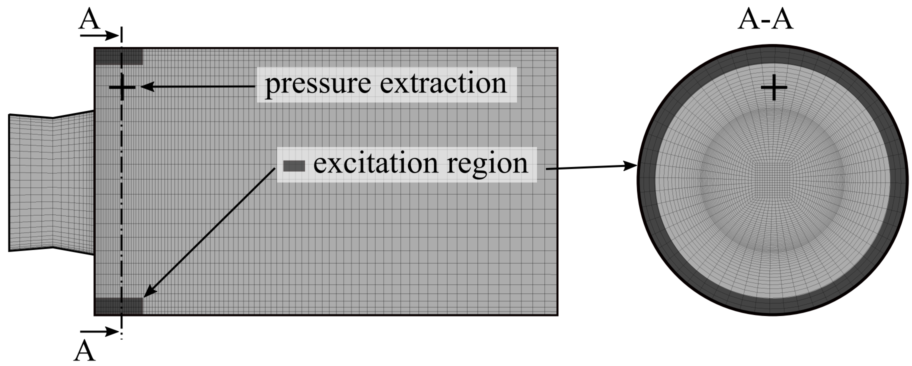

Figure E.1: *URANS CFD mesh with excitation region and pressure extraction point.*

The mesh in Fig. E.1 consists of approximately $282 \cdot 10^3$ cells and is the result of the mesh independence study presented in Fig. E.2. On the left side of Fig. E.2, evaluations of the volume-averaged turbulent kinetic energy for three different mesh refinement levels is presented. This quantity was determined at the end of each time step calculation. Similarly, pressure data was extracted for the three meshes at the position marked by the cross in Fig. E.1. These pressure traces are plotted in the right graph of Fig. E.2.

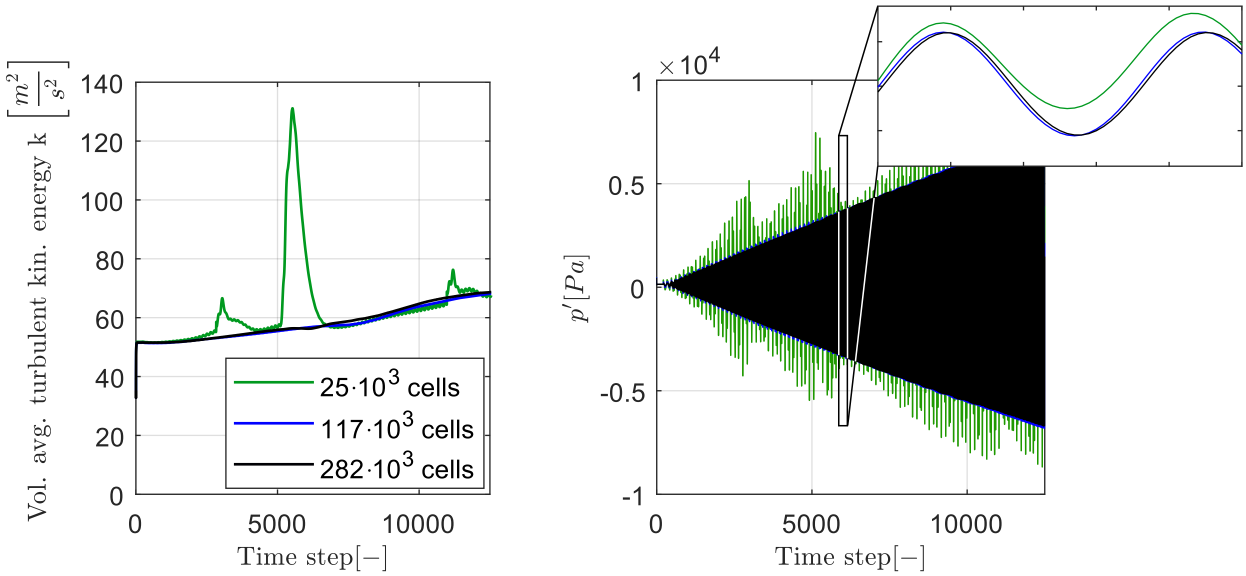

Figure E.2: *Results of the mesh independence study for the URANS CFD simulations. Left: volume-averaged turbulent kinetic energy k; right: pressure.*

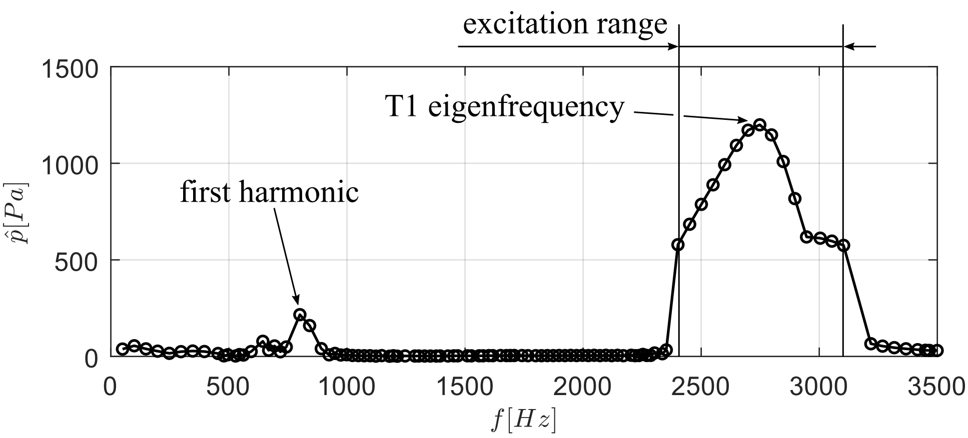

Figure E.3: *Computed frequency spectrum.*

E.2 Frequency Response Analysis

A frequency response analysis is performed to determine the T1 resonance frequency f_{T1} in Eq. (6.2). Therefore, the source term in Eq. (E.1) is used, which allows simultaneous excitation at multiple frequencies:

$$m_{p'}(r,\theta,x,t) = A_{p'}\delta_{p'}\sum_{j=1}^{j}\sin\left[2\pi f_j\left(t-t_{ref}\right)+\theta_{rot}\right] \tag{E.1}$$

In Eq. (E.1), f_j represents the forcing frequency. The summation symbol indicates that the source term $m_{p'}$ consists of a superposition of j harmonic signals. In this work, the A^2EV combustor is excited in a frequency range in between $2400\text{Hz} \le f_j \le 3100\text{Hz}$ in steps of 50Hz. The computed frequency spectrum is displayed in Fig. E.3. The peak in the frequency spectrum of Fig. E.3 is located at $f_j = 2750\text{Hz} = f_{T1}$, which corresponds to the T1 eigenmode.

F Comparison between T1 and T2 Eigenmodes

Figure F.1 compares damping, driving and growth rates of the T1 and T2 eigenmodes for 80 operational points of the A^2EV combustor (cf. Chapter 3) with each other[1]. Azimuthal periodicity of the two modes is exploited, which allows utilization of a highly resolved, two-dimensional mesh for the eigenfrequency analyses (see Section 2.4.2 and Appendix B for details). Information on how each growth rate is determined can be found in Section 5.2. About half of the 80 operational points were observed to be thermoacoustically unstable at the T1 eigenfrequency (open circles). The other operational points do not exhibit a T1 instability (filled circles). The T2 mode was always observed to be stable in the experiment. Notice that the T2 mode might be suppressed by the T1 mode in the experiment, which would be the result of non-linear modal interactions. This phenomenon cannot be captured by the presented linear CFD/CAA method but is addressed in Chapter 7 of this thesis.

Figure F.2 presents damping, driving and growth rates of T1 and T2 modes as a response to the pressure amplitude-dependency of the mean flow field. The left column shows the results for the T1 mode, which are also presented in Chapter 6. The right column presents the amplitude-dependent behavior of T2 growth rates with its individual contributions. The mean flow fields for the investigations with the T2 mode are obtained by an URANS CFD simulation, in which the source term of Eq. (6.2) is modified to mimic T2 oscillations in the A^2EV combustor.

[1] The T2 results presented in this appendix are used to study the modal suppression mechanisms in Chapter 7.

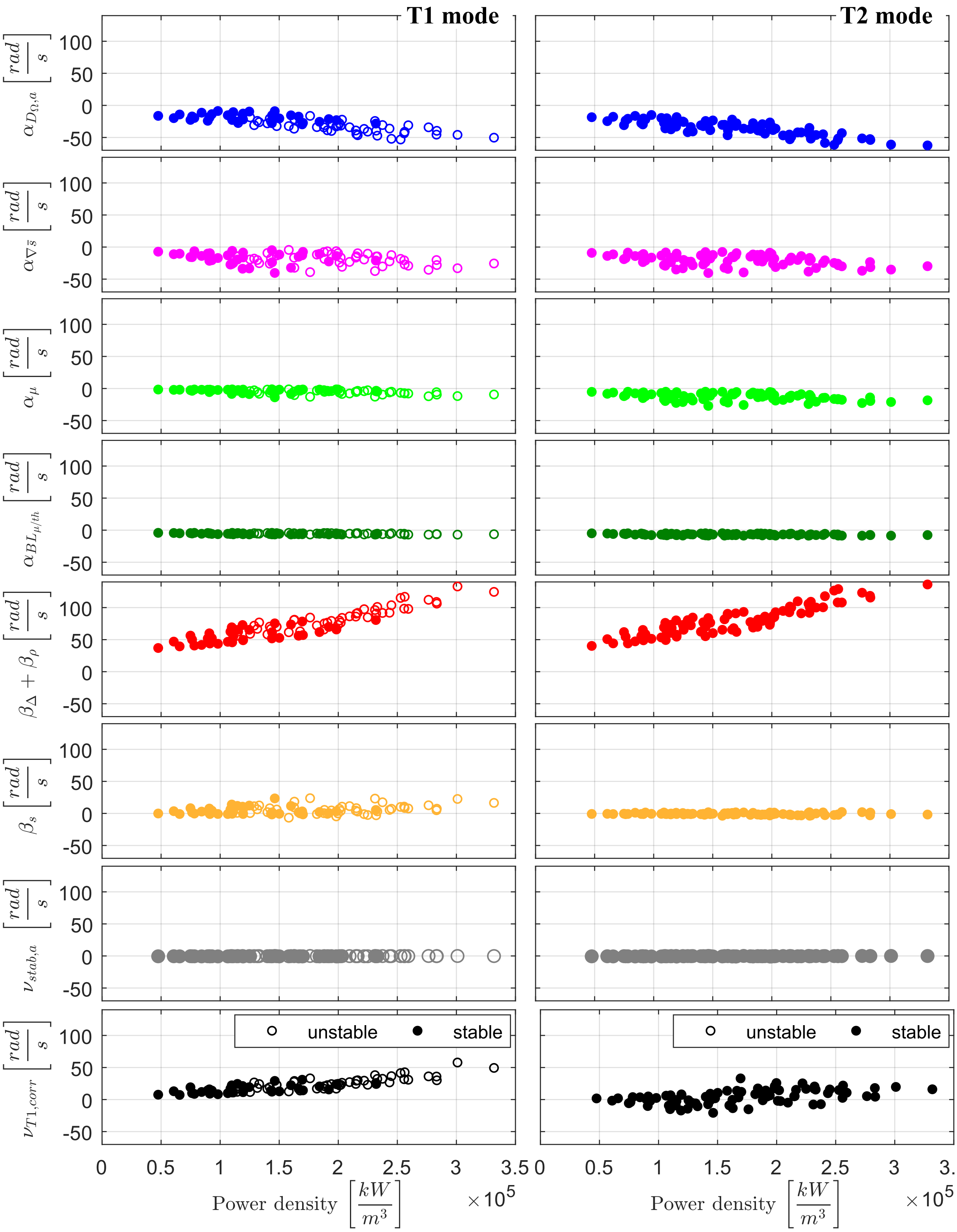

Figure F.1: *Computed T1 and T2 growth rates. Open and closed circles indicate the thermoacoustic stability behavior observed in the experiment.*

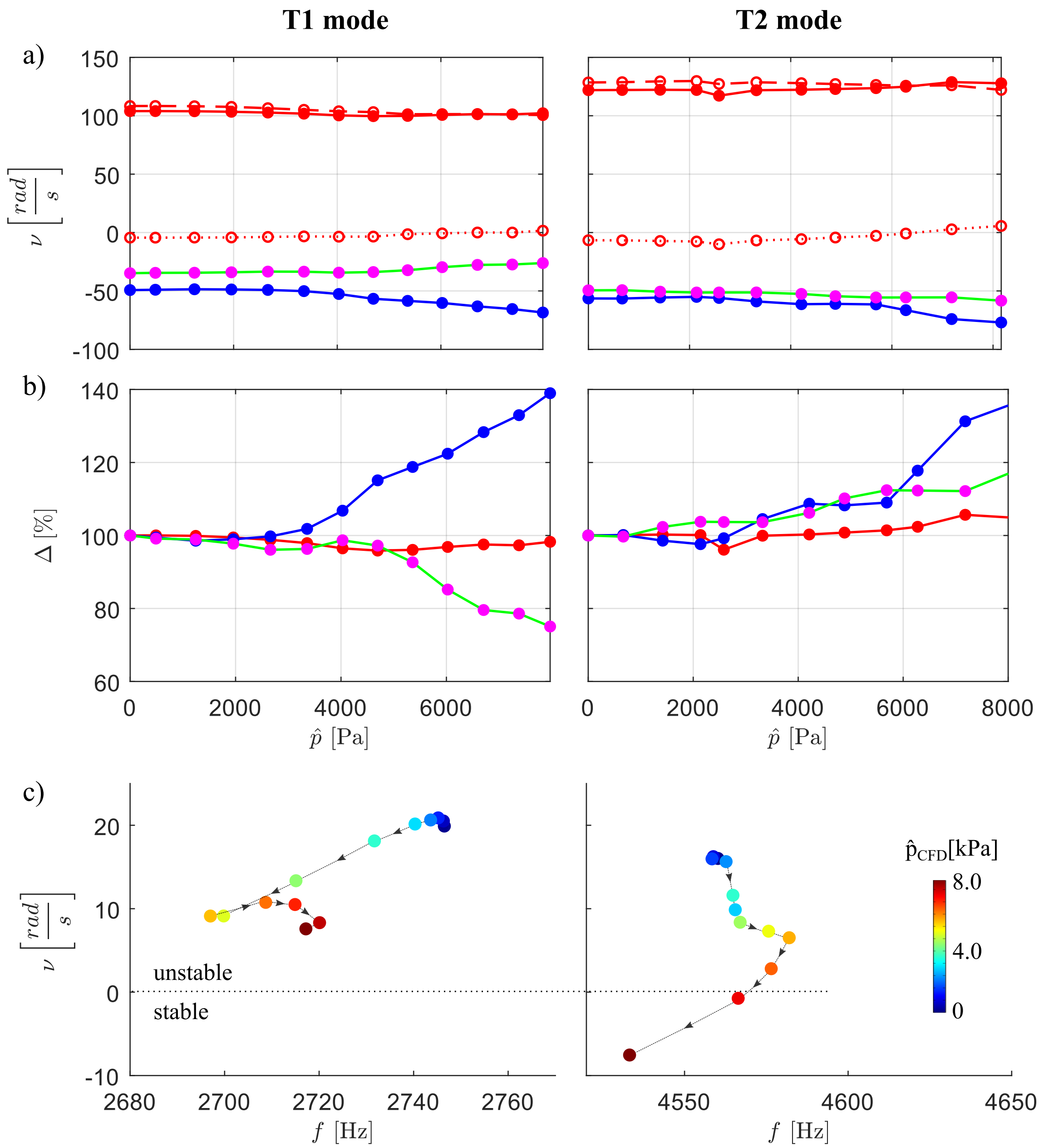

Figure F.2: *a) Absolute and b) relative evolution of T1 (left) and T2 (right) vorticity damping rates (blue line), flame driving rates (red lines) and remaining growth rate contributions (green-magenta colored line) plotted against increasing pressure amplitudes; c) eigenfrequency maps of T1 and T2 modes obtained by solving the parameterized eigenvalue problem of Eq.* (6.4) *without the impact of the flame-vortex source term and visco-thermal losses (information on the operational conditions:* $\bar{\dot{m}}_{in} = 120 g/s$, $\bar{T}_{in} = 623 K$, $\lambda = 1.2$*).*

G Theoretical Interpretation of the ROM

The ROM in Chapter 7 is equal to the isentropic LNSE (2.9)-(2.10) (based on the APE with additional damping contributions like vortex shedding and viscous effects, see Eq. (7.1)) in the time-domain with the flame displacement and deformation as well as vortex-flame FTFs (cf. Eq. (5.20)). Differentiation of the energy equation with respect to time, i.e. $\partial \text{Eq.(2.10)}/\partial t$, and subsequent combination with the divergence of the LNSE momentum Eq. (2.9) yields the inhomogeneous wave equation for variable mean temperature fields

$$\frac{\partial^2 p'}{\partial t^2} - \bar{\rho}\bar{c}^2 \nabla \cdot \left(\frac{1}{\bar{\rho}} \nabla p' \right) = \left(\gamma - 1 \right) \frac{\partial \dot{q}'}{\partial t} + \zeta' + \Xi \tag{G.1}$$

with the sources $\dot{q}'$, ζ' and Ξ on its r.h.s. The first term $\dot{q}'$ is associated with the heat release rate FTFs of Eq. (5.28). ζ' contains all terms with a dependency on the mean flow $\bar{\mathbf{u}}$ and viscosity μ as well as the effect of the vortex-flame FTF $\dot{q}'_{\mathrm{s}}$ in Eq. (5.20). Ξ mimics broadband combustion noise, which constantly excites acoustic waves in the flame. By assuming that the sources on the r.h.s. of Eq. (G.1) are small compared to its l.h.s., the eigenmodes of Eq. (G.1) can be approximated by the Sturm-Liouville equation [17, 141][1],

$$-\omega_{\mathrm{i}}^2 p' - \bar{\rho}\bar{c}^2 \nabla \cdot \left(\frac{1}{\bar{\rho}} \nabla p' \right) = 0, \tag{G.2}$$

Mathematically, this can be justified, if $f \gg \nu$. Physically, this implies that the sources $\dot{q}'$, ζ' and Ξ only weakly affect the natural eigenmodes of Eq. (G.2).

Replacing the second term on the l.h.s. of Eq. (G.1) by Eq. (G.2) yields the oscillator equation

$$\frac{\mathrm{d}^2 p'}{\mathrm{d}t^2} + \omega_{\mathrm{i}}^2 p' = \left(\gamma - 1 \right) \frac{\partial \dot{q}'}{\partial t} + \zeta' + \Xi. \tag{G.3}$$

In the ROM of this thesis, all effects influencing the thermoacoustic stability except of flame displacement and deformation (these are incorporated

[1] The Sturm-Liouville equation results after Laplace transformation of the homogeneous wave Eq. (G.1).

via local feedback loops, cf. Fig. 7.1) are considered by the system matrix $\tilde{\mathbf{A}}_{\mathrm{r}}$ and more specifically by the amplitude-dependent damping rates α_{T1} and α_{T2}. This promotes the introduction of an amplitude-dependent dissipation model for ζ' in Eq. (G.3) as a function of pressure, i.e.

$$\zeta' = \underbrace{\left[\beta_{\mathrm{s}} + \alpha_{\hat{p}=0\mathrm{kPa}}\left(1 - \epsilon p'^2\right)\right]}_{=\beta_{\mathrm{s}}+\alpha(p')} \frac{\mathrm{d}p'}{\mathrm{d}t}. \tag{G.4}$$

In Eq. (G.4), $\alpha_{\hat{p}=0\mathrm{kPa}}$ denotes the damping rate at zero acoustic amplitude. β_{s} is the amplitude-independent vortex-flame driving rate. The calibration factor ϵ denotes the sensitivity of the damping rate $\alpha(p')$ to the pressure amplitude. It can be determined by using the benchmark damping rates of Chapter 6.

A similar model is introduced for the heat release rate term $\dot{q}'$, which captures driving due to flame displacement and deformation. A linear driving model is used

$$\left(\gamma - 1\right) \frac{\mathrm{d}\dot{q}'}{\mathrm{d}t} = \beta \frac{\mathrm{d}p'}{\mathrm{d}t}. \tag{G.5}$$

In Eq. (G.5) β is the constant net driving rate. With reference to Chapter 6, this can be justified by the weak dependency of β on the pressure amplitude. Combining Eq. (G.3) with Eqs. (G.4)-(G.5) yields the governing oscillator equation, i.e.

$$\frac{\mathrm{d}^2 p'}{\mathrm{d}t^2} - \Big(\beta + \underbrace{\beta_{\mathrm{s}} + \alpha_{\hat{p}=0\mathrm{kPa}} - \alpha_{\hat{p}=0\mathrm{kPa}}\epsilon p'^2}_{=\beta_{\mathrm{s}}+\alpha(p')}\Big) \frac{\mathrm{d}p'}{\mathrm{d}t} + \omega_{\mathrm{i}}^2 p' = \Xi. \tag{G.6}$$

Equation (G.6) represents a *Van-der-Pol* oscillator, which is constantly forced by turbulent combustion noise Ξ (cf. box $\boxed{1}$ in Fig. 7.1). In conclusion, the ROM state-space model in Section 7.1 describes a system of coupled *Van-der-Pol* oscillators. In this thesis, T1 and T2 eigenmodes in the A^2EV combustor are the oscillators.

Based on the *Van-der-Pol* oscillator Eq. (G.6), so-called *amplitude-phase equations* can be derived for T1 and T2 modes. These equations can be used to investigate the long-term behavior of unstable acoustic modes. The results of these theoretical analyses can be used to validate the computations of the modified ROM from an analytic point of view. However, the validation is left to future work and in the following, only the governing equations for slowly varying T1 and T2 amplitudes as well as phases are derived, which can serve as the baseline for the analyses.

The first step to obtain the governing amplitude-phase equations comprises the application of a spatio-temporal pressure decomposition, i.e.

$$\begin{aligned} p'(\mathbf{x},t) =& \frac{1}{2}\left[\left(p'_{\mathrm{T1}}+p'^{*}_{\mathrm{T1}}\right)+\left(p'_{\mathrm{T2}}+p'^{*}_{\mathrm{T2}}\right)\right] = \\ & \frac{1}{2}\left[\left(\Psi_{\mathrm{T1}}\eta_{\mathrm{T1}}+\Psi^{*}_{\mathrm{T1}}\eta^{*}_{\mathrm{T1}}\right)+\left(\Psi_{\mathrm{T2}}\eta_{\mathrm{T2}}+\Psi^{*}_{\mathrm{T2}}\eta^{*}_{\mathrm{T2}}\right)\right] \end{aligned} \tag{G.7}$$

where $\Psi = f(\mathbf{x})$ and $\eta = f(t)$. The asterisk $()^*$ denotes the conjugate complex. Equation (G.7) is inserted into the *Van-der-Pol* oscillator Eq. (G.6). Next, the resulting equation is devoted to a spatial averaging procedure [141]. This is also known as *Galerkin projection* and exploits orthogonality between T1 and T2 modes in systems with continuous rotational symmetry (this is satisfied for the A^2EV combustor geometry and the corresponding mean flow fields). For this purpose, Eq. (G.6) with Eq. (G.7) is successively multiplied by Ψ^*_{T1} and Ψ^*_{T2} followed by a volume integration. The result is two coupled oscillator equations for T1 and T2 modes (the white noise term is neglected for reasons of clarity):

$$\begin{aligned} &\left(\ddot{\eta}_{\mathrm{T1}}+\nu_{\mathrm{T1},\hat{p}=0\mathrm{kPa}}\dot{\eta}_{\mathrm{T1}}+\omega^2_{\mathrm{T1}}\eta_{\mathrm{T1}}\right)\int_V \Psi_{\mathrm{T1}}\Psi^*_{\mathrm{T1}}\mathrm{d}V = \\ &\left(\alpha_{\mathrm{T1},\hat{p}=0\mathrm{kPa}}\epsilon_{\mathrm{T1}}+\alpha_{\mathrm{T2},\hat{p}=0\mathrm{kPa}}\epsilon_{\mathrm{T2}}\right)\Big[\left(\eta_{\mathrm{T1}}\eta_{\mathrm{T1}}\dot{\eta}^*_{\mathrm{T1}}+2\eta_{\mathrm{T1}}\eta^*_{\mathrm{T1}}\dot{\eta}_{\mathrm{T1}}\right)\int_V \left(\Psi_{\mathrm{T1}}\Psi^*_{\mathrm{T1}}\right)^2\mathrm{d}V+ \\ &2\left(\eta_{\mathrm{T1}}\eta_{\mathrm{T2}}\dot{\eta}^*_{\mathrm{T2}}+\eta_{\mathrm{T1}}\eta^*_{\mathrm{T2}}\dot{\eta}_{\mathrm{T2}}+\eta_{\mathrm{T2}}\eta^*_{\mathrm{T2}}\dot{\eta}_{\mathrm{T1}}\right)\int_V \Psi_{\mathrm{T1}}\Psi^*_{\mathrm{T1}}\Psi_{\mathrm{T2}}\Psi^*_{\mathrm{T2}}\mathrm{d}V\Big] \end{aligned} \tag{G.8}$$

$$\begin{aligned} &\left(\ddot{\eta}_{\mathrm{T2}}+\nu_{\mathrm{T2},\hat{p}=0\mathrm{kPa}}\dot{\eta}_{\mathrm{T2}}+\omega^2_{\mathrm{T2}}\eta_{\mathrm{T2}}\right)\int_V \Psi_{\mathrm{T2}}\Psi^*_{\mathrm{T2}}\mathrm{d}V = \\ &\left(\alpha_{\mathrm{T1},\hat{p}=0\mathrm{kPa}}\epsilon_{\mathrm{T1}}+\alpha_{\mathrm{T2},\hat{p}=0\mathrm{kPa}}\epsilon_{\mathrm{T2}}\right)\Big[\left(\eta_{\mathrm{T2}}\eta_{\mathrm{T2}}\dot{\eta}^*_{\mathrm{T2}}+2\eta_{\mathrm{T2}}\eta^*_{\mathrm{T2}}\dot{\eta}_{\mathrm{T2}}\right)\int_V \left(\Psi_{\mathrm{T2}}\Psi^*_{\mathrm{T2}}\right)^2\mathrm{d}V+ \\ &2\left(\eta_{\mathrm{T2}}\eta_{\mathrm{T1}}\dot{\eta}^*_{\mathrm{T1}}+\eta_{\mathrm{T2}}\eta^*_{\mathrm{T1}}\dot{\eta}_{\mathrm{T1}}+\eta_{\mathrm{T1}}\eta^*_{\mathrm{T1}}\dot{\eta}_{\mathrm{T2}}\right)\int_V \Psi_{\mathrm{T2}}\Psi^*_{\mathrm{T2}}\Psi_{\mathrm{T1}}\Psi^*_{\mathrm{T1}}\mathrm{d}V\Big] \end{aligned} \tag{G.9}$$

Notice that the dots and double dots in Eqs. (G.8)-(G.9) indicate first and second order time derivatives. The second terms on the r.h.s. of Eqs. (G.8)-(G.9) establish the coupling between the T1 and T2 modes, which is recognizable by the mixed subscripts. The volume integrals with the mixed T1 and T2 mode shapes (Ψ_{T1} and Ψ_{T2}) can be interpreted as the interaction volume, which defines the coupling strength between the unstable modes. Illustratively, the coupling strength becomes zero, if the interaction volume is zero. For instance, this would be the case, if two mode shapes do spatially not overlap. In this case, both unstable may coexist.

Next, the method of temporal averaging over one oscillating period is applied to Eqs. (G.8)-(G.9). Therefore, η_{T1}, η^*_{T1}, η_{T2} and η^*_{T2} are written as

$$\eta_{\mathrm{T1}} = \hat{p}_{\mathrm{T1}}(t)\exp(i(\omega_{\mathrm{T1}}t + \phi_{\mathrm{T1}}(t))) \tag{G.10}$$

$$\eta^*_{\mathrm{T1}} = \hat{p}_{\mathrm{T1}}(t)\exp(-i(\omega_{\mathrm{T1}}t - \phi_{\mathrm{T1}}(t))) \tag{G.11}$$

$$\eta_{\mathrm{T2}} = \hat{p}_{\mathrm{T2}}(t)\exp(i(\omega_{\mathrm{T2}}t + \phi_{\mathrm{T2}}(t))) \tag{G.12}$$

$$\eta^*_{\mathrm{T2}} = \hat{p}_{\mathrm{T2}}(t)\exp(-i(\omega_{\mathrm{T2}}t - \phi_{\mathrm{T2}}(t))), \tag{G.13}$$

where $\hat{p}$ and ϕ denote amplitude and phase of T1 and T2 modes. Substitution of Eqs. (G.10)-(G.13) into Eqs. (G.8)-(G.9) and presuming that amplitude and angular phase velocity vary slowly compared to oscillatory time scales (see for instance in Ref. [132]) yields the T1 and T2 amplitude and phase equations describing their slowly varying, temporal evolution:

$$\begin{aligned}\dot{\hat{p}}_{\mathrm{T1}} = \nu_{\mathrm{T1},\hat{p}=0\mathrm{kPa}}\hat{p}_{\mathrm{T1}} - \frac{1}{\int_V \Psi_{\mathrm{T1}}\Psi^*_{\mathrm{T1}}\mathrm{d}V}\left(\alpha_{\mathrm{T1},\hat{p}=0\mathrm{kPa}}\epsilon_{\mathrm{T1}} + \alpha_{\mathrm{T2},\hat{p}=0\mathrm{kPa}}\epsilon_{\mathrm{T2}}\right)\dots\\ \dots\left[\hat{p}^3_{\mathrm{T1}}\int_V\left(\Psi_{\mathrm{T1}}\Psi^*_{\mathrm{T1}}\right)^2\mathrm{d}V + 2\hat{p}_{\mathrm{T1}}\hat{p}^2_{\mathrm{T2}}\int_V \Psi_{\mathrm{T1}}\Psi^*_{\mathrm{T1}}\Psi_{\mathrm{T2}}\Psi^*_{\mathrm{T2}}\mathrm{d}V\right]\end{aligned} \tag{G.14}$$

$$i\hat{p}_{\mathrm{T1}}\dot{\phi}_{\mathrm{T1}} = 0 \tag{G.15}$$

$$\begin{aligned}\dot{\hat{p}}_{\mathrm{T2}} = \nu_{\mathrm{T2},\hat{p}=0\mathrm{kPa}}\hat{p}_{\mathrm{T2}} - \frac{1}{\int_V \Psi_{\mathrm{T2}}\Psi^*_{\mathrm{T2}}\mathrm{d}V}\left(\alpha_{\mathrm{T1},\hat{p}=0\mathrm{kPa}}\epsilon_{\mathrm{T1}} + \alpha_{\mathrm{T2},\hat{p}=0\mathrm{kPa}}\epsilon_{\mathrm{T2}}\right)\dots\\ \dots\left[\hat{p}^3_{\mathrm{T2}}\int_V\left(\Psi_{\mathrm{T2}}\Psi^*_{\mathrm{T2}}\right)^2\mathrm{d}V + 2\hat{p}_{\mathrm{T2}}\hat{p}^2_{\mathrm{T1}}\int_V \Psi_{\mathrm{T2}}\Psi^*_{\mathrm{T2}}\Psi_{\mathrm{T1}}\Psi^*_{\mathrm{T1}}\mathrm{d}V\right]\end{aligned} \tag{G.16}$$

$$i\hat{p}_{\mathrm{T2}}\dot{\phi}_{\mathrm{T2}} = 0 \tag{G.17}$$

The zero value of the slowly varying phase velocity in Eqs. (G.15) and (G.17) shows that the modified ROM is not capable of modeling synchronization phenomena (cf. Ref. [132]). From a physical point of view this means that the oscillating frequencies of T1 and T2 modes remain constant in time. The incorporation of synchronization effects to the ROM can thus be realized by modeling temporal changes of T1 and T2 oscillating frequencies f_{T1} and f_{T2} induced by the interaction with the other mode. In practice, this might be achieved by expressing the T1 and T2 frequency drifts ($\omega_i^2 - \omega^2$) as a function of the mode coupling strength $C = \int_V \Psi_{T2}\Psi_{T2}^*\Psi_{T1}\Psi_{T1}^* \mathrm{d}V$. This translates into the following additional synchronization term in the governing *Van-der-Pol* oscillator Eq. (G.6) for the T1 and T2 modes:

$$\frac{\mathrm{d}^2 p'}{\mathrm{d}t^2} - \Big(\beta + \underbrace{\beta_\mathrm{s} + \alpha_{\hat{p}=0\mathrm{kPa}} - \alpha_{\hat{p}=0\mathrm{kPa}}\epsilon p'^2}_{=\beta_\mathrm{s}+\alpha(p')}\Big)\frac{\mathrm{d}p'}{\mathrm{d}t} + \omega_\mathrm{i}^2 p' = \Xi - C(\omega_\mathrm{i}^2 - \omega^2)p'. \quad \text{(G.18)}$$

The last term on the r.h.s. of Eq. G.18 introduces changes of the slowly varying phases of the T1 and T2 and thus allows variations of the T1 and T2 oscillating frequencies. The implementation in the ROM is left to future work and might be realized in accordance with the damping rate adaption during run-time; however, by adapting the oscillating frequencies f_{T1} and f_{T2} in the state-space system matrix $\tilde{\mathbf{A}}_\mathrm{r}$ instead of α_{T1} and α_{T2}.

Previous Publications

Parts of this thesis were already published by the author in journal and conference papers [98, 104, 123, 134, 139]. All these publications are registered according to the valid doctoral regulations. However, not all of them are quoted explicitly everywhere. Whether these personal prior printed publications were referenced depends on maintaining comprehensibility and providing all necessary context.

Supervised Student Theses and Projects

Associated with this Ph.D. thesis, a number of student theses and projects were supervised by the author of the present work. These theses were prepared at the Lehrstuhl für Thermodynamik, Technische Universität München in the years 2018 to 2021 under the close supervision of the present author. Parts of these supervised theses may be incorporated into the present thesis. The author would like to express his sincere gratitude to all formerly supervised students for their commitment and support of this research project.

Name	Title, thesis/project type, submission date
Francisco García Villanueva	Quantification of Acoustic Driving Rates in Gas Turbine Combustion Chambers, Bachelor's thesis, September 5, 2018
Elizabeth A. Donlon	Numerical Investigation of High-Frequency Thermoacoustic Oscillations in Gas Turbine Combustors, Fulbright Research Fellowship, July 10, 2019
Benedikt Goderbauer	Entwicklung einer numerischen Methode zur Untersuchung von Interaktionen zwischen Akustik und Verbrennung in nicht-kompakten thermoakustischen Systemen, MSE Forschungspraktikums/student assistant project, March 25, 2019
Julian Läufer	Generation of Heat Release Perturbations due to Acoustically Induced Vortex Shedding in Non-Compact Thermoacoustic Systems, Master's thesis, May 8, 2020
Surya Bharathi Thangavelu	Simulation of an area jump case using PIANO, student assistant project, August 31, 2020

Bibliography

[1] Njiru, C. W., Letema, S. C., and Hu, J., 2018. "Energy Poverty and Its Implication on Standard of Living in Kirinyaga, Kenya". *Journal of Energy,* ***2018***, pp. 209 – 229.

[2] Ferguson, R., Wilkinson, W., and Hill, R., 2000. "Electricity Use and Economic Development". *Energy Policy,* ***28***(13), pp. 923 – 934.

[3] International Energy Agency, 2016. "World energy outlook 2019". *https://www.iea.org/reports/world-energy-outlook-2019.*

[4] Rabl, A., and Spadaro, J. V., 2000. "Public Health Impact of Air Pollution and Implications for the Energy System". *Annual Review of Energy and the Environment,* ***25***(1), pp. 601 – 627.

[5] Intergovernmental Panel on Climate Change, 2014. *Climate Change 2013-The Physical Science Basis: Working Group I Contribution to the Fifth Assessment Report of the Intergovernmental Panel on Climate Change.* Cambridge University Press.

[6] Heidari, N., and Pearce, J. M., 2016. "A review of greenhouse gas emission liabilities as the value of renewable energy for mitigating lawsuits for climate change related damages". *Renewable and Sustainable Energy Reviews,* ***55***, pp. 899–908.

[7] Ciscar, J., Iglesias, A., Feyen, L., Szabó, L., Van Regemorter, D., Amelung, B., Nicholls, R., Watkiss, P., Christensen, O. B., Dankers, R., Garrote, L., Goodess, C. M., Hunt, A., Moreno, A., Richards, J., and Soria, A., 2011. "Physical and Economic Consequences of Climate Change in Europe". *Proceedings of the National Academy of Sciences,* ***108***(7), pp. 2678 – 2683.

[8] Teske, S., Sawyer, S., Schäfer, O., T., P., Simon, S., Naegler, T., Schmid, S., Özdemir, E. D., Pagenkopf, J., Kleiner, F., Rutovitz, J., Dominish, E., Downes, J., Ackermann, T., Brown, T., Boxer, S., Baitelo, R., and Rodrigues, L. A., 2015. Energy [R]evolution - A sustainable World Energy Outlook 2015. Tech. rep., Greenpeace International, September.

[9] Goldthau, A., 2014. "Rethinking the Governance of Energy Infrastructure: Scale, Decentralization and Polycentrism". *Energy Research & Social Science,* ***1***, pp. 134 – 140.

[10] Crabtree, G., Misewich, J., Ambrosio, R., Clay, K., DeMartini, P., James, R., Lauby, M., Mohta, V., Moura, J., Sauer, P., Slakey, F., Lieberman, J., and Tai, H., 2011. "Integrating Renewable Electricity on the Grid". *AIP Conference Proceedings,* ***1401***(1), pp. 387 – 405.

[11] de Groot, M., Crijns-Graus, W., and Harmsen, R., 2017. "The effects of variable renewable electricity on energy efficiency and full load hours of fossil-fired power plants in the european union". *Energy,* ***138***, pp. 575 – 589.

[12] Gonzalez-Salazar, M. A., Kirsten, T., and Prchlik, L., 2018. "Review of the Operational Flexibility and Emissions of Gas- and Coal-Fired Power Plants in a Future with Growing Renewables". *Renewable and Sustainable Energy Reviews,* ***82***, pp. 1497 – 1513.

[13] McDonell, V., 2008. "Chapter 5-Lean Combustion in Gas Turbines". In *Lean Combustion*, D. Dunn-Rankin, ed. Academic Press, Burlington, pp. 121 – IV.

[14] United Nations, 2015. "Paris agreement 2015".

[15] National Academies of Sciences, Engineering, and Medicine, 2020. *Advanced Technologies for Gas Turbines.* The National Academies Press, Washington, D.C.

[16] Sattelmayer, T., 2010. "Grundlagen der Verbrennung in stationären Gasturbinen". In *Stationäre Gasturbinen*, C. Lechner and J. Seume, eds. Springer Berlin Heidelberg, Berlin, Heidelberg, pp. 397 – 452.

[17] Lieuwen, T. C., 2012. *Unsteady Combustor Physics.* Cambridge University Press.

[18] Kergomard, J., Debut, V., and Matignon, D., 2006. "Resonance Modes in a One-Dimensional Medium with two Purely Resistive Boundaries: Calculation methods, Orthogonality, and Completeness". *The Journal of the Acoustical Society of America,* ***119***(3), pp. 1356 – 1367.

[19] Culick, F., 2008. "Unsteady motions in combustion chambers for propulsion systems". Vol. TR-IST-028 of *RTO technical report,* N.A.T.O.

[20] Polifke, W., 2004. "Combustion Instabilities". *VKI Lecture Series.*

[21] Lieuwen, T., 2003. "Modeling Premixed Combustion-Acoustic Wave Interactions: A Review". *Journal of Propulsion and Power,* ***19***(5), pp. 765 – 781.

[22] Hummel, T., Berger, F., Hertweck, M., Schuermans, B., and Sattelmayer, T., 2017. "High-Frequency Thermoacoustic Modulation Mechanisms in Swirl-Stabilized Gas Turbine Combustors - Part II: Modeling and Analysis". *ASME. J. Eng. Gas Turbines Power,* ***139***(7). 071502.

[23] Buechner, H., Hirsch, C., and Leuckel, W., 1993. "Experimental Investigations on the Dynamics of Pulsated Premixed Axial Jet Flames". *Combustion Science and Technology,* ***94***(1-6), pp. 219 – 228.

[24] Hettel, M., Büchner, H., Habisreuther, P., Bockhorn, H., and Zarzalis, N., 2004. "Modeling of Ring Vortices and their Interaction with Turbulent Premixed Flames". *Combustion Science and Technology,* ***176***(5-6), pp. 835 – 850.

[25] Schuermans, B., Bellucci, V., Guethe, F., Meili, F., Flohr, P., and Paschereit, C. O., 2004. "A Detailed Analysis of Thermoacoustic Interaction Mechanisms in a Turbulent Premixed Flame". Vol. 1: Turbo Expo 2004 of *Proceedings of the ASME Turbo Expo 2004: Power for Land, Sea, and Air,* pp. 539 – 551. GT2004-53831.

[26] Lieuwen, T. C., and Yang, V., 2005. "Chapter 9.3.1 Flame-Vortex Interactions". In *Combustion Instabilities in Gas Turbine Engines - Operational*

Experience, Fundamental Mechanisms, and Modeling - Progress in Astronautics and Aeronautics, Volume 210. American Institute of Aeronautics and Astronautics (AIAA).

[27] Lee, J. G., Kwanwoo, K., and Santavicca, D., 2000. "Measurement of Equivalence Ratio Fluctuation and its Effect on Heat Release during Unstable Combustion". *Proceedings of the Combustion Institute,* ***28***(1), pp. 415 – 421.

[28] Rayleigh, J. W. S., 1926. "The Theory of Sound". volume 1 & 2, 2nd Edition, Macmillan.

[29] Schuermans, B., Bellucci, V., and Paschereit, C. O., June 16–19, 2003. "Thermoacoustic Modeling and Control of Multi Burner Combustion Systems". Vol. 2: Turbo Expo 2003 of *Proceedings of the ASME Turbo Expo 2003, collocated with the 2003 International Joint Power Generation Conference*, ASME, pp. 509 – 519. GT2003-38688.

[30] Betz, M., 2018. "Untersuchung passiver ma"snahmen zur erh"ohungder thermoakustischen stabilit"atvon ringbrennkammern".

[31] Lieuwen, T. C., and Yang, V., 2005. "Chapter 17.2 Control-System Models". In *Combustion Instabilities in Gas Turbine Engines - Operational Experience, Fundamental Mechanisms, and Modeling - Progress in Astronautics and Aeronautics, Volume 210.* American Institute of Aeronautics and Astronautics (AIAA).

[32] Bothien, M. R., Noiray, N., and Schuermans, B., 2013. "A Novel Damping Device for Broadband Attenuation of Low-Frequency Combustion Pulsations in Gas Turbines". *ASME. J. Eng. Gas Turbines Power,* ***136***(4). 041504.

[33] Zhao, D., and Li, X., 2015. "A Review of Acoustic Dampers Applied to Combustion Chambers in Aerospace Industry". *Progress in Aerospace Sciences,* ***74***, pp. 114 – 130.

[34] Field, C., and Fricke, F., 1998. "Theory and Applications of Quarter-Wave Resonators: A Prelude to their Use for Attenuating Noise Entering Buildings through Ventilation Openings". *Applied Acoustics,* ***53***(1), pp. 117 – 132.

[35] Bellucci, V., Flohr, P., Paschereit, C. O., and Magni, F., 2004. "On the Use of Helmholtz Resonators for Damping Acoustic Pulsations in Industrial Gas Turbines ". *Journal of Engineering for Gas Turbines and Power,* ***126***(2), 06, pp. 271 – 275.

[36] Bellucci, V., Schuermans, B., Nowak, D., Flohr, P., and Paschereit, C. O., 2005. "Thermoacoustic Modeling of a Gas Turbine Combustor Equipped With Acoustic Dampers ". *Journal of Turbomachinery,* ***127***(2), 05, pp. 372 – 379.

[37] Hummel, T., 2019. "Modeling and Analysis of High-Frequency Thermoacoustic Oscillations in Gas Turbine Combustion Chambers". *Ph.D. Thesis,* Technical University of Munich, Lehrstuhl für Thermodynamik.

[38] Richards, G. A., and Janus, M. C., 1998. "Characterization of Oscillations During Premix Gas Turbine Combustion". *ASME. J. Eng. Gas Turbines Power,* ***120***(2), 04, pp. 294 – 302.

[39] McManus, K., Poinsot, T., and Candel, S., 1993. "A review of active control of combustion instabilities". *Progress in Energy and Combustion Science,* ***19***(1), pp. 1 – 29.

[40] Dowling, A., 1995. "The Calculation of Thermoacoustic Oscillations". *Journal of Sound and Vibration,* ***180***(4), pp. 557 – 581.

[41] Dowling, A., and Stow, S., 2003. "Acoustic analysis of gas turbine combustors". *Journal of Propulsion and Power,* ***19***(5), pp. 751 – 764.

[42] Sujith, R., Waldherr, G., and Zinn, B., 1995. "An Exact Solution for One-Dimensional Acoustic Fields in Ducts with an Axial Temperature Gradient". *Journal of Sound and Vibration,* ***184***(3), pp. 389 – 402.

[43] Meindl, M., Albayrak, A., and Polifke, W., 2020. "A State-Space Formulation of a Discontinuous Galerkin Method for Thermoacoustic Stability Analysis". *Journal of Sound and Vibration,* ***481***. 115431.

[44] Dowling, A. P., 1997. "Nonlinear self-excited oscillations of a ducted flame". *Journal of Fluid Mechanics,* ***346***, pp. 271–290.

[45] Noiray, N., Bothien, M., and Schuermans, B., 2011. “Investigation of azimuthal staging concepts in annular gas turbines”. *Combustion Theory and Modelling,* ***15***(5), pp. 585 – 606.

[46] Moeck, J. P., Durox, D., Schuller, T., and Candel, S., 2019. “Nonlinear thermoacoustic mode synchronization in annular combustors”. *Proceedings of the Combustion Institute,* ***37***(4), pp. 5343 – 5350.

[47] Ghirardo, G., and Juniper, M. P., 2013. “Azimuthal instabilities in annular combustors: Standing and spinning modes”. *Proceedings of the Royal Society A: Mathematical, Physical and Engineering Sciences,* ***469***(2157). 20130232.

[48] Hummel, T., Hammer, K., Romero, P., Schuermans, B., and Sattelmayer, T., 2017. “Low-Order Modeling of Nonlinear High-Frequency Transversal Thermoacoustic Oscillations in Gas Turbine Combustors”. *ASME. J. Eng. Gas Turbines Power,* ***139***(7), 02. 071503.

[49] Schulze, M., Hummel, T., Klarmann, N., Berger, F., Schuermans, B., and Sattelmayer, T., 2017. “Linearized Euler Equations for the Prediction of Linear High-Frequency Stability in Gas Turbine Combustors”. *ASME. J. Eng. Gas Turbines Power,* ***139***(3). 031510.

[50] Gikadi, J., 2014. “Prediction of Acoustic Modes in Combustors using Linearized Navier-Stokes Equations in Frequency Space”. *Ph.D. Thesis,* Technical University of Munich, Lehrstuhl für Thermodynamik.

[51] Schuermans, B., Paschereit, C., and Monkewitz, P., 2006. “Non-Linear Combustion Instabilities in Annular Gas-Turbine Combustors”. In 44th AIAA Aerospace Sciences Meeting and Exhibit, American Institute of Aeronautics and Astronautics.

[52] Lieuwen, T., and Neumeier, Y., 2002. “Nonlinear pressure-heat release transfer function measurements in a premixed combustor”. *Proceedings of the Combustion Institute,* ***29***(1), pp. 99 – 105. Proceedings of the Combustion Institute.

[53] Bellows, B. D., Bobba, M. K., Seitzman, J. M., and Lieuwen, T., 2006. “Nonlinear Flame Transfer Function Characteristics in a Swirl-Stabilized Combustor”. *ASME. J. Eng. Gas Turbines Power,* ***129***(4), 12, pp. 954 – 961.

[54] Balachandran, R., Ayoola, B., Kaminski, C., Dowling, A., and Mastorakos, E., 2005. "Experimental Investigation of the Nonlinear Response of Turbulent Premixed Flames to Imposed Inlet Velocity Oscillations". *Combustion and Flame,* ***143***(1), pp. 37 – 55.

[55] Moeck, J., and Paschereit, C., 2012. "Nonlinear Interactions of Multiple Linearly Unstable Thermoacoustic Modes". *International Journal of Spray and Combustion Dynamics,* ***4***(1), pp. 1 – 27.

[56] Moeck, J. P., Durox, D., Schuller, T., and Candel, S., 2019. "Nonlinear thermoacoustic mode synchronization in annular combustors". *Proceedings of the Combustion Institute,* ***37***(4), pp. 5343–5350.

[57] Bonciolini, G., and Noiray, N., 2019. "Synchronization of thermoacoustic modes in sequential combustors". *Journal of Engineering for Gas Turbines and Power,* ***141***(3), p. 1149.

[58] Hummel, T., Berger, F., Schuermans, B., and Sattelmayer, T., 2016. "Theory and Modeling of Non-Degenerate Transversal Thermoacoustic Limit Cycle Oscillations". Proceedings of the International Symposium on Thermoacoustic Instabilities in Gas Turbines and Rocket Engines: Industry meets Academia, Technical University of Munich, Institute for Theromdynamics / Institute for Advanced Studies.

[59] Schuermans, B., Bothien, M., Maurer, M., and Bunkute, B., 2015. "Combined Acoustic Damping-Cooling System for Operational Flexibility of GT26/GT24 Reheat Combustors". Vol. 4A: Combustion, Fuels and Emissions of *Proceedings of the ASME Turbo Expo 2015: Turbine Technical Conference and Exposition.* GT2015-56680.

[60] Lorstad, D., Pettersson, J., and Lindholm, A., 2009. "Emission Reduction and Cooling Improvements Due to the Introduction of Passive Acoustic Damping in an Existing SGT-800 Combustor". Vol. 3: Heat Transfer, Parts A and B of *Proceedings of the ASME Turbo Expo 2009: Power for Land, Sea, and Air*, pp. 1355 – 1362. GT2009-48845.

[61] Berger, F. M., 2019. "High Frequency Transverse ThermoacousticInstabilities in Swirl and Reheat Combustors". *Ph.D. Thesis,* Technical University of Munich, Lehrstuhl für Thermodynamik.

[62] Tonon, D., 2011. "Aeroacoustics of Shear Layers in Internal Flows: Closed Branches and Wall Perforations". *Ph.D. Thesis.*

[63] Kriesels, P., Peters, M., Hirschberg, A., Wijnands, A., Iafrati, A., Riccardi, G., Piva, R., and Bruggeman, J., 1995. "High Amplitude Vortex-Induced Pulsations in a Gas Transport System". *Journal of Sound and Vibration,* ***184***(2), pp. 343 – 368.

[64] Schwing, J., Grimm, F., and Sattelmayer, T., 2012. "A Model for the Thermo-Acoustic Feedback of Transverse Acoustic Modes and Periodic Oscillations in Flame Position in Cylindrical Flame Tubes". Vol. 2: Combustion, Fuels and Emissions, Parts A and B of *Proceedings of the ASME Turbo Expo 2012: Turbine Technical Conference and Exposition*, pp. 553 – 566.

[65] Howe, M. S., 1979. "On the theory of unsteady high reynolds number flow through a circular aperture". *Proceedings of the Royal Society A: Mathematical, Physical and Engineering Sciences,* ***366***(1725), pp. 205 – 223.

[66] Howe, M. S., 1979. "Attenuation of sound in a low mach number nozzle flow". *Journal of Fluid Mechanics,* ***91***(2), pp. 209 – 229.

[67] Howe, M. S., 1980. "The dissipation of sound at an edge". *Journal of Sound and Vibration,* ***70***(3), pp. 407 – 411.

[68] Howe, M. S., 1984. "On the Absorption of Sound by Turbulence and Other Hydrodynamic Flows". *IMA Journal of Applied Mathematics,* ***32***(1 - 3), 01, pp. 187–209.

[69] Bechert, D., 1980. "Sound Absorption Caused by Vorticity Shedding, Demonstrated with a Jet Flow". *Journal of Sound and Vibration,* ***70***(3), pp. 389 – 405.

[70] Berger, F., Hummel, T., Schuermans, B., and Sattelmayer, T., 2018. "Pulsation-Amplitude-Dependent Flame Dynamics of High-Frequency Thermoacoustic Oscillations in Lean-Premixed Gas Turbine Combustors". *ASME. J. Eng. Gas Turbines Power,* ***140***(4), Apr. 041507.

[71] Poinsot, T., and Veynante, D., 2005. "Theoretical and numerical combustion".

[72] Smagorinsky, J., 1963. "General Circulation Experiments With The Primitive Equations". *Monthly Weather Review,* ***91***(3), pp. 99 – 164.

[73] Wolf, P., Staffelbach, G., Roux, A., Gicquel, L., Poinsot, T., and Moureau, V., 2009. "Massively Parallel LES of Azimuthal Thermo-Acoustic Instabilities in Annular Gas Turbines". *Comptes Rendus Mécanique,* ***337***(6), pp. 385 – 394. Combustion for aerospace propulsion.

[74] Selle, L., Benoit, L., Poinsot, T., Nicoud, F., and Krebs, W., 2006. "Joint Use of Compressible Large-Eddy Simulation and Helmholtz Solvers for the Analysis of Rotating Modes in an Industrial Swirled Burner". *Combustion and Flame,* ***145***(1), pp. 194 – 205.

[75] Ghani, A., Poinsot, T., Gicquel, L., and Staffelbach, G., 2015. "LES of Longitudinal and Transverse Self-Excited Combustion Instabilities in a Bluff-Body Stabilized Turbulent Premixed Flame". *Combustion and Flame,* ***162***(11), pp. 4075 – 4083.

[76] Favre, A. J. A., 1992. *Formulation of the Statistical Equations of Turbulent Flows with Variable Density.* Springer New York, New York, NY, pp. 324 – 341.

[77] Klarmann, N. E., 2019. "Modeling Turbulent Combustion and COEmissions in Partially-Premixed ConditionsConsidering Flame Stretch and Heat Loss". *Ph.D. Thesis,* Technical University of Munich, Lehrstuhl für Thermodynamik.

[78] Sattelmayer, T., Schmid, M., and Schulze, M., 2015. "Interaction of Combustion with Transverse Velocity Fluctuations in Liquid Rocket Engines". *Journal of Propulsion and Power,* ***31***(4), pp. 1137 – 1147.

[79] Inc., A. "Ansys fluent theory guide".

[80] Ferziger, J. H., and Perić, M., 2002. "Computational Methods for Fluid Dynamics".

[81] Berger, F., Hummel, T., Hertweck, M., Kaufmann, J., Schuermans, B., and Sattelmayer, T., 2017. "High-Frequency Thermoacoustic Modulation Mechanisms in Swirl-Stabilized Gas Turbine Combustors - Part I: Experimental Investigation of Local Flame Response". *ASME. J. Eng. Gas Turbines Power,* ***139***(7). 071501.

[82] Chu, B., and Kovásznay, L. S. G., 1958. "Non-Linear Interactions in a Viscous Heat-Conducting Compressible Gas". *Journal of Fluid Mechanics,* ***3***(5), pp. 494 – 514.

[83] Sattelmayer, T., 2003. "Influence of the Combustor Aerodynamics on Combustion Instabilities From Equivalence Ratio Fluctuations". *ASME. J. Eng. Gas Turbines Power,* ***125***(1), 1, pp. 11 – 19.

[84] Strobio Chen, L., Bomberg, S., and Polifke, W., 2016. "Propagation and Generation of Acoustic and Entropy Waves Across a Moving Flame Front". *Combustion and Flame,* ***166***, pp. 170 – 180.

[85] Weilenmann, M., Xiong, Y., and Noiray, N., 2020. "On the Dispersion of Entropy Waves in Turbulent Flows". *Journal of Fluid Mechanics,* ***903***, p. R1.

[86] Xia, Y., Duran, I., Morgans, A. S., and Han, X., 2018. "Dispersion of Entropy Perturbations Transporting through an Industrial Gas Turbine Combustor". *Flow, Turbulence and Combustion,* ***100***, pp. 481 – 502.

[87] Romero, P. V., 2021. "Numerical Modeling of High-Frequency Transverse Thermoacoustic Instabilities in Reheat Combustors". *Ph.D. Thesis*, Technical University of Munich, Lehrstuhl für Thermodynamik.

[88] Meindl, M., Silva, C., and Polifke, W., 2021. "On the Spurious Entropy Generation Encountered in Hybrid Linear Thermoacoustic Models". *Combustion and Flame,* ***223***, pp. 525 – 540.

[89] Ewert, R., and Schröder, W., 2003. "Acoustic Perturbation Equations based on Flow Decomposition via Source Filtering". *Journal of Computational Physics,* ***188***(2), pp. 365 – 398.

[90] Nicoud, F., and Wieczorek, K., 2009. "About the Zero Mach Number Assumption in the Calculation of Thermoacoustic Instabilities". *International Journal of Spray and Combustion Dynamics,* ***1***(1), pp. 67 – 111.

[91] Heilmann, G., Hirsch, C., and Sattelmayer, T. "Energetically Consistent Computation of Combustor Stability With a Model Consisting of a Helmholtz-FEM-Domain and a Low-Order Network". *ASME. J. Eng. Gas Turbines Power,* ***139***(7). 071501.

[92] Lele, S., 1997. "Computational Aeroacoustics - A Review". In *35th Aerospace Sciences Meeting and Exhibit.*

[93] Poinsot, T., and Lele, S., 1992. "Boundary Conditions for Direct Simulations of Compressible Viscous Flows". *Journal of Computational Physics,* ***101***(1), pp. 104 – 129.

[94] Myers, M. K., 1986. "An Exact Energy Corollary for Homentropic Flow". *Journal of Sound and Vibration,* ***109***(2), pp. 277 – 284.

[95] Myers, M. K., 1991. "Transport of Energy by Disturbances in Arbitrary Steady Flows". *Journal of Fluid Mechanics,* ***226***, pp. 383 – 400.

[96] Goldstein, M. E., 1976. *Aeroacoustics.* McGraw-Hill, New York and London.

[97] Motheau, E., Selle, L., and Nicoud, F., 2014. "Accounting for Convective Effects in Zero-Mach-Number Thermoacoustic Models". *Journal of Sound and Vibration,* ***333***(1), pp. 246 – 262.

[98] Hofmeister, T., Hummel, T., and Sattelmayer, T., 2021. "Impact of the Stabilized Finite Element Method On Acoustic and Vortical Perturbations in Thermoacoustic Systems". *ASME. J. Eng. Gas Turbines Power,* ***143***(6), June. 061012.

[99] Donéa, J., and Huerta, A., 2003. *Finite Element Methods for Flow Problems.* John Wiley & Sons, Ltd, ch. 1&2, pp. 1 – 78.

[100] Fries, T., and Matthies, H. G., 2004. "Review of Petrov-Galerkin Stabilization Approaches and an Extension to Meshfree Methods". *Informatik-Berichte der Technischen Universität Braunschweig,* ***2004-01***.

[101] Brooks, A. N., and Hughes, T. J., 1982. "Streamline Ppwind/Petrov-Galerkin Formulations for Convection Dominated Flows with Particular Emphasis on the Incompressible Navier-Stokes Equations". *Computer Methods in Applied Mechanics and Engineering,* ***32***(1-3), pp. 199 – 259.

[102] Tezduyar, T., Mittal, S., Ray, S., and Shih, R., 1992. "Incompressible Flow Computations with Stabilized Bilinear and Linear Equal-Order-Interpolation Velocity-Pressure Elements". *Computer Methods in Applied Mechanics and Engineering,* ***95***(2), pp. 221 – 242.

[103] Rao, P. P., and Morris, J., 2006. "Use of Finite Element Methods in Frequency Domain Aeroacoustics". *AIAA Journal,* ***44***(7), pp. 1643 – 1652.

[104] Hofmeister, T., Hummel, T., Schuermanns, B., and Sattelmayer, T., 2020. "Modeling and Quantification of Acoustic Damping Induced by Vortex Shedding in Noncompact Thermoacoustic Systems". *ASME. J. Eng. Gas Turbines Power,* ***142***(3). 031016.

[105] Hertweck, M. F., 2019. "Einfluss der Flammenposition auf transversale hochfrequente akustische Moden in zylindrischen Brennkammern". *Ph.D. Thesis,* Technical University of Munich, Lehrstuhl für Thermodyamik.

[106] Schwing, J. E., 2019. "Über die Interaktion von transversalen akustischen Moden, Strömung und drallstabilisierter Flamme in zylindrischen Flammrohren". *Ph.D. Thesis,* Technical University of Munich, Lehrstuhl für Thermodyamik.

[107] Mayer, C., 2019. "Konzept zur vorgemischten Verbrennung wasserstoffhaltiger Brennstoffe in Gasturbinen". *Ph.D. Thesis,* Technical University of Munich, Lehrstuhl für Thermodyamik.

[108] Cantrell, R. H., and Hart, R. W., 1964. "Interaction between Sound and Flow in Acoustic Cavities: Mass, Momentum, and Energy Considerations". *The Journal of the Acoustical Society of America,* ***36***(4), pp. 697 – 706.

[109] Helmholtz, H., 1858. "Über Integrale der hydrodynamischen Gleichungen, welche den Wirbelbewegungen entsprechen.". *Journal für die reine und angewandte Mathematik,* ***1858***(55), pp. 25 – 55.

[110] Bhatia, H., Norgard, G., Pascucci, V., and Bremer, P., 2013. "The Helmholtz-Hodge Decomposition: A Survey". *IEEE Transactions on Visualization and Computer Graphics,* ***19***(8), Aug., pp. 1386 – 1404.

[111] Pierce, A. D., 1990. "Wave Equation for Sound in Fluids with Unsteady Inhomogeneous Flow". *The Journal of the Acoustical Society of America,* ***87***(6), pp. 2292–2299.

[112] Lunze, J., 2010. *Verhalten linearer Systeme.* Springer Berlin Heidelberg, Berlin, Heidelberg, pp. 119 – 222.

[113] Gentemann, A., Fischer, A., Evesque, S., and Polifke, W., 2012. "Acoustic Transfer Matrix Reconstruction and Analysis for Ducts with Sudden Change of Area". 9th AIAA/CEAS Aeroacoustics Conference and Exhibit.

[114] Schulze, M., 2016. "Linear Stability Assessment of Cryogenic Rocket Engines". *Ph.D. Thesis,* Technical University of Munich, Lehrstuhl für Thermodynamik.

[115] Ronneberger, D., 1987. "Theoretische und experimentelle Untersuchung der Schallausbreitung durch Querschnittssprünge und Lochplatten in Strömungskanälen". Drittes Physikalisches Institut der Universität Göttingen, Göttingen, Germany, Report No. Ro-369-11-12-14.

[116] Zellhuber, M., 2019. "High Frequency Response of Auto-Ignition and Heat Release to Acoustic Perturbations". *Ph.D. Thesis,* Technical University of Munich, Lehrstuhl für Thermodynamik.

[117] D., K. N., 2019. "Chapter 7 - Vorticity Dynamics". In *Free-Surface Flow,* N. D. Katopodes, ed. Butterworth-Heinemann, pp. 516–565.

[118] Law, C. K., 2006. *Combustion Physics.* Cambridge University Press.

[119] Hirsch, C., Fanaca, D., Reddy, P., Polifke, W., and Sattelmayer, T., 2005. "Influence of the Swirler Design on the Flame Transfer Function of Premixed Flames". Vol. 2: Turbo Expo 2005 of *Proceedings of the ASME Turbo Expo 2005: Power for Land, Sea, and Air.* GT2005-68195.

[120] Searby, G., Habiballah, M., Nicole, A., and Laroche, E., 2008. "Prediction of the Efficiency of Acoustic Damping Cavities". *Journal of Propulsion and Power,* ***24***(3), pp. 516 – 523.

[121] Klarmann, N., Sattelmayer, T., Geng, W., Zoller, B. T., and Magni, F., 2016. "Impact of Flame Stretch and Heat Loss on Heat Release Distributions in Gas Turbine Combustors: Model Comparison and Validation". Vol. 4B: Combustion, Fuels and Emissions of *Proceedings of the ASME Turbo Expo 2016: Turbomachinery Technical Conference and Exposition*. GT2016-57625.

[122] Smith, G. P., Golden, D. M., Frenklach, M., Moriarty, N. W., Eiteneer, B., Goldenberg, M., Bowman, C. T., Hanson, R. K., S., S., Gardiner, W. C. J., Lissianski, V. V., and Qin, Z. "Gri-mech 3.0". `http://www.me.berkeley.edu/gri_mech/`.

[123] Hofmeister, T., and Sattelmayer, T., 2021. "Amplitude-Dependent Damping and Driving Rates of High-Frequency Thermoacoustic Oscillations in a Lab-Scale Lean-Premixed Gas Turbine Combustor". Vol. 4: Combustion, Fuels and Emissions of *Proceedings of the ASME Turbo Expo 2021: Turbomachinery Technical Conference and Exposition*. GT2021-58456.

[124] Bloxsidge, G. J., Dowling, A. P., and Langhorne, P. J., 1988. "Reheat Buzz: An Acoustically Coupled Combustion Instability. Part 2. Theory". *Journal of Fluid Mechanics*, ***193***, pp. 445 – 473.

[125] Langhorne, P. J., 1988. "Reheat Buzz: An Acoustically Coupled Combustion Instability. Part 1. Experiment". *Journal of Fluid Mechanics*, ***193***, pp. 417 – 443.

[126] Klarmann, N., and Sattelmayer, T., 2020. "Canonical Validation of a Modeling Strategy for Carbon Monoxide Emissions in Staged Operation of Gas Turbine Combustors". *Journal of the Global Power and Propulsion Society*, ***4***, pp. 161 – 175.

[127] Hummel, T., Berger, F., Schuermans, B., and Sattelmayer, T., 2016. "Theory and Modeling of Non-Degenerate Transversal Thermoacoustic Limit Cycle Oscillations".

[128] Noiray, N., Durox, D., Schuller, T., and Candel, S., 2008. "A Unified Framework for Nonlinear Combustion Instability Analysis based on the

Flame Describing Function". *Journal of Fluid Mechanics*, ***615***, pp. 139 – 167.

[129] Schimek, S., Cosic, B., Moeck, J. P., Terhaar, S., and Paschereit, C. O., 2015. "Amplitude-Dependent Flow Field and Flame Response to Axial and Tangential Velocity Fluctuations". *ASME. J. Eng. Gas Turbines Power*, ***137***(8), 08. 081501.

[130] Bourgouin, J., Durox, D., Moeck, J., Schuller, T., and Candel, S., 2015. "A new Pattern of Instability Observed in an Annular Combustor: The Slanted Mode". *Proceedings of the Combustion Institute*, ***35***(3), pp. 3237 – 3244.

[131] Bonciolini, G., and Noiray, N., 2019. "Synchronization of Thermoacoustic Modes in Sequential Combustors". *Journal of Engineering for Gas Turbines and Power*, ***141***(3), 03, p. 031010.

[132] Pikovsky, A., Rosenblum, M., and Kurths, J., 2001. *Synchronization: A Universal Concept in Nonlinear Sciences*. Cambridge Nonlinear Science Series. Cambridge University Press.

[133] Penelet, G., and Biwa, T., 2013. "Synchronization of a Thermoacoustic Oscillator by an External Sound Source". *American Journal of Physics*, ***81***(4), pp. 290 – 297.

[134] Hofmeister, T., Hummel, T., Schuermans, B., and Sattelmayer, T., 2019. "Quantification of Energy Transformation Processes between Acoustic and Hydrodynamic Perturbation Modes in Non-Compact Thermoacoustic Systems via a Helmholtz-Hodge Decomposition Approach". Vol. 4A: Combustion, Fuels, and Emissions of *Proceedings of the ASME Turbo Expo 2019: Turbomachinery Technical Conference and Exposition*. GT2019-90240.

[135] Mensah, G., Campa, G., and Moeck, J. P., 2016. "Efficient Computation of Thermoacoustic Modes in Industrial Annular Combustion Chambers Based on Bloch-Wave Theory". *ASME. J. Eng. Gas Turbines Power*, ***138***(8), p. 7. 081502.

[136] Haeringer, M., and Polifke, W., 2019. "Time-Domain Bloch Boundary Conditions for Efficient Simulation of Thermoacoustic Limit Cycles in (Can-)Annular Combustors". *ASME. J. Eng. Gas Turbines Power,* ***141***(12). 121005.

[137] Bloch, F., 1929. "Über die Quantenmechanik der Elektronen in Kristallgittern". *Zeitschrift für Physik*(52), pp. 555 – 600.

[138] Ghirardo, G., Di Giovine, C., Moeck, J., and Bothien, M. R., 2019. "Thermoacoustics of Can-Annular Combustors". *ASME. J. Eng. Gas Turbines Power,* ***141***(1). 011007.

[139] Hofmeister, T., Hummel, T., Berger, F., Klarmann, N., and Sattelmayer, T., 2021. "Elimination of Numerical Damping in the Stability Analysis of Noncompact Thermoacoustic Systems With Linearized Euler Equations". *ASME. J. Eng. Gas Turbines Power,* ***143***(3), March. 031013.

[140] Romero Vega, P., Berger, F. M., Hummel, T., Schuermans, B., and Sattelmayer, T., 2018. "Numerical Design of a Novel Reheat Combustor Experiment for the Analysis of High-Frequency Flame Dynamics". Vol. 4B: Combustion, Fuels, and Emissions of *Proceedings of the ASME Turbo Expo 2018: Turbomachinery Technical Conference and Exposition.* GT2018-77034.

[141] Culick, F. E. C., and V., Y., 1992. "Prediction of the Stability of Unsteady Motions in Solid-Propellant Rocket Motors". In: Nonsteady Burning and Combustion Stability of Solid Propellants. Progress in Astronautics and Aeronautics Series Vol. 143. American Institute of Aeronautics and Astronautics, Washington, D.C., pp. 719 – 779.